Hydrogen Sensing Using Palladium Coated Long Period Gratings

Richard Mark Carter

Submitted for the degree of Doctor of Philosophy

School of Engineering and Physical Sciences

Heriot-Watt University

December - 2011

Abstract

The use of palladium coated optical fibres containing an in-fibre long period grating (LPG) structure for the sensing of low concentrations of hydrogen has been investigated. Previous proof of principle experiments were refined and extended, demonstrating sensitivities of up to 60 pm for 1% hydrogen at an operating temperature of 70°C.

Characterisation of the Pd deposition technique (RF sputter coating) including XPS and SEM analysis to investigate surface roughness and contamination were carried out and are discussed. These measurements were prompted by the need to characterise and eliminate sensor drift associated with delamination of the sensor layer.

Particular care was taken to characterise the optical properties of Pd thin films, both in the presence of hydrogen and without, through ellipsometry and surface plasmon resonance, since values gained from the literature showed wide variations. The results presented in this thesis differ from published Pd refractive indices but are specific for the conditions used in this work.

Techniques to directly measure the refractive index profile within the core of an LPG were investigated and a possible solution is presented.

Theoretical models to calculate the transmission spectrum of a LPG, both with and without a Pd layer are presented, discussed and the implications due to the poor characterisation of the LPG are considered.

The potential use of higher order double cladding modes (with up to 20 times the sensitivity of the lower mode orders) as a sensing regime is investigated and the practical limitations discussed.

Acknowledgements

There are a great number of people who helped to make this thesis a reality. Foremost I would like to thank my supervisors Dr Maier and Dr Barton for their contributions, advice and continuous support. I would also like to thank my “unofficial supervisor” Dr MacPherson for his insight and encyclopaedic knowledge of all things optic and all the members of the IOP group.

Special thanks must also go to my sponsors at AWE, particularly Dr Scott McCulloch and Dr Ben Jones, not only for their financial but also their material support with loans of equipment and facilities without which several sections of this thesis would quite literally have not happened.

I would like to also give thanks to the staff at HWU, particularly the workshop, for their practical advice and seemingly limitless patience with my “projects”. Special mention must also go to the Inter Library Loans Staff for fulfilling my sometimes rather vague requests. Neil Ross also deserves thanks for the use of his facilities and technical expertise.

Acknowledgement must also go to my collaborators. Dr Felix Baumberger and Dr Anna Tamai at St-Andrews, for their help with the XPS analysis. The staff at the Edinburgh University School of Geoscience SEM and of course Dr Somnath Bandyopadhyay and Palas Biswas at the CGCRI for their expertise with LPG inscription and modelling.

Finally I would like to thank my family and other animals (those who have shared my office) for the moral support during writing up.

Chapter 1. Introduction

If curiosity killed the cat then it has ennobled mankind. Throughout recorded history humanity has struggled to explain the unexplained and to quantify the world around us. In no field is this more obvious than that of metrology, the science of measurement. Measurement has been essential to the development of human civilisation to the point where it is inconceivable for us to go through a single day without reference to some form of standardised measurement.

The story of metrology is thus as old as civilisation its self. From the very oldest, known, civilisation in the Indus valley with its quite remarkable standardised length measurements, good to ~1mm, through to the Egyptian 'foot' and the Roman 'uncial', each major civilisation group or empire maintained its own standard of measurement. Often these would be based on stylised lengths of the body and time units given by the periodic motion of the heavenly bodies. Alternatives included measurements based on local cultural or religious peculiarities. Interactions between these measurement standardisations were often complex and limited only to a small merchant class who would travel extensively enough to require knowledge of several such systems and the conversion factors between them.

The breakthrough in universal standardisation occurred in the 17th century after the French Revolution. The revolutionary government, keen to export the universal ideals of the revolution, decided to replace the discredited system of weights and measures within France with a new universal system. In contrast to previous systems which were based on comparison to particular artefacts (the king's foot or a particular length of wood defined to be a foot long etc.), this system was to be universal with weights and measures defined through universal constants. The system created, the metric system, while not a perfect implementation of the universal ideal, was swiftly adopted within France and exported wherever French culture held sway. The Napoleonic wars ensured rather slower adoption in the English speaking world but it is now close to a universal standard, with only a few countries, notably the United States, having not adopted it, and a few countries, like the United Kingdom, employing a mixed unit system.

The original definitions have been gradually updated over time to better reflect the meaning of a universal constant. For example, the original definition of the meter, as a

fraction of the earth's circumference through the North Pole and Paris, has been replaced with a more consistent unit based on 1/299 792 458 the speed of light in a vacuum [1]. The kilogram was originally defined as the weight of volume of sea water at specific pressure, temperature, latitude and altitude but this proved to be quite cumbersome and was instead replaced by an artefact, which is still in use [1]. All other units have now been defined in terms of distance and time in some form (and efforts are continuing to also define the kilogram in these terms) with time and distance related by the frequency of atomic (usually caesium) oscillations [1].

1.1. Optical Metrology

The SI units of measurement are, with the exception of the kilogram, defined in terms of time and space and these are linked through frequency. The electromagnetic, EM, spectrum may therefore provide some means to carry out measurement in a fundamental form. The EM spectrum is broad indeed spanning fourteen orders of magnitude, from gamma and x rays through the UV and visible up to the infrared and radio waves (Figure 1). The central, and usually more useful, part of this spectrum may be considered the UV through the visible up to the near IR a region of approximately 200 to 2000 nm or ~ 5 x10^{13} Hz to 5 x10^{15} Hz.

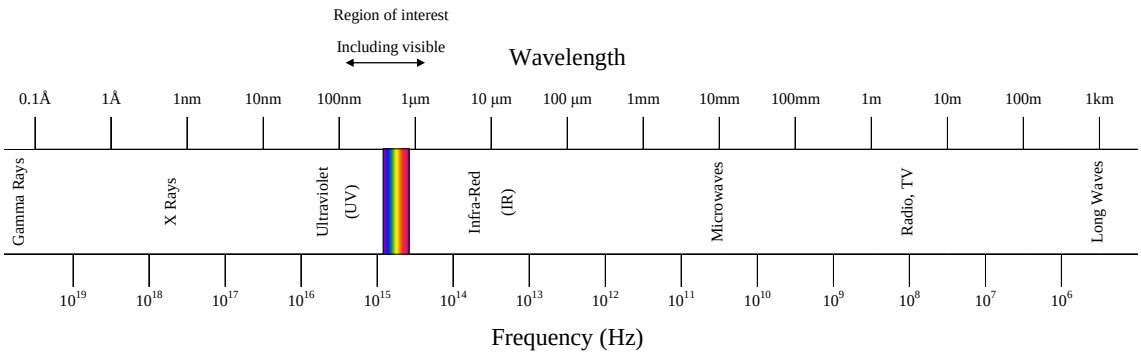

Figure 1: The Electromagnetic (EM) Spectrum

These frequencies are far too high for direct measurement of oscillations. As such it is necessary to employ the properties of waves to create a detectable effect. The simplest

approach is to mix two waves of differing frequency. These two frequencies (f_1 & f_2) will interfere with each other providing a new beat frequency (f_b) where $f_b = |f_1 - f_2|$. With a suitable choice of frequencies this beat frequency can be in the KHz range i.e. detectable through standard techniques. With the advent of lasers this has become relatively simple as laser line widths of a few 10s of Hz are commonly available across much of the EM spectrum. Alternatively a single frequency can be employed and with a suitable physical effect, such as temperature fluctuations of a vibration, a second frequency can be induced, usually with only a very small difference between the two. In this manner detection of the resultant beat frequency, now readily detectable, will provide a sensor for the physical effect.

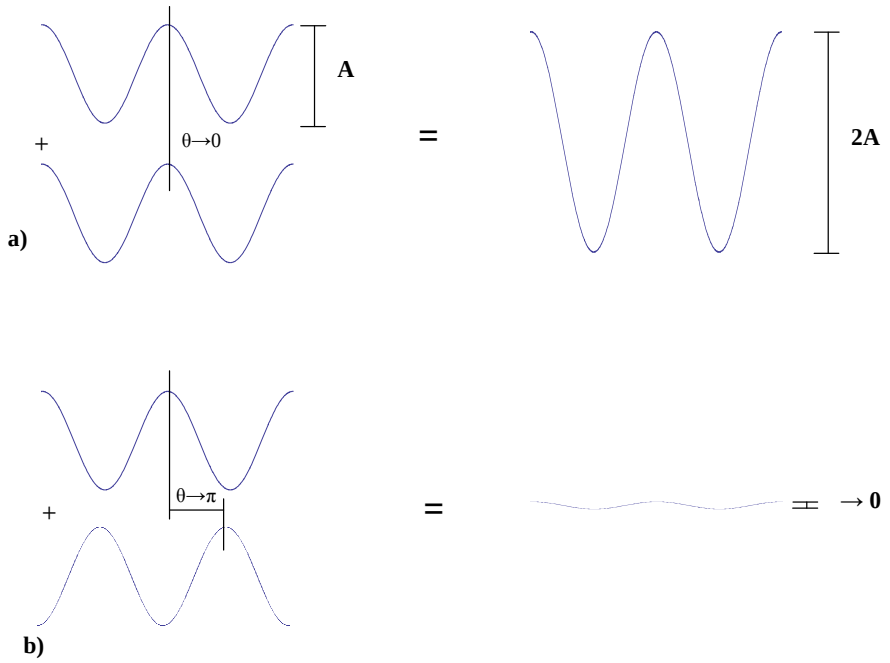

Figure 2: Illustration of a) constructive and b) destructive interference of two waves of the same wavelength and amplitude, A, and phase difference θ.

If there is no difference between two frequencies, e.g. the same beam split by a beam splitter, then the resultant mixed beam will not exhibit a beat frequency, but rather will interfere based on the relative phase difference between the two beams (Figure 2). This produces fringes of light and dark for each 2π of phase shift. This interferometric

technique has become the mainstay of distance based measurements, effectively forming a ruler from the wavelength of the radiation used. In theory the use of shorter wavelengths should allow for more accurate (i.e. finer toothed ruler) measurements but in practice operating outside of the central part of the EM spectrum requires the use of more exotic and therefore more expensive equipment particularly in the case of sources and detectors.

The experiments of Michelson and Morley in the late 19th century have spawned over a hundred years of increasingly complex and precise optical measurement. Three quantum leaps in development can be identified in the last 100 years. The development of Radar in the 1940s is probably still the largest scale out of laboratory use of optical metrology in use today and its development required the invention and implementation of what are now many standard techniques. The development of the laser in the 1960s allowed for the use of optical metrology with hitherto undreamed of μm and ultimately nm scale accuracies and corresponding time resolution. While the use of lasers for optical metrology provided the fine resolution required for precision measurements it is the development of optical fibre which has allowed these fine measurements to escape from the laboratory in a significant scale.

1.2. Fibre Optic technology

While fibre optic development did not begin until the 1960s the principle of guiding via total internal reflection had been demonstrated by Jean-Daniel Colladon in 1842 [2] using a “light fountain” or light pipe to guide light in a water stream. During the 1960’s the further development of computers generated a requirement for high-speed data transfer, and fibre optics were recognised as a possible solution. Due to limitations in the draw process, early fibres used a graded index arrangement and contaminants in the glass resulted in comparatively high losses outside of the 600-900 nm region (Figure 3).

By the 1980s, fibre drawing had improved sufficiently to produce single mode step index fibres, now an industry standard, and the purity of glasses improved to the point of opening the 1300 nm transmission window (Figure 3) by lowering the OH^- absorption peaks. The corresponding low loss quality optical fibre allowed the technology to be deployed worldwide. Fibre optic telecommunications cable started to

be used for long haul cross continental communications [3]. Since then the purity of the glass used for the fibres has improved to the point that the 1550 nm window has opened, with corresponding low loss (Figure 3) and is used almost universally for telecoms with the possibility now being discussed of a window, the U band, extending to 1700 nm [4].

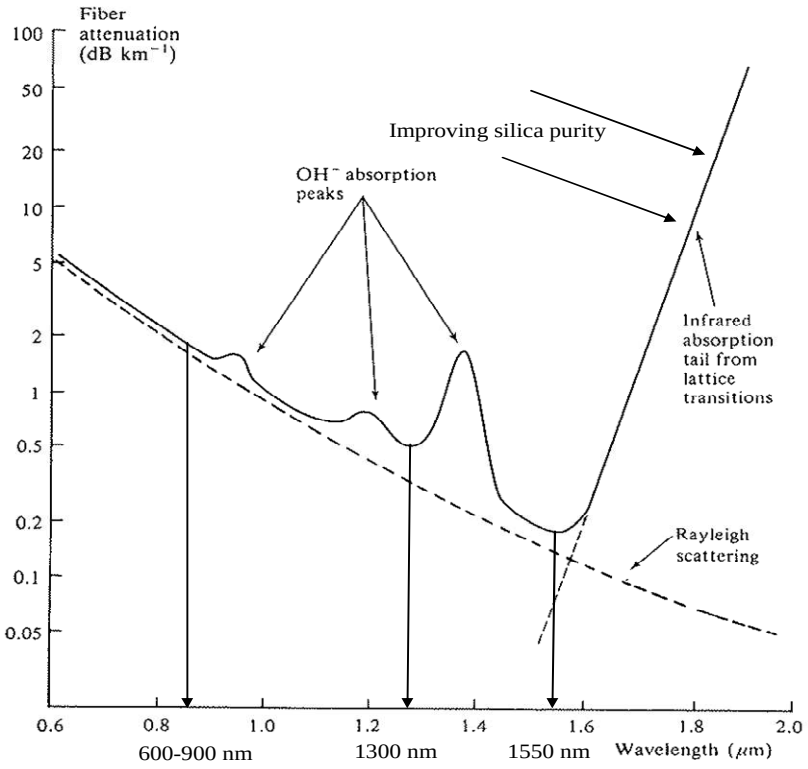

Figure 3: Graph of the losses in silica illustrating the fundamental Rayleigh scattering limit, the OH⁻ absorption peaks and the infrared absorption tail. Three key low loss windows have become available as the IR absorption is pushed back and the OH⁻ peaks minimised by increasing purity of silica. Adapted from [5].

Fibre optics lend themselves quite readily to sensing and provide the possibility of conducting remote, accurate measurement using small sensing elements as well as the possibilities of multiplexing sensing elements with the bandwidth of telecoms fibres. The explosion in fibre optic telecoms in the late 1980's has also served to set up a massive worldwide industry producing fibre optic components at the relevant wavelength. The result has been an increase in availability and quality of components and a drop in the cost, often by an order of magnitude. However, the periodic shift to

each new generation of ever higher wavelengths results in older components at lower wavelengths become harder to source and correspondingly more expensive and the danger of technology becoming obsolete is always present.

1.3. Fibre Optic Sensing

Generally and simplistically speaking, once light is in a fibre optic it stays there. The losses due to absorption in current fibres are so low that on the scale of meters they can often be ignored. Fibres can therefore be generally seen as a robust and idealised light guiding medium suitable for replacing equivalent bulk or freespace optics in a sensor system. By itself the fibre is designed to be fairly insensitive with respect to external stimuli to reduce noise and signal degradation. Single mode telecoms fibre has, however, been demonstrated to be affected by temperature, strain stress and even absorption of hydrogen. Such effects however are small and it is usually necessary to construct more elaborate apparatus to enhance detection. Through the use of splitters, combiners, polarisation controls, amplifiers, attenuators, depolarisers etc. all fibre coupled, it is possible to build an arbitrarily complex optical system. This can be readily used to get the light to and from a sensor or to construct interferometric apparatus.

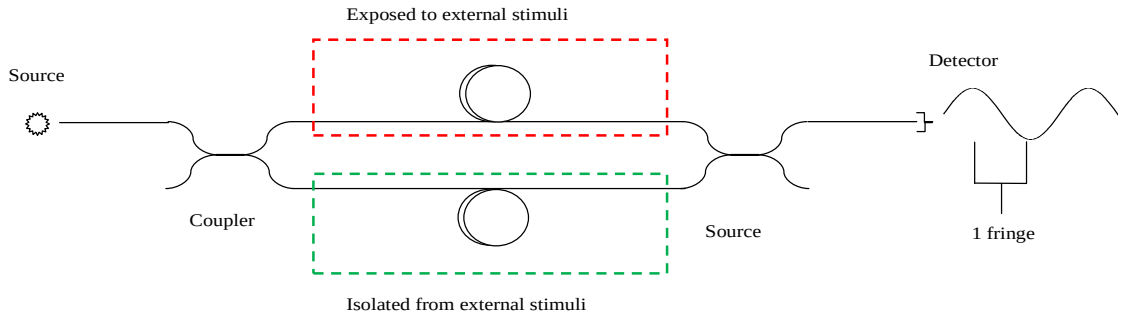

Figure 4: Illustration of in fibre Mach Zehnder Interferometer in fibre where a single fringe at the output detector represents a relative phase shift of 2π between the two arms.

The simplest, but by no means least useful of these arrangements is a Mach Zehnder interferometer (Figure 4). This form of interferometer allows for the direct comparison between the optical path length of two fibre arms where one arm is allowed to interact with the environment and the other, the reference arm, is insulated from external stimuli. This arrangement is a step further than using the fibre as an optical delivery system, as the fibre arm its self becomes the sensing element. This can be readily used, for example, as a temperature sensor as even very small changes to the optical properties of one of the fibre arms due to temperature translates to large shifts in the interference pattern at the recombined arm corresponding to several fringes.

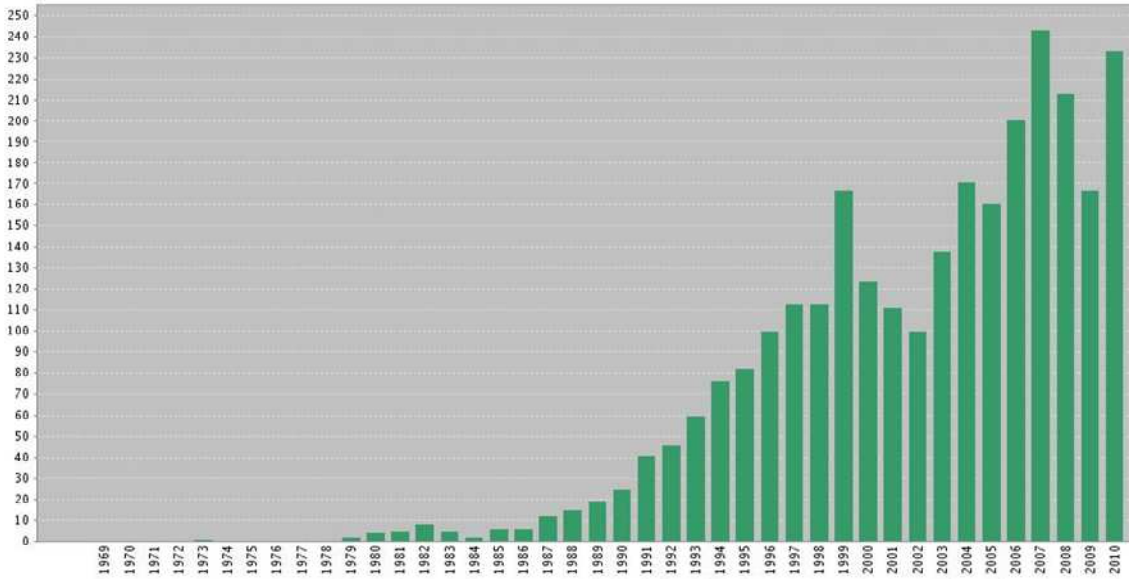

Figure 5: Plot of the number of papers containing the phrase "fibre optic" or "fibre optic" and "sensor" in the title against year. Search carried out through the Web of Knowledge on 6/11/09.

This form of interfermometry has been usefully applied to measure a range of stimuli but is limited in that the system is unable to detect the direction of change, i.e. both extension or compression of the fibre will register as a relative phase shift at the recombination of the arms. Although this can be overcome by using several wavelengths simultaneously it rapidly becomes a complex system. This is only one simple example of a fibre sensor. The field of fibre optic sensors has grown rapidly

over the last thirty years. The technology has always been closely linked to technological developments in fibre optic communications. A plot of the number of papers published against year illustrates this quite well (Figure 5). The number of papers increases rapidly with the implementation of low loss optical fibres in the 1980's and can be seen to mirror the boom in the telecoms industry through the nineties. As the telecoms bubble burst in the early 21st century there is a significant drop in publications for a few years. Fibre optic sensors is thus an industry that is yet to mature and come into its own, however there is considerable interest, as can be seen by the levels of publications and international conferences, with funding from industrial and governmental sources.

1.4. In Fibre Structures

It is possible to use fibre only as wiring between optical sensing components or in an interferometer arrangement to measure changes in the optical properties, i.e. optical length, of a fibre. An alternative is to write a sensing structure within the fibre whose characteristics are affected by an external stimulus and the response can be detected through the optical fibre. This requires a specific modification of the optical properties of the fibre within a small region which modifies the core mode in some form. The most common of these is the fibre optic grating. A more complete discussion of the development and application of gratings can be found in the review chapter (§2.1), suffice to say that these optical components serve to modify radiation which passes through them. The type, scale and effect of this modulation is dependent on the exact parameters of the structure, which are dependent on external environmental effects. This can then be used as the principle of optical sensing within a single optical fibre. This powerful technique minimises the size of sensors, while retaining the capability to make the most of the inherent bandwidth of the fibres for multiplexing of sensing elements. The disadvantage of such systems is generally to be found in the fact that such structures need to be written, inscribed etched or otherwise formed after the fibre has been drawn. Although a considerable amount of progress has gone into standardising this process, particularly for fibre Bragg gratings there is still a requirement to characterise each individual sensing element.

1.5. Problem Posed by AWE

AWE, the Atomic Weapons Establishment, provides and maintains the United Kingdom's nuclear deterrent. AWE have a requirement for optical based sensors as a compliment to their existing capabilities. The majority of the work in this thesis is a response to these requirements.

A significant portion of the work carried out at AWE involves the stockpile, stewardship and storage of nuclear devices. These devices are held in subterranean depositories over the long term and in order to guarantee their safety it is necessary to continually monitor their condition and environment.

There has been a strategic alliance between AWE and Heriot Watt University since 1992. The Applied Optics Group, and specifically the Fibre Sensing Group have contributed to this alliance through a series of collaborations. An aspect of this monitoring process which has yet to be satisfactorily resolved requires the detection of the slow accretion of hydrogen gas, up to ~10,000 ppm, (1%) in a sealed, essentially nitrogen atmosphere over a period of months and years. The requirement at AWE can be summarised:

- All Optical solution – no electronics at the sensing position
- Fibre optic coupling between source/detector and sensing position
- Small size sensor, sub mm scale for preference
- Detection of 0-10,000 ppm H_2 in balance N_2
- Long Term stability – up to 20 years without significant maintenance

There are numerous demonstrations of hydrogen sensors using both electrical and optical techniques [6, 7]. The remote, inaccessible, positioning of the containers and the levels of background ionising radiation, typically 80 kGy per annum, are prejudicial to the successful deployment of electrical based sensors which would exhibit high levels of interference.

Optical sensors by contrast offer much larger resistances to ionising radiation [8] (fused silica is highly resistant to the effect of radiation [9-11]). An optical based solution is therefore preferred due to increased resistance to radiation and the remote location of the sensing environment further limits discussion to fibre optic based sensing elements.

Several potential fibre based hydrogen sensors, almost exclusively dependant on Pd or at least a Pd catalytic layer, have been demonstrated [7]. Among these the majority depend on fibre tapers, cavities side polishing or other techniques which while increasing sensitivity significantly reduce the mechanical reliability of the fibres [7]. Grating structures, and particularly long period gratings (LPG), offer the combination of simple manufacture with reliability.

Optical fibres are, however, not made from pure fused silica. It is necessary to introduce dopants to either the core or cladding to provide the index contrast for total internal reflection. Germanium (core) doped, standard telecom, fibre has been shown to exhibit increased losses and temperature coefficients when exposed to large doses of radiation [8-11]. Radiation exposure is, however, a complex science. Given the, comparatively, low levels of radiation, short lengths for an LPG and the small dimensions of the fibre it is likely that the sensor will continue to operate (albeit with increasing losses) for some time. Of greater concern are the connecting fibres leading into and out of the LPG. Here losses approaching 150 dB km^{-1} would prove catastrophic [12]. Fluorine [13] and nitrogen [14] doped fibres have demonstrated larger radiation tolerances but neither fibre is particularly suitable for LPG inscription due to low photosensitivity. A sensible solution may therefore be to employ nitrogen or fluorine doped fibres as connectors with a short (~3cm) length of germanium doped fibre for the LPG element.

Some consideration must also go to the effect of radiation on a Pd layer. There is little published information on this, but studies on the desorption of hydrogen from metals induced by e^- beams [15] suggests that some interference with hydrogen absorption is to be expected. Radiation is therefore expected to have some detrimental effect on a Pd-LPG based system but this is outside the scope of this thesis.

1.6. Thesis Layout

The following chapter of the thesis is a review of fibre grating structures, LPGs in particular, and the palladium – hydrogen system. Following this general treatment conclusions are presented regarding the necessity to independently characterise our Pd thin films and LPGs in order to fully understand the LPG-Pd system.

The experimental work is therefore divided into four chapters. Initially work carried out to characterise our thin films in terms of surface quality, contamination and optical properties is presented and discussed. This is followed by the attempts to characterise the LPG refractive index profiles both experimentally and theoretically.

These two characterised systems are then combined to provide a model of the LPG-Pd system as a hydrogen sensor and is presented with the associated experimental work.

Finally conclusions are drawn concerning the LPG-Pd system paying particular care on the theoretically derived sensitivities of various LPG-Pd structures and specifications are presented for a high sensitivity LPG-Pd sensor element.

Chapter 2. Review

2.1. In Fibre - Gratings

2.1.1. Introduction

In fibre-gratings are a common form of mode modification structure often used in sensing applications. By inscribing a periodic change to the refractive index of the guiding, i.e. core region, of a waveguide, the propagating modes are modified. In the case of a periodic structure, this manipulation is often wavelength dependant. These structures have enjoyed a great deal of success in the telecoms industry as band pass or band rejection filters [16]. Changes to either the waveguide or the grating structure alter the nature of this mode modification and hence gratings are also commonly used in sensing applications. Two grating structures are commonly employed; fibre Bragg gratings (FBG) and long period gratings (LPG). The use of FBGs for sensing applications is well developed, particularly for stress, strain and temperature measurements while LPGs are an outgrowth from FBG development. There are number of texts devoted to the strict mathematical interpretations of grating structures. This thesis will be limited to the pertinent details and the reader is referred to texts such as Raman Kashyap's [17] excellent book or Othonos' and Kalli's description of FBGs [16] for further details not presented in this thesis.

An FBG and an LPG can be said to be fundamentally the same structure within a waveguide i.e. a periodic perturbation of the refractive index of the guiding, or core, region. However, they excite significantly different optical phenomena at different wavelengths. The relative schematics of an FBG and LPG can be seen in Figure 6.

At each periodic shift in the core refractive index there is a small Fresnel reflection. In an FBG the spacing of these reflections is similar to the designed reflection wavelength. These reflections are therefore all in phase giving a strong coherent reflection. The result is a Bragg reflection system whereby a single wavelength - or more properly a narrow range of wavelengths are reflected back down the fibre. Variations in the properties of the grating result in a change to the reflected wavelength and so gratings can be employed as a wavelength codified sensor. The key properties of the FBG can be defined as the period (defining the wavelength of coupling), the refractive index

perturbation amplitude, (affecting the mode coupling strength) and the length (total number of periods affecting the bandwidth of the mode coupling).

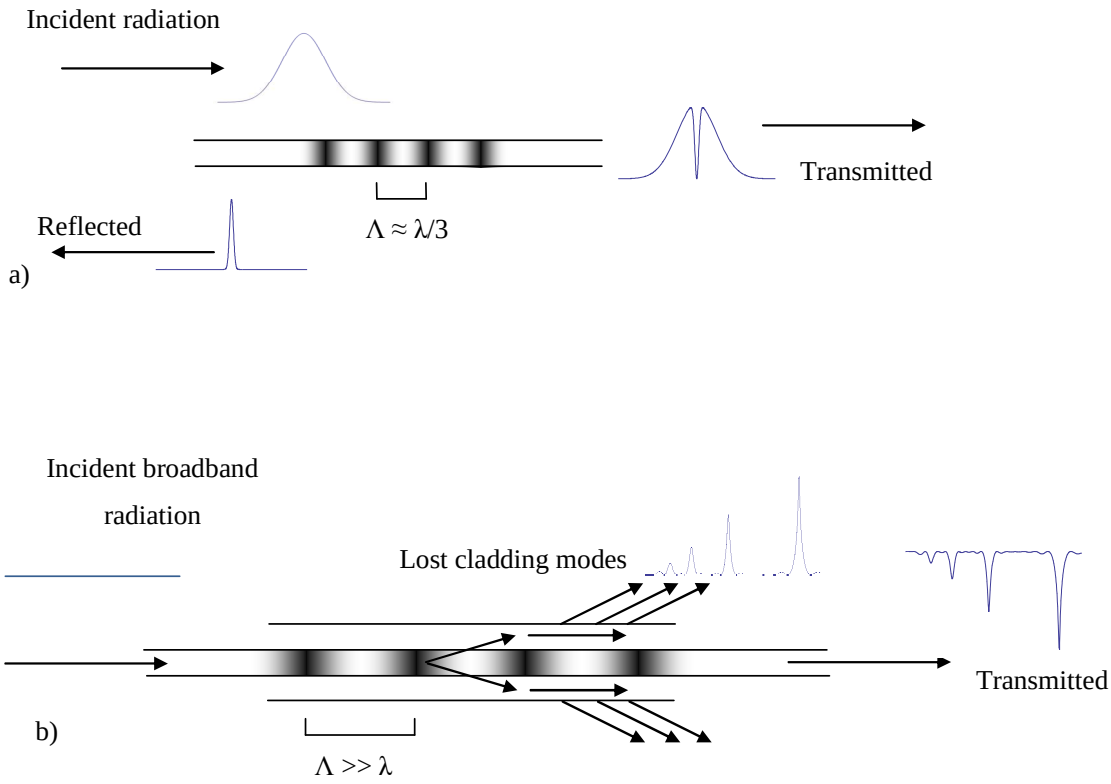

Figure 6: Illustration of the mode coupling of a typical a) FBG and b) LPG illustrating the differences in coupled modes and transmission spectrums.

This somewhat simplistic picture can be further expanded by considering that the FBG is a mode coupling structure. The period of the structure, the physical dimensions and the optical properties of the waveguide combine to give a phase matching condition which most strongly couples light into the counter-propagating fundamental mode, i.e. a reflection, Figure 7. While other modes (chiefly cladding and radiative modes in the case of a single mode fibre) are also present, the phase matching condition is such that the amount of power coupled into these modes are orders of magnitude lower than that coupled into the counter propagating core mode.

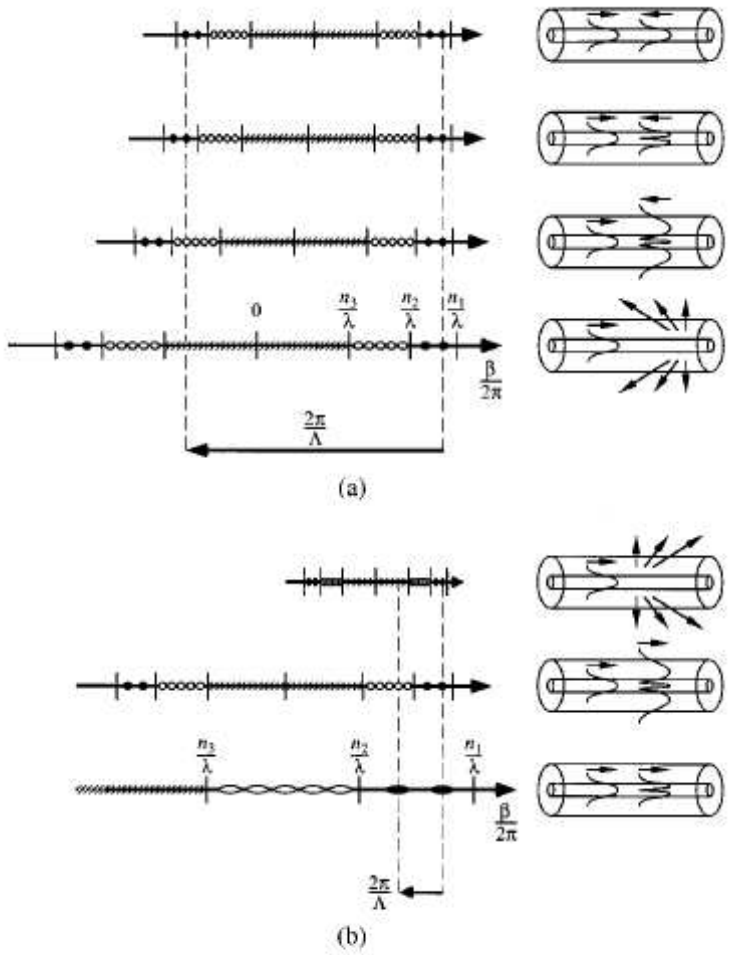

Fig. 7. Diagrams that illustrate the phase-matching conditions necessary for resonant coupling between two modes by a grating of period Λ. (a) For a short-period grating, counterpropagating coupling can occur between (top to bottom, longest to shortest wavelength) oppositely traveling similar core modes, two different core modes, a core mode and a cladding mode, and a core mode and radiation modes. (b) For a long-period grating, copropagating coupling can occur between (top to bottom, longest to shortest wavelength) a core mode and radiation modes, a core mode and a cladding mode, and two different core modes.

Figure 7: Schematic of the phase matching conditions for long and short period fibres taken from Erdogan [18] including original caption.

By contrast, an LPG has a much larger period relative to the incident wavelength. The phase matching condition for this longer period gives strong coupling to co-propagating cladding modes (Figure 7). In fact the LPG is more selective even than this as it couples only to a small subset of the symmetric $LP_{0,v}$ cladding modes. Due to the relative complexity of the LPG system there is, as yet, no single definitive theory or mathematical description encompassing all LPG properties. There are however a series of papers [18-25] detailing the mathematical interpretation of an LPG for various cases

and it is to Erdogan's [18, 21, 22] papers that this thesis most often refers for the discussion of the fundamental coupled mode theory.

It is an interesting conceptual point that the difference between an LPG and an FBG is only in reference to the scale of the period compared to the wavelength of excitation; a structure of period 400 μm will behave as an LPG to 1500 nm radiation but as an FBG to 1200 μm radiation, however the realities of producing a single mode fibre with such a large range of guided wavelengths are such that to my knowledge no device has been built to excite both sets of modes simultaneously.

2.1.2. Fibre Bragg grating (FBG)

In-fibre gratings were first observed by K.O. Hill et al. in 1978 [26]. Experiments in non-linear fibre processes had led them to using high, for the time, intensity beams in a germanium doped single mode fibre. After a period it was noticed that the fibre became less transparent to the incident radiation and that an increasing fraction of the power was reflected back down the fibre. Further investigation led them to understand that interference between the forward travelling core mode and backward travelling Fresnel reflection from the end of the fibre was setting up a standing wave within the fibre. Maxima of this standing wave induced a small but permanent refractive index change to the core fibre region, in effect writing an FBG with a periodicity suitable for affecting the source wavelength. Further experimentation demonstrated that the induced optical change was specific to reflecting the wavelength used for the inscription process, but that it could be tuned slightly by stretching the fibre or changing its optical properties (e.g. applying heat) either during or after the writing process.

Since this first discovery, the characterisation and writing of FBG elements has come on in leaps and bounds [26-28]. With the advent of more reliable, tuneable inscription system (cf. §2.1.6) the use of FBG elements as the basis for optical sensors became possible. As discussed in the introduction, an FBG has a period of the same order of magnitude as the wavelength of radiation (i.e. the period is usually $\sim\lambda/3$) to be coupled and as such are extremely sensitive to changes to this period. This can be a direct change to the period, i.e. strain-optic effects in the fibre or an indirect change to the period e.g. temperature (the thermo-optic coefficient of the fibre is such that a change to

the temperature gives a change to the optical length of the fibre as well as thermal expansion of the fibre directly). FBG elements are now widely deployed as temperature and strain sensors. Typically in a standard SMF-28® optical fibre a change of 1 K gives a resonance shift of ~10 pm, an equivalent shift to 10 micro-strain [16] (με), strain is a measure of extension typically as extension in m per m or m m^{-1}. As strain and temperature manifest as the same measurement, a shift in the reflected wavelength, a considerable amount of effort has gone into attempting to screen an FBG element from one or other effect for direct reliable measurement of a single variable [16]. There has been a large amount of interest in recent years in the use of FBGs as distributed or multiplexed sensing elements. The telecoms industry have a range of solutions for interrogating wavelength divided information, e.g. wavelength division multiplexing and the operating bandwidth of an FBG is narrow compared to the available signal bandwidth of an optical fibre. It is therefore quite feasible to insert several FBG elements into a single fibre each operating at a separate central wavelength and interrogate them all simultaneously [29]. Alternatively a large number of identical but weak gratings may be used and interrogated by pulse with the signal from each FBG separated by the return time [30].

FBG sensors and associated instruments for interrogation are available commercially, meaning that the technique has reached a certain level of maturity, making it possible to obtain multiple and essentially identical, well characterised elements. With this reliable base there has been considerable interest in adopting FBG sensors for the detection of a range of measurands using a range of packaging designs [16, 31, 32]. Examples include using an FBG as vibration sensors, bend sensors, using multiple or multicore polarisation maintaining fibres for directional strain or loading sensing, transverse strain sensing etc.

These applications, while effective, are of limited use for the purpose of this thesis. FBG sensor elements are not directly sensitive to the presence of hydrogen, as this does not produce either: stress, strain or temperature shifts in the fibre (one of the more useful aspects of FBG sensors is the limited sensitivity to anything other than temperature or strain). One method for using FBGs relies on an additional, external layer on the fibre to convert the presence of gas to strain. Pd expands in contact with hydrogen, see §2.2 for a more thorough discussion. By coating an FBG in Pd it is possible to detect hydrogen via strain introduced by the Pd layer. This has been

demonstrated [33] but the sensitivity of these devices has been found to be low, up to three orders of magnitude less than an equivalent LPG sensor [33]. Various attempts have been made to multiply the strain across an FBG element or to measure the deformation of Pd by alternative means [34]. These arrangements invariably require out of fibre mechanical or structural arrangements increasing the complexity, size, cost and introducing further reliability issues. The use of LPG based sensors is to be preferred on these grounds.

2.1.3. Long Period Gratings (LPG): Sensitivity to the Environment

An LPG is sensitive to any external stimuli which affects either the core or the cladding modes or which changes the grating used to couple between them. Sensitivity to temperature, strain, bend radius, and external refractive index have all been demonstrated [35]. An understanding of the effect of these can be derived by examination of the simplified mode matching condition for an LPG (Eq. 1).

$$\lambda_{res} = (\delta n_e)\Lambda \qquad \textit{Eq. 1}$$

Where Λ is the period of the LPG and δn_e is equal to $n_{co}(\lambda) - n_{cl}^{0,\nu}(\lambda)$, the difference between the effective index of the core, $n_{co}(\lambda)$ and the ν^{th} cladding mode, $n_{cl}^{0,\nu}(\lambda)$.

At higher mode orders, the effective refractive index of the cladding mode decreases and the difference between the core and cladding mode, δn_e increases. The coupling efficiency between the core and a particular cladding mode will detune as a function of wavelength. As an LPG is generally written with a specific wavelength or band in mind it is necessary to use a longer period to couple to lower orders, (e.g. an SMF-28® fibre a 400 μm period will couple to the 1-9th orders between 1200-1550 nm).

By taking the derivative of Eq. 1 in terms of the temperature, T (Eq. 2) $d\lambda/dT$ is derived, which represents the sensitivity of the LPG to temperature [36].

$$\frac{d\lambda}{dT} = \frac{d(n_{co} - n_{cl}^{0,\nu})}{dT}\lambda + (n_{co} - n_{cl}^{0,\nu})\frac{d\Lambda}{dT} \qquad \textit{Eq. 2}$$

This value can be positive or negative depending on the LPG structure, the fibre and the mode order [37]. On the right hand side of Eq. 2 there are two contributions to this sensitivity. The first term describes the change in the effective refractive indices as a function of the temperature, which is known as the material effect [37]. The second term, the waveguide contribution, describes the change to the period of the grating including changes to the length of the LPG (L). The material contribution is proportional to both the change in δn_e and difference to the varying effective indices, it is therefore highly dependant on the material of the fibre and on the mode order of the cladding mode in question [37]. At lower mode orders, and therefore larger periods (Λ>100 μm), the material effects will dominate [37, 38]. Conversely, for higher mode orders (Λ<100 μm) the material effects in standard fibres are negligible and the waveguide effect dominates [37, 38].

Appropriate choice of cladding mode, period and fibre material can result in the material and waveguide effects having opposite signs, minimising sensitivity to temperature. In standard telecoms fibres this requires coupling to higher order modes. This has been demonstrated to produce an LPG with as low as 1.8 pm K^{-1} [38], an order of magnitude lower than an FBG. Theoretically it is possible to produce a fibre where the material and waveguide contributions cancel each other out resulting in a temperature insensitive fibre. However the difficulties in fabrication (§2.1.6) make this a problematic prospect. Alternatively, the two signs can be the same, thereby producing an element which is particularly sensitive to temperature. In standard optical fibres LPG sensitivities of up to 100 pm K^{-1} [35] have been demonstrated, an order of magnitude larger than that of an FBG.

The differential equation describing strain sensitivity can be seen in Eq. 3 [37].

$$\frac{d\lambda}{d\varepsilon} = \frac{d\lambda}{d(n_{co} - n_{cl}^{0,\nu})}\left(\frac{n_{co}}{d\varepsilon} - \frac{n_{cl}^{0,\nu}}{d\varepsilon}\right) + \Lambda\,\frac{d\lambda}{d\Lambda} \qquad \textit{Eq. 3}$$

Similarly to the temperature case there are material (first) and waveguide (second) terms. At longer periods (Λ>100 μm) the material contribution is negative but the waveguide contribution is positive resulting in a relatively low sensitivity as low as ~0.04 pm $\mu\varepsilon^{-1}$ [38], an order of magnitude lower than a typical FBG strain sensor. At shorter periods (Λ<100 μm) both the material and the waveguide contributions are negative and as such a relatively high sensitivity to strain has been demonstrated (-2.2 pm $\mu\varepsilon^{-1}$ [38]).

Transverse, rather than axial, loading can also produce shifts of the resonant wavelength. In this case the strain field is not radially symmetric and produces birefringence in the fibre. The birefringence results in a splitting of transmission loss as each polarisation couples to a different wavelength. As the separation of the two loss bands is directly related to the scale of birefringence, increasing strain moves the peaks further apart giving a high sensitivity, 500 nm kg^{-1} mm^{-1} [39], differential transverse strain sensor, almost 800 times more sensitive than an FBG equivalent [39].

This combination of temperature and strain sensitivity allows LPGs to be sensitive to strain but not temperature (short period), or to temperature but not strain (longer period), or to produce an LPG without a particularly high sensitivity to either [37]. Additionally with careful choice of fibre period and wavelength, it is possible to create separate sensitivities for different modes which can all be interrogated simultaneously (due to the wavelength separation of cladding mode coupling) without the need for separate LPG elements. This gives LPGs a potentially powerful advantage over the equivalent FBG sensors.

While temperature and strain change the effective index of the core, the cladding modes and the period of the LPG, changes to the external index affect only the cladding modes. A more complete discussion of the effect of relative refractive index change and mode order is presented in §2.1.4 and §2.1.5 respectively. Essentially, a change to the external index of refraction will affect the cladding mode shifting the effective index, giving a change to the coupling wavelength conditions in Eq. 1. For temperature or strain measurement applications this is generally an unwanted effect and, as such, care must be taken to ensure that the external index is held constant during handling of the fibre, e.g. applying an adhesive may shift the LPG spectrum out of the intended operational range. The alternative is to write an LPG into a fibre with no external -

cladding mode interface. A depressed cladding fibre (Figure 8), where the cladding modes are confined by an additional layer has been demonstrated [40] to effectively eliminate the sensitivity to external index as well as reducing possible difficulties resulting from damage to the cladding external interface.

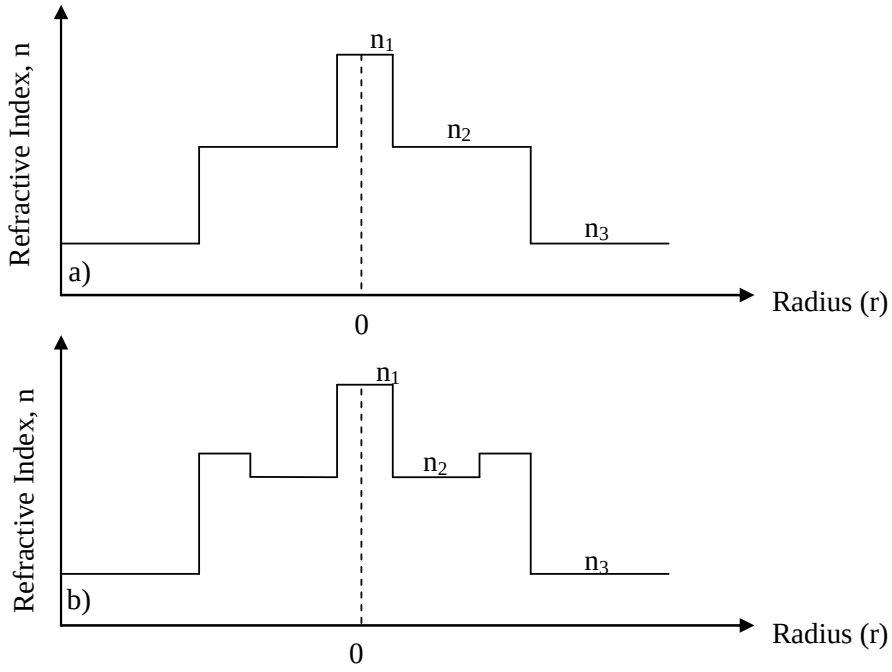

Figure 8: Example schematic of the refractive index crossection of a) standard fibre, b) depressed cladding fibre. In this case the raised outer index prevents the cladding modes from interacting with the surrounding medium (n_3). Scales have been exaggerated for clarity.

2.1.4. LPG Sensing Regimes (index contrasts)

Within an optical fibre, the core mode is confined by the process of total internal reflection (TIR). Similarly, the cladding modes of a standard fibre are confined via TIR, although these modes are lossy, resulting in loss-bands in the transmission spectrum of an LPG. Although the core-cladding interface, the optical properties and dimensions of the fibre are important to the properties of an LPG it is the cladding-external interface which is of primary interest to the subject of this thesis. This can be most readily seen by considering the effect of immersing an LPG element into a

medium of arbitrary dielectric refractive index (Figure 9). The transmission of spectrum of the LPG can be said to exhibit two distinct phases.

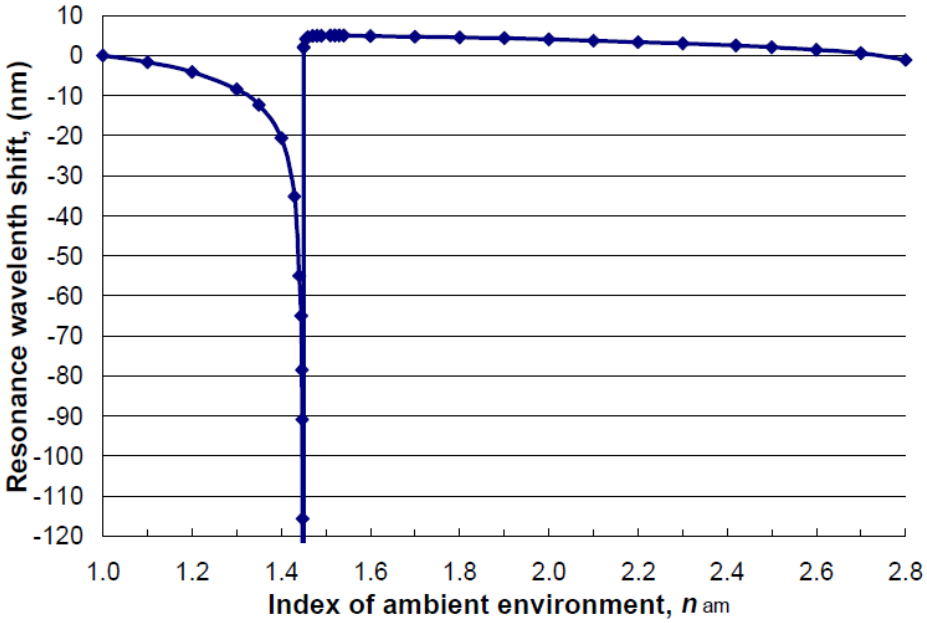

Figure 9: Plot of modelled resonant wavelength shift as a function of external index from Hou et al. [23], fibre has cladding index of 1.450 for this simulation.

The first, or normal phase, encompasses the region where the external index is lower than the cladding. In this regime the cladding modes are guided by TIR and strong resonant coupling can be expected between the core and co-propagating cladding modes. As the external index increases to approach that of the cladding the resonant position of a cladding mode becomes ever more sensitive to external index [23]. This continues to the point where the cladding index and external index are matched. At this position the cladding becomes effectively infinite and no cladding modes are supported, giving rise to the asymptote in Figure 9.

If the index increases further then it will become larger than that of the cladding. In this, the second regime, there is no TIR at the cladding external interface and hence no TIR guided cladding modes. It has, however, been demonstrated that mode coupling to cladding modes does exist within this regime [25] (Figure 10). While the external index is too large to support TIR it is not true to say that there is no reflection at the interface.

A small Fresnel reflection is present at this interface, setting up high attenuation guided cladding modes [23, 25, 41]. These modes couple across a broader range of wavelengths with lower coupling efficiencies resulting in a wider shallower loss band (Figure 10). Within this Fresnel guiding regime the gradient of resonance shift to index change is much flatter, giving a lower sensitivity of the coupling wavelength to external index variations (Figure 9) [25].

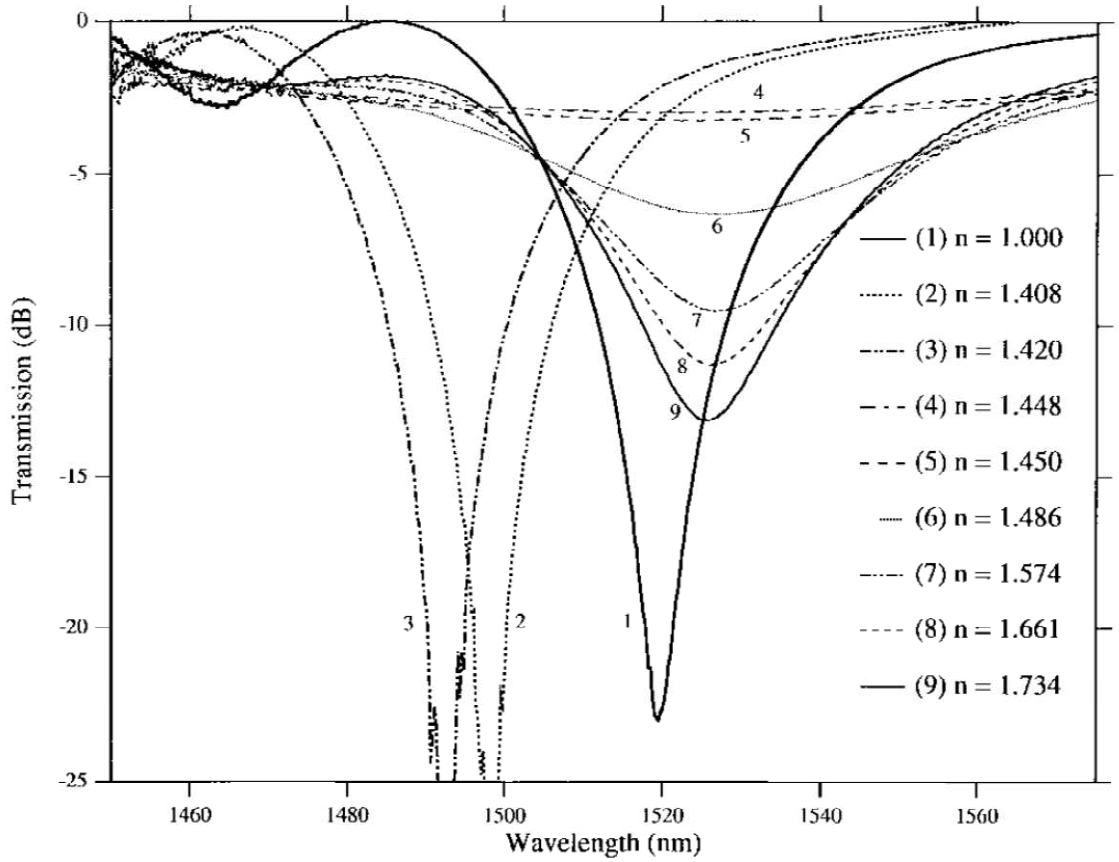

Figure 10: Transmission plot of a cladding mode loss band with various external indices of refraction from Stegall and Erdogan [25]. Traces 1-3 are for $n_{ex}<n_{cl}$, regime 1, traces 4,5 for the case $n_{ex} \approx n_{cl}$ and traces 6-9 for regime 2, $n_{ex} > n_{cl}$.

An additional regime can be considered in the case where the external index is that of a metal rather than a dielectric. In this case TIR is replaced by reflection from the metal giving a set of guided cladding modes. This is made possible due to the complex nature of the metal refractive index which provides for reflection and attenuation of incident radiation. In principle this metal layer could have a real component lower than the cladding index of the fibre, however, in practice there are almost no metals with such a

low refractive index in the wavelengths used for sensing and the system is therefore analogous to the second regime of a dielectric coating. Coupling to these modes has been demonstrated and only a few papers have investigated this regime qualitatively [24, 36] with no true quantitative analysis. Metal jacketed fibres have been demonstrated in the form of thermally tuneable filters [42, 43], propagating surface plasmon mode sensors [44, 45] and Pd jacketed hydrogen sensing [34]. For simplicity, we can consider that such a metal is non magnetic i.e. permeability μ, = 0 and extends to infinity since, in practice a thickness of the order of 100 nm will be sufficient for an infinite approximation [46, 47]. However, the validity of current models in the presence of a metal jacket has not been investigated. The development and investigation of such a model forms an important part of this thesis (§6.4).

2.1.5. LPG Mode Regimes (mode matching profiles)

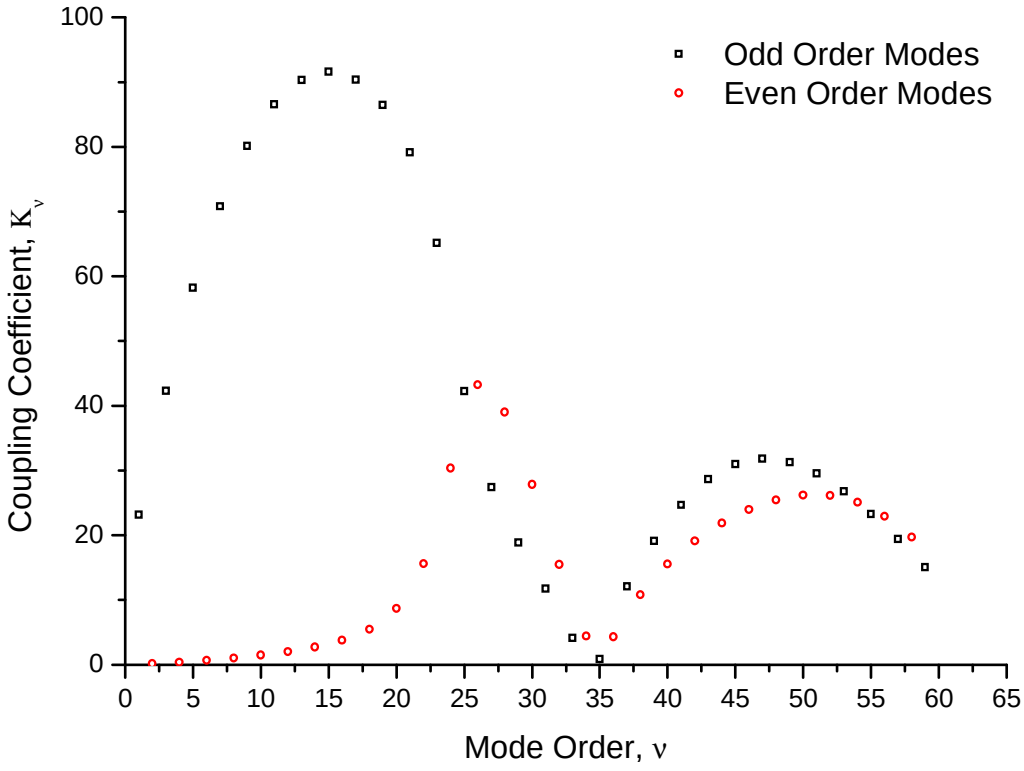

Figure 11: Plot of calculated coupling coefficient between the core and the first 59 cladding modes, $LP_{0,\nu}$, of an SMF-28® fibre (core index $n_1 = 1.46145$, cladding index $n_2 = 1.456$, external index $n_3 = 1$, core radius $a_1 = 4.1$ μm, cladding radius $a_2 = 62.5$ μm), calculated at 1550nm via my computational model, see §5.2.

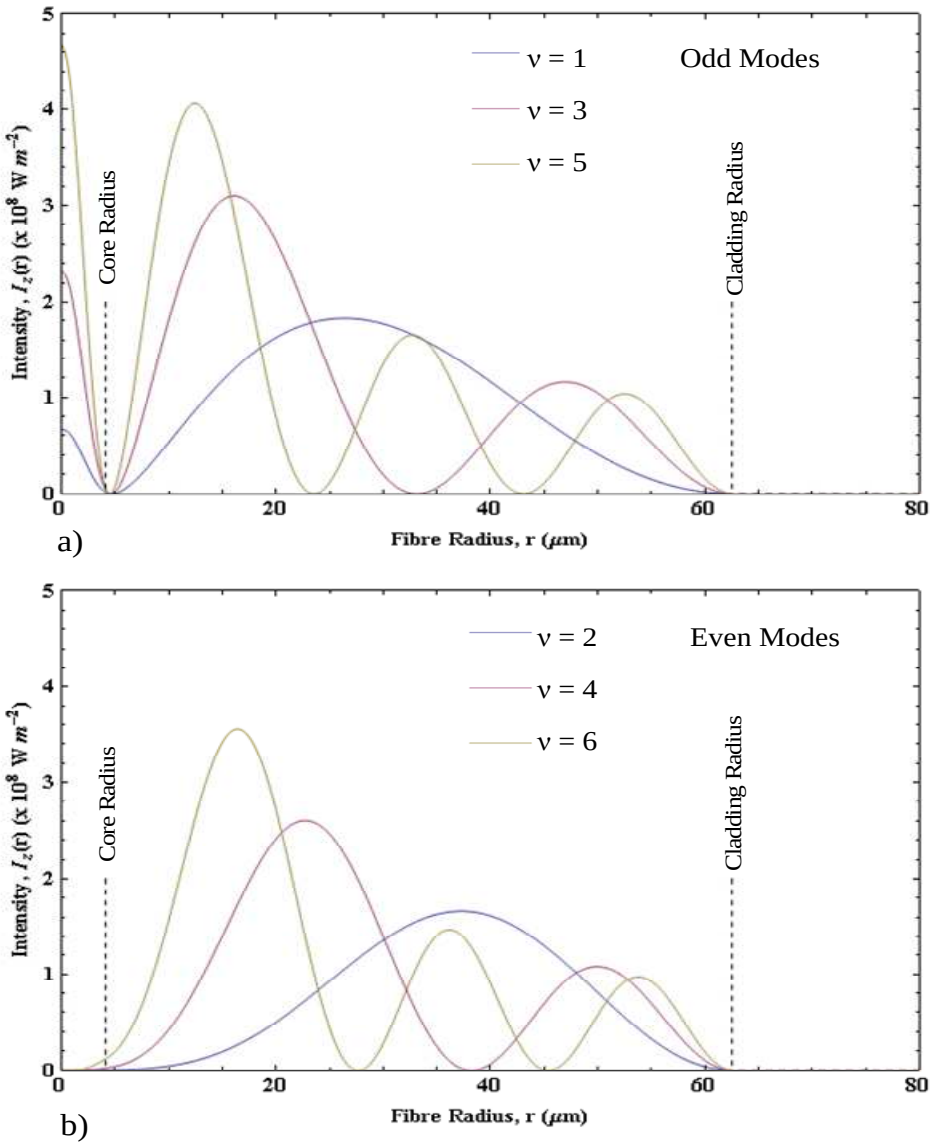

Figure 12: Plot of the first three a) odd and b) even order cladding mode intensities illustrating the difference between odd and even order modes in terms of the power in the core region. Calculated for the same fibre as Figure 11.

In addition to the external-cladding refractive index contrast it is also necessary to consider the effect of the order of cladding mode. While there are a very large number of cladding modes present in any given fibre, an LPG couples only to a specific subset of radially symmetric cladding modes, $LP_{0,\nu}$. Within this subset there are further differences particularly within the coupling efficiency. A plot of the coupling efficiency of the first 59 modes of a typical fibre is presented in Figure 11. The clear difference between the odd and even order cladding modes requires that they are considered

separately. Coupling efficiency is most strongly affected by the mode overlap between the core and the cladding mode. At low mode order, $\nu < 20$, there is little overlap between the even order modes and the core mode due to the presence of an intensity minimum in the core region (radius of ~4 μm, Figure 12b). By contrast the odd order modes exhibit excellent overlap due to the presence of a maximum in the core region (Figure 12a). Of note here is the distortion to the mode fields due to the presence of the core (Figure 13).

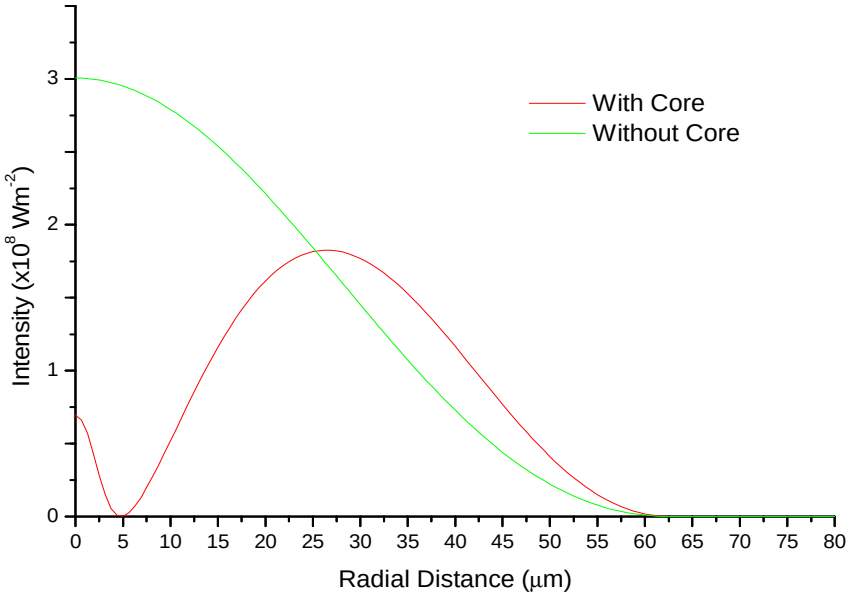

Figure 13: Comparative plot of mode profiles with the two layer approximation (no core, in green) and the three layer model (red) illustrating the distortion to the cladding modes due to the core.

The inclusion of this distortion, which is not included in the two layer approximation, is a critical factor in accurately modelling the overlap integrals between the core and cladding modes [18, 21]. As the mode order increases, there are more and more radial oscillations (intensity periods) to fit within the fixed radius of fibre. For mode orders above ~20 the sheer number of intensity periods within the cladding mean that some power is present for both even and odd cases, hence the difference between them is less obvious. Both odd and even order modes exhibit a slow variation in coupling coefficient with mode order. This is a result of the number of intensity periods and the ratio between core and cladding sizes. As more and more periods are squeezed into the

fibre, eventually a minima will move into the core region. This combined with the distortion effect of the core on the mode results in low coupling for these modes (e.g. ν=35, Figure 11).

The mode order will also affect the resonant wavelength of a mode, as discussed in section §2.1.3. A plot of the phase matching condition for lower, and higher order modes based on Eq. 1 (Figure 14) illustrates the difference between high and low orders. Low order modes have a steep gradient phase matching condition suggesting poor response to external stimuli. With increasing mode order the phase matching conditions become shallower suggesting a larger response to external stimuli. This flattening of the phase matching condition with increasing mode order reaches a zenith whereby certain modes exhibit a turning point [48].

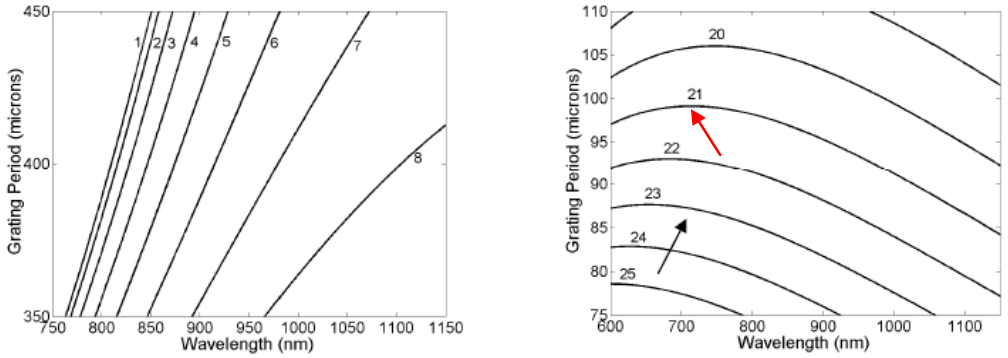

Figure 1. The relationship between the grating period and the wavelength at which coupling occurs to a set of symmetric cladding modes, assuming that the LPG was fabricated in an optical fibre of cut-off wavelength 670 nm. (a) for the 1st 8 modes (b) for modes 20 – 25. The numbers refer to the order of the cladding mode, LP_{0x}.

Figure 14: Mode matching curves for the a) first 8 mode orders illustrating a steep unresponsive gradient and b) the 20-25 order modes illustrating the phase match turning point. The red arrow indicates the turning point of the 21st order mode. Taken from [49], presented with original caption.

For periods below the turning point, the mode couples to two separate wavelengths resulting in a double dip transmission spectrum. With decreasing period (and here the period of the LPG can be considered to be analogous to a change in the external index) the two resonant wavelengths will move in opposite directions, effectively doubling the sensitivity of the device when used as a differential measurement. At higher period the

phase match plot would suggest that there is no coupling to the mode. However the phase matching condition in Eq. 1 is an approximation of the resonance coupling condition. When operating in this region the mode resonance increases and decreases in intensity rather than shifts in wavelength [50]. This is a potentially powerful tool as this changes a wavelength codified system to an intensity codified system. As an intensity based system only requires a narrow band laser and a, relatively, cheap detector rather than a broadband source and spectrum analyser, §2.1.9, this corresponds to significant reduction in cost but at a cost of increase in intensity noise. To what extent these features exist in metal jacketed fibres has been unknown, and the investigation of these forms an integral part of this thesis (§6.4.3).

2.1.6. Long Period Grating Writing Techniques

In order to maximise the mode coupling between the core and another mode the grating structure needs to be present at the position of mode overlap i.e. within the core of the fibre. The first experiment to, accidentally, create an FBG element did so by mixing two counter propagating confined core modes [26]. In fact, the experiment used the same mode reflected at the termination of the fibre, setting up a standing wave. Over time this standing wave created a permanent shift in the refractive index of the fibre exploiting the inherent photosensitivity of a Ge doped fibre to the wavelength used in the experiment.

Further experiments demonstrated that the process was dependant on the square of the power used, i.e. that the process was non-linear [28]. In fact it was found that the photosensitivity was a two photo absorption process at 488 nm. This immediately suggested that the, relatively weak, two photon inscription could be improved by shifting to the UV region at ~255 nm where single photon absorption could take place. It is understood that the photo sensitivity effect in germanium doped silicon is based on the presence of germanium oxygen deficient centres (GODC). There are a number of processes which lead to the generation of these centres, mainly taking place at the elevated temperatures present during the production of the raw materials, the production of the preform and during the drawing of the fibre. Germanium is introduced in the form GeO_2 as a dopant (to increase the core index over that of the cladding) which, at

elevated temperatures, can form GeO. This is a more reactive form able to create a range of cross links in the silica matrix. Irradiation by 255 nm light, where detailed analysis has shown the photosensitivity maximum, excites one of these GeO sites, generating a free electron. This electron has sufficient mobility to move away from the site becoming re-trapped after a number of interactions elsewhere in the structure. The original, now electron deficient, site has a modified bond structure giving a permanent shift to the refractive index.

Utilising this UV photosensitivity has become the industry standard for inscription of gratings, but the photosensitivity of germanium doped silica is still fairly low, making for a prohibitively long writing time. Hydrogen loading of germanium doped fibres was found to significantly improve photosensitivity [51] through improved electron mobility. The process used to hydrogenate the fibre is highly temperature dependant, but at room temperature and a pressure of 20MPa, 14 days is sufficient, although faster times or higher photosensitivity is possible by use of temperatures up to 150°C. The increased photosensitivity means that the gratings can be written in significantly shorter periods of time. This limits the amount of time that a fibre needs to be constrained for the writing period thus improving the quality of the resultant grating. At the same time this still requires only a germanium doped core fibre, e.g. telecoms industry standard SMF-28® fibre, which is readily available at low cost and high quality.

While the addition of hydrogen results in a more complex and ultimately more photosensitive bond structure, alternative co-dopants exist. Boron-germanium co-doping can lead to significant increases in photo-sensitivity. This has the advantage of decreased writing times without the need for the lengthy hydrogen loading process needed for standard fibres. The disadvantage lies with the use of a non-standard fibre type with corresponding increases in cost and increase in losses. This fact has been mitigated somewhat in recent years as the demand for B-Ge co-dope fibre for FBG elements has significantly decreased the cost per meter.

While hydrogen loaded Ge or B-Ge co-doped fibre irradiated with UV has become the industry standard for FBG inscription, there are a number of different techniques in use. The first demonstration by Hill [26] used a standing wave to generate a grating structure. The period of the grating is thus one third the wavelength of the radiation used for radiation and while pre-straining the fibre allows for some variation in

inscribed period the technique is fundamentally limited to the wavelength of the source. As the photosensitive wavelength is in the UV, or with non-linear absorption at ~488 nm or even at ~725 nm with three photon absorption [52]; the period of the grating is limited to these ranges. As such this inscription technique is rarely employed having been superseded by more flexible inscription techniques.

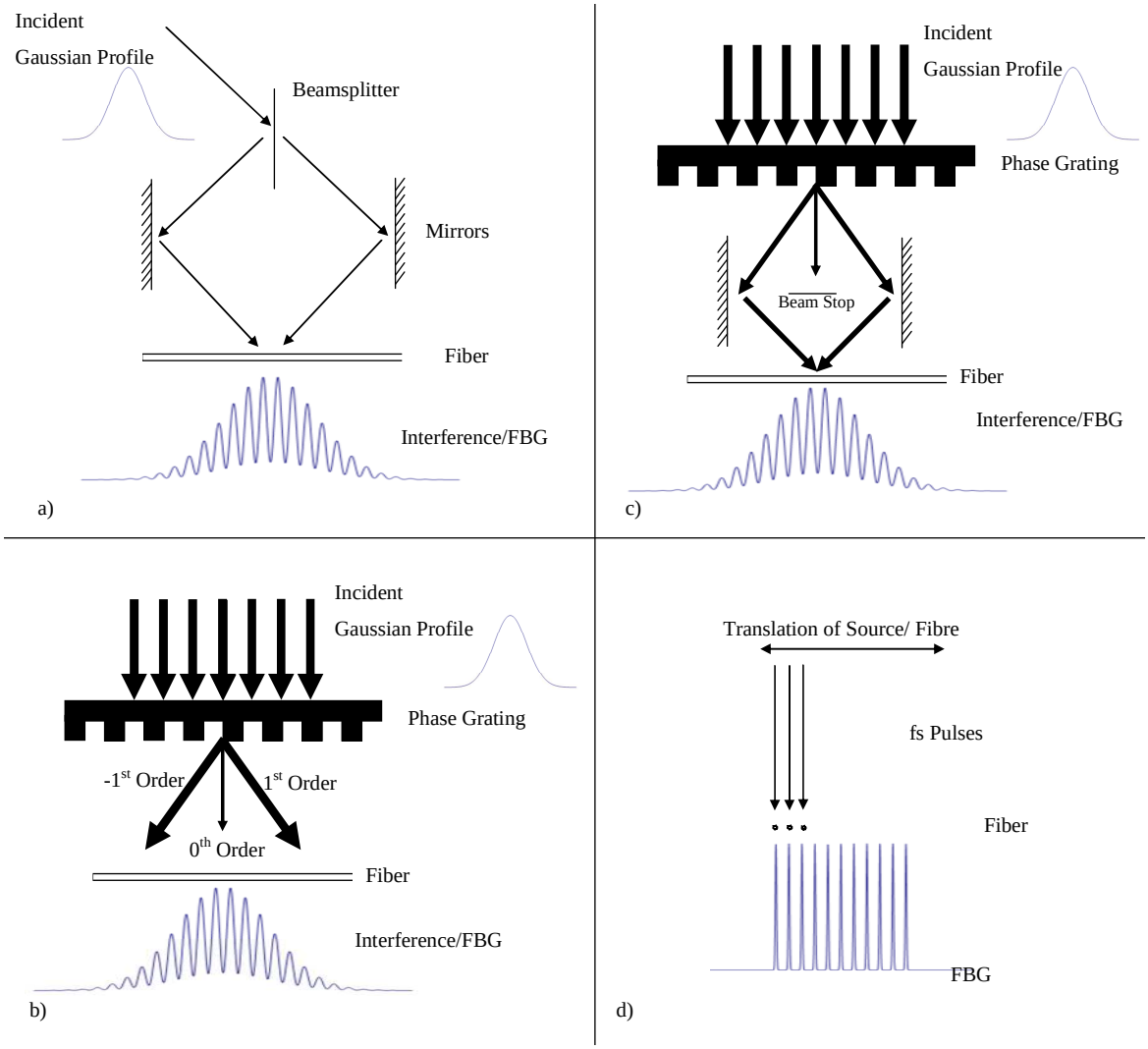

Figure 15: Illustration of four main FBG writing techniques [16]. a) Two beam interference, b) Phase grating, c) Combination phase grating and interference, d) Point by point fs laser inscription.

A more flexible approach for writing FBGs was developed by Meltz, Morey and Glenn [53]. This side writing interferometric technique can generate gratings over a wide

range of periods using the same irradiation source. Figure 15a illustrates the technique; a single beam is split and reflected from two symmetrically placed mirrors. The interference fringes within the core of the fibre can be tuned by tilting the beam splitter. This powerful technique opened up FBGs for further study as it became possible to inscribe in FBGs with an arbitrary period. Further developments rapidly followed simplifying improving and extending the ability to write FBGs. In particular further work by Hill improved the writing technique with the use of a phase mask enabling cheap mass production FBGs.

A phase mask is an etched transmission grating typically made from fused silica. Radiation incident on the grating is diffracted into a number of orders (Figure 15b). Typically the phase grating is etched to a depth equal to half the wavelength of the UV [16]. This minimises the amount of light coupled into the zeroth order, i.e. undiffracted, mode [16]. The fibre is placed close to the grating such that the $\pm 1^{st}$ order modes overlap in the core creating an interference pattern within a Gaussian envelope (Figure 15b). The manufacture of individual phase gratings is an expensive and time consuming process but is ideal for mass production of FBGs as each individual grating is near identical.

For research purposes, however, the process lacks flexibility as it is only possible to produce a very narrow range of periods from an individual phase grating. The problem can, and often is, solved by the introduction of additional optics. Beam stops and mirrors (Figure 15c) allow for manipulation of the interference pattern while eliminating unwanted higher, or residual zero, order radiation giving a higher quality grating. This allows a single phase grating to produce a much larger range of periods for research purposes.

The third technique commonly employed is a point by point writing system. In contrast to the two previous techniques this does not generally take advantage of the UV photosensitivity. Instead the fibre core is irradiated with a high power, usually fs, IR source which produce individual point like periods of index contrast through multi-photon absorption [54]. Due to spot size limitations these gratings are rarely of small enough period and as such are limited to second order FBGs. A grating can therefore be generated either by translating the fibre in the focus of the laser such that individual pulses become regularly spaced or by translating the focus of the laser, Figure 15d,

often by moving the whole laser across the fibre. Accurate positioning of the laser/fibre is thus key as individual periods are written independently. Errors in the translation process result in a poor quality grating, this along with polarisation sensitivity due to elliptical focusing effects in the FBG are seen as the most serious disadvantages of the system.

The three techniques produce differences in the refractive index profile of the gratings. The two interference writing techniques produce a sinusoidal profile generally within a Gaussian envelope, Figure 15. In contrast the point by point technique gives a grating consisting of almost delta function like points spaced at a particular period. The reflective spectrum of these two techniques does not generally differ significantly although there may be differences due to the inherent or applied apodization, cf. §2.1.8.

Inscription of LPG elements is fundamentally different due to the scale of the periods. Typically the period of an LPG is of the order of 300-600 μm and these cannot be generated by the same interference patterns of 240 nm UV radiation. Instead a number of techniques have been investigated and demonstrated; ion implantation [55], dopant diffusion [56], mechanical stress [57], electrical discharge [58] and CO_2 laser irradiation [59] have all been demonstrated but the use of fs [60] and UV irradiation [61] are most common due to the availability of equipment and expertise based on FBG inscription. The fs point by point technique differs little from the FBG writing technique, only the period and length of the inscription needs to be altered (Figure 16d). Again, the refractive index change is usually asymmetric due to focussing effects and as such the LPG demonstrates birefringence [60]. While this may actually be beneficial for this special case of transverse loading systems, in the case of most general sensors this further complicates an already complicated system and was deemed unsuitable for the work in this thesis.

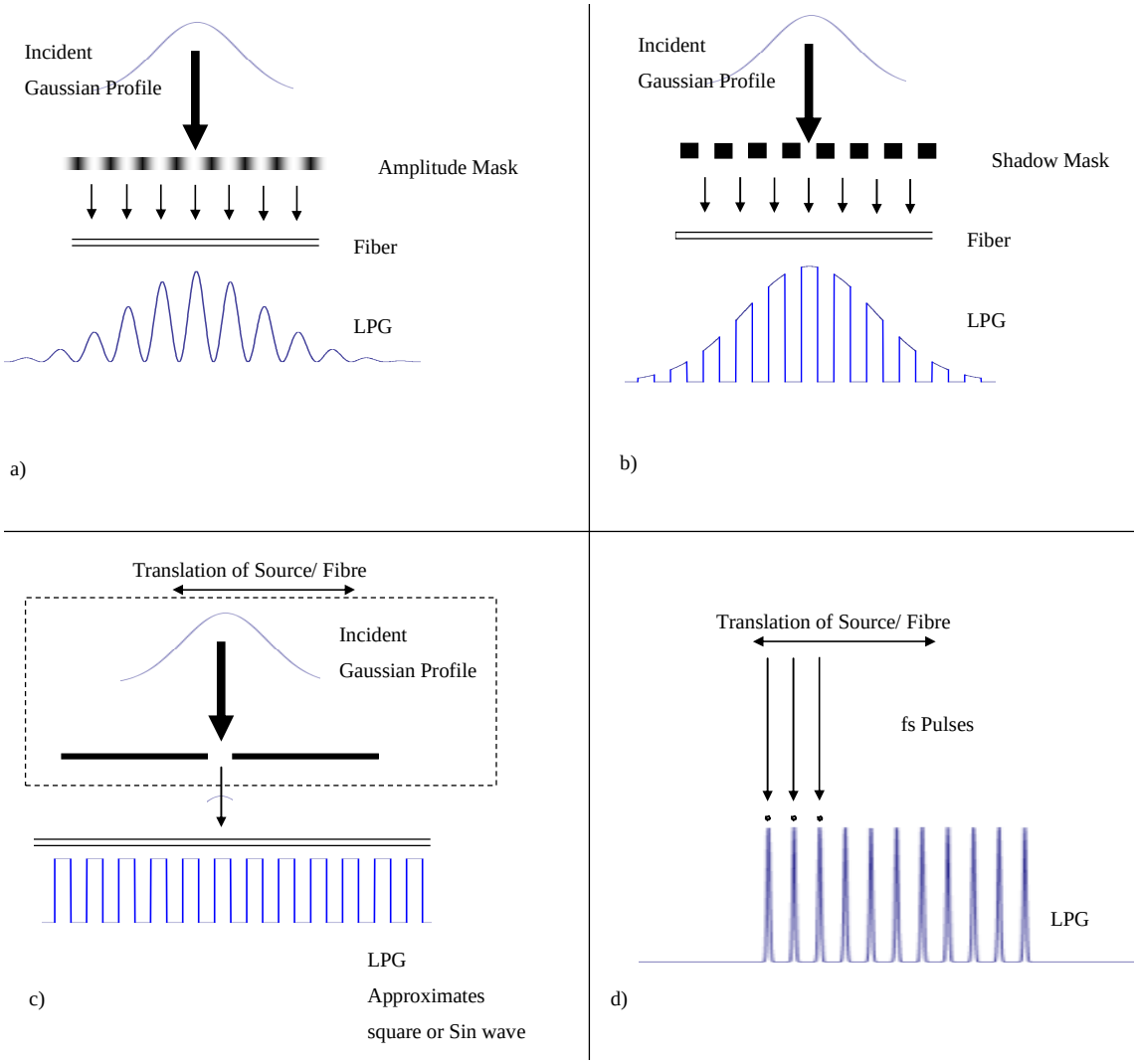

Figure 16: Illustration of common LPG manufacturing techniques. a) Amplitude mask UV inscription, b) Shadow mask UV inscription, c) Point by point multipass slit technique (CGCRI), d) Point by point fs laser inscription [16, 37].

As interference patterns cannot produce the required periods easily, masks are most commonly employed. A common UV technique uses an attenuation or shadow mask. This acts as an intensity filter to a broad UV beam giving a periodic sinusoidal or square wave refractive index variation within a Gaussian envelope, similar in result to the interference techniques used for FBGs (Figure 16 a & b). Another common alternative is to use a slit of the same order of magnitude as the period of the fibre. Such a slit is too wide to diffract the UV beam significantly but can be employed in a point by point system to write each period of the LPG separately. This is the technique employed at the Central Glass and Ceramic Research Institute (CGCRI) in Kolkata. The CGCRI

have kindly provided us with research grade LPG elements as part of an ongoing collaboration. The point by point system has therefore been used to inscribe the majority of the LPGs used in the experimental sections of this thesis.

The setup at the CGCRI consists of a Coherent[1] (formally TUI) BraggStar laser [62] producing 16 mJ at 248 nm. Individual periods are inscribed by irradiating the fibre through a 200 µm slit at a distance of 6 mm from the fibre core (Figure 17). The entire UV source is moved across the fibre between periods. Each pulse produces only a small refractive index shift but with multiple passes the desired refractive index change can be achieved. As the slit used is smaller than the period this gives the flexibility to inscribe a range of wavelengths with a single slit as each period of the fibre is created by overlapping a number of exposures through the slit (Figure 16c and Figure 18).

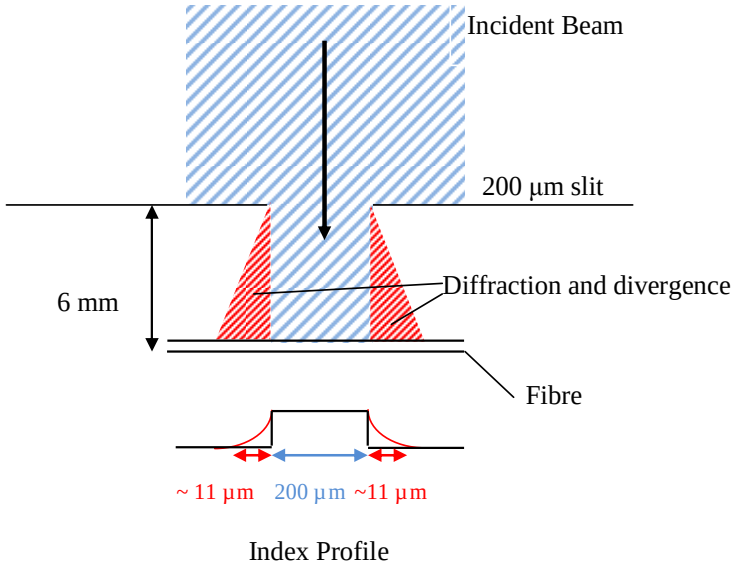

Figure 17: Illustration of the CGCRI setup with the effect of divergence and diffraction on the resultant refractive index profile.

While at first glance this would appear to produce a square wave refractive index profile the sharp edges of the index change will be smoothed due to diffraction from the slit and divergence of the source. An estimation of both effects can be made through the geometry of the setup and the divergence of the BraggStar laser. The FWHM divergence of the laser is quoted as 1 or 2 mrad [62] for vertical and horizontal

[1] Coherent Inc. 5100 Patrick Henry Drive Santa Clara, CA 95054 USA, http://www.coherent.com/

respectively. We can assume that the lower divergence direction has been used to irradiate along the axis of the LPG to minimise the effect of divergence. Given a separation of 6 mm the total divergence then becomes 6 µm. The effect of diffraction can be estimated as the angular separation between the central maxima and the first minima of an Airy disk [63] i.e. Eq. 4:

$$Sin(\theta) = 1.22\ {}^{\lambda}/_{d} \qquad \textit{Eq. 4}$$

Where θ is the angle of the first minima, d is the slit diameter and λ is the wavelength.

Given a wavelength of 248nm, a slit diameter of 200 µm and a fibre-slit separation of 6 mm this gives a divergence spread at the fibre core of 9.3 µm. To estimate the combined effect of both divergence and diffraction we can take the root of the summed squares i.e ~ 11µm of spread either side of the period (Figure 17).

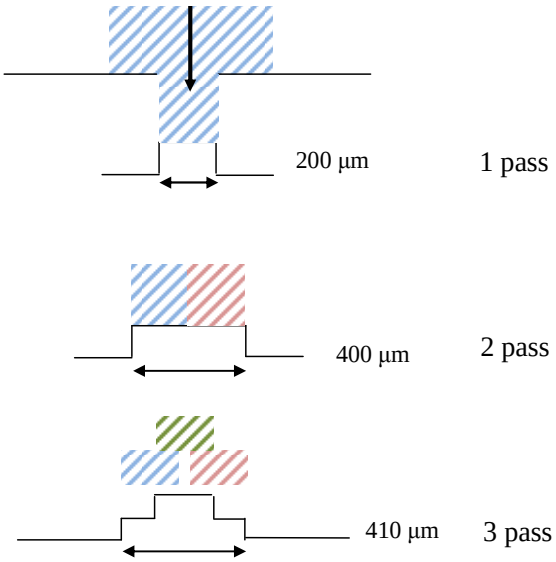

Figure 18: Illustration of 3 possible refractive index perturbations made by illuminating a fibre through a 200 µm slit with a UV source with 1-3 passes, note that the number of combinations of passes and index profiles is very large

This leads to significant uncertainties in the modelling of LPGs as the profile is neither a sinusoid nor a square wave although it is usual in such cases to assume that the refractive index profile can be approximated as sinusoidal.

2.1.7. Annealing

The changes to the bond structures within the core of the fibre, central to the photosensitivity process, can be undone with sufficient energy. As the interactions between dopant(s) and hydrogen are complex, there exist a range of bond structures and thus a range of energy levels which can be de-excited. With increased temperature, bonds begin to gain sufficient energy to de-excite, in effect bleaching the grating and slowly removing it. While it has been demonstrated that regenerated gratings (where increasing temperature forms a new grating structure with a period very similar to the original grating) can be formed at even higher temperatures [64] this is considered an unwanted effect in the context of this thesis. During operation of a sensing element it is necessary to assume some base line of stability. The bleaching process removes this stability as the coupling strength of the grating will continually decrease as a function of the maximum temperature that the grating has been exposed to. It is therefore preferable to expose the grating to temperatures above the maximum expected operational temperature before installation. This process is known as annealing [65].

The annealing process will bleach the grating resulting in a drop in coupling strength. It is therefore necessary to over-expose the grating in the writing process in expectation of bleaching during annealing. Typically gratings are annealed to 200-400 °C dependant on the expected operational requirements of the grating [65], for the fibres used in this thesis an annealing process of 200 °C for 2 hrs (or sufficient to ensure stability) was used, this ensured thermal stability and full hydrogen unloading during experimentation. A grating thus annealed can be said to be stable in terms of the temperature based bleaching up the annealing temperature. Estimating the required over exposure during the writing phase and, in the case of hydrogen loaded fibres, the shift to the LPG wavelengths and coupling strength due to temporary hydrogen induced refractive index changes makes inscribing a grating to fit a particular requirement challenging.

2.1.8. Apodization of Fibre Gratings

The first FBGs produced in 1978 exhibited large sidebands in their spectra which was a limiting factor in their usefulness as precise wavelength selective filters [16, 26]. Apodization, i.e. the modulation, or tailing off of the strength of the periodic

perturbation of the grating reduces these sidebands. The effect is analogous to the use of windowing in FFT analysis. In the case of FBGs, this has increased the effectiveness for use in band pass or band reflection filters and increased the resolution for sensors based on the wavelength codified position of the FBG reflection band by reducing the bandwidth of reflection [16].

In LPGs, the effect of apodization is similar and it reduces the presence of side bands in the transmission spectrum [22]. Again, this increases the effectiveness of LPG elements when used as band rejection filters [65]. The effect on an LPG is transmission spectrum can be seen in Figure 19, where the Gaussian, i.e. apodized grating, exhibits near zero sidebands and a narrowing of the loss band [22].

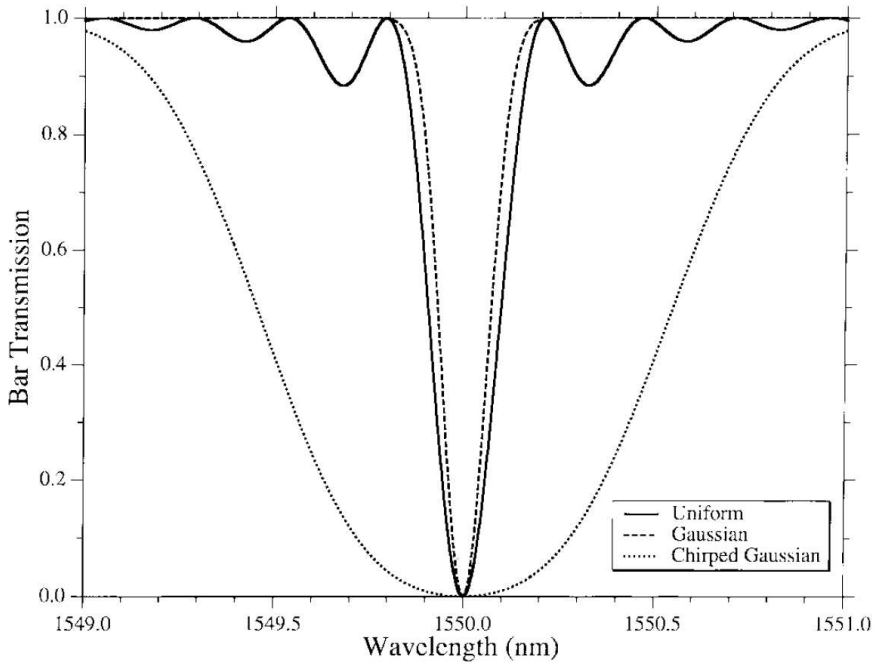

Fig. 15. Calculated bar transmission $t_{=}$ through a uniform grating (solid line), a Gaussian grating (dashed line), and a chirped Gaussian grating (dotted line) with grating parameters given in the text.

Figure 19: Illustration of the effect of apodization with a uniform (sinusoid) and apodized, (Gaussian) envelope LPG transmission plotted. Taken from Erdogan [22] with original caption.

Creating apodized FBG filters is now standard for industrial applications and indeed the common methods used to create FBG elements "naturally" produce an apodized

element due to the use of a Gaussian beam cf. §2.1.6 [16]. In the case of an LPG, apodization is easily achievable with a large Gaussian beam [37] and a shadow or attenuation mask or, potentially, by varying the pulse power in fs laser inscription. While the system used at the CGCRI does allow for apodization, this increases the complexity of the inscription process and has not been implemented as it was felt to be more important to have a well characterised grating for the work in this thesis.

2.1.9. Interrogation of LPG elements

FBG based sensor technology has benefited in recent years from the development of dedicated FBG interrogation hardware. One of the most widely used systems for interrogating FBGs consists of a tuneable laser scanned over a wide spectral range and the simultaneous recording of the reflected intensity as a function of wavelength. Alternative systems consist of a broadband source illuminating an FBG and a swept wavelength analysis of the reflected light or an array based detection in combination with a dispersive grating [16, 17]. Depending on the configuration, data rates between 0.1 Hz and 10's kHz can be achieved [16, 17] , allowing either high accuracy absolute wavelength determination of the FBG's centre wavelength or a high speed analysis of a relative change (although there are numerous alternative systems each dedicated to a particular application or form of sensor).

LPG elements are fundamentally different. In contrast to FBGs they operate only in transmission. The transmission spectrum consists of a number of discrete loss bands each corresponding to a single cladding mode. Individually each of these cladding mode loss bands is significantly wider than the reflected bandwidth of an FBG, and together the whole multi loss-band spectrum occurs over a bandwidth of about a micron.

In order to measure such a large spectrum in its entirety, it is necessary to employ an ultra-broadband source, i.e. white light radiation source, often a tungsten filament or a supercontinum source, and a spectrum analyser. There is a substantial trade off between the resolution of the system and the time taken to carry out a single scan. Timescales of 5-10 s per scan are common, e.g. 0.2 Hz, which for many sensing applications may be substantially slower than the rate of change in measurand. The larger spectral range can

often be mitigated by considering that the various modes do not all respond to external stimuli equally (§2.1.5). It is often only necessary to measure one of these loss bands at any given time, reducing the spectral requirements from 1000 nm to some 100 nm [22]. This is compatible with FBG interrogators which, provided that the loss band is inscribed to match the operating wavelength of the interrogator, can be usefully employed to measure relatively small shifts in the order of sub nm. More commonly, it is necessary to interrogate the LPG using either a broadband white light source (tungsten), a super luminescent LED (SLED) or amplified spontaneous emission (ASE) source with a typical bandwidth of 60 nm. Use of a white light source gives the flexibility to monitor any of the loss bands regardless of the scale of shift which occurs in their spectrum. Use of an SLED, for which there are a large range of available wavelengths, gives greater power and thus allows for higher resolution and faster monitoring. In either case a broadband spectrum analyser is the preferred detection technique giving 10s of pm resolution across the 1000-2000 nm range. Due to the flexibility of this arrangement, it has been used extensively within this thesis with fibre optic interrogators employed only where the increased temporal resolution is a critical factor.

2.1.10. Modelling of Gratings

There are a number of commercially available software packages designed to model the propagation of radiation through waveguides. These packages can be divided roughly into two categories: propagation models and mode calculations. The propagation model type involves a gridded model of the waveguide, including any grating, and applies a finite difference algorithm to directly model the electric and magnetic field components at each grid step over time. This provides a complete solution to the Maxwell equations for a given simulation providing an accurate calculation of modal propagation. Due to the relatively large size of an LPG in comparison to the wavelength of radiation to be modelled, these simulations become unmanageably large in the case of LPGs. The alternative is to calculate the available cladding modes and apply coupled mode theory, the mode calculation type of software. The difficulty here is in the commercial aspect of the software; it contains proprietary information. This results in the user being presented with a black box like interaction with results essentially being presented with

no indication on the exact method, or assumptions, being used to calculate them. Attempts were made to simulate LPGs using Optiwave™ (Optigrating™) and BeamProp™ (GratingMod™) but both were found to be unsatisfactory. In particular the software is optimised for calculation of FBG-type core-core mode coupling, and it was found that the simultaneous calculation of cladding and core modes was inconsistent in the returned effective indicies. Additionally some behind the scenes assumptions raised questions as to the reliability of calculated results, particularly in the automatic removal of even order cladding modes and the re-indexing of the remaining odd order modes. In essence the results derived from these simulations were found to be inaccurate, unreliable and derived from unknown assumptions giving questionable validity. The decision was therefore made to carry out my own simulation calculations.

There are several standard models for the theoretical modelling of a long period and short period gratings [18, 19, 21-24]. In a standard single mode optical fibre there are hundreds of available core, cladding and radiative modes. In general, a complete solution to grating mode coupling is too complex to implement, so by necessity each model is based around a number of key assumptions. These assumptions mean that each individual model is valid only for a particular fibre type, grating or refractive index profile. These systems do, however, have a number of fundamental steps in common. Generally speaking, the models require the calculation of the effective refractive index of the core mode, the effective indicies of the available cladding modes (or counter propagating core mode in the case of the FBG) and then coupled mode theory calculates the mode interactions and therefore the transmission spectrum. A more complete discussion of the model applied for this thesis can be found in Chapter 4 and §6.4 and in the code is presented in Appendix A.

Calculating the available core mode in single mode fibre is trivial, thanks to the work done in perfecting optical telecoms fibre. By solving the dispersion relation of the fibre the mode propagation constants, i.e. effective refractive index of the allowed mode(s) can be found. These standard solutions are sufficient to describe the core mode of our LPG systems and a complete derivation of these equations is not presented here but may be found in many standard texts on the subject the most detailed of which may be found in Tsao's book [66]. Of interest is that these calculations assume an infinite cladding, i.e. that there is no cladding external interface In standard fibres, the core mode is well confined and it is to be expected that this approximation makes little or no difference to

the calculated core mode effective refractive index while significantly simplifying the solution.

In the case of an LPG it is necessary to also calculate the available cladding modes. In principle it is possible to calculate them in the same manner as the core mode, i.e. a two layer system ignoring the fibre core. Due to the larger size of the cladding there will be multiple solutions to the dispersion relation and with the correct approximations only the circularly symmetric cladding modes of interest need to be found. In practice this approximation is wholly unsuitable for LPG modelling [18]. The coupling between core and cladding modes takes place at the position of mode overlap i.e. in the core of the fibre. This makes calculating the mode profiles in this region critical.

Instead it is necessary to calculate the cladding modes by considering a three layer system, core, cladding and external layers. This adds a significant layer of complication to the model and calculating the effective indices of the available cladding modes is the most laborious part of a simulation. This can be simplified significantly by considering that not all the modes need to be modelled. Over a given wavelength range and LPG period there is a limit to the range of effective indices which can be coupled, cf. Eq. 1. It is interesting to note that the solution of the three layer dispersion equation also produces the solution of the core mode. This can be directly compared to the solution for two layer approximation where the difference is of the order of 10^{-6} refractive index units (RIU) validating the two layer approximation used to calculate the core mode.

With the core and cladding modes calculated, the remaining step is to calculate the amount of power coupled form one mode to another thus deriving the transmission spectrum of the LPG. There are two common techniques to this solution. The first is to apply a simplified form of the coupled mode equation. The second applies matrix transfer functions whereby the power in the modes is described as a matrix and each period of the LPG as a transfer matrix [19, 67]. The difference between the two techniques is primarily conceptual. In the case of this thesis the first technique, based on Erdogan's [18, 21, 22] papers was chosen, primarily because it was felt that it could be most easily adapted to the inclusion of metallic layers.

2.1.11. Chemo-Optic Hydrogen Layers

There are a number of materials which, when exposed to hydrogen, exhibit a change in optical properties. In some cases this change is dramatic enough to result in a change in the colour of the material, while in others it is a more subtle change to the optical constants (refractive index). As these layers change their refractive index in response to some external stimuli of interest, they are known as chemo-optic layers. An LPG is in principle sensitive to any change in the refractive index of a coating placed on the outer surface of the cladding. As we have seen from §2.1.4, the sensitivity is dependent on the refractive index contrast at this boundary. It is therefore sensible to assume that not all materials will produce the same shift in resonance condition even with the same scale of shift in refractive index.

In terms of the measurement of hydrogen, a large number of materials have been demonstrated to be sensitive to hydrogen and, at least in principle, available for use as a coating for a hydrogen sensing LPG. A complete list of hydrogen active layers would be the subject of a study in its own right, but we can consider three main families of materials. Rare-earth elements, often combined with additional catalytic or adhesion layers, have been demonstrated to exhibit large optical changes in the presence of hydrogen [68-72]. The transition metals all exhibit some form of change with hydrogen absorption, although this is often to a lesser degree than Pd and requires a catalytic layer [68, 73-79]. Finally, Pd and Pd based alloys have been used extensively due to the high absorption of Pd and the uniquely selective dissociative catalytic activity, cf. §2.2 [80-83]. In practice, only tungsten oxide, WO_3, and Pd have enjoyed widespread patronage. Where WO_3 demonstrates superior long term stability but a lower response and often requires a catalytic surface Pd layer to assist in absorption. In part this is due to reversibility issues with the more exotic coating designs which require specific conditions to purge absorbed hydrogen, or it is due to operating temperature. More generally though, it is a case of complexity. In most cases, including WO_3, it is necessary to include a thin catalytic layer of Pd on the surface of the material in order to dissociate the hydrogen molecules into atomic form [73]. This atomic form can then be absorbed by the chemo-optic layer giving the required change in refractive index [73].

This catalytic layer has all the same vulnerabilities and disadvantages of a Pd detector layer with the added vulnerabilities, disadvantages and increased deposition complexity

of the chemo-optic layer. While the response of these layers may be larger, the system as a whole becomes far more complex than is nessersary. In terms of the scope of this thesis, the development of a robust understanding of LPG-Pd interactions, of the behaviour of Pd and of metal jacketed LPGs in general is of primary interest. While the existence of alternative optically active layers is therefore acknowledged they fall outside of the scope of the thesis.

2.2. The Palladium-Hydrogen System

2.2.1. Introduction

Palladium, Pd, is one of the eight platinum group metals [80]. Geologically these metals occur together and palladium is often found as the junior partner of platinum alloys [80]. The isolation of Pd as an element was not accomplished until the 19th century and since that time considerable effort has gone into studying not only the material properties of Pd and its alloys, but also the interaction between Pd and hydrogen [80, 84-87].

Most bulk elements absorb hydrogen to some extent, but it is the platinum metals which do so most effectively and palladium which does so to an extreme [80, 84-86]. So effective is Pd at absorbing hydrogen that it can absorb up to 900 times its own volume [80], a fact which has led to Pd being adopted as a possible storage medium for hydrogen [80]. Since the first observation in the early 1860's [80] a number of studies have looked into the interactions of Pd and hydrogen, more so than any other metal - gas interaction [80]. While the studies of Pd have been intensive they have not been exhaustive and a completely comprehensive model of the Pd-H system has yet to be formed [80, 88-91]. This review is therefore limited to those aspects which are directly relevant to this thesis namely thin but homogeneous films. In particular the study of "Pd black" and Pd electrolysis, while interesting, is of little direct relevance [80, 83].

2.2.2. Absorption Process of Hydrogen in Palladium

The absorptive properties of Pd are a result of the catalytic properties with respect to molecular hydrogen, H_2. The absorption process can thus be broken down into two distinctive phases. First, molecular hydrogen is dissociated at catalytic sites on the Pd surface from where it is subsequently adsorbed as atomic hydrogen into the body of the Pd lattice [80, 92, 93]. The desorption process can be seen as the reverse with hydrogen atoms migrating to the surface to recombine into molecular hydrogen or, in the presence of oxygen as OH^- radicals which can subsequently form water at these catalytic.

This dissociative property is what leads Pd to adsorb of such large volumes of hydrogen. Atomic hydrogen is much more easily absorbed into the lattice structure. The range of hydrogen based devices that include at least a catalytic layer of Pd bears witness to this property [73, 94, 95]. What happens to the hydrogen atoms once absorbed into the lattice of Pd is a matter of some small debate [80, 84-86, 89, 93, 96-100]. Early work supposed that the hydrogen reacted in some manner with the Pd forming a hydride, hydrogenium or some similar semi-permanent molecular solid bond [80, 84-86, 89]. However, more recently, the opinion has shifted towards hydrogen being absorbed into the solid structure where it exists in a loosely bound state at specific sites in the lattice. Considerable work has gone into the understanding of the energy levels and lattice deformation energies created by inserting atomic hydrogen into the octahedral and tetrahedral sites [93]. For the purposes of this study it is sufficient to concede that the hydrogen atoms sit at interstitial sites within the lattice structure. The comparatively small size of individual hydrogen atoms allow them to take these positions with a minimal disturbance to the surrounding Pd lattice [93].

Naturally the presence of hydrogen atoms within the lattice provides some localised strain and as such the distribution, and ultimately the adsorbed concentration, become a matter of balancing the internal strains and the external hydrogen pressure – the so called partial pressure balancing [80, 92]. As there is no formal direct chemical bonding between hydrogen and Pd [93], rather a balancing of energies resulting in a shift of the outer Pd^{4d} band, the hydrogen is free to move about the lattice provided there is sufficient energy (i.e $T > 100$ K) [97]. This ensures that the absorption is not confined to a surface adsorption layer but rather the hydrogen is diffused throughout the Pd more or less equally until equilibrium is reached. In this equilibrium state the macroscopic

characteristics of the Pd will be stable even as hydrogen continues to circulate microscopically at some drift velocity [83] and a molecular/atomic dynamic exchange of hydrogen takes place at the Pd surface.

At low hydrogen concentrations it is therefore possible for the Pd lattice to maintain its structure without significant alteration, aside of a 3D expansion which is known as the α phase [80]. As hydrogen concentrations increase, individual stress fields generated by hydrogen atoms begin to overlap and the Pd lattice is no longer able to maintain its structure without a significant shift towards a new β phase [80]. The precise turning point between these two phases is highly dependent on temperature and pressure, but below a critical 573 K and 20 atm [99] the two phases will co-exist simultaneously at hydrogen concentrations above ~3% in nitrogen (Figure 20).

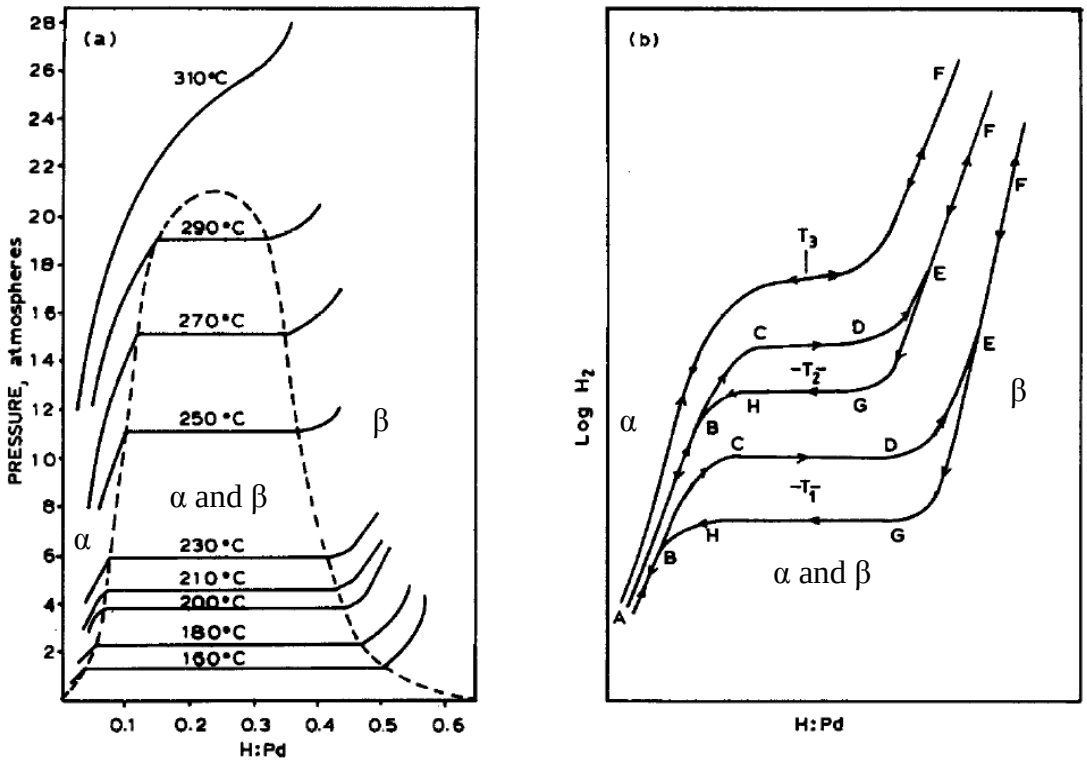

Figure 20: Plots a) temperature and pressure and b) hysteresis of hydrogen absorption in Pd over the α, β phase change adapted from [80, 84] respectively.

These two phases, α and β, have significantly different lattice constants - 3.889 Å and 4.04 Å respectively - a 4% shift [101] reflecting the effective expansion to

accommodate increased hydrogen concentration [46, 102]. This significantly complicates the model of Pd-H, introducing hysteresis (Figure 20b), non-reversible hydrogen absorption and macroscopic changes to the lattice [46, 80, 102, 103]. Multiple cycles between the two phases will deform the structure of multi-crystalline Pd to the point of destroying a sensing element based on it (Figure 21) [80, 101]. At the same time the large shifts in micro and macroscopic properties due to this phase shift makes the system potentially useful for a single shot measurement technique [103]. Some of the original data presented by Lewis [80], upon which much of the understanding of Pd-H has been based, makes the oversimplification of a linear response within the α, β and mixed phases with a transition point between them. An assumption which has validity only when considering single crystal, defect free, Pd.

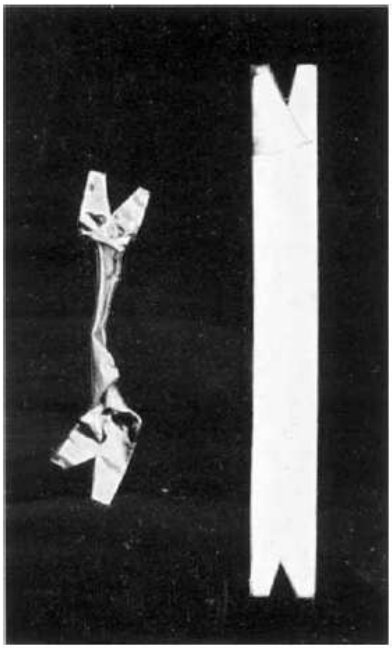

Figure 21: Comparative image of pure Pd (left) and PdAg, ~25% Ag an alloy which has a higher threshold of phase shift, (right) bars after thirty cycles hydrogen absorption through the α-β phase shift. The bars were originally of the same size. Taken from Hunter [104].

Within the concentration and temperature ranges of interest to us, ~1-2 atm 0-1% H_2 in N_2 283-373 K (cf. §1.5), we can assume that the system operates exclusively within the α phase and as such can be described as a non-linear though reversible absorption

process. The effect of temperature on the absorption of hydrogen within this regime is a non-linear dual effect. With increased temperature the absorption rate increases but the change to the lattice decreases. It should be noted that the literature cannot rule out the possibility of hysteresis as the β phase is approached [80] and it is possible that once exposed to hydrogen a minimum level will be retained within the structure permanently or at least over a period of months [101]. All of these processes are temperature dependant.

2.2.3. Optical Changes within the Hydrogen-Palladium System

Thus far we have discussed the absorption of Pd as a purely strain effect. While these strain effects are easy to visualise, the operating principle of LPG type sensors requires an optical change; although a strain based LPG sensor is possible an FBG is better suited for this measurement [34]. Conceptually it is easy to imagine that a change to the lattice bond structure (a deformation of the Pd^{4d} bond) will result in a change to the electrical conductivity, or resistivity of the Pd [105, 106]. Indeed it is this change which is most often exploited to form electrical Schottky Diode type hydrogen sensors where the resistance increases with hydrogen absorption [94, 95].

As it is the interaction between electron energy levels and photons that characterise the optical properties of metals these will also change with the change in conductivity [106]. The situation is further complicated as there is relatively little agreement between published sources as to the complex refractive index of thin (1-100nm) Pd films [107-110]. This is due to the various forms of Pd used in the studies. Bulk Pd differs from particulate Pd (often called Pd black [80]), which differs from thin film Pd and even within those groups, sample preparation, measurement technique and sample creation technique all influence the resultant optical properties [110-112]. It is therefore necessary to talk, not of the optical properties of Pd, but rather of the optical properties of particular films produced by a particular method.

It is possible to infer the scale and the direction of the changes to the permittivity of Pd as a function of hydrogen absorption, again provided that there is no crystalline phase change. We expect there to be a drop in both the real and imaginary component of the permittivity, corresponding to a decrease in reflectivity, of Pd as a function of hydrogen

absorption (Figure 22) but that this process should be non-linear with respect to hydrogen up to the phase boundary [113].

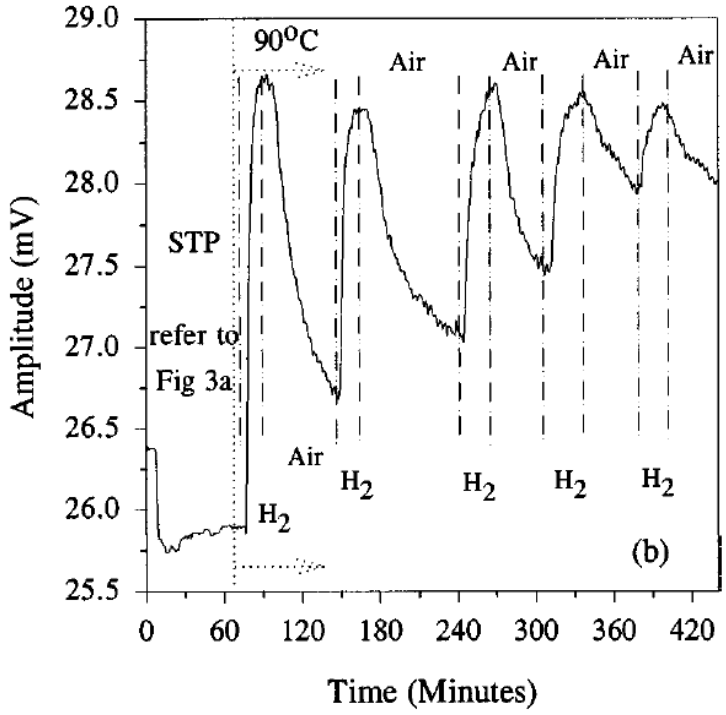

Figure 22: Plots of the reflected amplitude from a 5 Å thick Pd film over several cycles of 4% hydrogen in balance air and air. Taken from Kalli et al. [114].

2.2.4. Palladium Alloys and Contamination

As a metal, the optical properties of Pd are impossible to separate from the surface science of Pd. Since films over ~70 nm in thickness are optically opaque, over the 1000-2000 nm wavelength range, we expect the optical properties to be defined by this ~70 nm layer for which surface quality forms an critical part. With the introduction of the Pd-H interaction the resultant system gains further complexity in regard to possible contamination. This can be seen as three separate contamination issues:

1. Surface contamination through adsorbed material.
2. Bulk contamination from absorbed material.
3. Extra surface Pd-H interference.

It should be noted that for the LPG-Pd system the optically active layer, monitored by the radiation transmitted through the LPG, is removed from the catalytic Pd layer by the thickness of the film; i.e. the adsorbing layer is separated from the fibre by the bulk of the Pd film (Figure 23). As such the surface contamination leading to direct optical changes is of less interest but may impact attempts to characterise the refractive index of Pd.

Adsorbed materials are surface contaminants which will effectively alter the refractive index of the material as observed from that side [115]. In addition, contaminants may interact and block the catalytic dissociation sites on the surface of the Pd which will have an effect on the rate of hydrogen absorption and desorption [115, 116]. Specifically, we must consider sulphur/sulphides [115-118] and complex hydrocarbons [115-117]. Hydrocarbon chains do not, in themselves, interfere with the adsorption or dissociation of hydrogen but in the presence of hydrogen these compounds will fragment and these fragments may become lodged in catalytic sites [115-117]. Similarly sulphur will preferentially sit in the catalytic sites impeding the adsorption desorption and dissociation of hydrogen [117, 118].

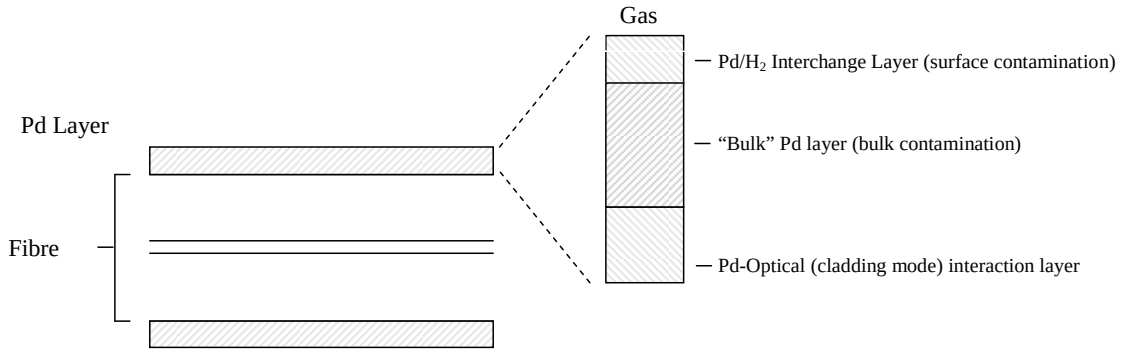

Figure 23: Schematic of the metal, glass interface in the LPG-Pd system illustrating the absorption, bulk and optical interaction layers.

While palladium does not readily form an oxide a very, almost atomically, thin layer of palladium oxide, PdO, can be expected to form over time in the presence of oxygen. PdO has a substantially different refractive index to Pd [119] and its formation

interferes with the critically important catalytic sites reducing the rate of absorption and desorption significantly [119, 120]. Adsorbed, or oxide, contaminants can be readily removed from the Pd surface with thermal or gaseous purging. In particular it is expected that the PdO and sulphur will be effectively removed with repeated cycles of hydrogen provided that there is sufficient catalytic activity to allow hydrogen adsorption.

The second forms of contaminants are absorbed into the body of the Pd. This is most often accomplished during the Pd thin film deposition. These contaminants effectively act as dopants causing irregularities in the Pd lattice interfering with the bulk absorption of hydrogen as well as altering the refractive index of the material [115]. With careful control of the deposition technique it is possible to almost completely eliminate unintentional dopants (typically 99.99% purity, also known as 4-9's purity) [115]. Instead it may be of benefit to consider adding intentional dopants in the form of alloys. The two most common alloys are silver and copper. Silver alloys typically increase the amount of hydrogen which can be absorbed by the structure without a phase change allowing a sensor to operate at elevated concentrations, pressures and or temperatures (Figure 21). Copper alloys by contrast are used to provide resistance to surface contamination particularly in the presence of sulphur. The drawback is that the alloy forms of Pd are less sensitive to hydrogen concentrations as the optical and mechanical changes are muted.

Finally, it is necessary to consider interference with the Pd-H system. Thus far we have limited our discussion to the presence of hydrogen within inert gases. It is necessary to consider the possibility that certain species will prevent the dissociation of hydrogen, or the adsorption/desorption process. Most common of these is oxygen. In the presence of oxygen the system equilibrium is shifted in favour of desorption. In effect the hydrogen is drawn out from the structure to form water on the surface. This prevents the absorption of hydrogen meaning that the Pd will act as if no hydrogen were present. In a humid environment water will evaporate from the Pd surface less rapidly acting as a barrier to hydrogen desorption or absorption [115, 116]. This has the additional effect of preventing the Pd-H system from responding to hydrogen concentration changes or to slow it considerably [115, 116].

2.2.5. Conclusions

The Pd-H system is one of the most heavily studied and complex metal-gas interactions. This review can only provide an incomplete overview of the more relevant information. The sheer complexity of the system makes it difficult to make assumptions or simplifications for a general case. The complex interaction of Pd-H can be significantly simplified if we limit the consideration to the range ~1 bar 0-1% hydrogen in nitrogen and 283-373 K. Within this range phase changes, hysteresis and irreversibility can be ignored providing a reversible, though likely, non-linear absorption corresponding to a decrease in the transmission and permittivity of Pd. The precise changes to the permittivity of Pd will have to be characterised for a particular deposition technique and range of thicknesses as well as a function of hydrogen concentration. Additionally care must be taken to eliminate or compensate for possible contamination, particularly in the presence of water, oxygen and complex organic compounds. A study to characterise our thin film Pd layers is therefore essential to develop sufficient understanding of the LPG-Pd system for practical modelling. This forms the subject of the next chapter.

Chapter 3. Characterisation of Pd Thin Films

3.1. Introduction

As discussed in §2.2 there is little commonality in the available literature on the optical properties of Pd. This is particularly true of Pd thin films. The exact refractive index of these films is highly dependent on the deposition method and precise deposition parameters [110]. As a result it is necessary to thoroughly characterise and calibrate the Pd films manufactured with our in house coating system.

3.2. Coating Technique

Our coating chamber is capable of both RF sputter coating and thermal evaporation. As RF coating has greater control, decreased thermal effects and produces a superior homogeneity – particularly for thin films it is the preferred method for creating all of our Pd thin films. The thermal evaporation unit has been limited to providing Al and Ag coating for thickness measurements as discussed in §3.4.

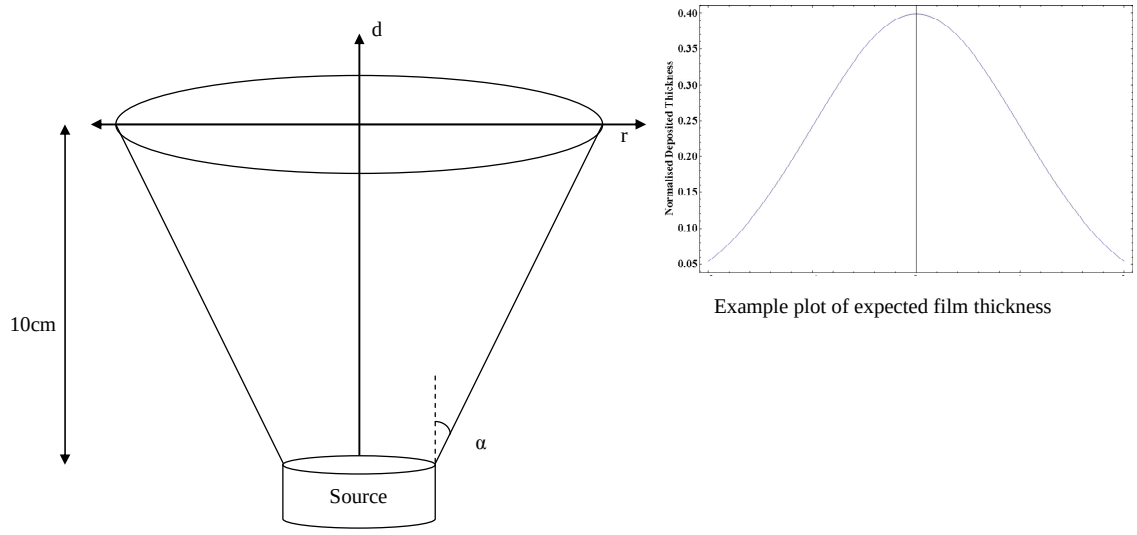

Figure 24: Schematic illustration of Gaussian deposition from RF or thermal source.

The coating chamber is an adapted Edwards Auto 206 Vacuum Chamber capable of pressures to around 1 $x10^{-8}$ mb although 1 $x10^{-5}$ mb is used for most coatings. This chamber is a general resource available to the group and by extension to the university as a whole for deposition of various metals and compounds. As such there is a risk of cross contamination with a variety of elements particularly Au, Ag, Cu, Al and ITO. Assessment of the purity of the deposited films is therefore of importance (cf. §3.5). The internal geometry of the chamber leads to more or less uni-directional coating particularly for the RF unit. A motor is necessary to rotate fibres to ensure even coating and masks may be used for selective deposition. As the evaporation or RF sputter deposits with an essentially solid angle model with a roughly Gaussian distribution (Figure 24) above the target, care must be taken to ensure that the distance separating the substrate and source/target is kept at a constant both during a particular deposition and between coatings, this is particularly important for rotating mounts. This ensures reproducible coating rates (thicknesses) and surface quality, although some variation in deposition thickness must be expected both between and across individual samples.

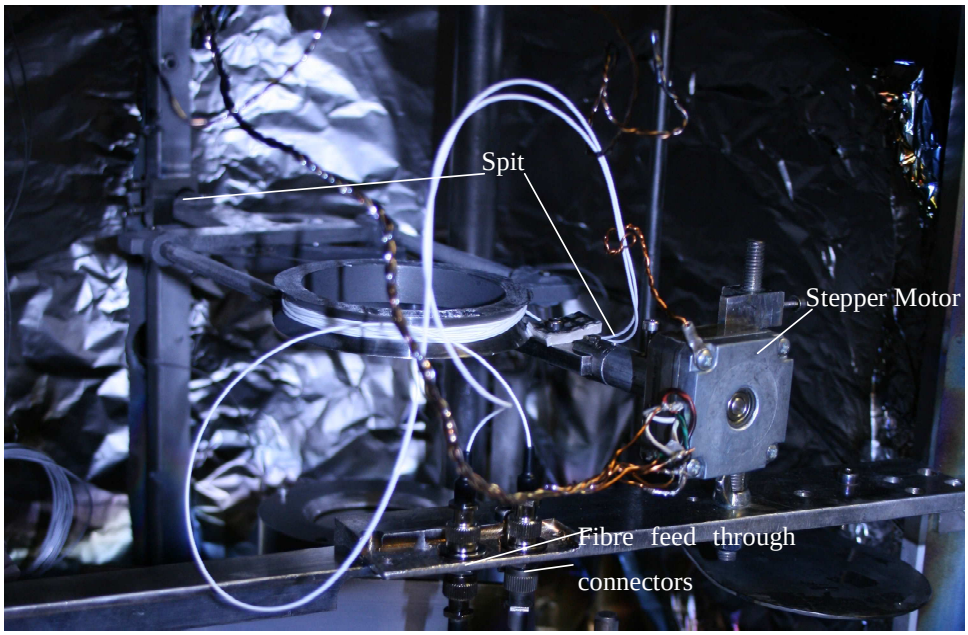

Figure 25: Fibre rotation setup showing stepper motor driven spit with optical feed through.

For fibre coating, a stepper motor is employed that is attached to a specially made spit (Figure 25). The motor is rotated at a rate of ~0.25 Hz and in the case of the fibre being connectorised for in situ measurements (§6.3.2), it rotates ~1.5 times before reversing direction. The spit is anchored at both ends (via the motor and a pivot point attached to the back of the coating chamber). This provides mechanical stability and helps to ensure reproducible placement with respect to the target. The spit itself is designed to be balanced in weight (two spools either side of the rotational axis) and the fibre to be coated (max 10cm) is held securely and taught along the axis of rotation.

For flat samples, a metal plate sitting on brackets both front and back of the chamber is used. This ensures reproducibility of the source-fibre distance between deposition runs and provides a medium to attach masks to. Some samples require both RF and the thermal unit to be used (§3.4), in which case a rotating arm and stop markers are employed to allow the substrate to be moved during the coating process (Figure 26).

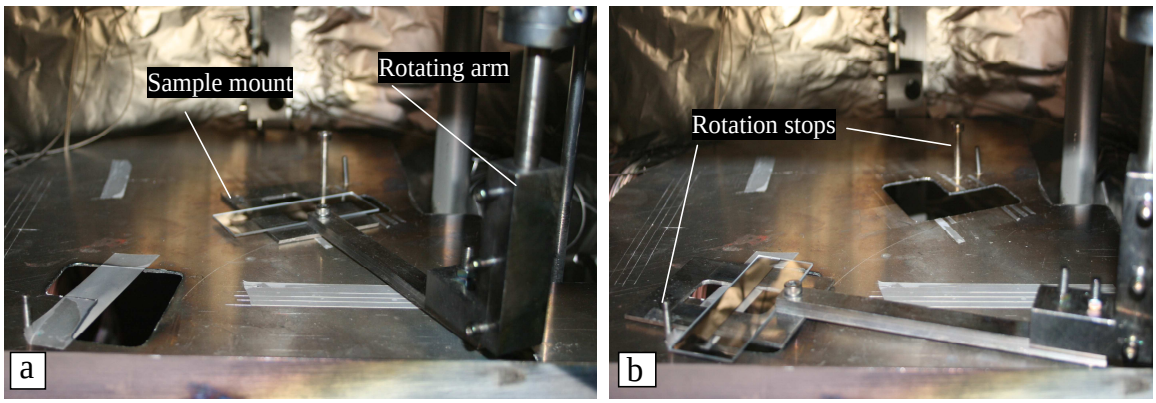

Figure 26: Armature used for flat sample deposition. Rotation of armature from position a to b allows for both RF and thermal deposition respectively.

Both the RF and thermal units require a pressure of at most $1x10^{-6}$ mb which takes approximately 2hrs to pump down to from atmospheric pressure. The RF unit is controlled via a Dressler Lesar RF Power Generator and for standard Pd coatings it is run at 70 W plasma power in a 9.5 $x10^{-4}$ mb flowing Ar atmosphere, although a pressure of 6.0 $x10^{-3}$ mb is needed to ignite the plasma. With 10 cm separating the Pd target from the substrate this provides a coating rate of typically ~0.5 nm sec^{-1}. A shutter is used to shield the sample from coating during the plasma ignition process and

for the first 60 s operation of the plasma to clean off any contaminants. It should be noted that the simultaneous use of the shutter and the fibre spit is not possible as the rotation of the spit would be stopped by the shutter, a symptom of the size of the chamber. In this case the 60 s pre-burn is carried out shortly before loading the fibre into the chamber and pumping down. This pre-burn ensures that any contaminants that may have built up on the surface of the target, particularly oxides, are removed before the sample is exposed to coating. All distances and parameters are held constant between coatings ensuring repeatability of deposition.

The thermal evaporation unit operates by passing a current of up to 6 A[2] through an evaporation vessel. A movable shield is used to provide some control of coating times and a quartz crystal can be used to monitor the deposition rates. The crystal is exposed to a known density of deposition over a known surface area. Film thickness can be calculated to an accuracy of ~1 nm during coating by measurement of the change in the resonance frequency of the crystal, an automated process. This system can be used for both the thermal evaporation and the RF unit but due to the roughly Gaussian solid angle of deposition (Figure 24) the measured deposition will not accurately reflect the thickness on the sample. As such it is necessary to make an independent measurement of the deposited thickness either on the sample directly or by use of a witness slide placed as close as possible to the sample.

3.3. Surface Smoothness

The modelling of metal jacketed fibres (§6.4), ellipsometry based measurements and the surface plasmon resonance experiments all require a flat homogeneous layer of Pd. Published investigations of the surface quality of RF deposited thin films suggests that under certain conditions, particularly Ar pressure above 0.02 mb, surface structure or roughness can occur [112]. Care was taken during our deposition process to ensure that no such surface structure should form through control of Ar pressure and deposition energies. In order to determine the quality of the thin films scanning electron microscope images taken from Pd layers deposited onto SMF-28® single mode fibres and deposited on Si wafer (§3.6).

[2] 6 A is the current as read from the control interface, once through the transformer the current through the filament would be much higher (e.g. ~ 30 A)

A first attempt to analise the surface quality was made using an in house SEM equipped with a tungsten filament electron source. Unfortunately the source used is of too high an energy. By focusing the electron spot size to the resolution required to detect the expected feature sizes, ~10-100 nm, the Pd film becomes damaged through excess charge build-up making accurate scans impossible. An alternative, lower energy and therefore higher resolution, field emission gun (FEG) SEM was located at AWE in a classified area. Due to security considerations I was unable to be present for the scans. Instead suitable samples were created, packaged in a nitrogen atmosphere and delivered by next day courier to be scanned as soon as possible after arrival; minimising the potential for contamination to occur.

The results of the scans (Figure 27 and Figure 28) illustrate that our deposition process is successful in creating a homogeneous flat film with no structure on 10's of nm scale validating the homogeneous flat approximation.

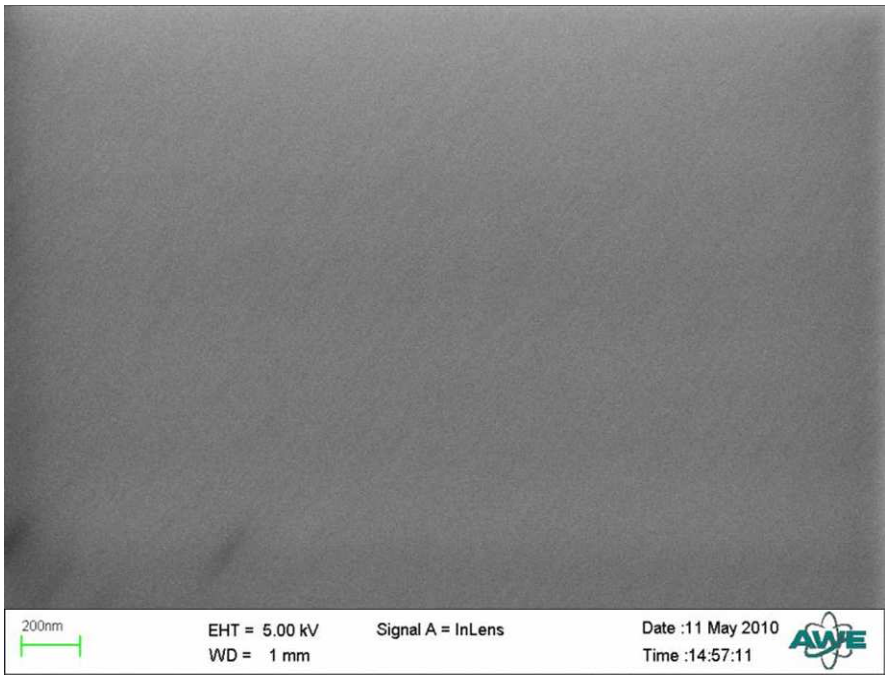

Figure 27: SEM scan of Pd thin film deposited on a Si wafer using our in-house RF deposition technique. Horizontal lines in the image, if present, are an artefact of printing.

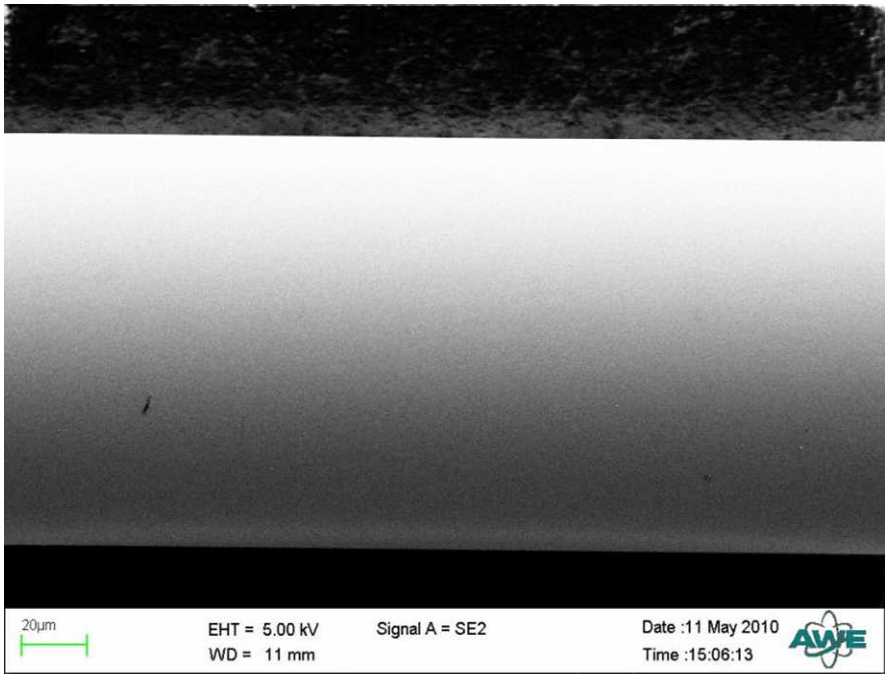

Figure 28: SEM scan of Pd thin film (~100nm thick) deposited onto SMF-28® fibre. Horizontal lines in the image, if present, are an artefact of printing.

3.4. Film Thickness

As mentioned in §3.2 the RF unit creates a solid angle of deposition. At 10 cm separation the FWHM is approximately 30 cm. As my sample/films are typically of order 2 cm in length, this gives an expected thickness variation of the order of 0.4%. As such, thickness variations are not expected to be large across individual samples.

Direct measurement of the sample thicknesses has been attempted using two methods. A stylus, e.g. Dektak, can be used to track across a step function or post deposition scratch in the film giving a change in height and thus film thickness accurate to a few nm. This, mechanical process, gives a film thickness which is dependent on the hardness of the material and may not be entirely suitable for optical characterisation. As such it has been used only for estimating film thicknesses or the difference between two films rather than for absolute film thickness.

An alternative technique is to use a white light interferometer (WLI). This technique relies on tracking fringes across a sample surface, usually a step function between

uncoated and coated regions, through a microscope as the sample is translated through the coherence position of the WLI. The fringes from a broadband white light source are intensely localised and hence may be used as an accurate means of determining relative distances [121]. By monitoring these fringes across a step function it is possible to calculate the step height. Properly calibrated this can provide a measurement of the film thickness accurate to ~1 nm. Additionally as an optical technique the measured film thickness is more appropriate for optical characterisation. Unfortunately the nature of the thin Pd films we are investigating complicates the system.

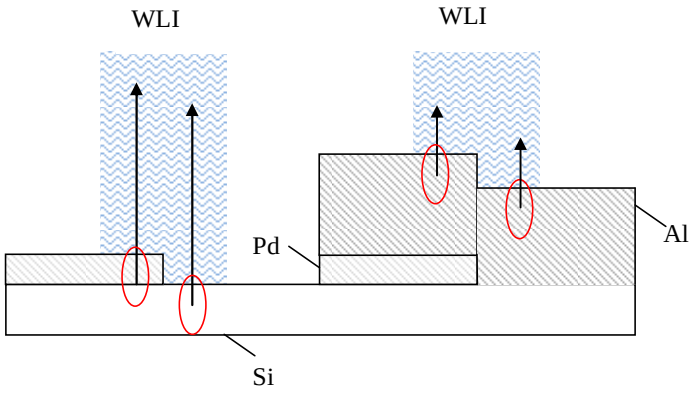

Figure 29: Illustration of the uncertainty in the reflection from thin film Pd, the red oval shows the range of optical penetration depths during reflection. Reflections from the Pd/Si interface are clear on the Si side but unclear on the Pd side as some light penetrates to the Si surface. With an aluminium overcoat the reflections are clear on both sides of the step.

Pd films below ~60 nm are not 100% reflective, but are partially transmissive [46]. As such the surface from which the reflection and therefore fringes originate is not clear and a derived film thickness becomes meaningless (Figure 29). To compensate we developed a new technique, a second film is deposited over the first. 100 nm of Al deposited via thermal evaporation provides a surface that is optically opaque, providing an unambiguous reflection surface while retaining the step-function of the underlying Pd. Additionally both sides of the step are made of the same material with the same optical properties. This allows for a direct comparison of the height of the two sides without having to compensate for the difference in reflective properties and phases. The

use of thermal evaporation also allows both coating processes to be accomplished in a single run for flat substrates (cf. §3.2). For rotating fibres it is necessary to remove the witness slide from the spit and re-mount it for an Al overcoat. This provides a film thickness with a resolution of ~1 nm but there is an expected systematic error due to the provided calibration step being quoted with only 10 nm accuracy.

3.5. Film Purity

As discussed in chapter §2.2.4, the presence of contaminants on the surface of a Pd thin film or within the bulk Pd can significantly alter the absorption of hydrogen into the structure and the resultant change in refractive index. A common technique to measure surface contamination is X-ray Photoelectron Spectroscopy (XPS). XPS operates by illuminating a sample in an ultra high vacuum with a particular x-ray emission line, usually Al K^{α} (1486.6 eV) or Mg K^{α} (1253.6 eV). These are absorbed on surface of the sample and electrons are emitted via the photoelectric effect. These electrons can be detected and, with suitable calibration, their binding energies measured. As the binding energy of an electron in a particular element to another element is unique, this provides some information on the relative abundance of particular elements, as well as information on what those elements are bound to, i.e molecular information. For example, there is a small change in the binding energy of an electron of Pd in the presence of a molecular bond to oxygen compared to Pd only molecular bonds. The technique is well suited to the characterisation of thin films, as the electrons typically travel only very short distances, limiting the effective depth of the measurement to a few nm. As the system requires the interaction of particular electrons with the x-ray smaller, more confined shell states (e.g. those in hydrogen and helium), cannot be detected as the probability of collision with the electron cloud is simply too small.

I was able to test a two Pd coated silicon samples using the XPS system of the Angle-Resolved Photoemission Group in the Physics Department at the University of St-Andrew's. Two separate samples were chosen, both deposited onto a thin silica substrate (microscope cover slip). Both samples were prepared at the same time. One was sealed in a nitrogen atmosphere while the other had been exposed to a cycling of 100% nitrogen and 1% hydrogen in balance nitrogen over the course of a week until the

surface plasmon resonance suggested a contamination of the surface (cf. §3.7). Both samples were transported to St-Andrews in sealed sample containers in a nitrogen atmosphere. The samples were mounted with conductive tape onto a gold slide for loading into the machine. Plots of the recorded binding energy against the number of counts provide characteristic peaks for each element. Plots of these, including higher resolution plots of regions of interest can be seen in Figure 30 and Figure 31. A table of the binding energies present and the corresponding elemental bond is presented below (Table 1). It should be noted that small differences in the recorded binding energies are to be expected between individual measurements due to calibration errors in the detector [122].

Table 1: Lists of binding energies and their corresponding bonds for the two XPS samples

Bond	No cycling sample bond energy (eV)	Post cycling sample bond energy (eV)
Pd^{4p}	52.7	52.7
Pd^{4s}	87.0	87.1
Si^{2p}	101.8	102.1
Si^{2s}	153.4	153.3
S^{2p}	166.3	NA
S^{2s}	228.8	NA
C^{1s}	284.5	284.6
$Pd^{3d5/2}$	337.3	337.0
$PdO_2{}^{3d5/2}$	335.1	335.1
$Pd^{3d1/2}$	340.0	340.3
$Pd^{3p3/2}$	531.0	531.8
$Pd^{3p1/2}$	560.0	560.0
Pd^{3s}	671.0	671.4

.

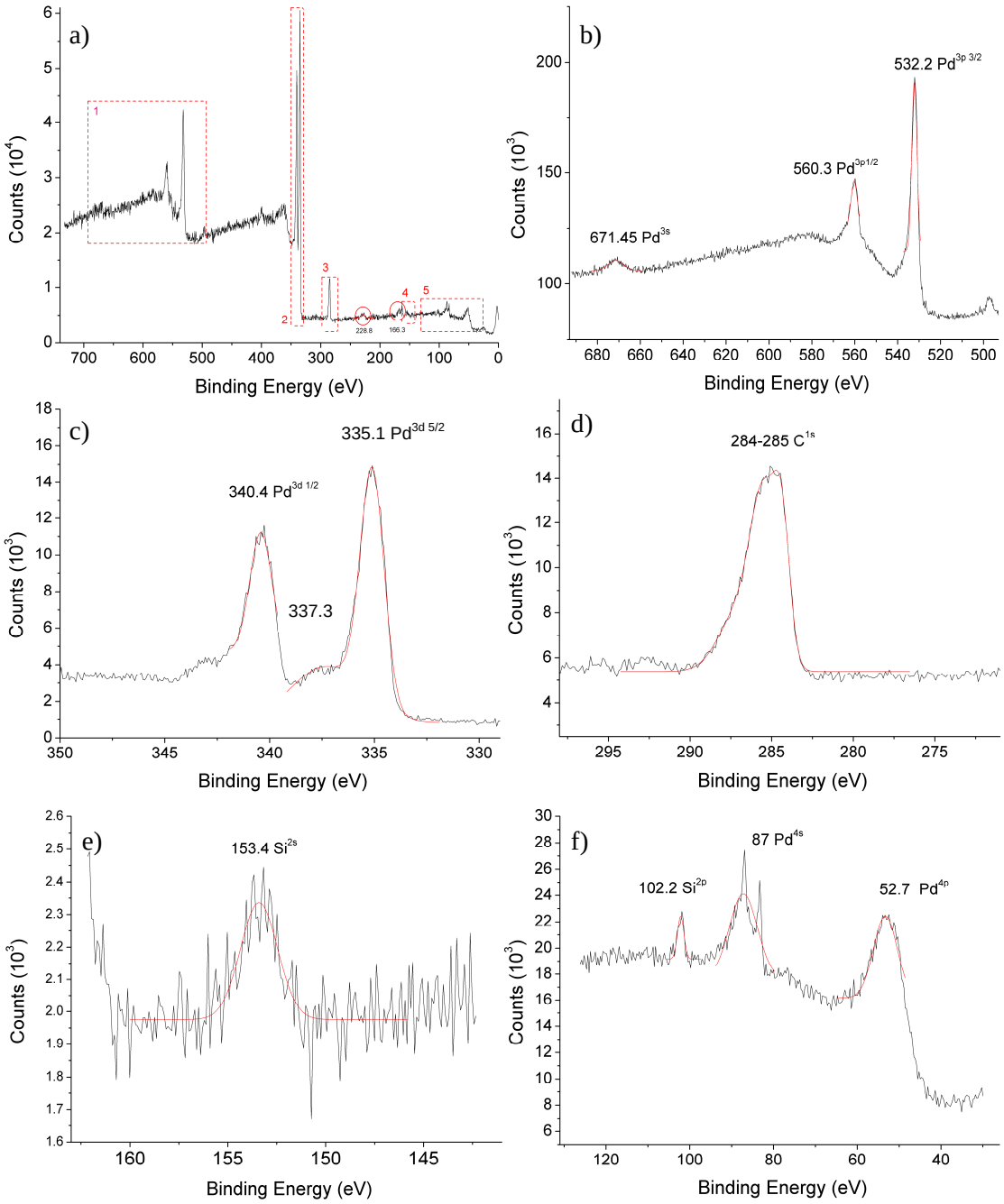

Figure 30: XPS scans of Pd film before contamination. a) overview, b) higher resolution scan of area 1, c) higher resolution scan of area 2, d) higher resolution scan of area 3, e) higher resolution scan of area 4 and d) higher resolution scan of area 5. Fitted peaks are in red.

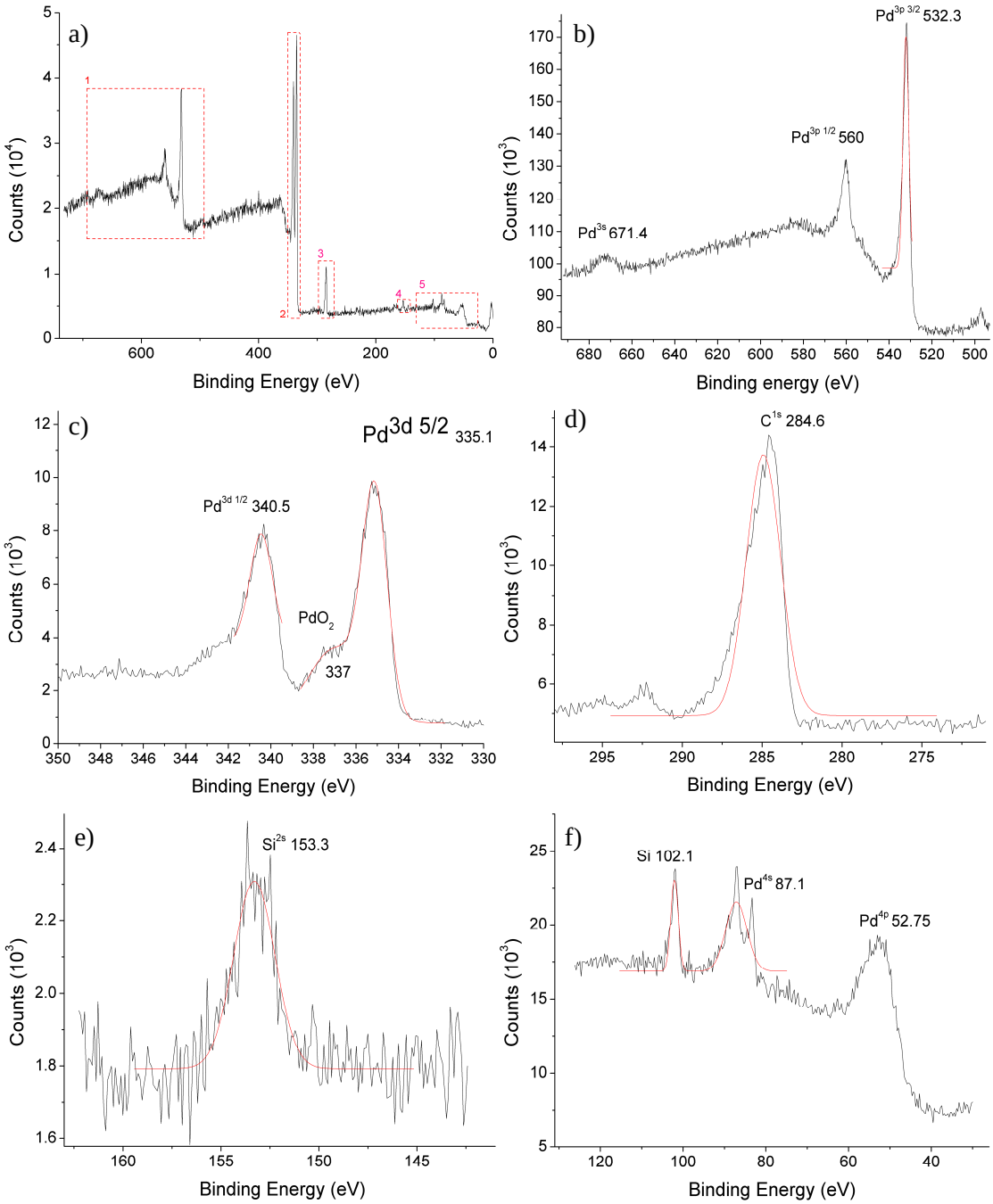

Figure 31: XPS scans of Pd film after contamination. a) overview, b) higer resolution scan of area 1, c) higher resolution scan of area 2, d) higher resolution scan of area 3, e) higher resolution scan of area 4 and d) higher resolution scan of area 5. Fitted peaks are in red.

Figure 30 shows the XPS results from the uncontaminated sample stored in nitrogen. Strong Pd peaks are expected and careful analysis of the splitting of the $Pd^{3d5/2}$ peak suggests the presence of a very thin layer of PdO_2, which most likely formed during the handling and transport of the sample after coating. Additionally the two Si peaks suggest that the glass substrate was exposed, indeed a visual inspection of the sample after XPS showed that some scratches had developed during XPS mounting and handling, exposing the substrate. There are also two S peaks present. As these are not present in the post cycling sample, and due to their small size we can assume that they are due to contamination from the pump oil used for the coating chamber. This sulphur contamination has probably been driven off the second by hydrogen cycling [116]. Finally there is a fairly strong carbon peak the position of which suggests a $(CH_2)^n$ structure i.e. a polymer. This is most likely a result of the use of a plastic sample container.

The second sample (Figure 31) shows the same peaks as the first, although we notice some key differences (Table 1). Firstly there is no evidence of sulphur. This is consistent with the sulphur originating from the oil/grease of the coating chamber pumps. On exposure to hydrogen this would be removed from the Pd [116] (§2.2.4). Secondly we note that there is only slightly more PdO_2 present, which is consistent with this film being exposed to roughly the same amount of oxygen i.e. air. The third difference is that there is more carbon present. As this sample was in the container for considerably less time than the other we can assume that the difference is due to contamination during the cycling process, most likely due to the plastic tubing used for the gases which would be more liable to produce loose polymer strands due to the presence of hydrogen [115-117]. The presence of these contaminants on the surface of the Pd would slow the absorption of hydrogen and interfere with the SPR measurements [115-117, 123] (§3.7).

In conclusion, we see that, although there is some small sulphur contamination of the sample during coating, the surface is otherwise pure Pd and neither Al, Ag or Au or any other contaminants are present. Although it is not possible to rule out the presence of a thin layer of PdO_2.

3.6. Refractive Index

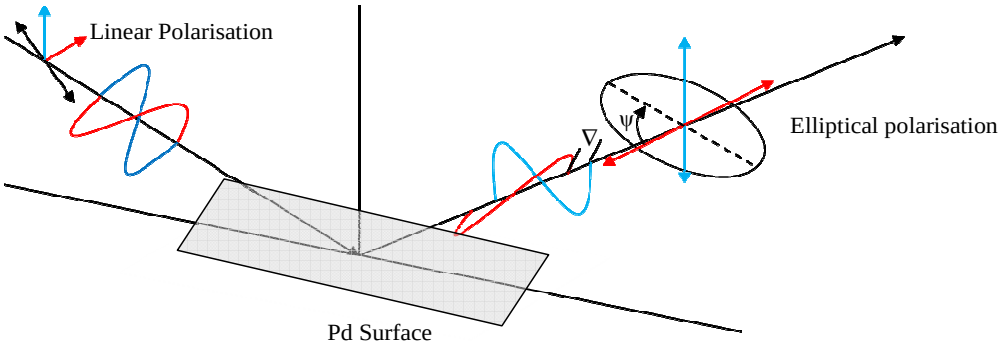

Figure 32: Illustration of the principle of ellipsometry.

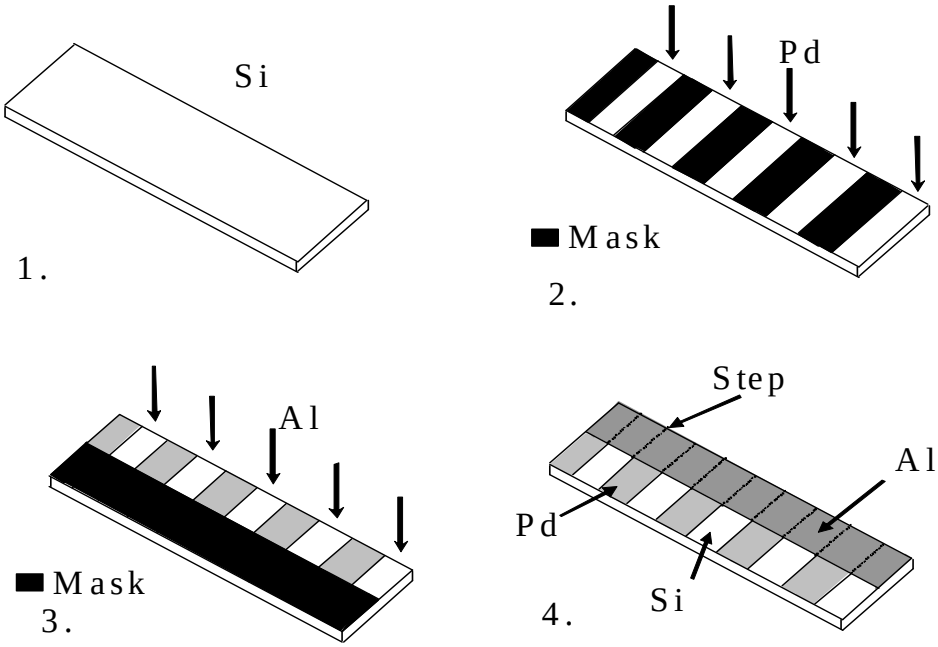

Figure 33: Illustration of the two stage coating process required to generate samples for ellipsometry and WLI analysis.

With a reliable means to measure film thickness it is possible to characterise the complex refractive index of Pd as a function of film thickness. Ellipsometry is specifically designed to measure the refractive index and film thickness of thin films [112, 124]. It operates by measuring the change in the polarisation of linearly polarised light reflected from the thin film on a known substrate at a known angle (Figure 32).

The two measured angles of polarisation rotation, Ψ and ∇, can then be fitted to a theoretical model of the sample. With the assumption that the substrate and film are both flat there are only two degrees of freedom in this model, the film thickness and the refractive index. The SEM analysis of the films suggests a homogeneous flat layer of sufficient flatness for an ellipsometry measurement (§3.3). As the refractive index of Pd is complex (a metal) it is necessary to independently measure the film thickness using the WLI interferometry method outlined in chapter §3.4 above. As the WLI requires a different sample surface (a step function over coated in Al) it is necessary to use a pair of masks and two coatings to provide the required sample structure (Figure 33).

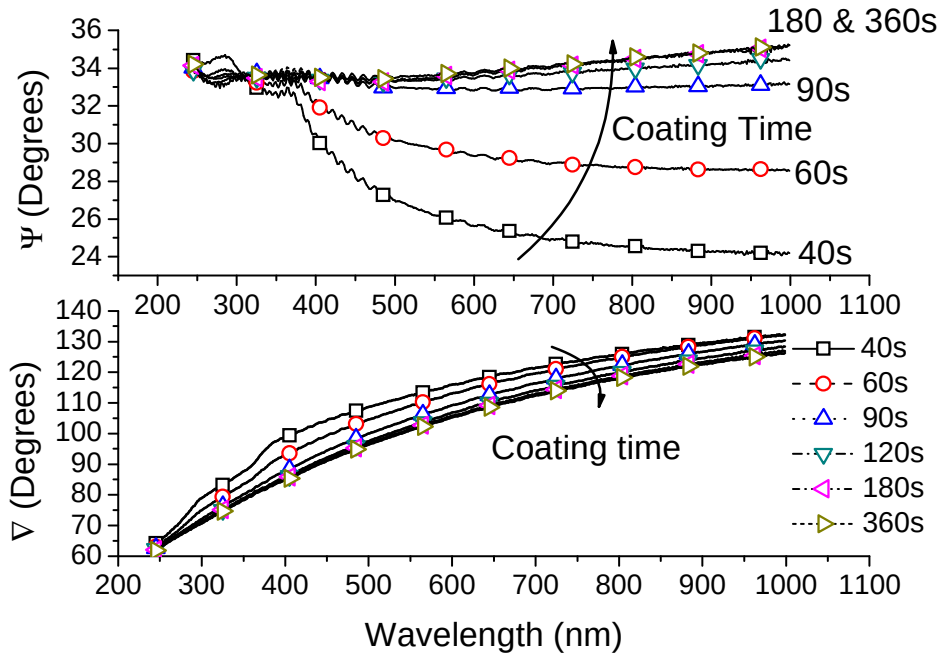

Figure 34: Plot of measured Ψ and ∇ as a function of the deposition time of Pd.

Figure 34 shows a plot of measured Ψ and ∇ for a range of prepared samples. As the film thickness is expected to be directly proportional to the coating time this has been used to label samples. The plot clearly demonstrates a trend indicating a proportionality of coating time to both Ψ and ∇. This is expected and can be attributed to a combination of change in film thickness with coating time and a contribution by the

change in refractive index which in itself is expected to be dependent on film thickness especially for very thin samples [47, 125].

In order to analyse the data it is necessary take each assumption in turn. By assuming that the proportionality of Ψ and ∇ to sample coating time shown in Figure 34 a is due solely to a change in film thickness, we may use previously published values for the refractive index of Pd [111] to recover the film thickness. Figure 35 shows a comparison of the film thickness retrieved by this assumption and that directly measured for the same samples by WLI. Of note is the generally good agreement between the two sets of data below a thickness of 40 nm. At longer coating times, i.e. 120 s giving about ~40 nm thickness, the deposited Pd film becomes more opaque and ellipsometry is unable to derive an accurate film thickness resulting in a plateau at about 40 nm.

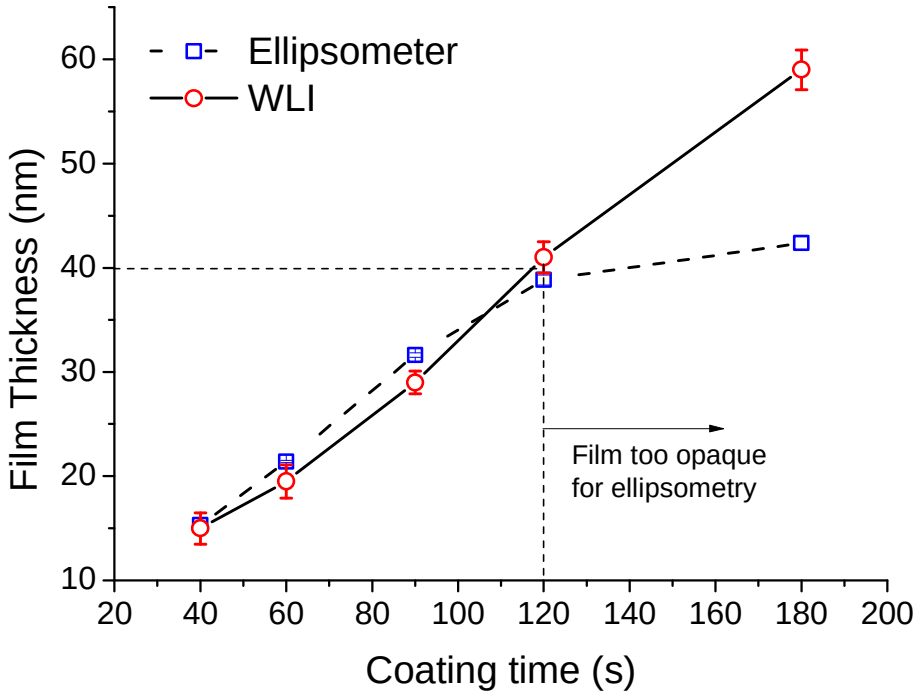

Figure 35: Plot of film thickness measured via WLI and derived via ellipsometry.

Of greater interest is that the two measurement techniques maintain good agreement for thinner films. If the refractive index of the films were dependant on film thickness then we would expect the two datasets presented in Figure 35 to be divergent for thinner

films. As this is not the case this suggests that the refractive index of the films is indeed independent of film thickness over the investigated range, 15-100 nm.

The alternative hypothesis is to assume that the WLI measurements for film thickness are accurate and to attempt derive the complex refractive index of the films from the Ψ and ∇ data. These data can be seen in Figure 36. Of interest here is the loss of clear proportionality between film thickness and complex index compared to the proportionality in Figure 34. Again this suggests that there is little or no dependence between film thickness and refractive index in the investigated range.

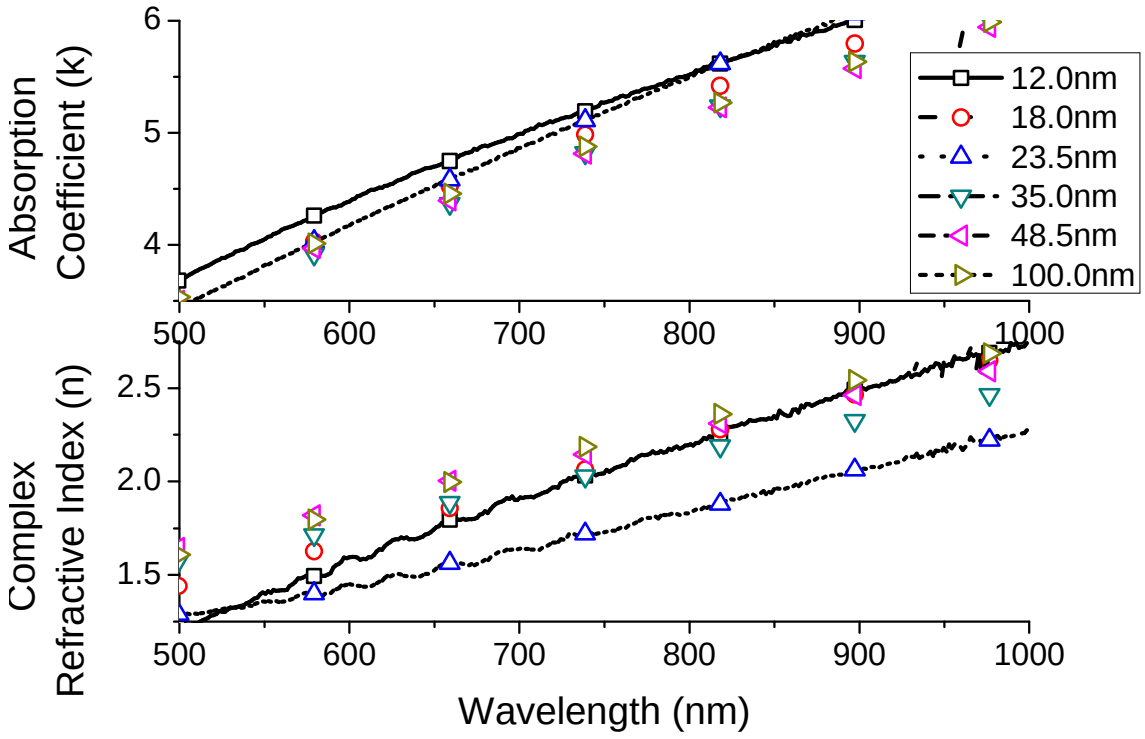

Figure 36: Plot of calculated complex refractive index derived via the WLI measured film thicknesses.

As the complex refractive index of Pd has been demonstrated to be independent of film thickness above 15 nm, we can use ellipsometry to characterise the complex refractive index of a thicker, ~100 nm, film. As the film is effectively too thick for a reflection from the Pd/Si interface to be visible, the film thickness is not a required variable of the fitting model and the complex index can be measured directly. This provides the required n(λ) from 1200-1600 nm of our Pd thin films.

Additionally a sample of 100nm thickness was sent to Woolam[3] for independent measurement. The results show excellent agreement (Figure 37) with those carried out at AWE. Interestingly, these results for n and k sit between the published data for RF sputter deposited Pd [110] and bulk Pd [111], illustrating the need to measure these values for a particular coating process.

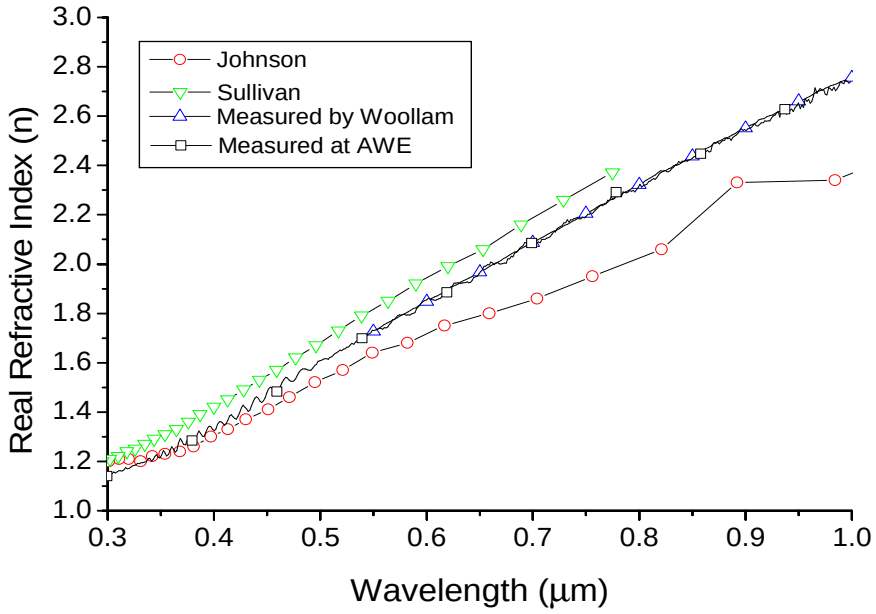

Figure 37: Comparative plot of published refractive index for RF sputtered Pd, Sullivan [110], bulk Pd, Johnson [111] and our films measured by ellipsometry at AWE, measured, and measured by ellipsometry by Woolam.

3.7. Palladium Hydrogen

Measuring the change in refractive index of our Pd layers as a function of hydrogen absorption provides more of a challenge, as the measurements must be carried out in a system where the precise gas concentrations can be altered. Although this is in principle possible, it would have required significant changes to the ellipsometer setup, which was deemed impractical due to time considerations. Therefore an alternative technique had to be devised. The alternative is to take advantage of the extremely sensitive surface plasmon resonance conditions which can be found in a Kreschmann prism arrangement [126] (Figure 38). Here, a thin metal (Pd) film is deposited onto the

[3]Woolam Europe, L.O.T. Oriel, Im Tiefen See 58, 64293 Darmstadt, Germany: http://www.lot-oriel.com

hypotenuse face of a prism. Light incident onto the back of the prism's will couple via the reflected beam evanescent field to a lossy surface plasmon mode on the air/metal interface, resulting in a dip in reflected power. The coupling conditions for the surface plasmon mode are dependent on the film thickness, the refractive indices of the prism and metal layers, the polarisation of the incident beam and the angle of incidence [123, 127]. The surface plasmon mode can therefore be characterised by a plot of the reflected system power against angle of incidence where resonant coupling is represented by a loss in the reflected power [123, 127]. By fitting these data to a rigorous model of the reflected power, it is possible to derive the permittivity of the metal layer.

3.7.1. Theoretical Model

In general there are two approaches to modelling a surface plasmon resonance in the Kreschmann setup. The simpler method (e.g. [128, 129]) models coupling with angles of incidence above the critical angle which is quite suitable for the modelling of narrow surface plasmon resonances (e.g. silver). Palladium, however, couples across almost all available angles and as such the more complex (and complete) solution, including modelling of angles below and about critical, is required. This analysis therefore closely follows that of Chen [127], although additional parameters have been included to deal with the additional sources of loss. Here we are assuming that the incident light is purely TM polarised with respect to the plane of the metal/dielectric interface as TE does not excite the surface plasmon [123, 127].

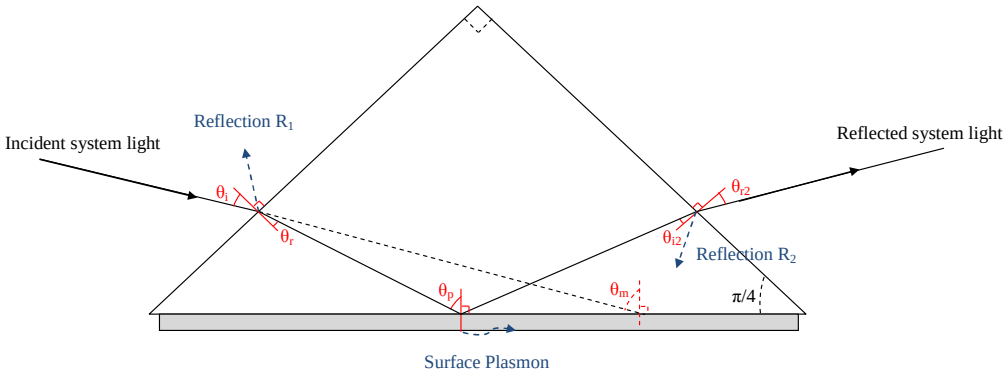

Figure 38: Schematic illustration Kreschmann configuration [126], angles have been exaggerated for clarity.

The angle measured by the rotation of the prism θ_m can be related to the various angles of incidence, refraction and the actual angle of incidence at the surface plasmon interface by simple trigonometry and Snell's law: Eq. 5 - Eq. 9.

$$\theta_i = \frac{\pi}{4} - \theta_m \qquad \textit{Eq. 5}$$

$$\theta_r = \sin^{-1}\left(\frac{\sin\theta_i}{n_p}\right) \qquad \textit{Eq. 6}$$

$$\theta_p = \frac{\pi}{4} - \theta_r \qquad \textit{Eq. 7}$$

$$\theta_{i2} = \frac{\pi}{4} - \theta_p \qquad \textit{Eq. 8}$$

$$\theta_{r2} = \sin^{-1}\left(\frac{\sin\theta_{i2}}{n_p}\right) \qquad \textit{Eq. 9}$$

Where n_p, assumed to be a constant over the linewidth of the laser, is the refractive index of the prism and the refractive index of the medium outside the prism is assumed to be air, i.e. 1 (although the refractive index of air, nitrogen and hydrogen are all fractionally greater than 1 the difference is insignificant to the modelling in this case).

If we assume that the material absorption is small then there are three separate losses to account for in order to calculate the complete reflected system power.

1. Reflection from Air/Prism interface R_1
2. Surface Plasmon and Prism/Metal interface
3. Reflection from Prism/Air interface R_2

The reflections are simple to calculate as these are pure Fresnel reflection coefficients dependant on only the refractive index of the prism and the angle of incidence in each case: Eq. 10 & Eq. 11.

$$R1 = \frac{\left(\cos(\theta_r) - n_p\cos(\theta_i)\right)^2}{\left(\cos(\theta_r) + n_p\cos(\theta_i)\right)^2} \qquad \textit{Eq. 10}$$

$$R2 = \frac{\left(n_p\,cos(\theta_{r2}) - cos(\theta_{i2})\right)^2}{\left(n_p\,cos(\theta_{r2}) + cos(\theta_{i2})\right)^2} \qquad \textit{Eq. 11}$$

The reflected power at the prism metal interface is: Eq. 12.

$$R = \left| \frac{\gamma_{p,m} + \gamma_{m,a} e^{2iK_{Zm}d}}{1 + \gamma_{p,m}\gamma_{m,a} e^{2iK_{Zm}d}} \right|^2 \qquad \textit{Eq. 12}$$

Where d is the metal film thickness K_{zi} is the wavevector component perpendicular to the interface in medium i, p,m and a are indices indicating the prism, metal and air respectively such that $\gamma_{i,j}$ and K_{zi} are: Eq. 13 - Eq. 15.

$$\gamma_{i,j} = \frac{\epsilon_i K_{zj} - \epsilon_j K_{zi}}{\epsilon_i K_{zj} + \epsilon_j K_{zi}} \qquad \textit{Eq. 13}$$

$$K_{z\,i} = \sqrt{\epsilon_i \frac{\omega^2}{c^2} - {K_x}^2} \qquad \textit{Eq. 14}$$

$$K_x = n_p \frac{\omega}{c} \sin(\theta_m) \qquad \textit{Eq. 15}$$

where ω, ε and c take their usual meanings of angular frequency, permittivity and the speed of light. Note that while ε_p and ε_a are real ε_m is complex.

These three losses can be converted to dB and added to provide the reflected system power, R_s: Eq. 16.

$$R_s = 10[\log_{10}(1 - R_1) + \log_{10}(1 - R_2) + \log_{10}(R)] \qquad \textit{Eq. 16}$$

As the refractive index (and permittivity) of the prism are known, and the Pd film thickness and permittivity have been measured it is possible to plot the expected reflected power as a function of angle of incidence.

In general the actual film thickness and permittivity of the metal layer will differ slightly from the measured values and as such it is necessary to fit the model to the data for each film in the presence of nitrogen using the data from the ellipsometry as the expected data. This gives an excellent fit and provides a film thickness for further measurements of varying hydrogen concentration (and therefore permittivity).

3.7.2. Experimental Setup

An experimental system to carry out these measurements has been constructed (Figure 39). It consists of an optically chopped, collimated, polarised light source (1524 nm HeNe laser) set to provide TM polarisation at the prism/metal interface. A polarisation maintaining beamsplitter ensures that the light incident at the back of the prism is solely TE polarised, while a second beamsplitter provides an optical power reference. The prism is mounted on a rotation stage to change the angle of incidence and a second detector mounted on a rotation arm measures the system reflected power.

Care must be taken to ensure that the incident beam is perpendicular to the plane of the hypotenuse of the prism and passes over the centre of the translation stage. Errors in either will result in difficult to predict errors in calculating the angle of incidence at the prism/metal interface. Alignment of the back of the prism to the centre of the rotation stage is not critical.

A small gas chamber (Figure 39b) is mounted onto the back of the prism allowing for the Pd film to be exposed to an arbitrary hydrogen concentration controlled via mass flow controllers. The thickness of the metal layer is critical to coupling to the surface plasmon, too thin (i.e. below ~15 nm c.f. §3.6) and the refractive index may vary with film thickness [47, 125], too thick and the metal/air interface will be too far from the reflected beam to couple via sthe evanescent field; a film thickness of 20-40 nm is typically acceptable [123, 127].

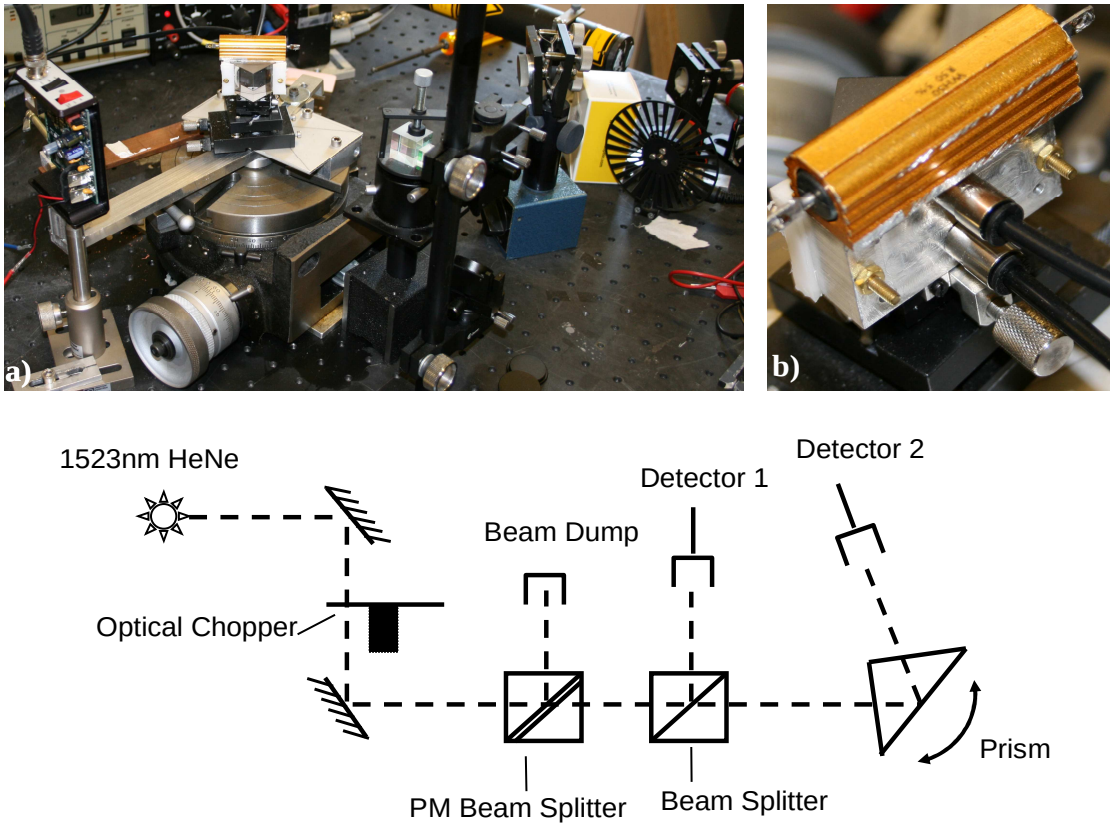

Figure 39: Photographs of Surface Plasmon Resonance setup a) Overview and b) rear view of prism gas ports with schematic of the setup below.

The reflected light power is monitored with a detector mounted on a rotation arm. Care has been taken to ensure that the height of the detector, in relation to the prism table, does not change as it is rotated about the same axis as the prism table. The arm is controlled via a screw giving fine angular control, but individual power readings must be taken at a position of maximum intensity rather than a measured angle. Errors for a single measurement are therefore possible in the alignment of the prism, the angle of the prism and the position of the detector.

3.7.3. Results

As a measure of the stability of this system it is possible to record the reflected power at a particular angle (within the range of the surface plasmon resonance) over time as multiple cycling of gas concentration are carried out. This process may also be used to monitor the rate at which the hydrogen is absorbed/desorbed by the system. The

response may be monitored through a change in the gas concentration until an equilibrium state is reached. Once achieved, a scan of the full angular range of the setup can be made and fitted to record the permittivity.

Due to limitations in the mechanical arrangement of the detector arm it is impossible, from a practical standpoint, to replace both the detector arm and the prism to precisely the same position after each angular scan. This translates into an offset in the recorded power before and after a completed scan. Figure 40 illustrates a typical response for this system. Here the offset, marked in red, has been removed for clarity with the original dataset as a comparison. The data demonstrates a limiting factor of this system; namely that the surface quality degrades after a period of ~4hrs. The surface plasmon resonance technique is critically sensitive to the surface quality of the metal film, up to a few Å. In our case care has been taken to ensure the surface quality during the coating process. Similar care was taken with the test rig for the experiment however, it is not possible to guarantee quality over a longer period.

XPS analysis reveals no new species on the sample after cycling (§3.5). It is suspected that the use of plastic rather than metal tubing, particularly in the presence of hydrogen, results in hydrocarbon species being released, contaminating the Pd surface. These hydrocarbons can become temporarily trapped on the Pd surface and while essentially a molecularly thin film this provides a significant and noisy change to the surface plasmon resonance conditions [123]. Their presence on the surface will also act to mask the catalytic dissociation sites on the Pd surface slowing the rate at which hydrogen can be absorbed by the metal film (Figure 40) [115-117]. Hydrocarbon trapping on the surface of the Pd over the propagation of the surface plasmon resonance would provide a significant change to the surface plasmon resonance [123]. The data analysed has therefore been restricted to that taken within the 4hr window i.e. before a sample becomes obviously and irreparably contaminated. Fortunately for the Pd coated LPG this is not expected to be an issue. In this case the interaction surface is the one facing the fibre and as such is not subject to surface contamination, although a gradual decrease in the response speed will be expected as surface contaminants interfere with the absorption of hydrogen on the gas facing surface of the Pd film [115-117].

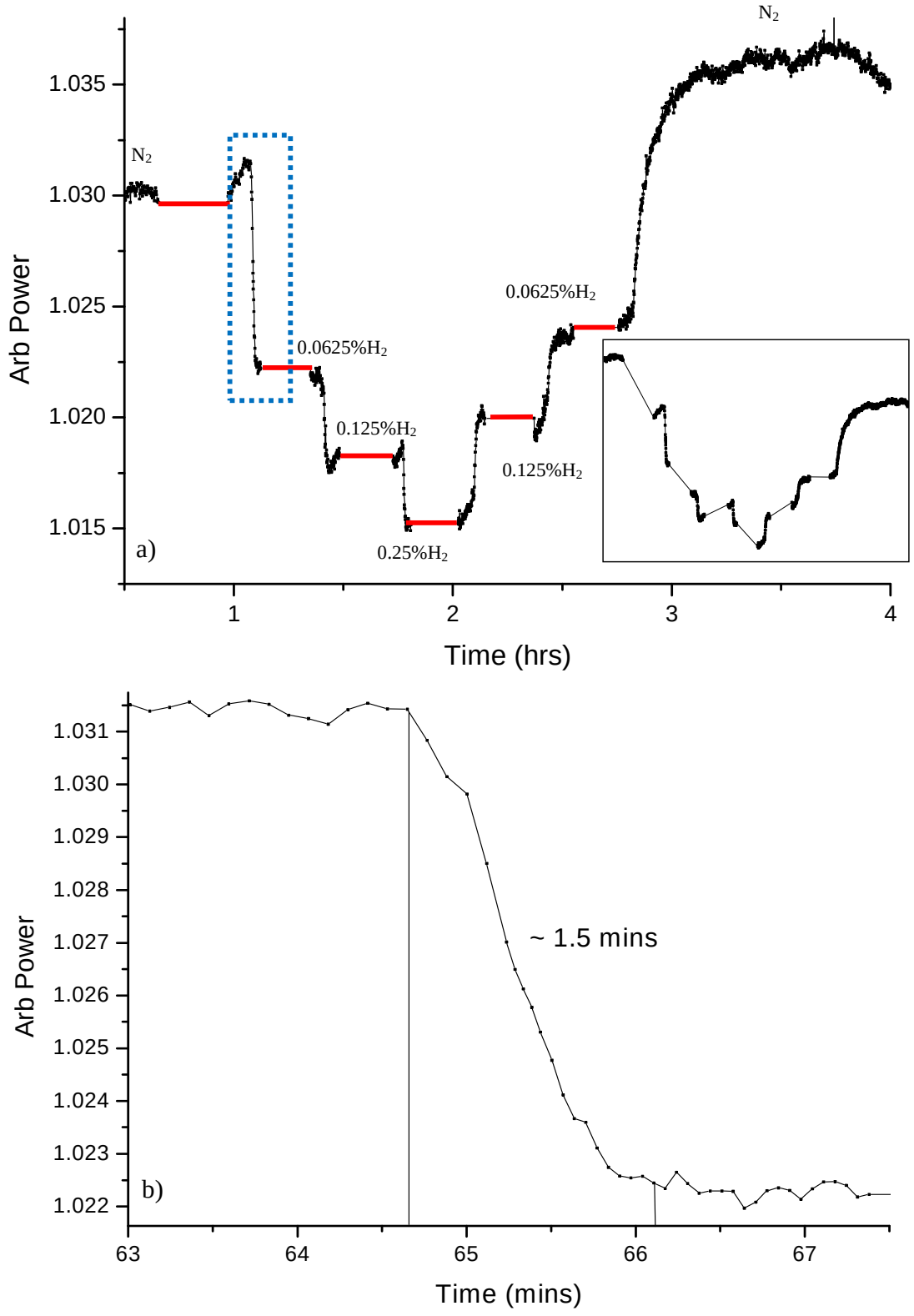

Figure 40: Example plot of normalised measured reflected power vs time. Red lines are used to mark the positions of full angular scans – where no data was taken. a) Full data: offsets have been removed by eye for illustrative purposes, original data is presented in the insert b) Enlarged view of absorption of 0.0625% hydrogen, marked in blue.

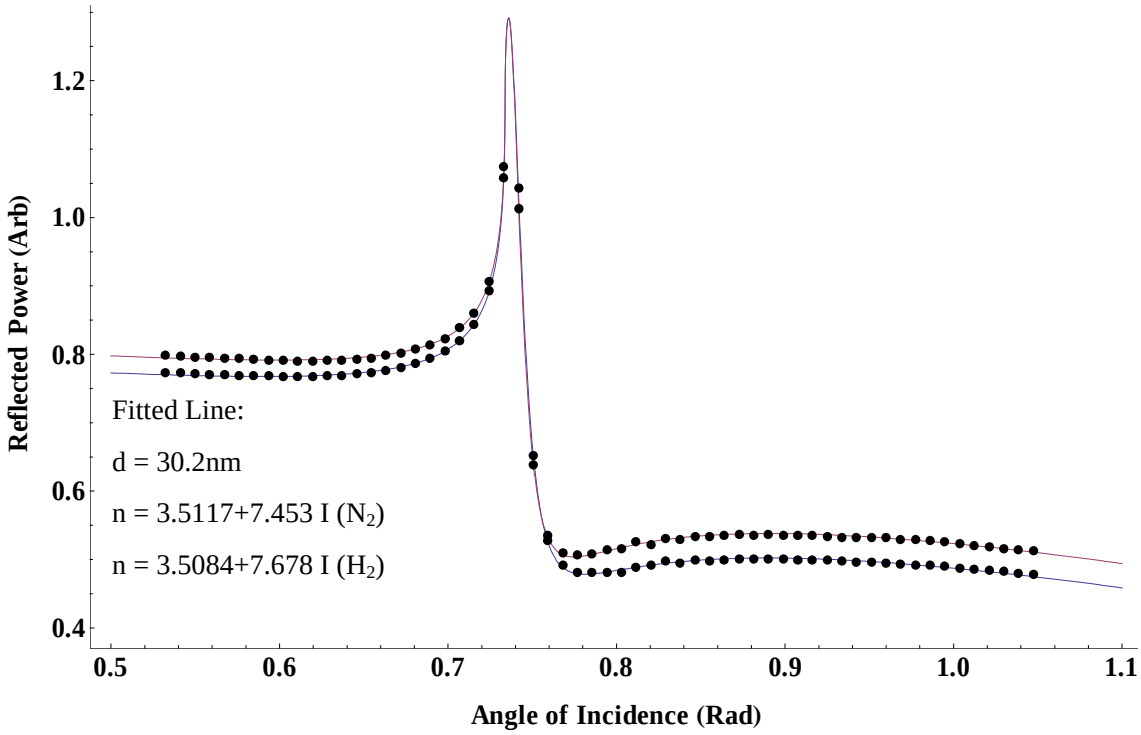

Figure 41: Example plot of surface plasmon resonance with experimental (dots) and theoretical fit (line).

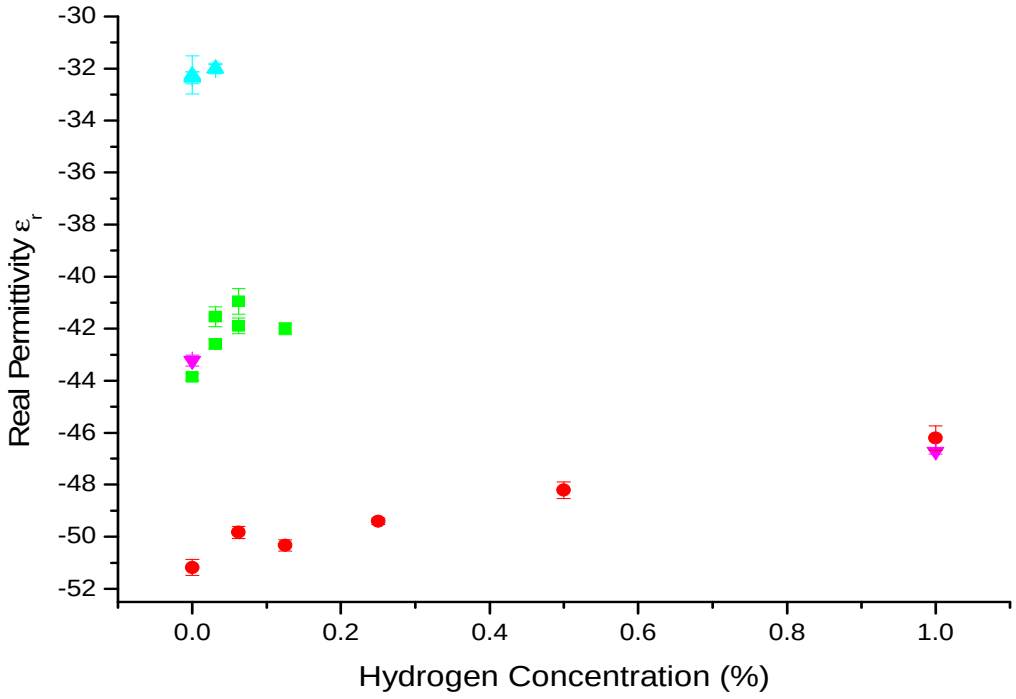

Figure 42: Plot of the real component of the permittivity of Pd thin films determined by surface plasmon resonance. Note that each film, separated by colour, has a different, although consistent permittivity.

Fitting the recorded angular scans of the films to the SPR model is a two stage process. For each deposited thin film it is necessary to take a calibration scan in the presence of nitrogen only. Although estimated values for the film thickness and the permittivity have been recorded via WLI and ellipsometry respectively, some variation in these values for each film is to be expected. For each film therefore a fit is made to the model based on the estimated permittivity and film thickness of the Pd (Figure 41). With this fit made, the film thickness is effectively determined and only the permittivity is expected to change as a function of the hydrogen concentration. The α phase expansion at such low concentrations is negligible. At each hydrogen concentration a new scan is made and fitted to the model with only the permittivity used as a variable.

Unfortunately fitting these data to the experiment has been more difficult than anticipated. Although individual scans fit to theory extremely well and there is excellent repeatability for the same angular scan, i.e. without changing the concentration, there is rather poor agreement between the permittivity of individual films (Figure 42). The range of the permittivities is in fact so large that some fundamental explanation of the issue must be sought. Further analysis of the data reveals that the permittivity of an individual film is roughly constant over multiple cycles of hydrogen and nitrogen. Figure 43 illustrates this interesting point. Here the data has been normalised for the permittivity defined in the control experiment, in the presence of nitrogen with only the variation from this permittivity plotted. For each film, colour coded for clarity, the nitrogen values, determined each time the system is cycled back to nitrogen atmosphere, are in good agreement. This suggests that the measurement results shown in Figure 42 are real. The large differences between the films recorded permittivities suggest that there is some form of surface contamination issue in the system. A thin, but stable layer on the surface of the Pd with either varying refractive index or varying thickness would explain the discrepancy. The stability of this layer indicates that it is most likely the result of the deposition or the handling before mounting in the SPR setup. The XPS analysis proves that there is no introduction of new species onto the Pd surface except for $(CH_2)^n$ chains and a PdO layer.

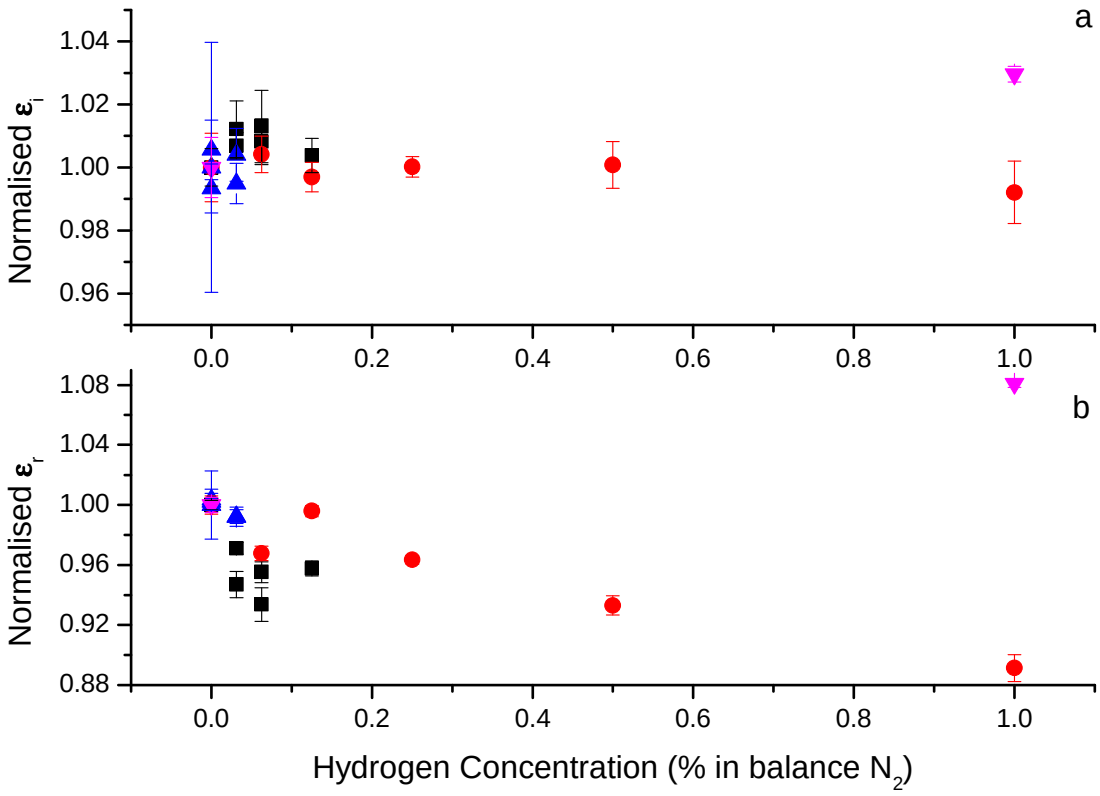

Figure 43: Plots of the change of a) imaginary and b) permittivity as a function of hydrogen absorption.

The effect of hydrocarbon trapping on the surface of the Pd on the surface plasmon is hard to quantify, but it is unlikely to be the sole cause of the problem. The data presented in Figure 40 demonstrates that hydrocarbon trapping increases over time and is fundamentally noisy due to the mobility of the hydrocarbons. By contrast the data presented in Figure 43 illustrates that the measured permittivity is consistent albeit with large discrepancies between the films. The effect of PdO is somewhat simpler to quantify; at 1550 nm the refractive index of PdO is lower than Pd [119], 2.873 + 0.044i compared to 3.6057 + 8.4929i for Pd. As the permittivities measured for the films are all by varying degrees lower than that measured by ellipsometry this may well be evidence of a PdO layer. While this is expected to be a very thin layer the thickness may vary between depositions due to the samples being exposed to varying amounts of oxygen during the handling process, this would give a shift to the surface plasmon resonance between deposited samples. However we would expect that a PdO layer

would be purged in the presence of hydrogen but the contamination layer appears to be stable over multiple hydrogen-nitrogen cycles.

The alternative is to consider the possibility of the formation of a contaminant layer which, although present in the lab, would disappear in the time interval between deposition and transportation to either AWE, for ellipsometry, or St-Andrews, for XPS. A possibility here is acetone which is known to form extremely thin contaminant layers on samples. As acetone is present in our lab and in St-Andrews, but to my knowledge not present at AWE, this is unlikely to provide an explanation.

Whatever the cause of the contamination it is still possible to derive the scale and direction of the change in the refractive index of Pd due to hydrogen absorption (Figure 43). Here the shift acts to reduce the real and imaginary components of the permittivity but unequal amounts corresponding to a 10% decrease in real and 2% decrease in the imaginary component over 1% hydrogen absorption. This corresponds to an increase of the real and a decrease in the imaginary component of the refractive index by approximately 2% and 4% respectively. This stands in direct contrast to previous assumptions of the change in the refractive index [113].

Table 2: Comparative list of approximate permittivity and refractive index shifts in Pd due to the absorption of 1% hydrogen.

Coefficient	100% N_2	1% H2 in N_2	Shift
Real Permittivity (ε_r)	-58.095	-52.286	-10%
Imaginary Permittivity (ε_i)	60.166	58.963	-2%
Real Index (n)	3.573	3.641	+2%
Imaginary Index (k)	8.418	8.096	-4%

3.8. Conclusions

Given the lack of consistency in the published refractive index of Pd, it has been necessary to characterise our thin film Pd. SEM scans have revealed that our RF deposition technique gives a flat homogeneous film while the ellipsometry analysis

proves that the refractive index is independent of film thickness above ~15nm. The measured refractive index of our Pd film sits mid way between published bulk and RF deposited Pd thin films. XPS and SPR analysis suggests that there is most likely some thin film surface contamination, most likely either PdO, hydrocarbon trapping or a chemical mono-layer of unknown composition. While the presence of this film has complicated the characterisation of the refractive index shift due to hydrogen exposure it has been possible to determine that the shift increases the real and decreases the imaginary component of the refractive index equally in the range 0-1% hydrogen in nitrogen by approximately 4% for 1% hydrogen.

This study of the Pd layer, and its response to hydrogen, forms one half of a characterised Pd-LPG system. To complete this process it is necessary to characterise the LPG refractive index profile (un-coated) then combine the information to produce a complete understanding of the LPG-Pd system.

Chapter 4. Experimental Characterisation of LPG Refractive Index Profile

4.1. Introduction

An LPG consists of a length of fibre with a periodic refractive index perturbation designed to couple light from the core to co-propagating cladding modes. The multi-pass fabrication process for LPGs at the CGCRI (§2.1.6) produces an LPG created to approximate a particular required transmission spectrum but the exact longitudinal refractive index profile of the LPG is unknown, a result of the adaptive writing process. While an estimated refractive index profile is usually sufficient as a first approximation and gives an adequate result for general shape and position of LPG lossbands, the fine details of the refractive index profile can make a substantial difference to a modelled transmission spectrum particularly when trying to model and predict the effect of metal coatings on the LPG (Chapter 6). It is therefore preferable to be able to directly measure the longitudinal refractive index profile for an LPG and use this information as the basis for theoretical modelling. No standard technique exists for measuring the index profile of an LPG although techniques have been demonstrated for FBGs [16, 17].

4.2. Scanning Interferometer Technique

One standard technique to measure the index profile of an FBG is to characterise the core mode by investigating back reflections. These best resolve the index profile when measured as a function of length within the fibre. A technique for this is to use a scanning Michelson interferometer. In an FBG, the refractive index changes within the core are over a small distance, typically 400-1500 nm with a change in refractive index of ~1.4620 to 1.4625 giving an average index gradient of 5×10^{-7} nm^{-1} (assuming an interference pattern writing system with a sinusoidal index profile). Reflections from such significant gradients are quite strong. As the coherence position of the interferometer moves through the FBG region, individual reflections can be isolated, measured and used to calculate the core index changes and profile as a function of fibre length.

This technique relies on the core mode being partly reflective or that the coupling to the counter propagating core mode is strong. In the case of an LPG, individual changes in refractive index are of a similar scale (Δn ~0.0005) to an FBG but occur over much larger distances.

These distances are hard to directly quantify due to uncertainties in the exact refractive index profile of the LPG which vary according to the inscription process. Our fibres, inscribed by the CGCRI slit method (cf. §2.1.6) can be assumed to be a square wave although the edges of each index change will be smeared due to diffraction from the slit and beam divergence (§2.1.6). Combined these give an approximate 0.0005 index change over ~ 11 µm i.e. an index gradient of $4.5 \times 10^{-8}\ \mathrm{nm}^{-1}$, an order of magnitude slower transition.

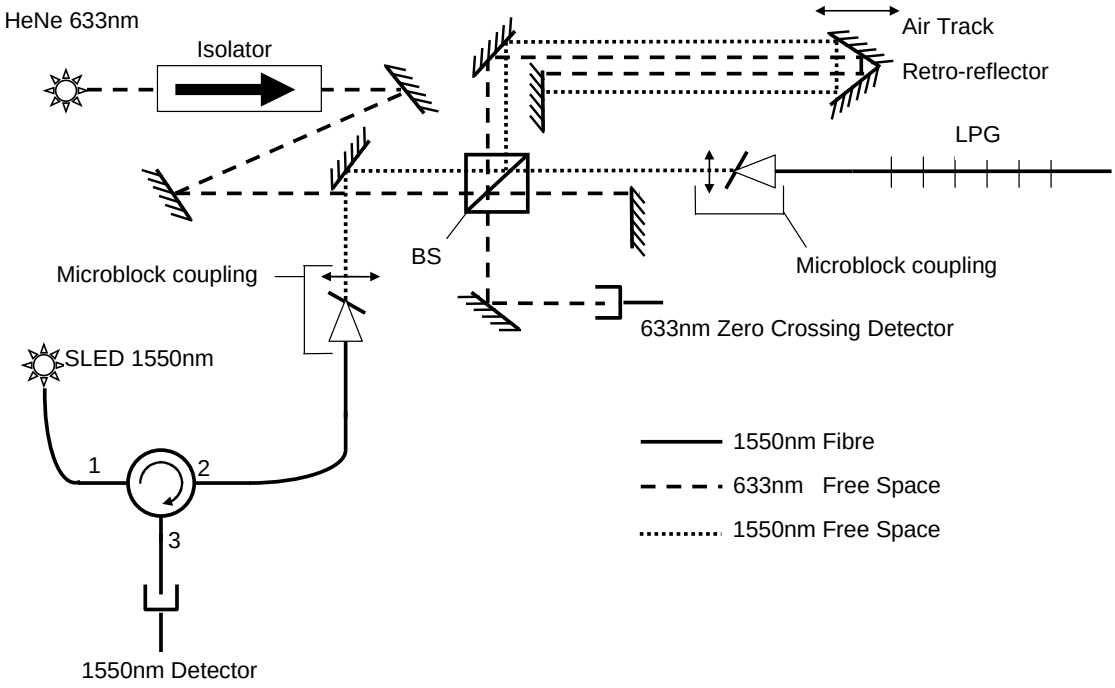

Figure 44: Scanning Interferometer Setup

Nevertheless it was hoped that a sufficiently high finesse system would be able to isolate these weak reflections and with suitable analysis return the refractive index profile. Figure 44 shows the scanning interferometer adapted from Peter Harrison's fibre Bragg grating measurement system [130-132] used for this experiment. The

system consists of a dual beam utilising a 633 nm HeNe and a fibre coupled infra-red Super Luminescent Light Emitting Diode (SLED) centred at 1537 nm with a FWHM of 50 nm. The two beams are coupled into the system such that they run parallel into the beam splitter (BS). The scanning arm consists of a retro reflector (RR) mounted on an air-track and a mirror normal to the beams. The HeNe measurement arm consists of a single return mirror. The recombined HeNe is incident on a zero crossing point detector providing a distance calibration for the air-track. The IR measurement arm is coupled into the LPG under test and the recombined arm returns through the fibre to a detector via a fibre circulator.

The broadband IR beam has a sufficiently large FWHM to provide a small, 22 µm, coherence length which determines the resolution limiting factor for this device and is sufficient to detect the presence of a 400 µm period LPG. Both IR and HeNe detectors are linked to a computer controlled data acquisition system. Individual IR measurements are triggered from HeNe zero crossing points (i.e. each 158.25 nm distance in the scanning arm due to the folding of the scanning arm (Figure 44)) and a light gate attached to the air track acts as a reference position to the start of the data acquisition process. Careful alignment of the system is required to ensure that both beams are parallel, exhibit minimum divergence and follow their respective paths.

Despite extremely careful alignment and adjustment of the power ratio of the two arms the system failed to record any reflections from an LPG directly. Further statistical analysis using FFT techniques to search for components of similar frequency to the period of the LPG failed to find any relevant components in the Fourier Transform. This suggests that much higher beam intensities and sensitivities are required to recover the low intensity and widely distributed reflection from a 400 µm LPG. This was confirmed by use of a optical backscatter reflectometer (OBR). This device has sufficient sensitivity to detect Rayleigh back scatter but was unable to detect back reflections from the index changes. Hence an alternative method was investigated as described in §4.3.

4.3. Quantitative Phase Microscopy (QPM)

4.3.1. Technique Description

QPM is a technique to recover phase information for an object based on the transport of intensity equation [133]:

$$-k\frac{\partial I}{\partial z} = \nabla \cdot [I \nabla \phi] \qquad \textit{Eq. 17}$$

This equation relates the phase information, ϕ, to the change in intensity, ∂I, between two planes, separated axially ∂z. In a practical application $\frac{\partial \mathrm{I}}{\partial \mathrm{z}}$ is approximated from the subtraction of two intensity images taken at planes equally spaced from focus (Figure 45). In general the solution of Eq. 17 is not trivial. A simplified algorithm to solve Eq. 17 has been adapted from Barty [133]. This requires that two assumptions are made concerning the illumination conditions.

1. Plane wave illumination of the object in transmission
2. Partially coherent illumination (i.e bandwidth of ~10 nm, this is in part to avoid issues arising from laser speckle and the masking of phase information due to low coherence but also allows the Born approximation to be used, in order to simplify the modelled transport of radiation through the object [134])

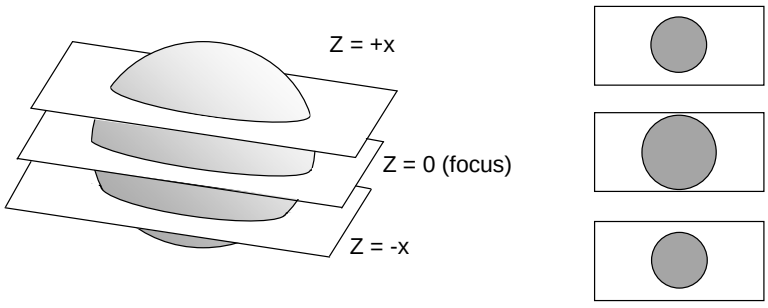

Figure 45: Illustration of the three planes of imaging

In practice both assumptions are possible, standard Kohler illumination provides planar (or near planar) wave fronts [133] at the object and an interference filter can be used to tailor the bandwidth of the illumination source to the requirements. Phase subtraction may also be employed to remove small phase aberrations introduced by the imaging optics.

With these conditions met, the phase may be recovered:

$$\phi = A\,\hat{f}\left(f\left(dI_{a,b}\right)\cdot T_{n,m}\right) \qquad \textit{Eq. 18}$$

Where f and $\hat{f}$ are the Fourier transform and inverse transform respectively, dI is the intensity difference matrix between the two planes of illumination, A is a calibration factor for a given system and $T_{n,m}$ is the transfer matrix:

$$T_{n,m} = \frac{a\,b}{(2\,\pi)^2\,(m^2\,b^2 + n^2\,a^2)I_0} \qquad \textit{Eq. 19}$$

Where a and b are the sizes of the dimensions of the subtracted intensity matrix $dI_{a,b}$, n and m are the indices of the Fourier Transform corresponding to the dimensions a and b respectively and I_0 is the mean intensity at focus.

Thus far, this follows the analysis of Barty and Nugent [133, 135] closely. However a problem occurs due to the form of the transfer matrix, since the matrix is inversely proportional to the Fourier components it amplifies the low frequency components. This will result in phase aberrations in the recovered profile. This can be most easily corrected by the application of a mask in the Fourier plane by altering Eq. 18 above to the following form:

$$\phi = A\,\hat{f}\left(f(dI)\cdot T_{n,m}\cdot M_{n,m}\right) \qquad \textit{Eq. 20}$$

Where $M_{n,m}$ is a Fourier mask which in its simplest implementation is a cross pass eliminating the low frequency components of the Fourier of the form:

$$M_{n,m} = \begin{cases} 0 \; \forall \; m,n \; \leq f \\ 0 \; \forall \; m \leq f \wedge n \geq N - f \\ 0 \; \forall \; m \geq M - f \wedge n \leq f \\ 0 \; \forall \; m,n \; \leq M,N - f \\ 1 \; else \end{cases} \qquad \textit{Eq. 21}$$

Where f describes the size of the filter in use and M and N are the size of the Fourier Matrix.

This has the general form illustrated in Figure 46.

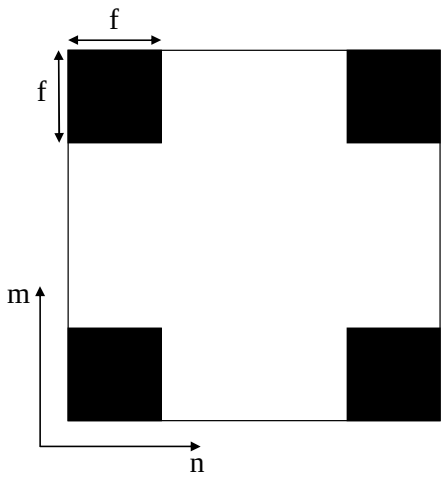

Figure 46: Illustration of cross filter defined in Eq. 21.

The choice of Fourier mask and corresponding A will need to be calibrated for a given optical system. Once this has been done the algorithm produces a quantitative phase map in x and z for a fibre imaged in the z, x i.e. transverse plane (Figure 47). A cross-section along z can then be recovered to provide the desired phase profile of the LPG while information in the x, z plane provides an estimation of the change in index outside the core.

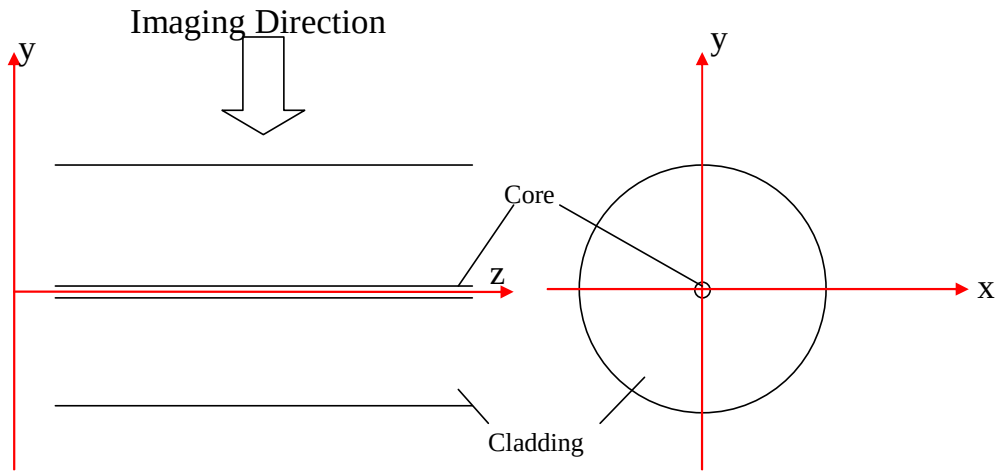

Figure 47: Fibre Imaging Geometry

4.3.2. Preliminary Quantitative Phase Microscopy Results

A QPM system was set up using a Raman Spectroscopy Microscope, an existing microscope within the university. Although for the purposes of this experiment the Raman source is unnecessary, the system includes a computer controlled x, y, z stage, transmission imaging and a collimator capable of approximating the required illumination conditions. The bandwidth conditions were met by simply inserting a suitable interference filter with a centre wavelength of 633 nm and a 10 nm width. As a proof of principle experiment I decided to attempt to recover the phase generated by imaging through the core of a standard SMF-28® fibre. This should prove that a) the system can resolve the difference between core and cladding indices and b) give a measure of the change in phase in the y plane, which should give an idea of the finesse of the system. While in general this process involves the analysis of 2D images in matrix form, for the purposes of a proof of principle these data can be collapsed into a 1D array along x.

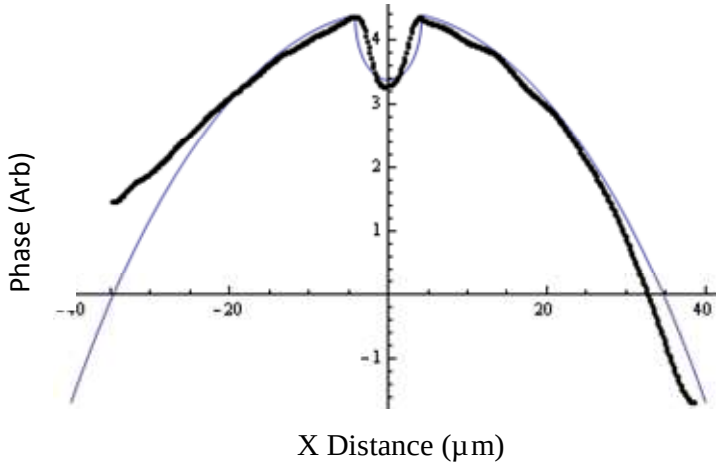

Figure 48: Plot of retrieved phase (black) and theoretical phase (blue) from the Raman Microscopy setup

The illumination conditions must be very carefully calibrated and as this microscope is in more or less constant use, it is a general tool within the department, this became impractical. The illumination conditions are difficult to set up correctly and it is impossible to exactly replicate them between imaging sessions. A cross-sectional plot of derived phase can be seen in Figure 48. This demonstrates the general expected phase profile but there is clearly a phase aberration as a function of the distance to centre of image (core) due to illumination problems. In addition, the finesse is clearly insufficient to detect the expected ~0.0005 RIU index variations due from the LPG structure within the core.

4.3.3. Curved Grating QPM

An alternative to a standard microscope arrangement, as described in §4.3.2, can be found by using diffractive optical elements. Prof Alan Greenaway (Heriot Watt University) has reported that a curved grating is capable of quasi 3D real time imaging [136]. By diffracting the image plane into three (or more depending on the grating) images the object may be resolved as a series of layers spatially separated in the z direction. As only the original zeroth order, or undiffracted path, images in the original focal plane, the higher diffracted orders will be defocused. With the correct choice of grating and alignment the higher order pairs, principally ± 1st orders, will be at equal y

displacement about focus (Figure 47). This technique allows for simultaneous imaging of the three planes required for QPM with a guarantee of the same illumination conditions, magnification and planar separations between images (Figure 49). A slit is used to prevent overlap of the separate images. Unfortunately due to time constraints it was not possible to create a full imaging system and only an adapted microscope system was used, but the results from this system are extremely encouraging. To our knowledge this technique has not been applied to measure the index profile of a long period grating.

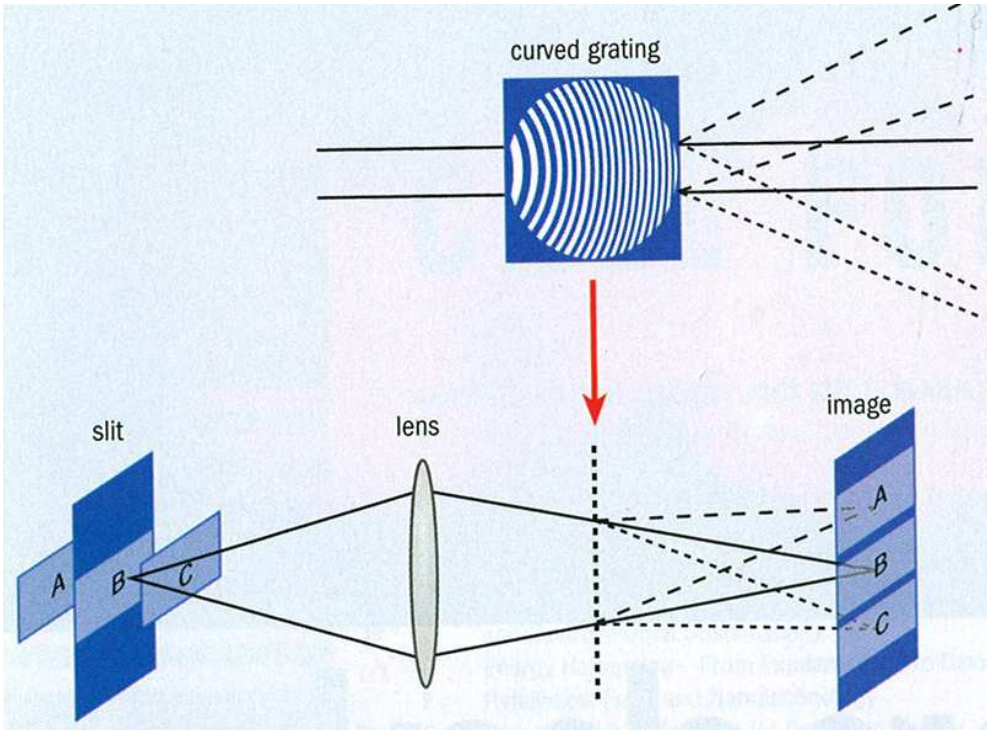

Figure 49: Illustration of curved grating imaging technique resulting in simultaneous imaging of three focal planes. Taken from Physics World [136].

A schematic of the proof of principle system may be seen in Figure 50. The system uses a white light source (WLS) in tandem with a collimator to generate Kohler illumination. This provides plane waves which approximate the required illumination conditions discussed in §4.3.1. The fibre is held between a silica flat, chosen to minimise additional phase aberrations due to surface roughness, and a microscope coverslip, which is sufficiently thin to allow the condenser to approach the fibre. Index

matching fluid is also used to effectively remove the curvature of the cladding. A microscope objective, typically x20, is used to image the fibre in what is a traditional transmission microscope system. A re-imaging system is bolted on to the microscope consisting of a 1:1 magnification lens (with a focal length 150 mm) system, an interference filter (with 10 nm bandwidth), the curved grating and a CCD camera. In contrast to the schematic shown in Figure 49 the proof of principle system, based on an existing imaging setup, incorporates five separate images at five separate heights (+2, +1, 0, -1, -2). However, only the +1, 0 and -1 are used (Figure 49). The central image represents the in focus plane while diagonally opposite images are equally spaced images at ~4 µm, top left, and, ~8 µm top right, respectively. Each pair of images must be extracted and centred using a simple centroid finding algorithm. They can then be satisfactorily overlapped and subtracted to provide the required *dI*.

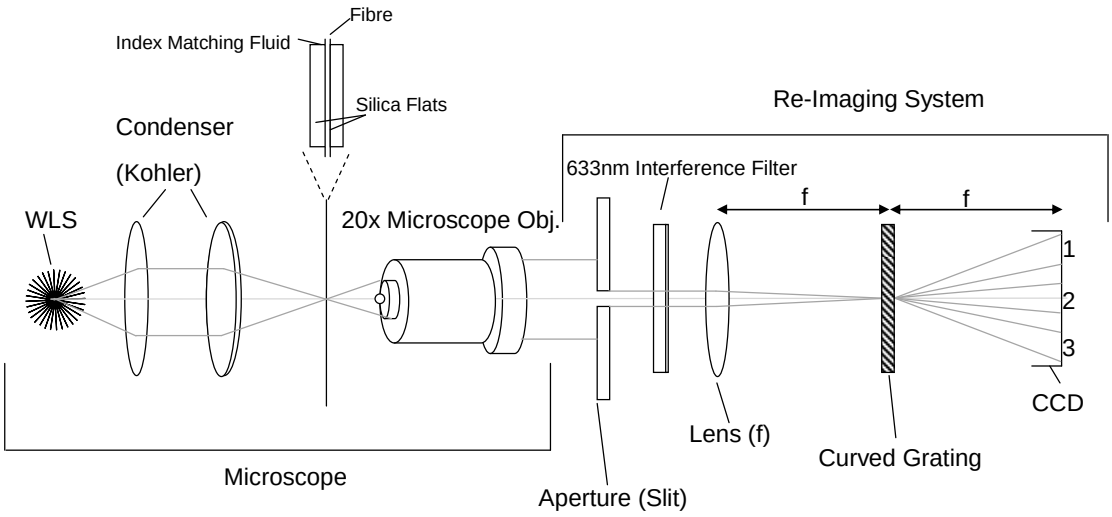

Figure 50: Schematic of curved grating imaging system

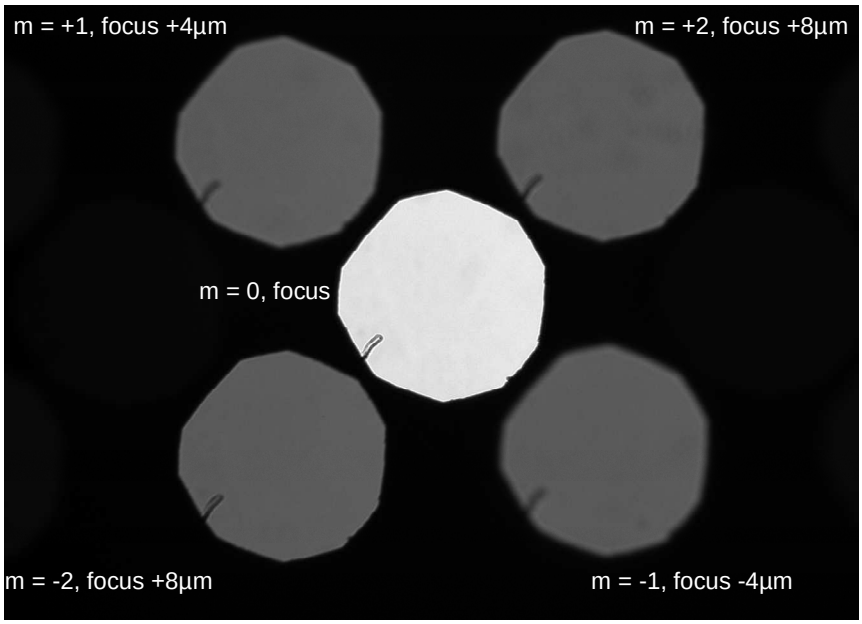

Figure 51: Intensity image demonstrating the resolution of 5 separate image planes with central image in focus using the microscope based QPM setup.

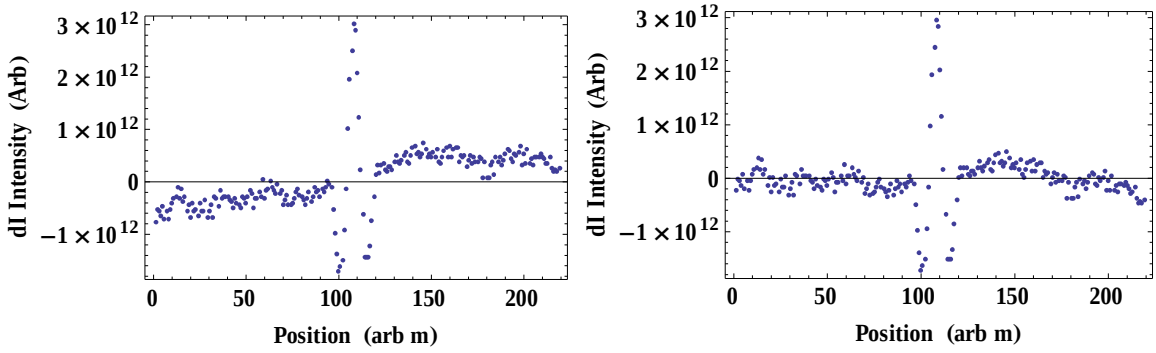

Figure 52: Plot of collapsed 1D fibre intensity data for left: Un-filtered, right: background subtracted data

The resultant plot of data reveals that the system still does not exhibit perfectly flat wavefronts as there is a clear gradient in the subtracted intensity (Figure 52 left) while trivial to correct by fitting and subtracting a background (Figure 52 right) the lack of planar waves generates some error in the phase analysis.

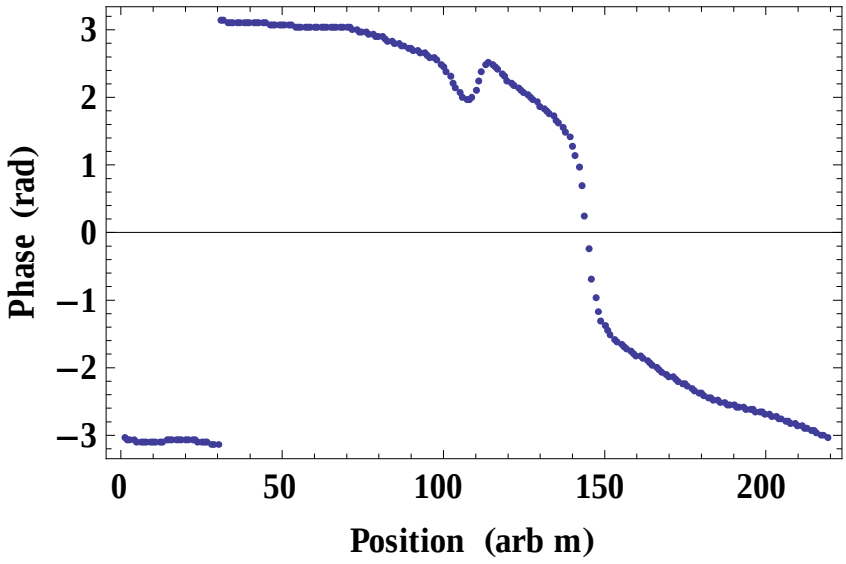

Figure 53: Recovered phase information from collapsed 1D data with 0 frequency masking (f=0). With no frequency masking the image shows clear phase aberrations and phase wrapping.

Once the images have been extracted and centred, a process which can be optimised and automated for a specifically designed system, the images are subtracted and processed using the phase algorithm outlined in Eq. 20. This requires a choice of suitable phase mask. In our case a cross pass filter has been used to remove the low frequency components. Due to the digital, pixelated, nature of the images the cross filter takes the form such that a square of pixels are removed from the corners of the Fourier transform (Figure 46). The side length, in pixels, of this square is the masking parameter f (Eq. 21). The size of this parameter therefore dictates the high pass frequency of the filter. Figure 53 illustrates the effect of using no Fourier mask, i.e. f = 0. The resultant phase map demonstrates clear phase artefacts generated by the amplification of low frequency components as well as phase wrapping. But by the choice of a suitable Fourier mask, f = 5, these artefacts can be removed and a much cleaner phase map is recovered (Figure 54). The choice of Fourier mask for the system requires more analysis and more robust mathematical treatment than the essentially arbitrary approach used here. In the case of this analysis the quality of the data from this, non optimal system, is not sufficient to justify the amount of time and effort required to fully analyse and justify the Fourier mask. As the fibre in this case is immersed in index matching fluid the expected phase map should reflect the cross-section of the core only. These

data suggest that it should be possible to recover the phase changes in an LPG using a more stable system. In particular the Fourier mask can be further improved by a more subtle Weissman approach and a dedicated system should be able to improve the planar wave-fronts and remove background intensity.

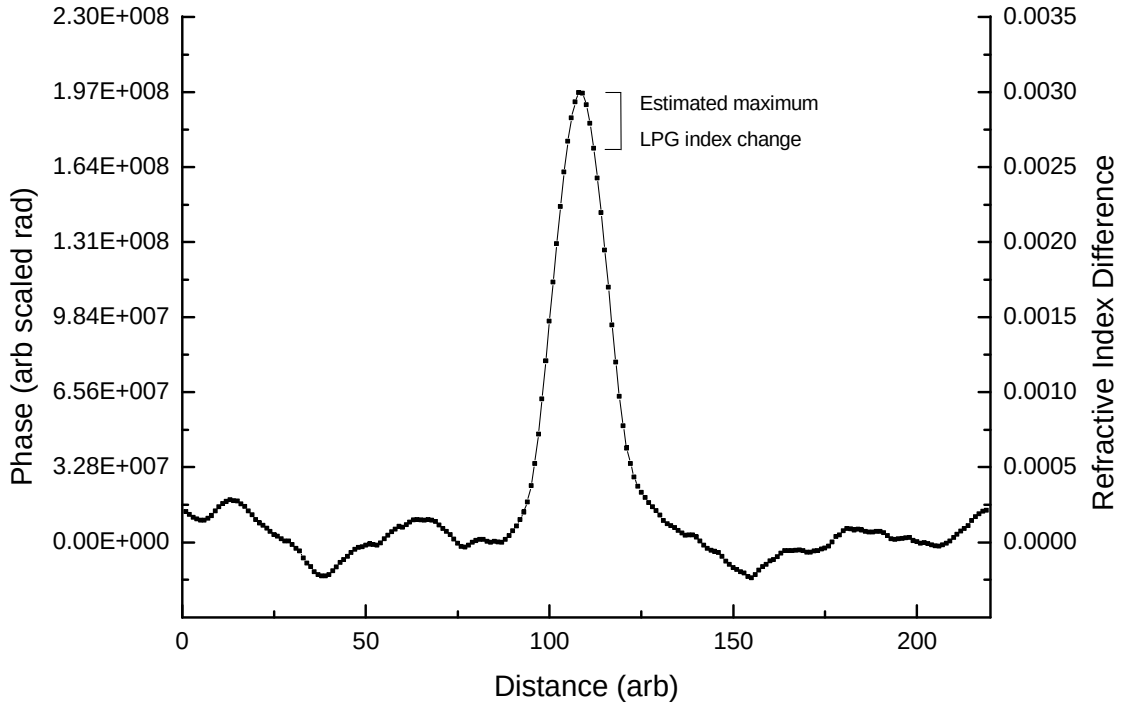

Figure 54: Recovered phase information with a 5 point low frequency phase mask in place based on the collapsed 1D image. The derived refractive index change from the cladding index and estimated index change in an LPG has been included for comparison.

In addition, the scale difference between the x/y and z of an LPG (10 μm vs 5 mm, Figure 47) gives a trade off between magnification and field size and in general several images are required to image the length of the LPG. Combined with the irreproducible nature of the illumination conditions between experiments and exact x, y, z positioning of images between calibrations makes imaging in this manner difficult for conventional microscopes.

4.4. Conclusions

While I was unable to recover the exact LPG profile data, the process has illustrated the difficulty of directly measuring small refractive index changes within a fibre. For the purposes of the LPG modelling it should be possible to continue with only an estimate of the refractive index profile and a statistical method can be used to alter the model accordingly. However the proof of principle experiment, using the QPM to extract phase, and therefore refractive index information, has been sufficiently encouraging to set up a continuing collaborative effort between our group, the CGCRI and Prof. Greenaway to build a dedicated LPG characterisation setup using specially designed and optimised curved gratings for the investigation of LPGs.

Accurate determination of the LPG refractive index profile is still, however, important for modelling of the LPG transmission spectra and, more importantly, sensitivities. As I have been unable to directly measure this refractive index profile it is necessary to attempt to fit the measured transmission spectrum to the theoretical model of an LPG through coupled mode theory. This will be the subject of the next chapter.

Chapter 5. Long Period Grating Modelling

5.1. Introduction

As mentioned in the review chapter, §2.1.10, the model employed for this thesis is closely based on the work of Erdogan [18, 21, 22] which shares the notation of Tsao [66]. There are some differences between my implementation and Erdogan in the notation and in some of the calculation steps. The modelling of LPG transmission spectra is a complex calculation, so the necessary steps are reproduced / produced here with an emphasis on the differences between this approach and that presented by Erdogan. The Mathematica code implementing these equations can be found in Appendix A.

5.2. Mathematical Modelling of LPG

5.2.1. Mathematical representation of the LPG

The optical fibre itself is represented by a standard cylindrical polar coordinate system with the z axis aligned to the propagation mode direction (Figure 55). Within this fibre it is assumed that the refractive index perturbations making the LPG element are confined to the core region i.e. $r \leq a1$. Using Erdogan's notation the refractive index of the core in the LPG region may be defined as:

$$n(z) = n_1(\lambda)\left(1 + \sigma(z)\left(1 + m\ cos\left[\frac{2\pi}{\Lambda}z\right]\right)\right) \qquad \textit{Eq. 22}$$

Where $n_1(\lambda)$ is the dispersive refractive index of the core, $\sigma(z)$ is the grating envelope, m is the fringe modulation ($0 \leq m \leq 1$) and Λ is the grating period.

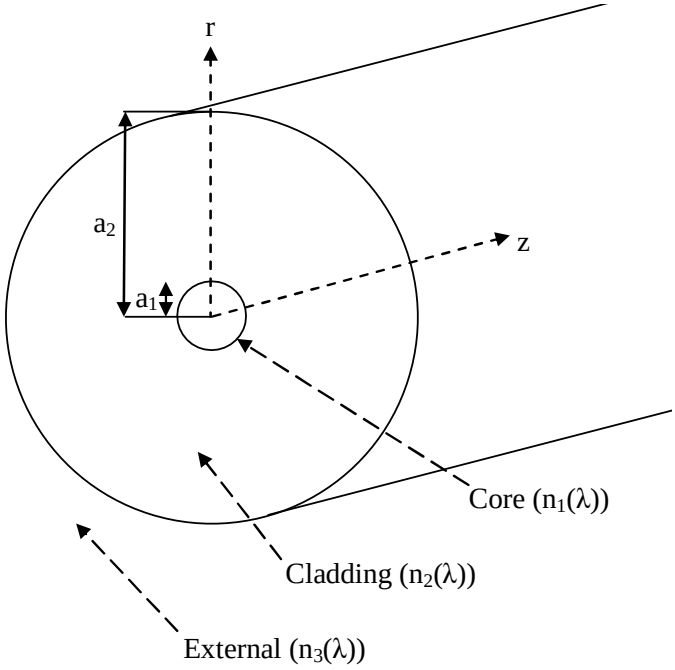

Figure 55: Schematic illustrating the notation used for coordinates, physical dimensions and refractive indices used for optical fibres in this thesis. In a two layer approximation a_2 is assumed to be infinite.

Eq. 22 provides a general form of the refractive index perturbation for which there are two specific cases worthy of further consideration; a Gaussian envelope and a pure sinusoid. For a Gaussian envelope, e.g. a grating written with an amplitude mask (cf. §2.1.6), σ(z) takes the form of Eq. 23.

$$\sigma(z) = \sigma e^{-4ln2\frac{z^2}{\omega^2}} \qquad \textit{Eq. 23}$$

Where ω and σ define the Gaussian envelope (Figure 56).

While Gaussian, i.e. apodized, envelopes are common, the majority of LPG elements used in this thesis are of the sinusoidal envelope form. In this case the fringe modulation becomes m = 1 and σ(z) takes the form of Eq. 24.

$$\sigma = \frac{\Delta n}{2\, n_1(\lambda)} \qquad \textit{Eq. 24}$$

Where Δn gives the amplitude of the refractive index perturbation (Figure 56).

Note that Eq. 22 cannot reproduce a square wave or step type function for the refractive index perturbation without modification. In the case of the LPG elements used throughout this thesis this is not an issue as the profile is approximated as a sinusoid in the absence of evidence to the contrary.

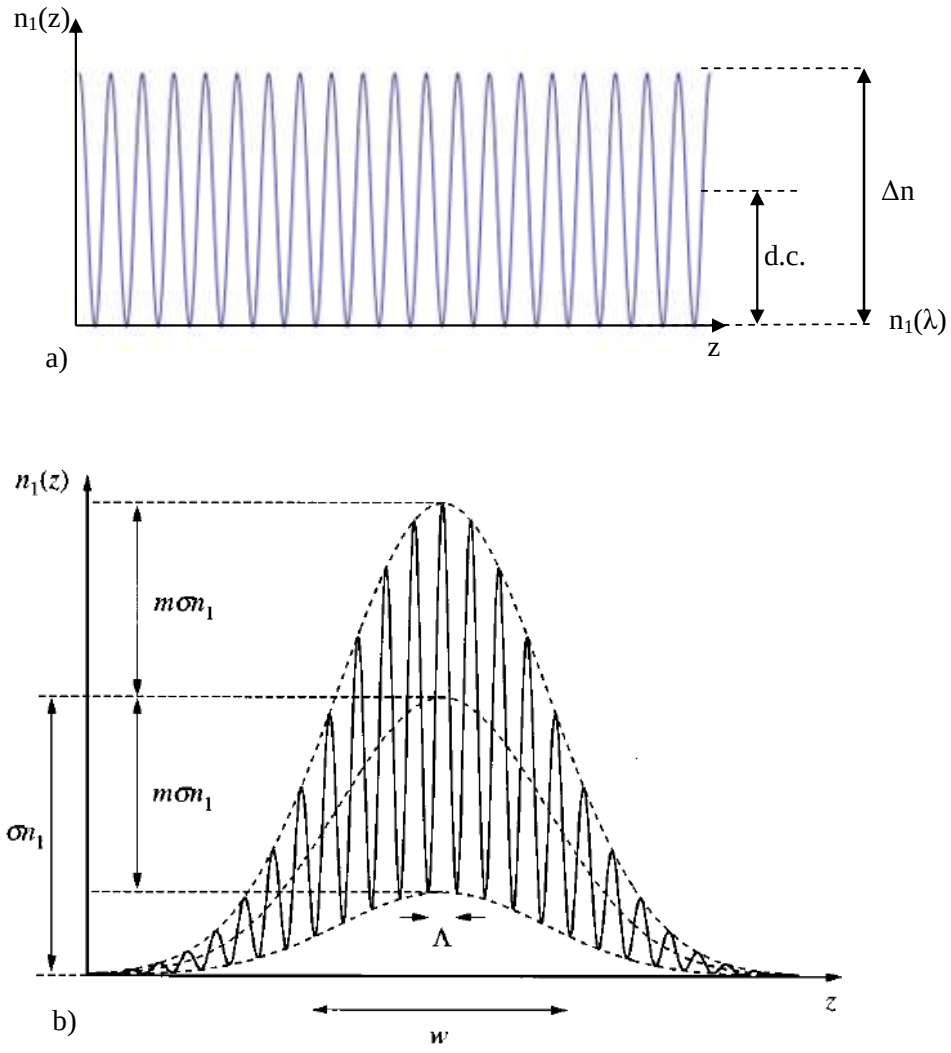

Figure 56: Illustration of the two common sinusoidal LPG perturbation envelopes. a) top-hat envelope with an effective dc offset from un perturbed refractive index, b) Gaussian envelope taken from Erdogan [18] illustrating his notational system.

5.2.2. Core mode effective index calculation

The calculation of the allowed modes in single mode fibre is a well documented subject [66]. It is not therefore necessary to derive the calculations from first principles but instead the practical end of the calculations is presented here. We start by assuming the linearly polarised approximation, a standard approximation for radially symmetric fibres [18, 66]. With a further two layer approximation (Figure 55) the dispersion relation of the fibre is: Eq. 25.

$$V(\lambda)\sqrt{1-b(\lambda)}\,\frac{J_1\left[V(\lambda)\sqrt{1-b(\lambda)}\right]}{J_0\left[V(\lambda)\sqrt{1-b(\lambda)}\right]} = V(\lambda)\sqrt{b(\lambda)}\,\frac{K_1\left[V(\lambda)\sqrt{b(\lambda)}\right]}{K_0\left[V(\lambda)\sqrt{b(\lambda)}\right]} \qquad \textit{Eq. 25}$$

Where J and K are Bessel functions of the first and of the second (modified) kind in their usual notation. V(λ) is the V number of the fibre given by Eq. 26 and is a function of the wavelength. b is the normalised effective index given by Eq. 27.

$$V(\lambda) = \frac{2\pi}{\lambda} a_1 \sqrt{n_1(\lambda)^2 - n_2(\lambda)^2} \qquad \textit{Eq. 26}$$

Where $n_1(\lambda)$ and $n_2(\lambda)$ are the refractive indices of the core and cladding respectively and a_1 is the core radius illustrated in Figure 55.

$$b(\lambda) = \frac{n_{eco}(\lambda)^2 - n_2(\lambda)^2}{n_1(\lambda)^2 - n_2(\lambda)^2} \qquad \textit{Eq. 27}$$

Where $n_{eco}(\lambda)$ is the effective refractive index of the core mode(s).

By substituting Eq. 26 & Eq. 27 into Eq. 25 and rearranging the dispersion relation can be solved in terms of $n_{eco}(\lambda)$. For a single mode fibre there will be one solution to this dispersion relation which will be close to the core refractive index i.e. $n_1(\lambda) - n_{eco}(\lambda) \ll 1$. While this can in principle be done analytically, in practice it is simpler to calculate a numerical solution for a range of wavelengths of interest i.e. 1200 nm – 1600 nm in 1 nm steps.

5.2.3. Cladding mode effective refractive indices

The calculation of the effective refractive index of the cladding modes is somewhat more complex as a three layer approximation is necessary. The third layer introduces a third refractive index, that of the external medium $n_3(\lambda)$ shown in Figure 55. Again a linearly polarised approximation is used and the complete derivation of the Equations is not presented and instead the reader is referred to standard texts e.g. Tsao [66]. In this case the dispersion relation Eq. 28 is more complicated. For simplicity the use of $f(\lambda)$ to denote a function of wavelength is abandoned as almost all parameters are now wavelength dependant. Here my notation differs slightly from that used by Erdogan due to the implicit limitation to cladding modes of azimuthal order 1 and the explicit evaluation of the factors p_l, q_l, r_l, s_l, Eq. 40 - Eq. 43, at the cladding - external interface, r = a2.

$$\xi_0(\lambda) = \xi_0'(\lambda) \qquad \textit{Eq. 28}$$

$$\xi_0(\lambda) = \frac{1}{\sigma_2}\frac{u_2\left(\boldsymbol{JK} + \frac{\sigma_1\sigma_2 u_{21}u_{32}}{{n_2}^2 a_1 a_2}\right)p_l - \boldsymbol{K}q_l + \boldsymbol{J}r_l - \frac{s_l}{u_2}}{-u_2\left(\frac{u_{32}}{{n_2}^2 a_2}\boldsymbol{J} - \frac{u_{21}}{{n_1}^2 a_1}\boldsymbol{K}\right)p_l + \frac{u_{32}}{{n_1}^2 a_2}q_l + \frac{u_{21}}{{n_1}^2 a_1}r_l} \qquad \textit{Eq. 29}$$

$$\xi_0'(\lambda) = \sigma_1\frac{u_2\left(\frac{u_{32}}{a_2}\boldsymbol{J} - \frac{{n_3}^2 u_{21}}{{n_2}^2 a_1}\boldsymbol{K}\right)p_l - \frac{u_{32}}{a_2}q_l - \frac{u_{21}}{a_1}r_l}{u_2\left(\frac{{n_3}^2}{{n_2}^2}\boldsymbol{JK} + \frac{\sigma_1\sigma_2 u_{21}u_{32}}{{n_1}^2 a_1 a_2}\right)p_l - \frac{{n_3}^2}{{n_1}^2}\boldsymbol{K}q_l + \boldsymbol{J}r_l - \frac{{n_2}^2 s_l}{{n_1}^2 u_2}} \qquad \textit{Eq. 30}$$

Where σ_1, σ_2, u_2, u_{21}, u_{32}, p_l, r_l, s_l, **J** and **K** are all defined below and a_2 is the radius of the cladding, Figure 1. N.b. **J** and **K** , the Bessel function derivative ratios, should not be confused with Bessel functions of similar notation.

$$\sigma_1 = in_{ecl}/Z_0 \qquad \textit{Eq. 31}$$

$$\sigma_2 = in_{ecl}Z_0 \qquad \textit{Eq. 32}$$

$$u_{21} = \frac{1}{{u_2}^2} - \frac{1}{{u_1}^2} \qquad \textit{Eq. 33}$$

$$u_{32} = \frac{1}{{\omega_3}^2} + \frac{1}{{u_2}^2} \qquad \textit{Eq. 34}$$

$$u_1 = \frac{2\pi}{\lambda}\sqrt{{n_1}^2 - {n_{ecl}}^2} \qquad \textit{Eq. 35}$$

$$u_2 = \frac{2\pi}{\lambda}\sqrt{{n_2}^2 - {n_{ecl}}^2} \qquad \textit{Eq. 36}$$

$$\omega_3 = \frac{2\pi}{\lambda}\sqrt{n_{ecl}{}^2 - n_3{}^2} \qquad \textit{Eq. 37}$$

$$\boldsymbol{J} = \frac{J_1'[u_1 a_1]}{u_1 J_1[u_1 a_1]} \qquad \textit{Eq. 38}$$

$$\boldsymbol{K} = \frac{K_1'[\omega_3 a_2]}{\omega_3 K[\omega_3 a_2]} \qquad \textit{Eq. 39}$$

$$p_l = J_1[u_2 a_2]N_1[u_2 a_1] - J_1[u_2 a_1]N_1[u_2 a_2] \qquad \textit{Eq. 40}$$

$$q_l = J_1[u_2 a_2]N_1'[u_2 a_1] - J_1'[u_2 a_1]N_1[u_2 a_2] \qquad \textit{Eq. 41}$$

$$r_l = J_1'[u_2 a_2]N_1[u_2 a_1] - J_1[u_2 a_1]N_1'[u_2 a_2] \qquad \textit{Eq. 42}$$

$$s_l = J_1'[u_2 a_2]N_1'[u_2 a_1] - J_1'[u_2 a_1]N_1'[u_2 a_2] \qquad \textit{Eq. 43}$$

Where n_{ecl} is the effective index of the cladding mode, *N* is a Bessel function of the second kind with the usual notation, $Z_0$is the electromagnetic impedance in a vacuum (~377 Ω), J_1', N_1' and K_1' represent their respective Bessel functions differentiated in respect to their total argument. The explicit derivatives are provided in Eq. 44 - Eq. 46 below.

$$J_1'[x] = \frac{1}{2}(J_0[x] - J_2[x]) \qquad \textit{Eq. 44}$$

$$N_1'[x] = \frac{1}{2}(N_0[x] - N_2[x]) \qquad \textit{Eq. 45}$$

$$K_1'[x] = \frac{1}{2}(-K_0[x] - K_2[x]) \qquad \textit{Eq. 46}$$

Again it is possible to solve the dispersion relation in terms of $n_{ecl}(\lambda)$ but in the case of the vast majority of fibres there are hundreds of solutions to the dispersion equation. Due to the complexity of this dispersion relation a numerical solution is necessary. A plot of the dispersion relation (Figure 57) illustrates the difficulty in a practical solution to the problem. The equation is complicated and some modes provide only a very small distortion to the overall form of the dispersion relation. The solution implemented is a rather inelegant, brute force, solution. A more elegant solution was not forthcoming. This involves numerically evaluating the dispersion relation across a range of possible effective refractive indices. These data can then be interrogated to determine positions of change in sign and these values used as the basis for guess values in a numerical solution of the dispersion relation. This is simplified by the consideration that the effective refractive index of the cladding modes is less than the cladding and decreases with increasing mode order. In addition the simplified mode matching condition

constrains the maximum $\delta n_e = (n_{eco} - n_{ecl})$ for a given wavelength range of interest and a particular LPG period: Eq. 47.

$$\lambda_{res} = (n_{eco} - n_{ecl})\Lambda \qquad \textit{Eq. 47}$$

Nevertheless it is necessary to perform a huge number of calculations for each wavelength of interest. This part of the calculation requires the majority of the processing power and correspondingly time. The calculations were performed on a 2.44 GHz processor over a wavelength range of 1200-1600 nm at 1 nm steps with a maximum δn_e of 0.004 for a total calculation time of ~5 hrs. However once calculated for a particular fibre it is not necessary to repeat the calculation as this effectively defines the available cladding and core modes for an LPG element to act upon.

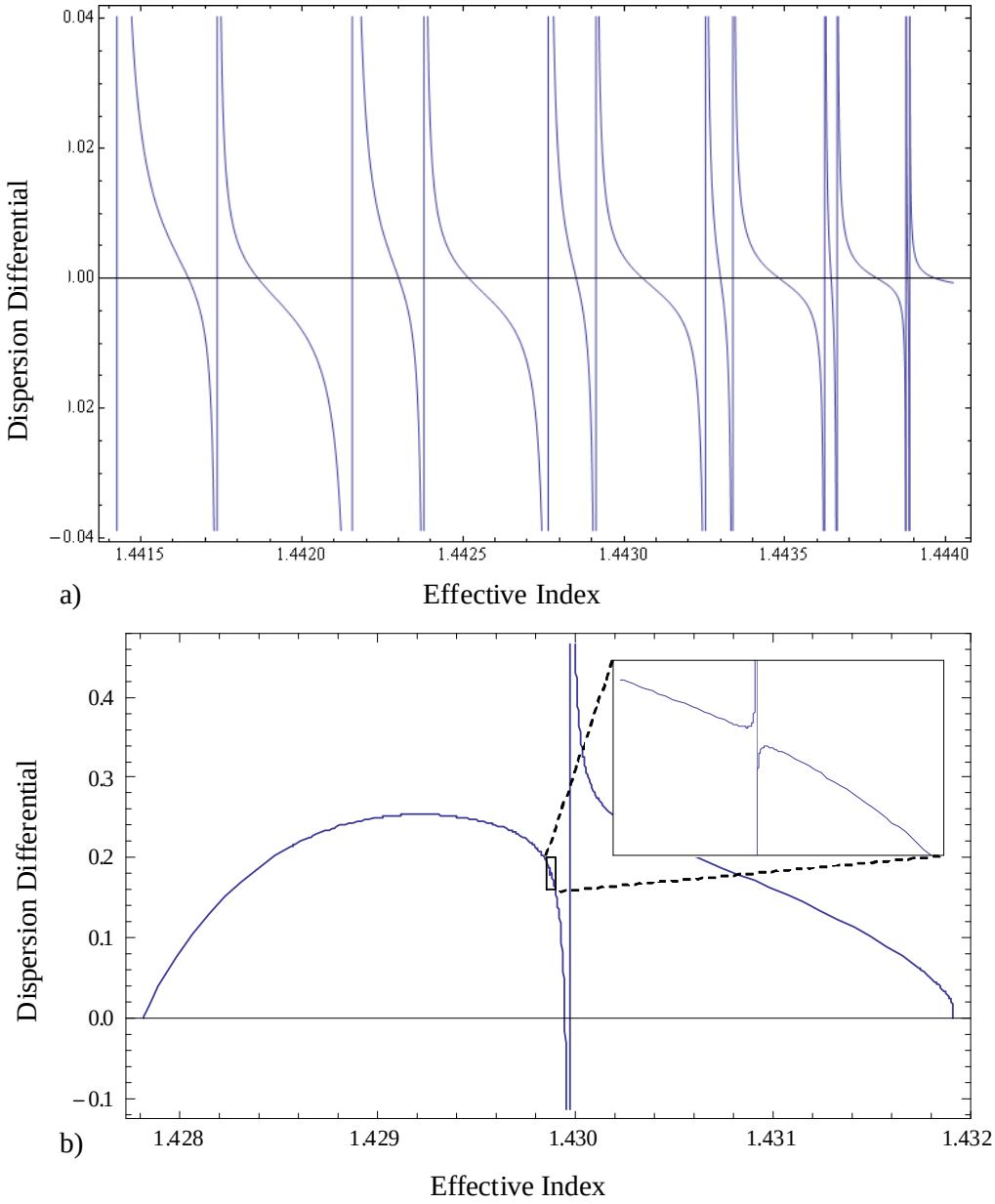

Figure 57: Example plots of the dispersion differential: $\xi_0 - \xi_0'$ evaluated at 1550 nm, zero crossing points exist at allowed cladding mode effective indices. a) overall shape, b) example of a hard to find small distortion mode.

5.2.4. Mode normalisation constants

Implementing the desired form of the coupled mode equations requires that individual modes have their mode field parameters defined and the mode normalisation constant is calculated. The mode normalisation constant is critical to the mode overlap integrals as

it is necessary to evaluate modes with equivalent total power. In common with the notation adopted by Erdogan [18] a total mode power of 1 W has been selected.

In the case of the core mode, the field definitions are again well documented [66]. For the purposes of the coupled mode equations it is only necessary to consider the E mode fields within the core, Eq. 48 & Eq. 49.

$$E_{r}^{co,co} \cong i\boldsymbol{E}_{01}^{co} J_0\left[\frac{V\sqrt{1-b}\,r}{a_1}\right] e^{i\theta+i(\beta z-\omega t)} \qquad \textit{Eq. 48}$$

$$E_{\varphi}^{co,co} \cong -\boldsymbol{E}_{01}^{co} J_0\left[\frac{V\sqrt{1-b}\,r}{a_1}\right] e^{i\theta+i(\beta z-\omega t)} \qquad \textit{Eq. 49}$$

Where $\mathbf{E}_{01}^{co}$ is the mode normalisation constant for the core mode evaluated for 1 W total power, Eq. 50. The notation $E_{r}^{x,y}$ has been used to label mode fields where x indicates the mode (core or cladding) and y indicates the region, core cladding or external.

$$\boldsymbol{E}_{01}^{co} \cong \sqrt{\frac{Z_0 b}{\pi n_2\sqrt{1+2b\Delta}}}\,\frac{1}{a_1 J_1\left[V\sqrt{1-b}\right]} \qquad \textit{Eq. 50}$$

Where Δ is the relative refractive index contrast of the fibre: $\Delta = (n_1 - n_2)/n_1$

In the case of the cladding modes it is necessary to consider the core, cladding and external regions in order to properly calculate the mode normalisation constant, for simplicity we shall omit the z dependant E_z and H_z field equations Eq. 51 - Eq. 62.

$$E_{r}^{cl_\nu,co} = i\boldsymbol{E}_{\boldsymbol{\nu}}\frac{u_1}{2}\left(J_2[u_1 r] + J_0[u_1 r] - \frac{\sigma_2\xi_0}{{n_1}^2}\left(J_2[u_1 r] - J_0[u_1 r]\right)\right)e^{i\theta+i(\beta z-\omega t)} \qquad \textit{Eq. 51}$$

$$E_{\varphi}^{cl_\nu,co} = \boldsymbol{E}_{\boldsymbol{\nu}}\frac{u_1}{2}\left(J_2[u_1 r] - J_0[u_1 r] - \frac{\sigma_2\xi_0}{{n_1}^2}\left(J_2[u_1 r] + J_0[u_1 r]\right)\right)e^{i\theta+i(\beta z-\omega t)} \qquad \textit{Eq. 52}$$

$$H_r^{cl_\nu,co} = \boldsymbol{E_\nu}\frac{u_1}{2}\big(i\sigma_1(J_2[u_1 r] - J_0[u_1 r]) + i\xi_0(J_2[u_1 r] + J_0[u_1 r])\big)e^{i\theta+i(\beta z-\omega t)} \quad \textit{Eq. 53}$$

$$H_\varphi^{cl_\nu,co} = -i\boldsymbol{E_\nu}\frac{u_1}{2}\big(i\sigma_1(J_2[u_1 r] + J_0[u_1 r]) + i\xi_0(J_2[u_1 r] - J_0[u_1 r])\big)e^{i\theta+i(\beta z-\omega t)} \quad \textit{Eq. 54}$$

$$E_r^{cl_\nu,cl} = i\boldsymbol{E_\nu}\frac{\pi a_1 {u_1}^2 J_1[u_1 a_1]}{2}\left(-\frac{\boldsymbol{F_2}}{r}p_l + \frac{1}{u_2 r}q_l - \frac{\sigma_2}{{n_2}^2}\left(u_2\boldsymbol{G_2}r_l - \frac{{n_2}^2\xi_0}{n_1^2}s_l\right)\right)e^{i\theta+i(\beta z-\omega t)} \quad \textit{Eq. 55}$$

$$E_\varphi^{cl_\nu,cl} = \boldsymbol{E_\nu}\frac{\pi a_1 {u_1}^2 J_1[u_1 a_1]}{2}\left(\frac{\sigma_2}{{n_2}^2}\left(\frac{\boldsymbol{G_2}}{r}p_l - \frac{{n_2}^2\xi_0}{{n_1}^2 u_2 r}q_l\right) + u_2\boldsymbol{F_2}r_l - s_l\right)e^{i\theta+i(\beta z-\omega t)} \quad \textit{Eq. 56}$$

$$H_r^{cl_\nu,cl} = \boldsymbol{E_\nu}\frac{\pi a_1 {u_1}^2 J_1[u_1 a_1]}{2}\left(-i\frac{\boldsymbol{G_2}}{r}p_l + i\frac{{n_2}^2\xi_0}{{n_1}^2 u_2 r}q_l + i\sigma_1(u_2\boldsymbol{F_2}r_l) - s_l\right)e^{i\theta+i(\beta z-\omega t)} \quad \textit{Eq. 57}$$

$$H_\varphi^{cl_\nu,cl} = i\boldsymbol{E_\nu}\frac{\pi a_1 {u_1}^2 J_1[u_1 a_1]}{2}\left(i\sigma_1\left(\frac{\boldsymbol{F_2}}{r}p_l - \frac{1}{u_2 r}q_l\right) - iu_2\boldsymbol{G_2}r_l + i\frac{{n_2}^2\xi_0}{{n_1}^2}s_l\right)e^{i\theta+i(\beta z-\omega t)} \quad \textit{Eq. 58}$$

$$E_r^{cl_\nu,ex} = i\boldsymbol{E_\nu}\frac{\pi a_1 {u_1}^2 {u_2}^2 J_1[u_1 a_1]}{4\omega_3 K_1[\omega_3 a_2]}\left(-F_3(K_2[\omega_3 r] - K_0[\omega_3 r]) + \frac{\sigma_2\boldsymbol{G_3}}{{n_3}^2}(K_2[\omega_3 r] + K_0[\omega_3 r])\right)e^{i\theta+i(\beta z-\omega t)} \quad \textit{Eq. 59}$$

$$E_\varphi^{cl_\nu,ex} = \boldsymbol{E_\nu}\frac{\pi a_1 {u_1}^2 {u_2}^2 J_1[u_1 a_1]}{4\omega_3 K_1[\omega_3 a_2]}\left(-\boldsymbol{F_3}(K_2[\omega_3 r] + K_0[\omega_3 r]) + \frac{\sigma_2\boldsymbol{G_3}}{{n_3}^2}(K_2[\omega_3 r] - K_0[\omega_3 r])\right)e^{i\theta+i(\beta z-\omega t)} \quad \textit{Eq. 60}$$

$$H_r^{cl_\nu,ex} = \boldsymbol{E_\nu}\frac{\pi a_1 {u_1}^2 {u_2}^2 J_1[u_1 a_1]}{4\omega_3 K_1[\omega_3 a_2]}\big(-i\sigma_1\boldsymbol{F_3}(K_2[\omega_3 r] + K_0[\omega_3 r]) - i\boldsymbol{G_3}(K_2[\omega_3 r] - K_0[\omega_3 r])\big)e^{i\theta+i(\beta z-\omega t)} \quad \textit{Eq. 61}$$

$$H_{\varphi}^{cl_{\nu},ex} = i\boldsymbol{E_{\nu}}\frac{\pi a_1 {u_1}^2 {u_2}^2 J_1[u_1 a_1]}{4\omega_3 K_1[\omega_3 a_2]}\big(i\sigma_1 \boldsymbol{F_3}(K_2[\omega_3 r] - K_0[\omega_3 r]) - \boldsymbol{G_3}(K_2[\omega_3 r] + K_0[\omega_3 r])\big)e^{i\theta + i(\beta z - \omega t)} \quad \textit{Eq. 62}$$

Where F_2 G_2 F_3 G_3 are defined below in Eq. 63 - Eq. 66, $\mathbf{E_\nu}$ is the mode normalisation constant for the ν^{th} cladding mode, r, θ and z are the orthogonal cylindrical coordinates (Figure 55) and n_{ecl} becomes the νth cladding mode effective index calculated via the dispersion equation in §5.2.3.

$$\boldsymbol{F_2} = \boldsymbol{J} - \frac{u_{21}\sigma_2\xi_0}{{n_1}^2 a_1} \quad \textit{Eq. 63}$$

$$\boldsymbol{F_3} = -\boldsymbol{F_2}p_l + \frac{q_l}{u_2} \quad \textit{Eq. 64}$$

$$\boldsymbol{G_2} = \xi_0\boldsymbol{J} + \frac{u_{21}\sigma_1}{a_1} \quad \textit{Eq. 65}$$

$$\boldsymbol{G_3} = -\frac{{n_3}^2}{n_2}\left(\boldsymbol{G_2}p_l - \frac{{n_2}^2\xi_0}{{n_1}^2 u_{21}}q_l\right) \quad \textit{Eq. 66}$$

Erdogan [18, 21] provides a set of equations for determining the normalization constant of the ν^{th} cladding mode in Appendix B of his paper. Unfortunately these equations contain an error, the normalisation constants do not result in a power of 1 W and there are discontinuities present in the boundary conditions between the core-cladding and cladding-external interfaces; although I have been unable to find it the most likely cause is a typographical error [21]. However it is trivial to implement a numerical evaluation of the normalisation constant separately from this calculation by considering the power in the mode through Eq. 67 - Eq. 69.

$$P = \frac{1}{2}\int_0^{2\pi} d\varphi \int_0^{\infty} r dr \left(E_r H_{\varphi}^{*} - E_{\varphi} H_r^{*}\right) \quad \textit{Eq. 67}$$

Where * indicates the complex conjugate and:

$$E_i = \begin{cases} E_i^{cl_{\nu},co}, & 0 \le r \le a_1 \\ E_i^{cl_{\nu},co}, & a_1 \le r < a_2 \\ E_i^{cl_{\nu},co}, & a_2 \le r \end{cases} \quad \textit{Eq. 68}$$

$$H_i = \begin{cases} E_i^{cl_\nu,co}, & 0 \le r \le a_1 \\ E_i^{cl_\nu,co}, & a_1 \le r < a_2 \\ E_i^{cl_\nu,co}, & a_2 \le r \end{cases} \qquad \textit{Eq. 69}$$

For i = φ or r.

The boundary conditions of the core, cladding and external regions can be seen in the infinitesimal overlap of the regions at r = a_1 and a_2.

The mode normalisation constants given by evaluating P at $E_\nu = 1$, Eq. 70, for each wavelength of interest:

$$\boldsymbol{E_\nu}(\lambda) = \frac{1}{\sqrt{P(\boldsymbol{E_\nu} == 1)}} \qquad \textit{Eq. 70}$$

5.2.5. Coupling Coefficients and Transmission Calculation

Eq. 25 - Eq. 70 are notable as there is no implementation of the LPG; the equations are solely calculating the available modes although care must be taken to include a dc component of the LPG refractive index perturbation within the definition of $n_1(\lambda)$ if one is expected (cf. §5.2.1). With the core mode and available cladding modes defined the remaining steps calculate the mode coupling between them in the presence of an LPG structure as defined in §5.2.1. A full derivation of the approximations and calculations from the generalised coupled mode equation is presented in Erdogan [18, 21, 22] and as it is not directly necessary for the calculation of the transmission spectrum it will not be reproduced here. The two key terms of interest are the coupling coefficient between the core and ν^{th} cladding mode K_ν given by Eq. 71 and the small detuning parameter, a measure of the bandwidth of mode coupling, for the ν^{th} cladding mode, δν, Eq. 72.

$$K_{\boldsymbol{\nu}} = \sigma\frac{2\pi}{\lambda}\sqrt{\left(\frac{\pi\, b}{Z_0 n_2\sqrt{1+2b\Delta}}\right)}\frac{{n_1}^2 u_1}{{u_1}^2 - \frac{V^2(1-b)}{a_1}}\Big(1 + \frac{\sigma_2\xi_0}{{n_1}^2}\Big)\boldsymbol{E_\nu}\left(u_1 J_1[u_1 a_1]\frac{J_0\left[V\sqrt{1-b}\right]}{J_1\left[V\sqrt{1-b}\right]} - \frac{V\sqrt{1-b}}{a_1}J_0[u_1 a_1]\right) \quad \textit{Eq. 71}$$

$$\delta_\nu = \pi\left(\frac{\left(n_{neco} - n_{necl,\nu}\right)}{\lambda} - \frac{1}{\Lambda}\right) \quad \textit{Eq. 72}$$

The power, P of wavelength λ coupled to the νth cladding mode across the length (L) of the LPG can be calculated via these two parameters Eq. 73:

$$\boldsymbol{P_\nu}(\lambda) = 1 - cos\left[L\sqrt{{K_\nu}^2 + {\delta_\nu}^2}\right]^2 + \frac{sin\left[L\sqrt{{K_\nu}^2 + {\delta_\nu}^2}\right]^2}{1 + {K_\nu}^2/{\delta_\nu}^2} \quad \textit{Eq. 73}$$

As the coupling between each individual cladding mode and the core mode is separated in wavelength space, it is possible to ignore cross coupling and to sum the individual coupling losses of the core mode through the fibre to derive the complete transmission spectrum in dB Eq. 74:

$$\boldsymbol{T}(\lambda) = -10\sum_{\nu=1}^{vmax} log_{10}[1 - \boldsymbol{P_\nu}(\lambda)] \quad \textit{Eq. 74}$$

5.3. Discussion of the Effect of Modelling Parameters

5.3.1. Effect of LPG period, Λ

Eq. 47 gives the direct proportionality of the LPG period, Λ, to the coupling wavelength of an LPG. With increasing LPG period the entire LPG spectrum is shifted, to higher wavelengths for increasing period (Figure 58). This is qualitatively trivial to understand as increasing the period will simply couple a longer wavelength to the same cladding mode. As discussed in §2.1.5 increasing the LPG length allows the LPG to couple to lower order cladding modes and vice versa.

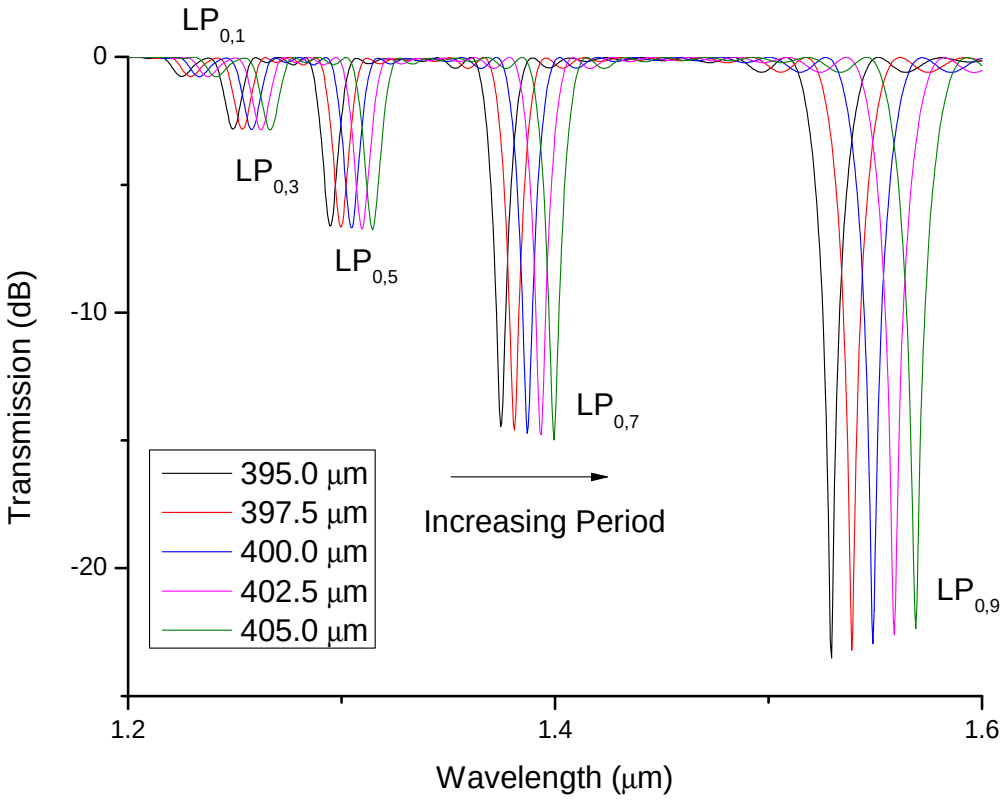

Figure 58: Modelled transmission spectrum of a typical LPG (L=24 mm, Δn=3.4 x10^{-4} RIU) with a variety of periods between 395 and 405 μm. Changing the length also shifts the resonant wavelength resulting in a change to the coupled power.

5.3.2. Effect of LPG Length, L and Maximum Index Contrast, Δn

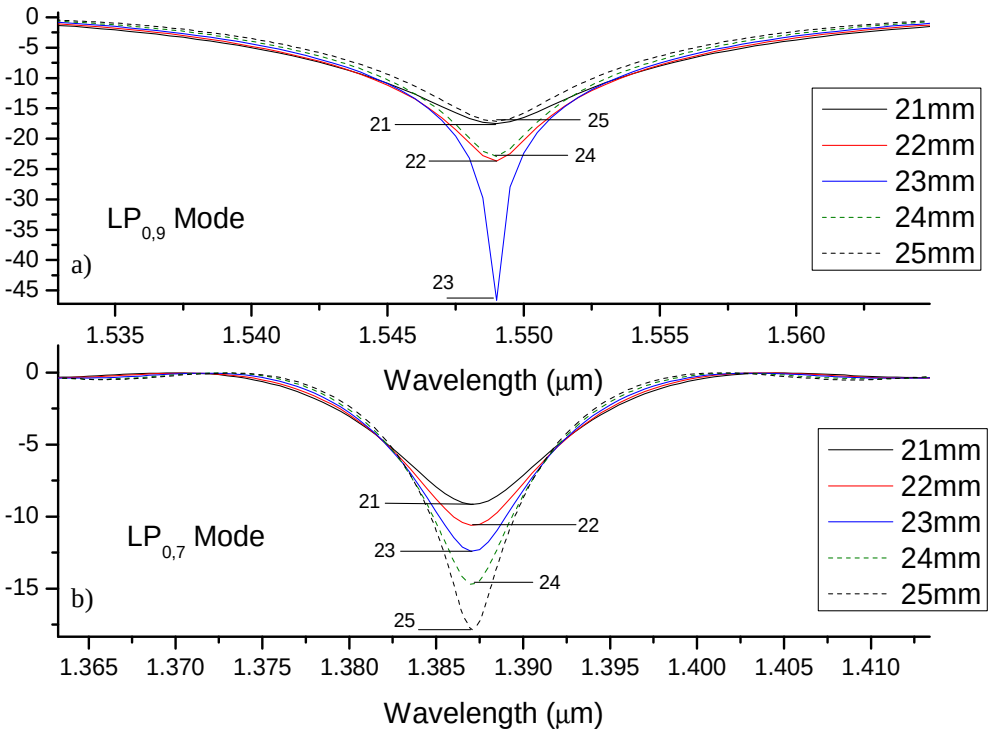

Figure 59: Modelled transmission spectra for the a) 9th and b) 7th order cladding modes for a typical LPG (Λ 400 μm, Δn 3.2 x10-4 RIU) with various LPG lengths. The 9th order mode shows resonant coupling at ~23 mm before over coupling while the 7th order mode is under coupled at all lengths up to 25 mm.

Mathematically the effect of the length of the LPG on the transmission spectrum is described by Eq. 73. Here the power coupled between modes is proportional to the sum of the cosine and sine squared. In other words the response will exhibit periodicity with respect to length. Increasing the length, i.e. number of periods, will increase the amount of radiation coupled to a cladding mode. At a particular number of periods, starting with the higher order modes, a maximum coupling will be experienced i.e. the phase matching is optimised across the length of the LPG. Above this number of periods, radiation will be coupled from the cladding back into the core until a minimum coupling is reached, a process known as over coupling. Figure 59 illustrate this principle. In this case the 9th order mode is close to resonant coupling at 21 mm length. As the length is increased the mode experiences maximum coupling, at ~23 mm, before over coupling. By contrast the 7th order mode experiences increasing coupling over the modelled

length with resonance and over coupling occurring at longer lengths. Increasing the length therefore provides preferential coupling to lower order modes.

The dependance of the phase matching condition on length also has notable effects in the side lobes of non-apodized LPG elements (Figure 60). As the length of the LPG increases, the lack of apodization becomes more apparent as more power is coupled into the mode side lobes. The wavelengths of these side lobes also change as they move closer together for increasing LPG lengths. This behaviour forms a convenient means to fit the length of an LPG element to an experimental transmission spectrum – particularly in regard to identifying over coupled cladding mode resonances which will exhibit stronger side lobes.

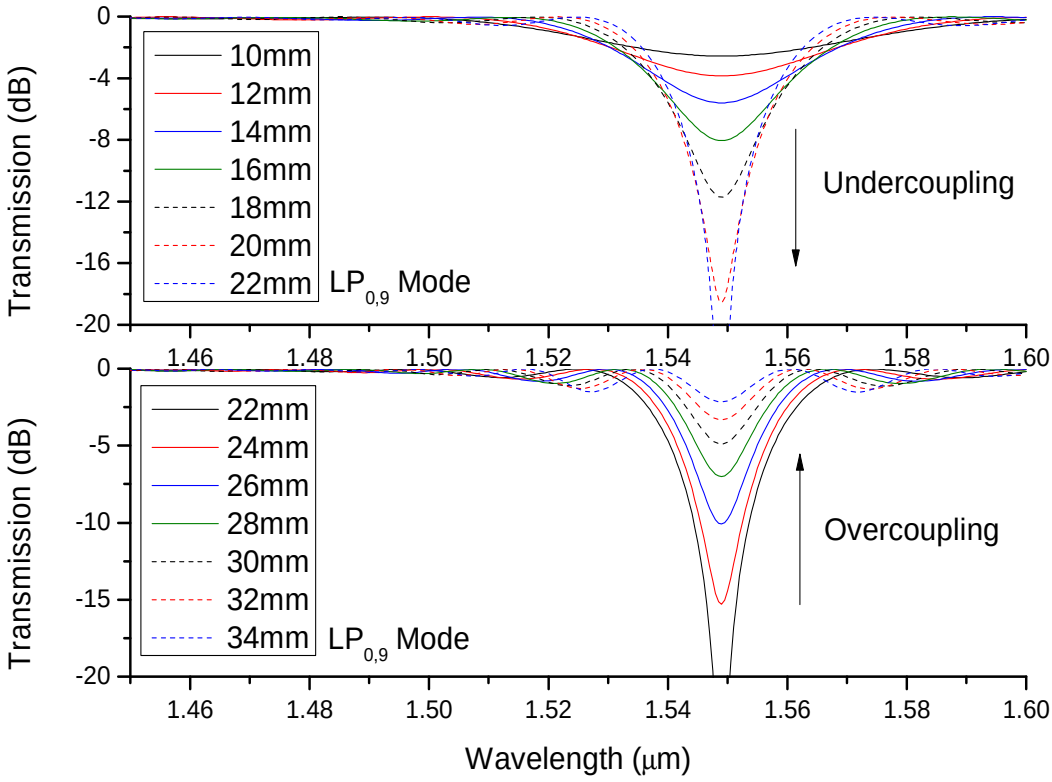

Figure 60: Illustration of the behaviour of the 9th order mode as LPG length is increased for a typical LPG element (Λ 400 μm, Δn 3.2 x10^{-4} RIU). Resonant coupling in this case is achieved at ~22 mm length.

The amplitude of the refractive index perturbation within the core, Δn, affects the coupling coefficient between core and cladding modes. Eq. 71 illustrates that the

coupling coefficient is directly proportional to Δn. A plot of the effect of varying Δn within a typical LPG is presented in Figure 61. Similarly to varying the length of the LPG there is a resonant coupling condition such that with increasing Δn an individual mode will experience a maximum before over coupling (Figure 62). Of further interest is that the refractive index amplitude has little effect on the side lobes for the cladding modes, only changing the amplitude with little shift to the wavelength.

The effect of length and Δn can be considered to be tied together through Eq. 71. K_ν is directly proportional to Δn and δ_ν is a constant for a given cladding mode in a fibre. Therefore to maximise the coupling to a particular cladding mode it is necessary to change both simultaneously. In practice, due to the complexity of LPG writing systems, it is usually easier to change the length of an LPG by adding additional periods than it is to change the refractive index (which would require multiple passes or variations in laser power for inscription).

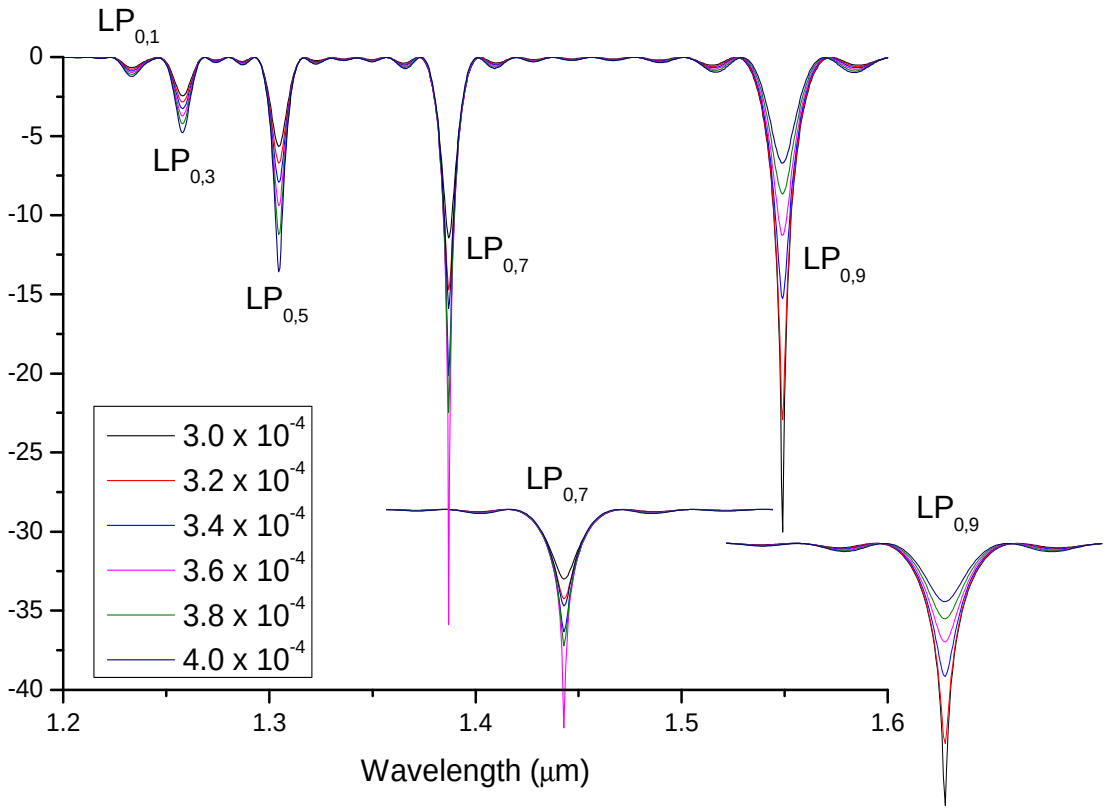

Figure 61: Modelled transmission spectra for a typical LPG (Λ 400 μm, L 24 mm) with various LPG amplitudes, Δn (3.0-4.0 x10^{-4} RIU).

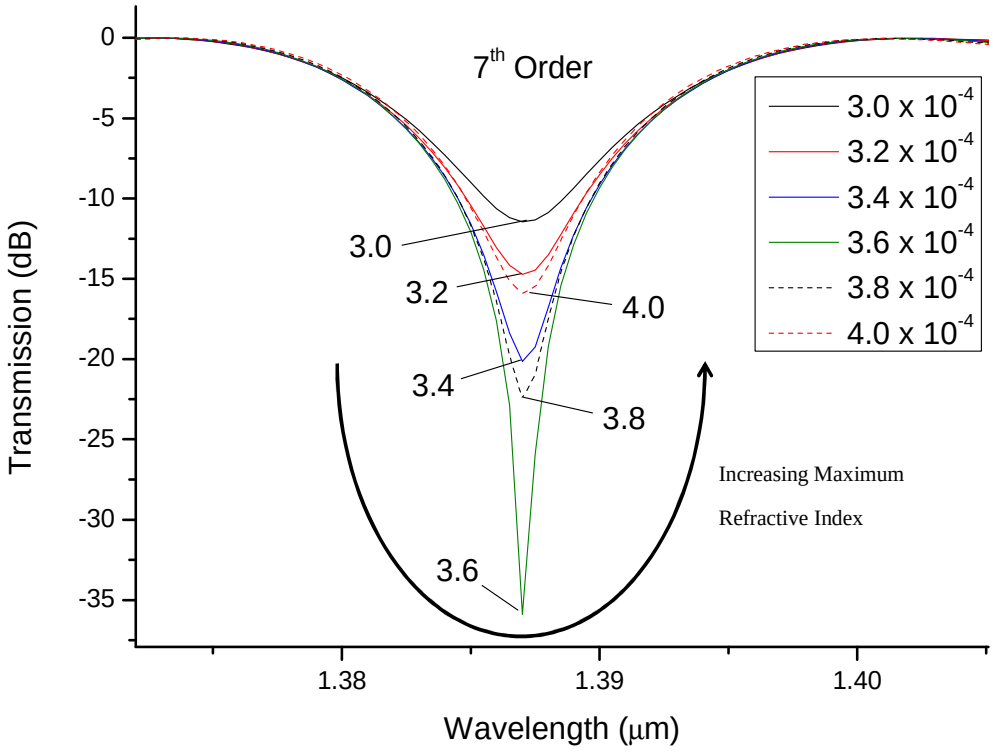

Figure 62 Expanded view of the modelled transmission spectrum of the 7th order mode from Figure 61. Here the mode demonstrates increasing coupling to a resonance at ~3.6 x10-4 RIU before over coupling.

5.4. Fitting Model to Experimental Data

5.4.1. Estimating Optical Constants

The majority of the fibres used for the work described in this thesis are Corning® SMF-28® fibres with LPGs inscribed by CGCRI scanning slit point by point technique (§2.1.6). An SMF-28® fibre has a pure fused silica cladding and a Ge-doped core. The refractive index of fused silica is well documented and may be derived from the Sellmeier equation, Eq. 75.

$$n(\lambda) = \sqrt{1 + \sum_{i=1}^{3} \frac{A_i \lambda^2}{\lambda^2 - B_i^2}} \qquad \textit{Eq. 75}$$

Where A_i and B_i are the Sellmeier coefficients, which for fused silica are A_1=0.6961663, A_2=0.4079426, A_3=0.8974794, B_1= 0.0684043, B_2= 0.1162414, B_3=9.896161 and λ is the wavelength in μm. Coefficients are taken from Malitson [137] and the notation used is for convenience.

The refractive index perturbation generated in the core of these LPGs is unknown but is generally approximated as a sinusoid within a top-hat envelope. This refractive index perturbation will, most likely, include a dc change to the refractive index of the core in the region of the LPG. This, unknown, change to the refractive index needs to be included in the model of n1(λ) in order to correctly calculate the available core and cladding modes within the LPG region. For that matter the Sellmeier coefficients for the core of a Corning® SMF-28® fibre are unpublished. It is therefore necessary to estimate or derive the correct refractive index for the core region. Fortunately it is a fairly simple matter to estimate by virtue of the phase matching condition in Eq. 47. The transmission spectrum of an LPG of known period, Λ, can be measured with a broadband tungsten lamp and spectrum analyser.

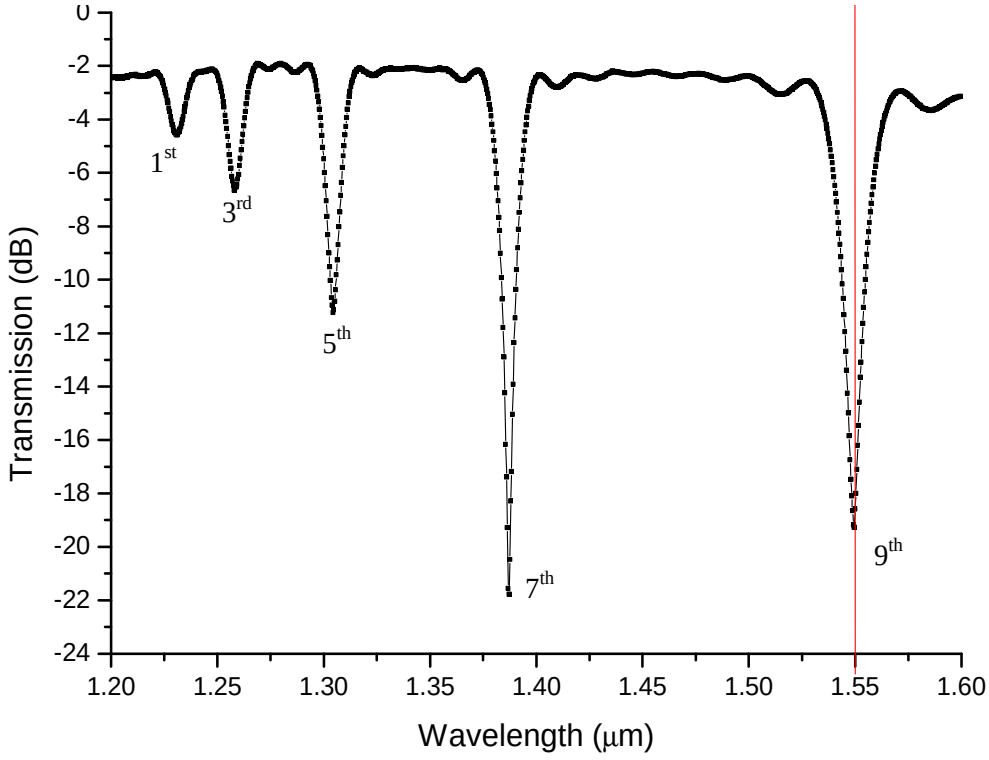

Figure 63: Measured transmission spectrum of a CGCRI LPG with a period of 400 μm showing 5 loss bands in the 1200-1600 nm including one at ~1550 nm.

Within this transmission spectrum are a series of loss bands each corresponding to a mode of, generally unknown, order (Figure 63). Fitting a Gaussian to these loss bands, which although a poor fit in general, accurately determines the peak resonant position for each mode. These loss band positions may then be used to determine the difference in the effective refractive index of the core and cladding mode in question via Eq. 47. The mode order for each band is also required, and can be determined by plotting the phase matching conditions assuming that the core index is ~0.005 greater than the cladding (Figure 64).

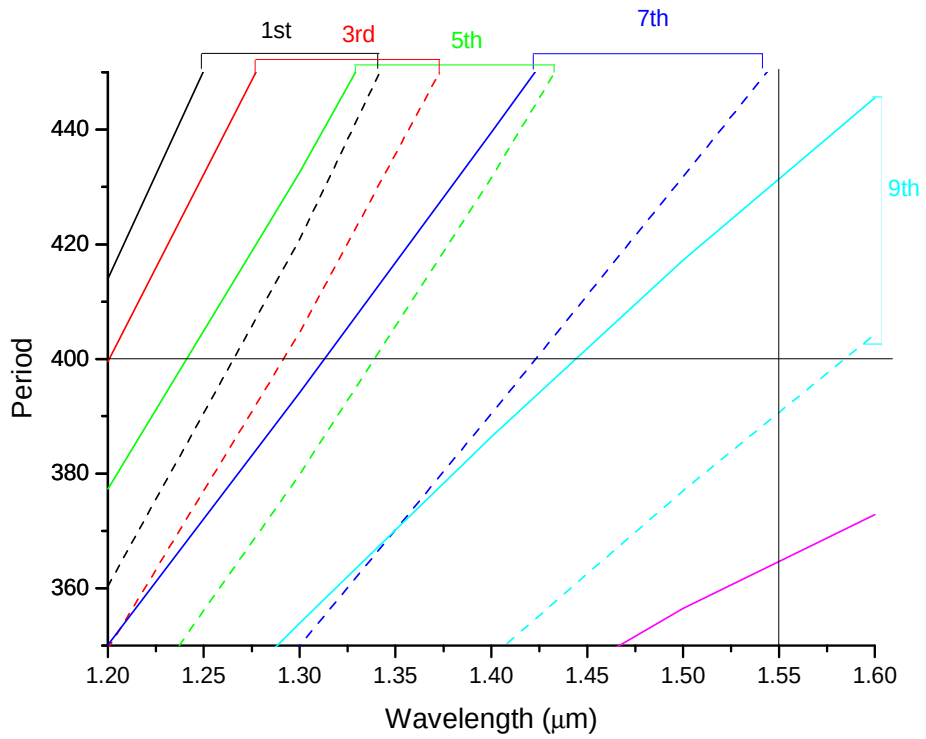

Figure 64: Calculated phase matching condition for an SMF-28® fibre with cladding index determined by Eq. 47 and core index at n_2+.005, solid lines, and n_2+.0055, dashed lines, for the first 6 odd order modes. A resonance peak at 1550 nm and a period of 400 μm must be the 9th order mode.

This gives a series of five known mode orders, their resonant wavelengths, the difference between the core and cladding effective indices and the cladding index at those wavelengths. The dispersion equation for the core and cladding modes may be solved numerically for core refractive index at each of the mode resonant wavelengths.

This determines 5 values of the core refractive index which give the peak mode coupling positions at the required wavelengths. These five core indicies serve as the base for a fit to derive a new set of Sellmeier coefficients to describe the core index (Figure 65). In this case the position of the lowest, 1st, order mode has been ignored for the purposes of the fit. Why this particular value is so poorly placed for derived core refractive index is not entirely clear. It is most likely a result of a poor signal to noise ratio giving a larger error in the fitted resonant wavelength position, in what is the smallest and broadest of the resonant positions. The determined Sellmeier coefficients for the core are A1=0.7042628, A2=0.415638, A3=0.895311, B1=0.064067, B2=0.111816, B3=9.896570.

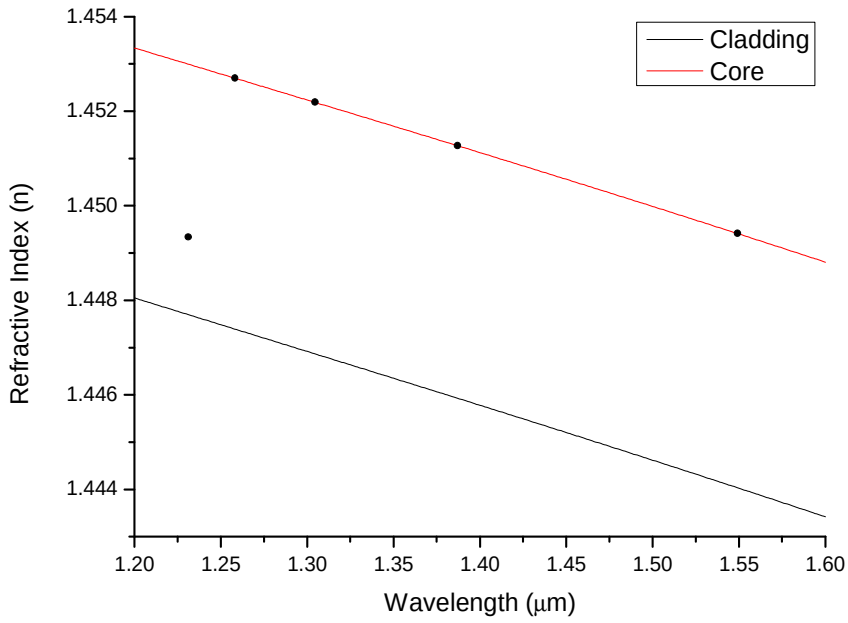

Figure 65: Plot of the core and cladding refractive index as a function of wavelength. Cladding index is that of fused silica from Eq. 75, the core index has been derived from the transmission spectrum of the LPG in Figure 63. The points are the derived refractive indices of the core based on the position of the LPG loss bands. The left most point has been ignored for fitting the Sellmeier equation, the inaccuracy of this point is likely due to a poor identification of the resonant position in this shallow wide noisy loss band (cf. Figure 63). Data spot size is larger than the error.

5.4.2. Fitting Length, L, and Maximum Core Index Perturbation, Δn

With the refractive index of the core and cladding of the SMF-28® fibres defined (along with any dc offset to the core index created through the writing process) the parameters remaining for fitting the LPG are the period, Λ, maximum refractive index perturbation, Δn, and the length of the LPG, L. The LPG elements provided by the CGCRI are all of similar design. They are specified as 400 μm (there is no error quoted on this which has caused complications), with a length of "~25 mm", there is no specification of the index perturbation although it is estimated to be in the region of 3-4 $x10^{-4}$ RIU. The period of the LPG has been assumed to be accurate throughout the analysis. Recall that the period was used as the basis for calculating the refractive index of the core mode of the fibre hence it cannot be used as a free variable in the analysis or the fitting. An error in the LPG period is liable to produce a complicated, and difficult to predict effect on the transmission spectrum. The method used at the CGCRI, a slit illumination method, is not expected to give much error in the period of the LPG. However it must be conceded that an error in the period of the LPG will result in follow on errors in the rest of the analysis. As the core index has been fitted to give loss bands for the first nine odd modes at the observed wavelengths, we do not expect much of an error in the spectral positions of the loss bands. The power coupled to each of the cladding modes will be determined by the length and the refractive index perturbation.

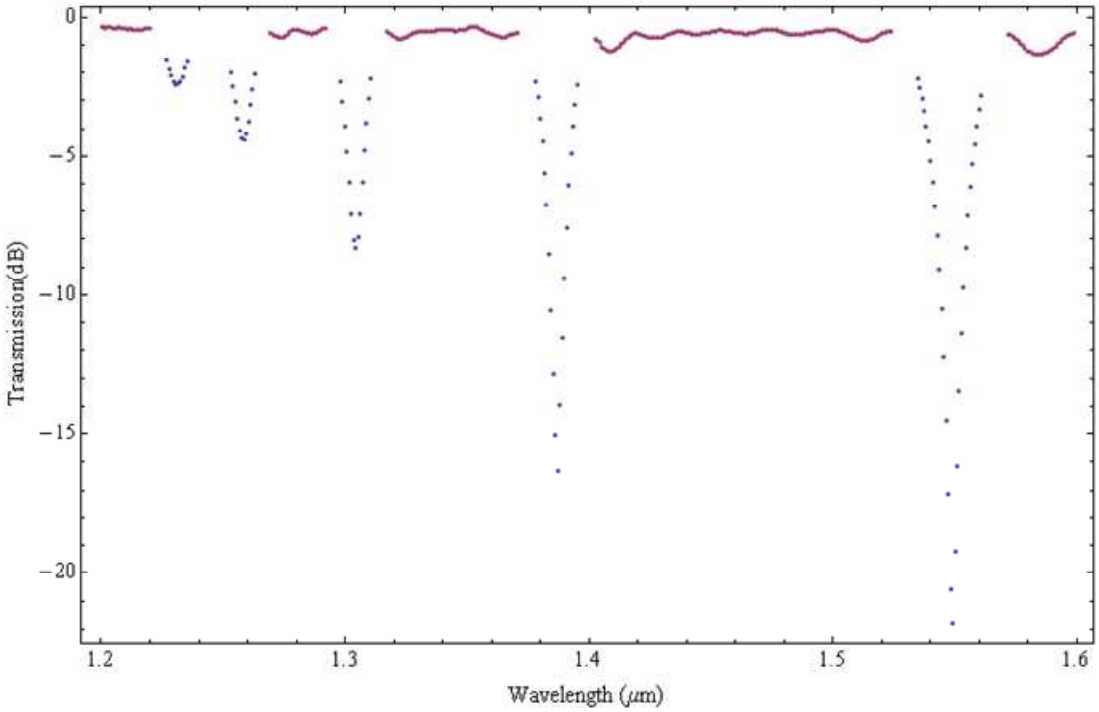

Figure 66: Plot of the division of a single transmission dataset between lobe, red and peak, blue data. Note that the two sub-sets do not overlap, ~5 data points separate them.

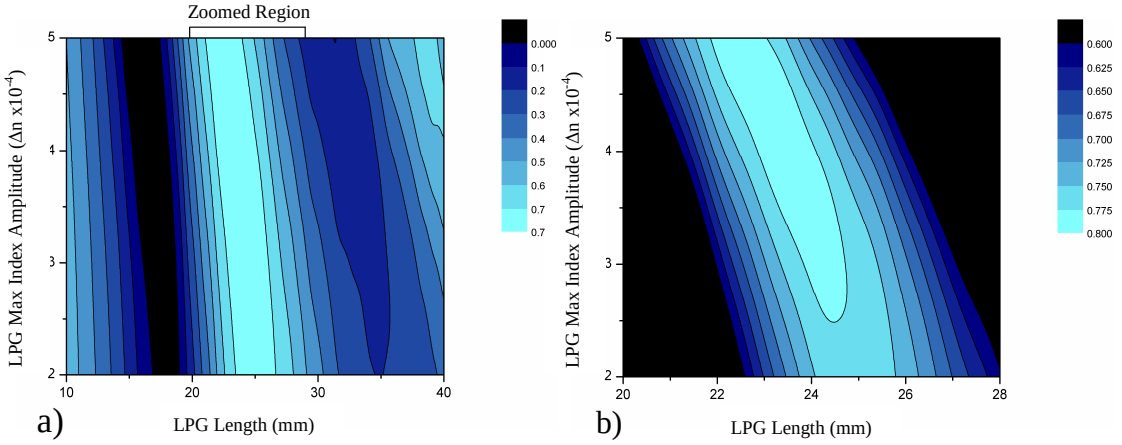

Figure 67: Plot of the correlation between measured and fitted transmission spectra in the region of the side lobes (cf. Figure 66). Higher correlation suggests a better fit with a correlation of 1 being perfect. a) overall plot, b) zoomed in on region of interest.

As discussed in §5.3.2, the shape and, more importantly, the wavelength of the side lobes are strongly dependant on the length (or number of periods) of the LPG. Analysis of this region of the transmission spectrum, both measured and modelled, should accurately fit and therefore represent the length of the LPG (Figure 66). Data used are extracted from the transmission spectrum and a correlation is performed between the experimental and the theoretical data. A plot of this correlation (Figure 67) illustrates that the fit, within the side lobe region, is indeed a function primarily of the length with the refractive index perturbation having less effect. This effectively narrows down the length range to 22-25 mm – slightly shorter than the specification of ~25 mm.

Likewise, an analysis of the correlation between the theoretical and experimental data in the region of the loss bands only, illustrates that the coupling resonance conditions are a function of both length and Δn (Figure 68). This suggests that, over the length 22-25 mm, Δn should be of the order ~2.5-4.0 x10^{-4} RIU.

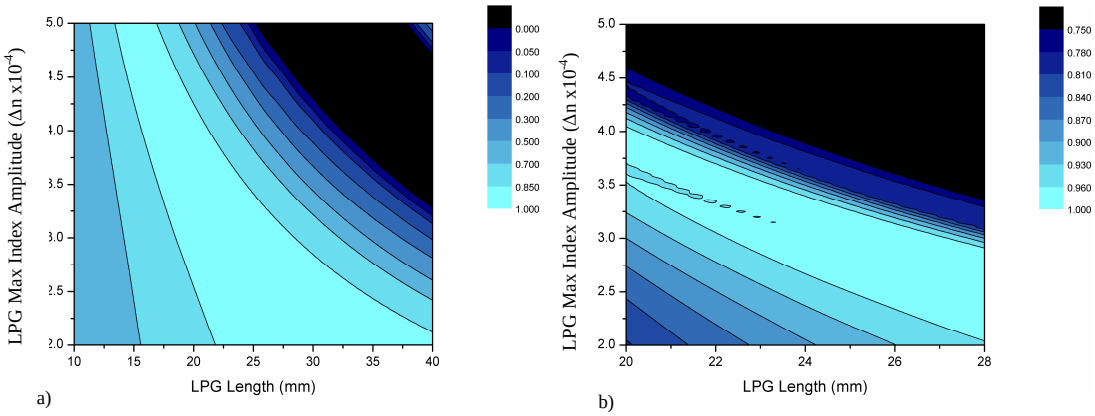

Figure 68: Plot of the correlation between measured and fitted transmission spectra in the region of the peak resonance (cf. Figure 66). Higher correlation suggests a better fit with a correlation of 1 being perfect. a) overall plot, b) zoomed in on length of interest. The island-like structures in b are an artefact of the resolution.

As both analyses attempt to fit separate sections of the transmission spectrum it is expected that the best fit will occur in the region where both correlation plots provide a maximum. This can be found by normalising both datasets to 1 and plotting their sum. A direct overlap of peak positions would result in a particular combination of L and Δn

giving a correlation of 2. In this case the maximum is found to be 1.996 suggesting an excellent agreement on the best fit parameters (Figure 69). Not that the error analysis here does not include any component from an error in the LPG period.

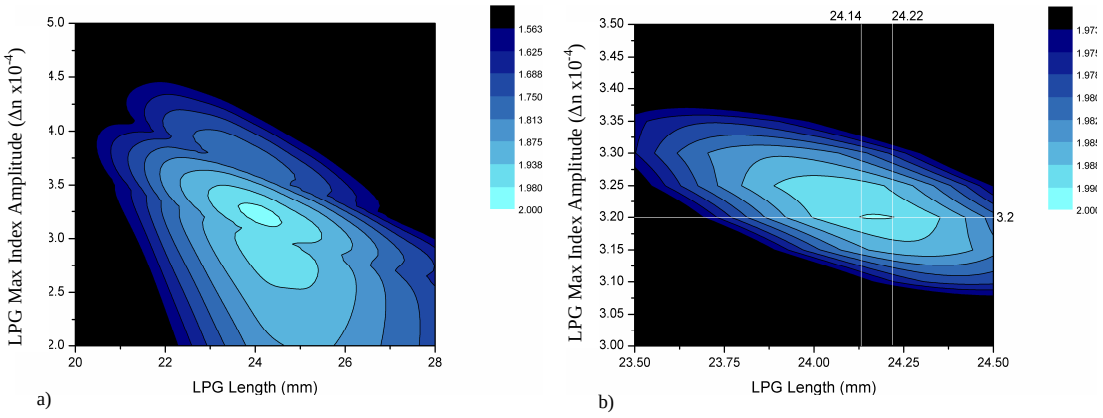

Figure 69: Plot of the sum of the normalised correlation of both the peak and lobe datasets. Higher correlation suggests a better fit with a correlation of 2 being perfect. a) overall plot, b) zoomed in plot of maximised correlation. Note that the resolution of these plots is .05 x10^{-4} RIU and .01 mm respectively giving a fit of $\Delta n = 3.20 \pm 0.025$ x10^{-4} RIU and $L = 24.18 \pm 0.04$ mm.

With L and Δn derived via correlation analysis a plot of the modelled transmission spectrum can be directly compared to the experimental data (Figure 70). This shows excellent agreement between the two sets. Of note is that the correlation between the amount of power coupled into each mode decreases with mode order. This suggests that there is a systematic error in the refractive index of the core and cladding. As these have been derived from the grating period it is most likely due to an error in this value. Alternatively the refractive index perturbation within the core has been approximated as a sinusoid while in reality it is more likely to exhibit a square or step like profile due to manufacture with a 200 μm slit (cf. §2.1.6). An error in this will have a direct effect on the coupling coefficient and hence the amount of power coupled to each mode, particularly in the side lobes.

Nevertheless the fit is sufficiently accurate, particularly at the higher order modes, to be of practical use. As each fibre has been inscribed by the same writing technique it is reasonable to assume that the lengths and Δn of each LPG element will not differ significantly from these values.

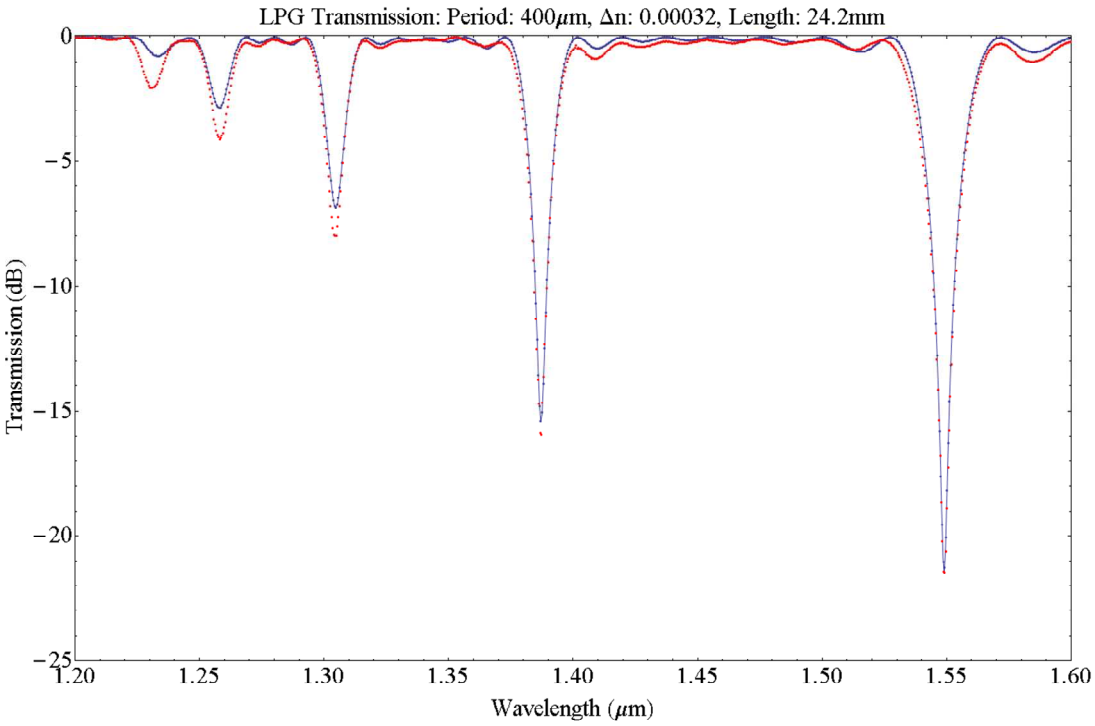

Figure 70: Plot of the modelled, blue line with points, and experimental, red points, transmission spectrum for CGCRI LPG element 2.4. Note that a 0.4 dB loss has been included due to measured connector losses in the measurement system. Fitted values for L and Δn have been derived via correlation analysis while the period, Λ, has been set at 400 μm.

The work presented in this chapter provides a complete picture of the dispersive optical constants and LPG profile. In order to use the LPG to detect hydrogen however it is necessary to introduce a layer of palladium onto the cladding. This has a significant effect on the available cladding modes and coupling coefficients. In order to adequately model the transmission spectrum and predict the sensitivity of the sensor it is necessary to re-evaluate the model in the presence of this metal layer; the subject of the next chapter.

Chapter 6. Palladium Jacketed Long Period Gratings

6.1. Introduction

The use of a Palladium (Pd) coated Long Period Gratings (LPGs) for the detection of hydrogen has been previously reported by, among others Maier [34]. These experiments have, in the most part, been only proof of principle without detailed analysis. In particular details on the coating process, characterisation of Pd coatings and the dynamics of hydrogen absorption have been absent. As a first step in the characterisation process I attempted to replicate these data.

Although we possess the in house capability to coat fibres with Pd we do not have the capability to write our own LPG elements. All the LPG elements used in these experiments were sourced externally. The first experiments were attempted with LPG elements provided by Aston University on an ad-hoc basis. The results of these experiments demonstrated issues in the reproducibility, reliability and characterisation of these LPGs.

An alternative source of LPGs was therefore required. Through an existing collaboration within the university between Prof. Ajoy Kar and the Central Glass and Ceramic Research Institute (CGCRI) the CGCRI was contacted agreed to supply research grade LPGs on a more formal collaborative basis. The study of Pd coated LPG elements can therefore be broken down into two phases, proof of principle and characterised gratings.

6.2. Proof of Principle Experiments

6.2.1. Experimental Setup

An LPG test rig was inherited from Dr Maier's proof of principle work [34] and with a few adjustments to improve the computer control interface it was pressed into service. A sketch of the setup is provided in Figure 71. It consists of a double walled chamber with gas flowing via a pair of Mass Flow Controllers (MFC) and gas flow switch. The gas enters the outer wall of the chamber where it is heated via resistive heaters before

flowing through the inner chamber, over the LPG and existing via a vent at the base of the rig. The LPG is held in a vertical position under a small amount of constant strain (eliminating strain and bending effects in the LPG) in the centre of the pipe. It is held in place via a rubber bung with a slit in the side at the top end of the pipe. While not providing a perfect seal, the pipe is held at positive pressure and flow, as such gas entrainment was not thought to be an issue although it was observed in later experiments (cf. §6.3.1).

The system is illuminated with a super luminescent light emitting diode (SLED) operating at a centre wavelength at 1550 nm with a FWHM of ~50 nm, chosen to adequately illuminate the $LP_{0,9}$ mode. Interrogation is via a computer controlled (LabView) optical spectrum analyser (OSA) (cf. §2.1.9). LPG temperature is provided through the use of the internally mounted Pt-100. Combined with the measured temperature coefficient of the fibre this allows for compensation of low frequency temperature variations within the chamber (note the thermo optic coefficient of Pd is low enough to ignore for the purposes of this form of temperature compensation). The gas flows are controlled via MFC with set flow rates and the concentration is altered via a timed gas switch.

Individual elements were coated using our in-house spit arrangement (cf. §3.2), although these early experiments lacked adequate homogeneity in the resultant coating (cf. §3.3). Over a period of several months data was gathered indicating the response to hydrogen at various concentrations and temperatures. Due to the lack of specifications for the gratings and their irregular designs there was considerable variation in the responses. In particular the periodicities of the gratings were either not supplied or were subject to significant inaccuracies. The results presented here are therefore representative of these early experiments.

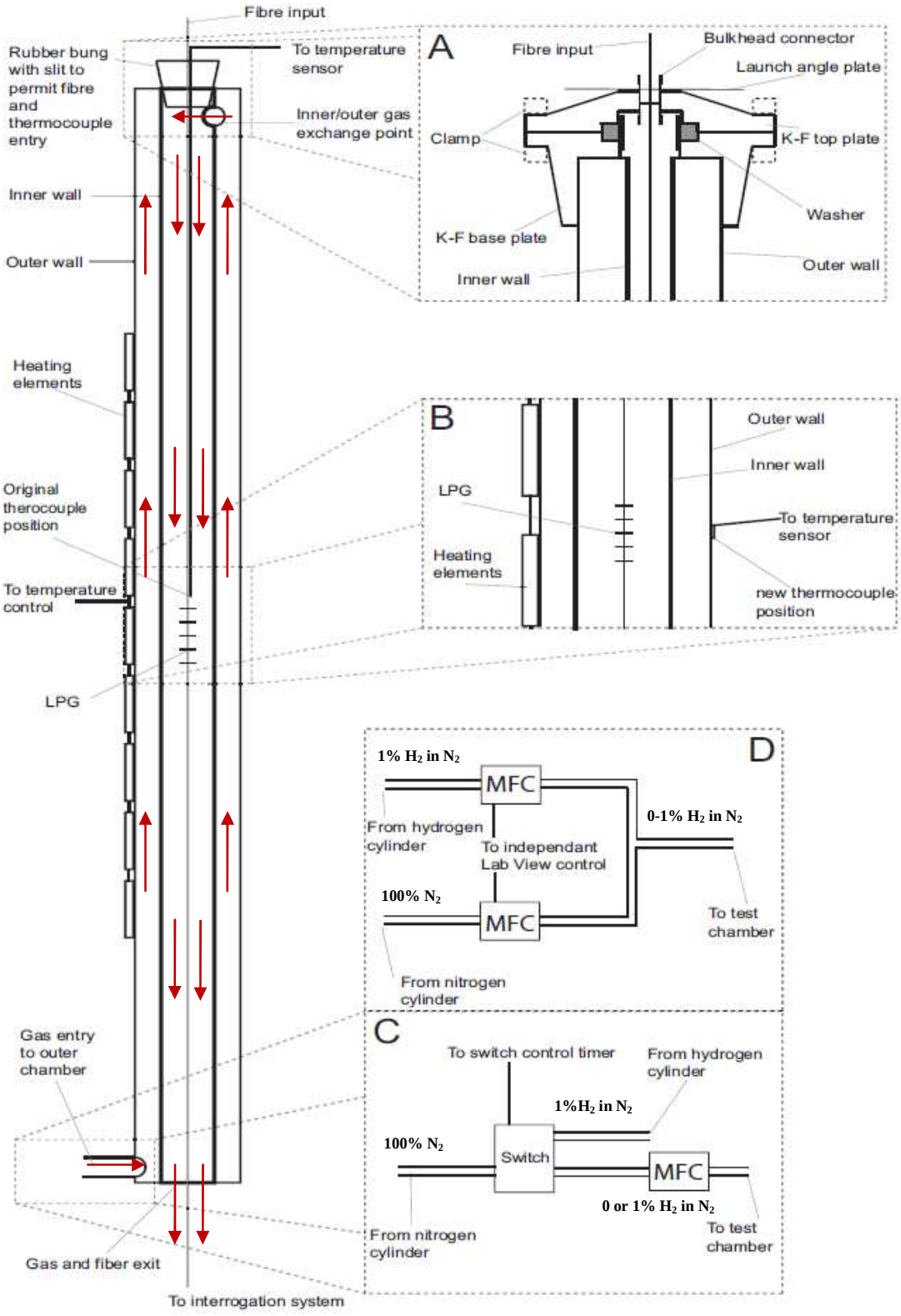

Figure 71: Schematic of LPG test rig, gas flow marked in red. Original design (right and gas control: inset C). Inserts A, B and D illustrate the changes made to improve stability, §6.3.1.

6.2.2. Hydrogen Concentrations

The peak coupling position, i.e. position of minimum transmission, of the $LP_{0,9}$ mode was monitored as a function of hydrogen concentration (note that due to lower sensitivities the $LP_{0,1-7}$ modes did not exhibit any change in wavelength due to hydrogen). Figure 72 shows the result of several cycles between a mix of 10,000 - 156.25 ppm of H_2 in balance N_2 and pure N_2. Here we see the expected repeatability and reversibility of the absorption-desorption process and, while not entirely clear on this timescale, the desorption process can be seen to be slower (cf. Figure 75). The peak shift in the resonance position for 10,000 ppm (1%) hydrogen is measured at ~60 pm, in this case the $LP_{0,9}$ resonance has a FWHM of 13 nm. Measuring such a small shift in such a large feature is challenging and made even more so by the maximum accuracy (±15 pm) of the OSA.

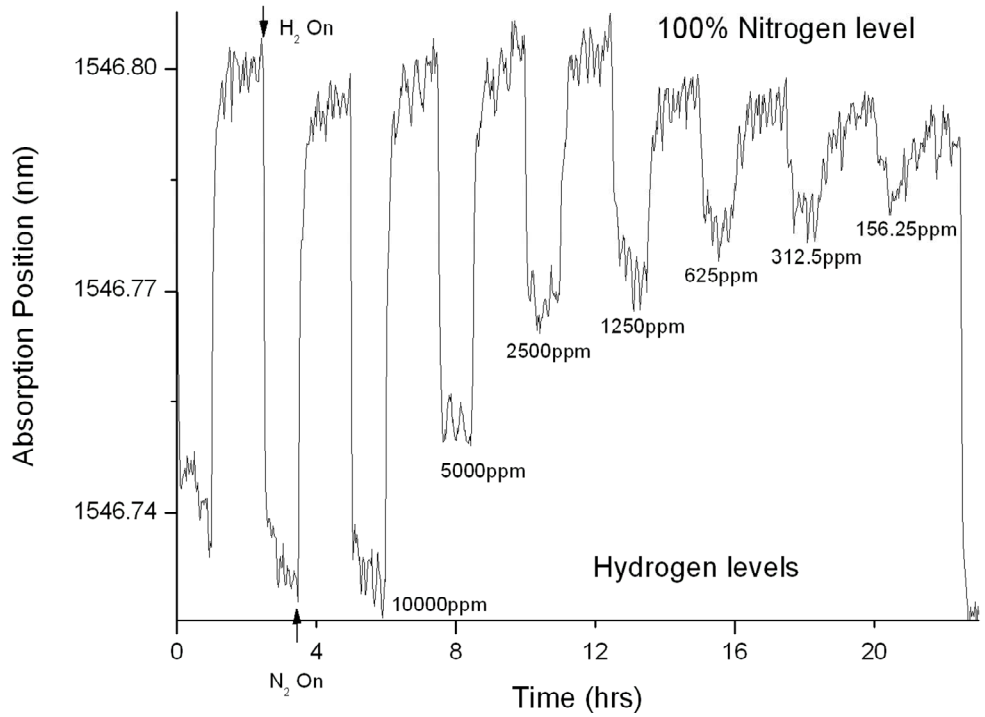

Figure 72: Plot of the response of an LPG-Pd element to a variety of cycled H_2 gas concentrations in balance N_2.

From Figure 72 it is also possible to observe that the response to hydrogen is, as expected, non linear in the 0-1% range. A log-log plot (Figure 73) of the mean peak position of each concentration illustrates the non-linearity well.

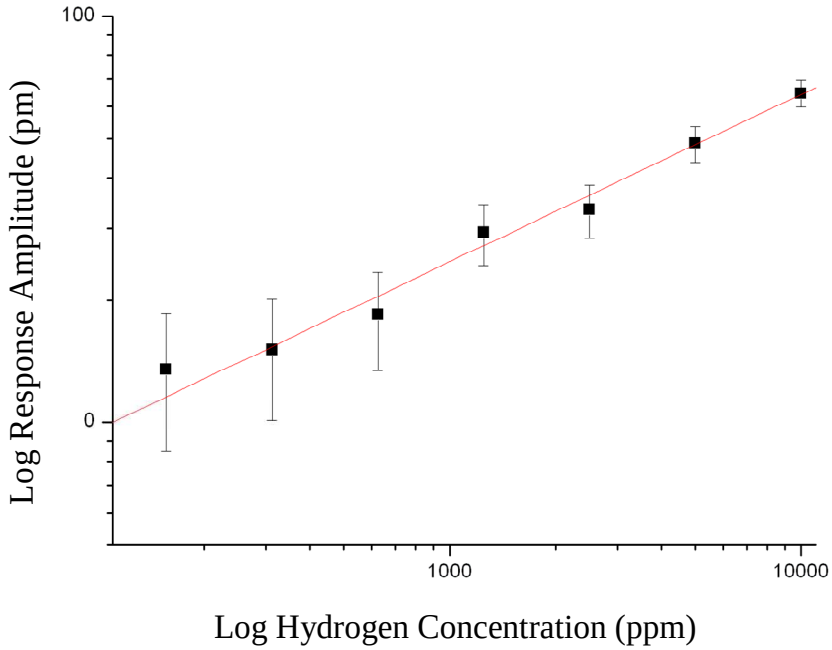

Figure 73: Plot of mean peak position (errors are one standard deviation) at each hydrogen concentration indicated in Figure 72.

6.2.3. Temperature Effects

From our knowledge of the Pd-H system and of LPGs in general (§2.1.3 & §2.2.3) we expect that there should be two distinct temperature effects on the LPG-Pd system. The first is a consequence of the thermal dependence of the refractive indices of the fibre. As the temperature changes the resonant coupling wavelength will also shift. Although the thermal conductivity of the fibre is poor (at least in the silica) the dimensions are such that it is possible to assume that the entire LPG is at a constant temperature. As such we expect this temperature shift to be more or less instantaneous. The second effect is that of temperature on the absorption of hydrogen in Pd. Here a decrease in temperature will result in a higher hydrogen permeation equilibrium state and thus an increase in the strain on the lattice. At the same time the decreased mobility energies

gives slower absorption and desorption. In effect the response to hydrogen increases in strength but decreases in speed at lower temperatures.

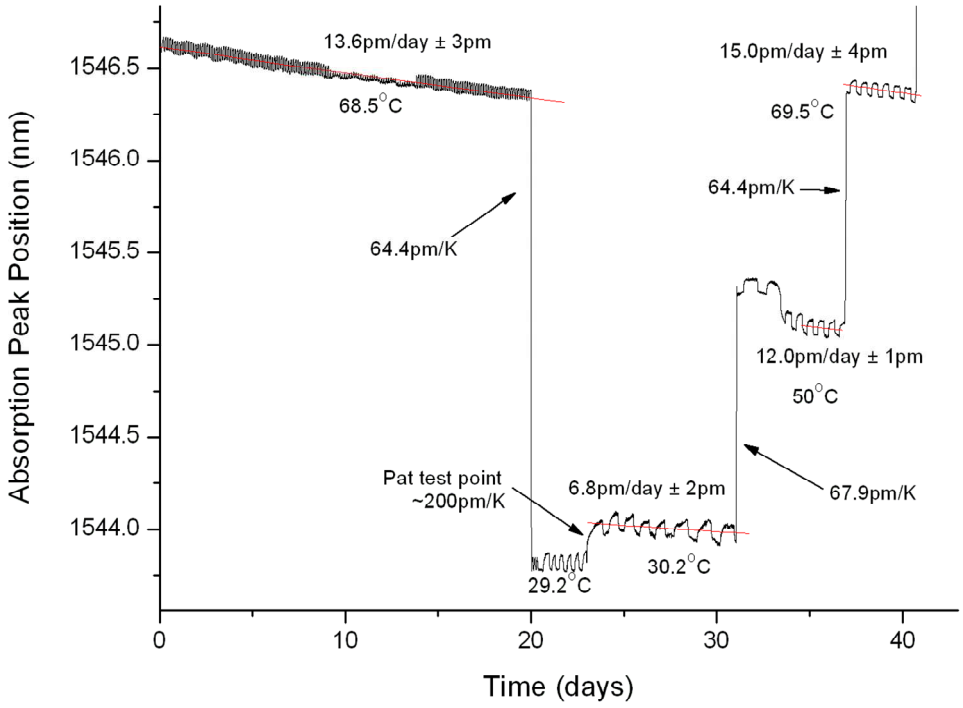

Figure 74: Plot of the central position of the $LP_{0,9}$ mode resonance of an LPG when exposed to a variety of temperatures. Note that a PAT electrical safety test (at 24 days) interrupted the experiments between 29.2 and 30.2°C creating an artificial increase in the peak position which persisted to day 34.

Figure 74 shows the experimental data from these early temperature experiments at five separate temperatures. Again the LPG is exposed to cycling between 1% H_2 in N_2 and N_2 giving a square wave like component to the trace. At a change in temperature there is an almost instantaneous (the rig requires some time to cool or to heat) change in the central wavelength of the LPG. Measurement of this shift gives a temperature coefficient of the order of 65 pm K^{-1}. It is also possible to see that there is a drift in the overall peak position as a function of time, suggesting a degradation of the LPG-Pd system (§6.2.4). The rate of this drift can also be seen to be proportional to temperature.

To observe the shift in the Pd-H system it is necessary to take a closer look at individual cycles at each of the temperatures. Figure 75 shows cycles at four of these temperatures. As expected, the strength of the response is inversely proportional to temperature while the rate of absorption and desorption is proportional to the temperature, giving a system with a fundamental trade-off between speed and strength of response.

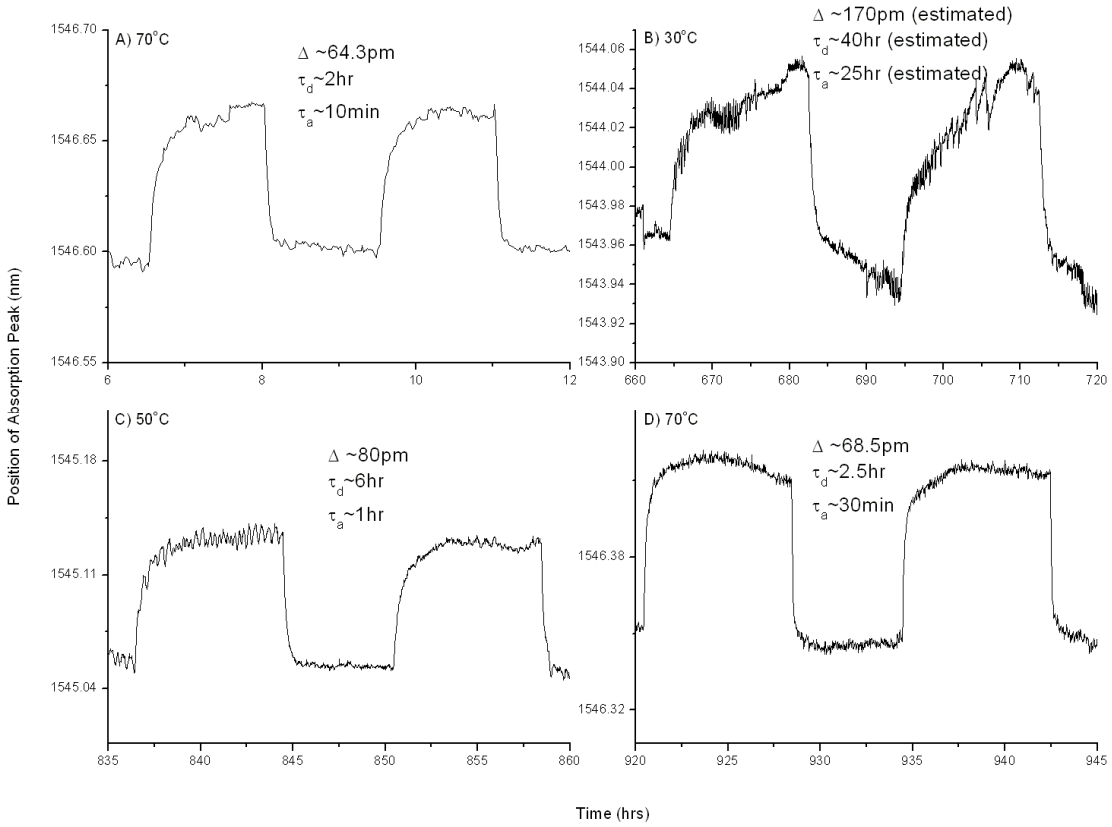

Figure 75: Comparative plots of the response of an LPG to cycling between 1% H_2 in balance N_2 and pure N_2 at three separate temperatures. The high frequency noise in plots B and C is due to the lab air-conditioning.

6.2.4. Long Term (Drift) Effect

The drift observed in the temperature experiments (Figure 74 §6.2.3) raised some interest as this was not expected. It suggests that there is a long term problem with the stability of the LPG-Pd system. To further investigate this issue, an LPG element was

permitted to continue cycling over three months. In this experiment the LPG was exposed to H_2 and N_2 cycling, N_2 and (lab) Air for extended periods. These data (Figure 76) shows that the drift is independent of gas concentration. This suggests that the problem is not an issue with the lattice strains caused by repeated absorption and desorption of hydrogen.

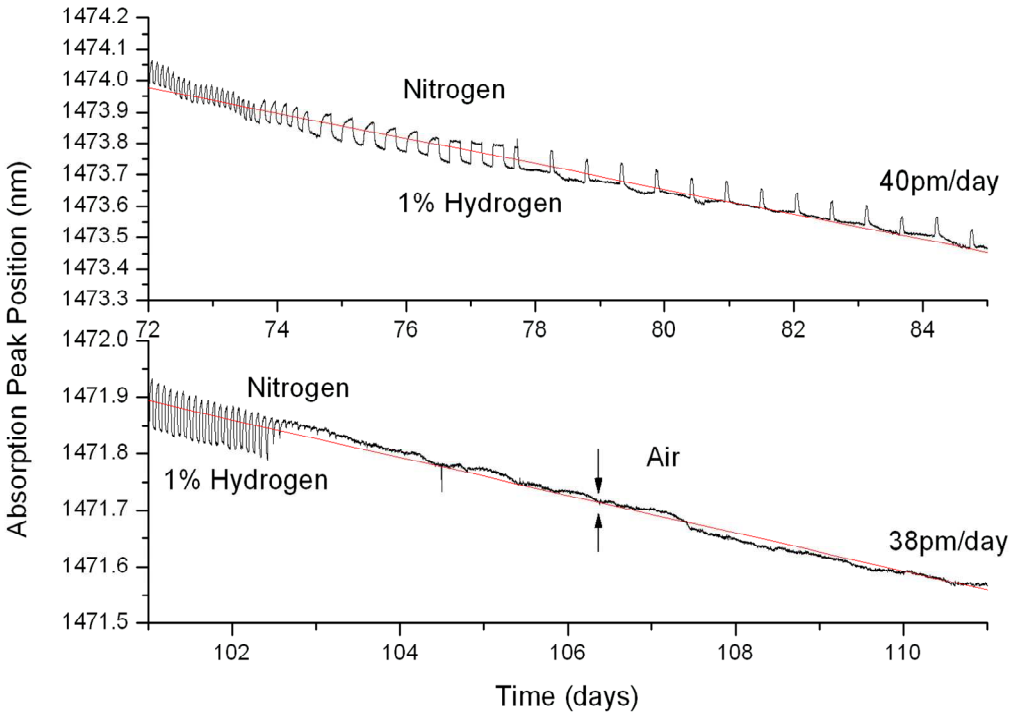

Figure 76: Plot of drift in the peak position of an early LPG over time illustrating the independence of the drift with respect to gas concentration at 70°C. Note that this LPG is different to that plotted in Figure 77.

Additionally it was noted that the direction of the drift is towards the uncoated LPG spectral position, i.e. decreasing wavelength. This, combined with the temperature dependence of the drift, suggested that it was some form of delamination process. As one of the earlier experiments in this thesis, the coating process had not been completely characterised and it was felt that it was possible that the Pd may deposit with some form of microstructure. Over time the poor adherence of the Pd to the silica would result in patches of the Pd delaminating, popping off or blistering, along these microstructure lines. This would be an essentially random process, increasing with the increased

energies of higher temperatures. As such it should result in an exponential decay towards the uncoated LPG state.

On the timescale of 100 days the results shown in Figure 76 appear to be roughly linear although the total drift over 100 days is a fraction of the total expected drift. In order to test the delaminating hypothesis, a separate LPG element was exposed to a higher temperature (110°C) effectively speeding up the aging process over a period of two weeks. A plot of the results (Figure 77), again cycling between nitrogen and hydrogen, clearly shows the exponential decay of the results. A fit to these data gives an estimated end point for the drift at 1542.1 nm, which when compensated for the temperature dependence of the LPG gives an end point of 1535.7 nm at 25°C, a figure which compares very well with the measured uncoated LPG position at 1536 nm.

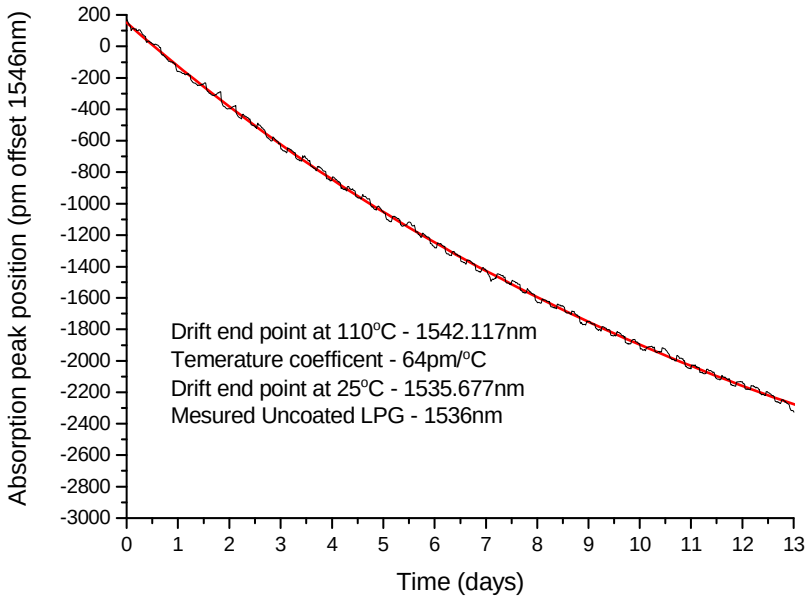

Figure 77: Plot of the drift of an LPG central resonant wavelength with time. Data was recorded at the elevated temperature of 110°C to increase the rate of drift revealing the exponential form decaying toward the uncoated LPG position. Fitted exponential is in red.

A sample of this aged LPG element was preserved and once the apparatus became available was scanned using a scanning electron microscope (SEM) at AWE (§3.3). The image (Figure 78) shows a mottled surface further validating the hypothesis of

localised delaminating. These observations led directly to the characterisation of the Pd deposition process and the improvement of the Pd surface quality by more careful control of the deposition parameters.

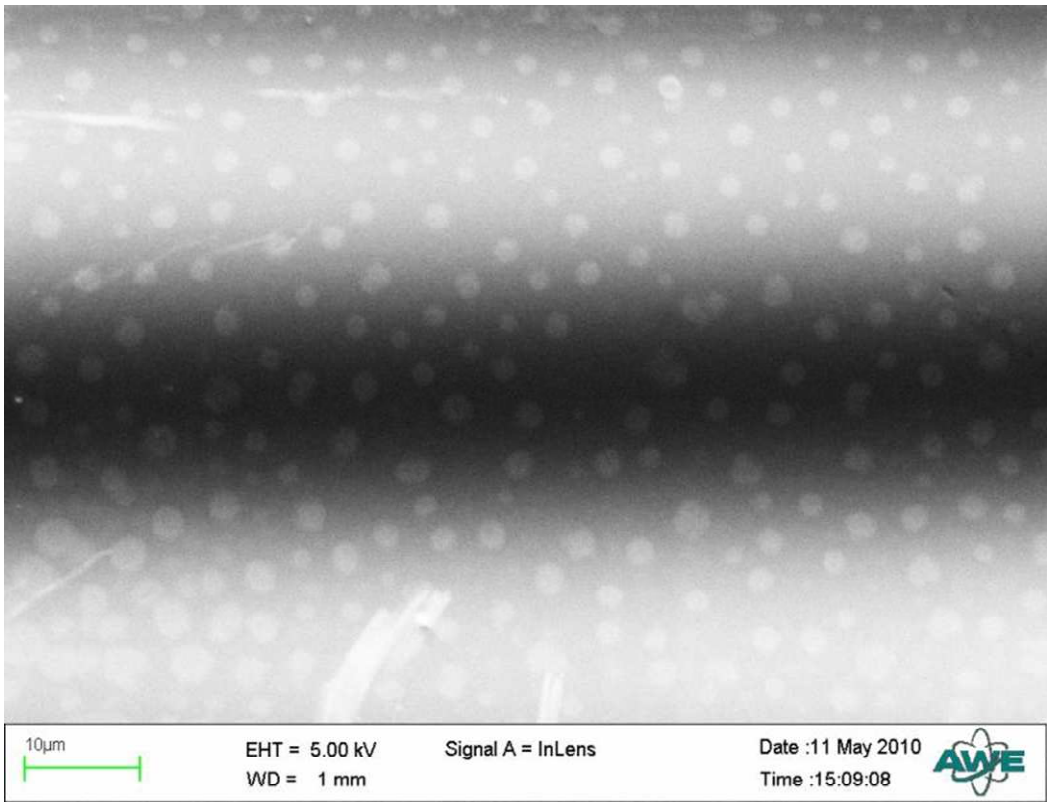

Figure 78: SEM image of an aged fibre indicating localised delamination, blistering or crystallisation of the Pd surface.

6.3. Characterised Gratings

6.3.1. Setup

During the proof of principle experiments, some issues were discovered with the opearation of the experimental test rig. At low flow rates (<100 ppm), the response to hydrogen became a function of the flow rate, suggesting gas entrainment. In order to eliminate this entrainment, the bung was replaced with a specifically designed sealing clamp arrangement. A vacuum KF plate was adapted for use by gluing it to the top of the inner chamber (using epoxy) and mounting a fibre bulkhead adaptor in the KF end

piece (Figure 71 A). This arrangement is airtight but requires that an LPG must be attached to a pigtail with a specific length (30-40 cm) of fibre in order to remain in the chamber.

Additionally the original position of the temperature sensor on the outside of the outer wall of the test rig presented a problem in temperature compensation. There was a delay between the temperature measured at the Pt-100 and the effect seen by the LPG caused by the physical separation of the two positions. This was solved by mounting a new Pt-100 within the inner wall of the test rig (Figure 71 B). The necessary holes in the walls were sealed with epoxy to prevent the temperature variations, effectively eliminating the problem.

Finally the gas flow was improved by replacing the single MFC and switch with two MFCs. With the addition of custom made interface circuits these could be controlled from the master LabView program, giving arbitrary gas flows (10-500 sccm and 0.1-1% hydrogen) for arbitrary times (Figure 71 D).

6.3.2. In Situ Measurements

The in-situ measurements produced two sets of data. A full spectrum from 1200 nm to 1600 nm was recorded before and after the coating process using a broadband tungsten halogen lamp for illumination. The second set of data consists of a record of the peak loss and wavelength corresponding to the $LP_{0,9}$ loss band during the coating process for a 0-~100 nm Pd coating. The results of two separate LPGs (LPG1 and LPG2) are presented here.

Figure 79 shows the transmission spectrum of LPG1 before and after the coating process. There is relatively little difference between the two spectra. The effective indices of the modes have only shifted slightly (to increased wavelength) with a decrease in the coupling coefficient (strength of coupling). By appealing to the mode coupling condition (Eq. 1) we note that this corresponds to a decrease in the effective index of the cladding modes, assuming that the core mode effective index is unaffected by the presence of the Pd. The dramatic decrease in coupling efficiency is more confusing as a small shift to the effective refractive index (as evidenced by the small

wavelength shift) should have little effect on the coupling efficiency although there is a shift to the mode profile.

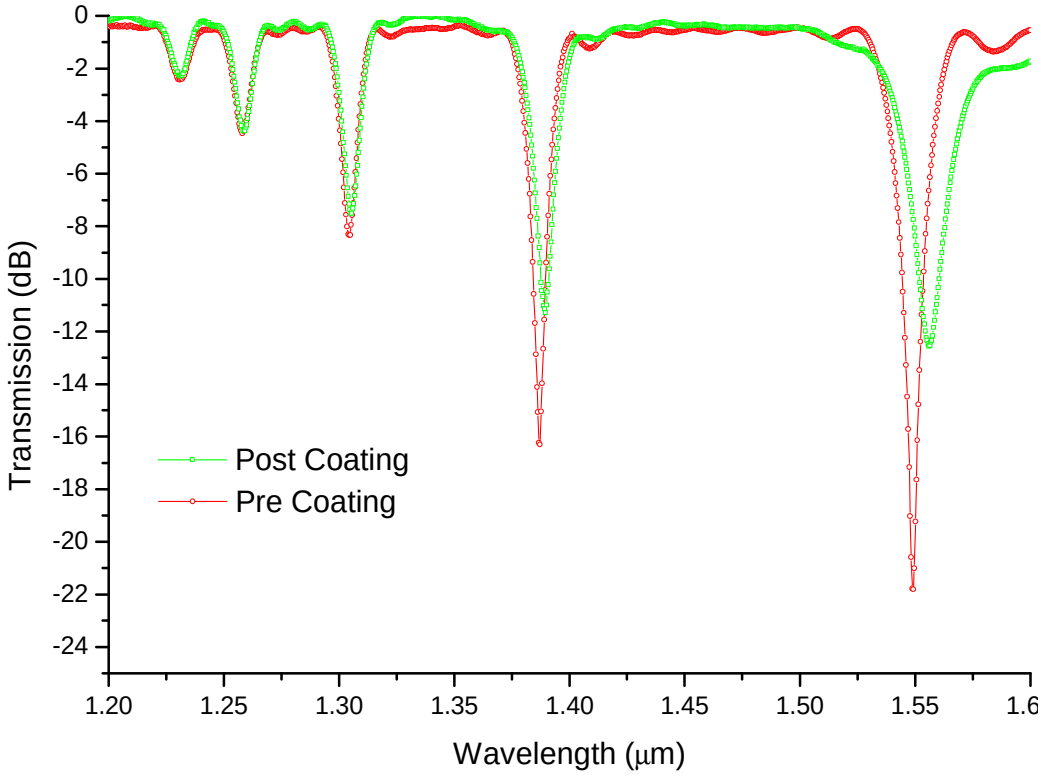

Figure 79: Plots of the transmission spectrum of LPG1 before and after ~100 nm of Pd is applied. Temporal noise in the background spectrum of the tungsten lamp has resulted in some dB distortion between the two spectra. The $LP_{0,9}$ loss band has shifted to a higher (+8 nm) wavelength from its uncoated position.

Figure 80 plots the data corresponding to the change in the wavelength and strength (maximum loss) of coupling to the $LP_{0,9}$ mode during the coating process. The wavelength data shows discrete shifts at various stages. There is a small shift as argon is allowed to enter the chamber (a), caused most likely by a temperature shift as the argon is stored outside the lab, slightly below room temperature. As the coating process begins (b) there is a rapid shift to the wavelength position over the first few seconds indicating that the majority of the optical change to the fibre occurs as a result of the first ~10 nm of Pd, as would be expected by the low penetration distance of the cladding mode evanescent field outside the fibre in the presence of a metallic jacket [36, 66]. After this initial rapid change there is a longer term, apparently linear, shift in the peak position throughout the coating process up to a maximum of 10.5 nm. Once the coating

plasma is turned off (c) there is a stabilisation of the wavelength position which is maintained until the chamber is vented (d). Venting the chamber (and returning the LPG to room temperature) results in a third shift in the wavelength to that recorded as the final coated spectrum (Figure 79) suggesting that this and the linear increase are temperature effects.

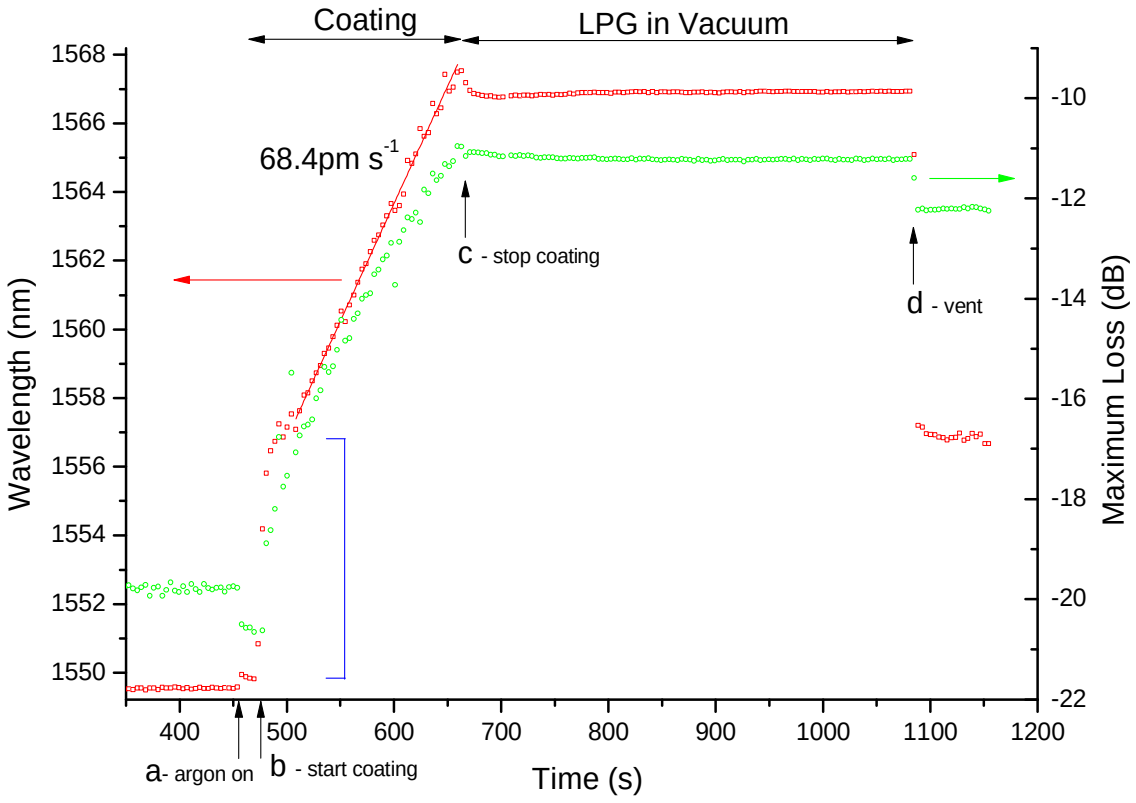

Figure 80: Plot of the amplitude (green) and spectral position (red) of the $LP_{0,9}$ loss band of LPG1 during the application of a 100 nm Pd coating. The temporal position of locations of interest are included: a) Turn on argon and motor b) strike plasma (begin coating), c) stop plasma, d) vent chamber. The significant shift at the start of coating (in blue) suggests the shift in spectral position due to Pd occurs entirely over the first 10 nm. The more gradual shift in spectral position (fitted in red) has been determined to be a temperature effect.

From §6.2.3 the approximate temperature coefficient of an LPG is expected to be of the order of 60 pm K^{-1} (cf. Measurement in §6.2.3). In Figure 80 the second component of the wavelength shift is of the order of 10.5 nm, corresponding to a temperature increase

of ~175 K a figure far higher than can be expected for RF sputter coating. This discrepancy prompted a further experiment to directly measure the temperature during the coating process by monitoring an FBG during the coating process. In this case the FBG was not strained to eliminate possible strain effects and effectively isolate the response as being a result of temperature. Figure 81 shows the recorded FBG peak reflection position as a function of the coating process.

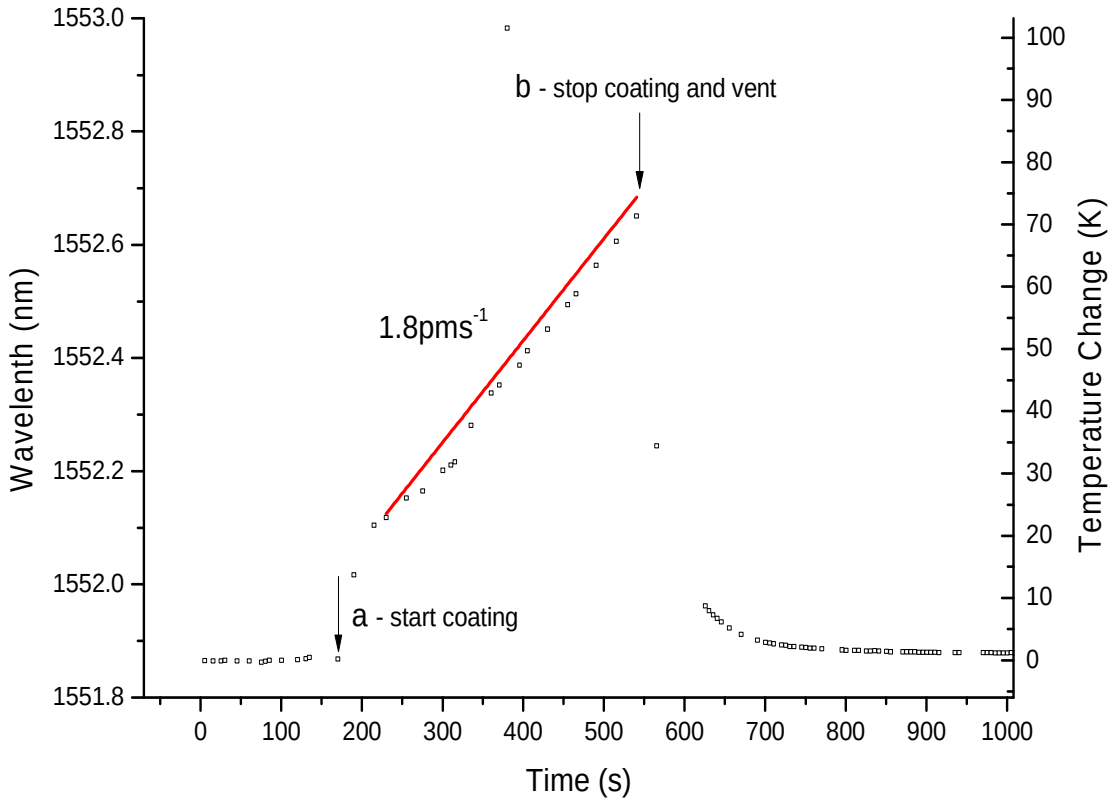

Figure 81: Plot of the recorded reflected wavelength of an FBG during the deposition of ~100 nm of Pd. Position a) coating start, b) coating end and vent chamber. The temperature has been calculated based on a coefficient of 11 pm K^{-1} with the rate estimated based on a linear fit to data (in red).

Again there are two distinct changes to the temperature, an initial rapid change followed by a longer term slow accumulation of temperature. Once vented the FBG returns to its initial spectral position, demonstrating that it is indeed a temperature effect. It is possible to estimate the rate of the longer term accumulation of temperature by fitting

linearly (Figure 81, 1.8 pm s^{-1}) and taking the value of 11 pm K^{-1} for the FBG as 0.16 K s^{-1}. This corresponds to a maximum temperature increase of the order of 20 K over the ~200 s coating time. The discrepancy between the reversible temperature based shift in the FBG and the LPG can be partially addressed by considering the fibre mount. In both cases the fibre has been mounted on an aluminium spit. In the case of the LPG the fibre is held taught (under low strain) across the spit in order to provide a clear transmission spectrum (to eliminate the effect of bending on the transmission spectrum). In the case of the FBG the fibre is held loosely in order to prevent the accumulation of stress during the coating process. In effect the LPG is exposed to the stress caused by the thermal expansion of the aluminium mount while the FBG is not.

The thermal expansion of aluminium is 23 x10^{-6} m m^{-1} K^{-1}. The strain coefficient of our LPGs has not been directly measured but can be calculated based on the theoretical model described in Chapter 5. Strain can be modelled as an increase in the length and the period of the LPG. One micro strain (1 με) corresponds to an increase in length of 1 μm over a length of 1 m. The period of the grating therefore changes to $\Lambda(1+\varepsilon)$, where ε is the strain. While the length of the grating also increases this has no impact on the spectral position of the loss band and can therefore be ignored for simplicity. The change in the spectral position of the fitted LPG from §5.4.2 as a function of several values of strain (ε) were calculated and tabled below (Table 3).

Period (μm)	Strain (mε)	Peak Position (nm)	Shift (nm)	pm $\mu\varepsilon^{-1}$
400	0	1548.96	0	NA
400+2/5	1	1550.545	1.584	1.58
400+4/5	2	1552.133	3.171	1.59
400+6/5	3	1553.722	4.761	1.59
400+8/5	4	1555.315	6.353	1.59

Table 3: Modelled effect of strain on the peak position of the $LP_{0,9}$ loss band of LPG1 based on the fitting parameters calculated in §5.4.2.

Over the range 0-4 mε the strain coefficient can therefore be seen to be almost linear. Taking the value of 1.59 pm $\mu\varepsilon^{-1}$ for the LPG and the figure of 23 x10^{-6} m m^{-1} K^{-1} for the expansion of aluminium we arrive at 36.45 pm K^{-1} for the strain effect of the aluminium spit. As the effect of strain and temperature are not interdependent in an LPG (strain gives a change in the period while temperature is a change in the optical properties of an LPG) the two effects can be added together giving a total coefficient of 105.07 pm K^{-1}. Assuming the same temperature gradient during coating of the FBG as the LPG this should result in a shift of 16.81 pm s^{-1} during the second phase of the coating process which does not compare well with the measured 68.4 pm s^{-1} suggesting that there is an additional, reversible, temperature based effect in the deposition process. The thickness of the Pd deposition (~100 nm) precludes the possibility of this being a purely optical change as the refractive index of Pd does not depend on the film thickness above ~20 nm (cf. §3.6) and the evanescent field of the cladding mode will not penetrate to this depth of film.

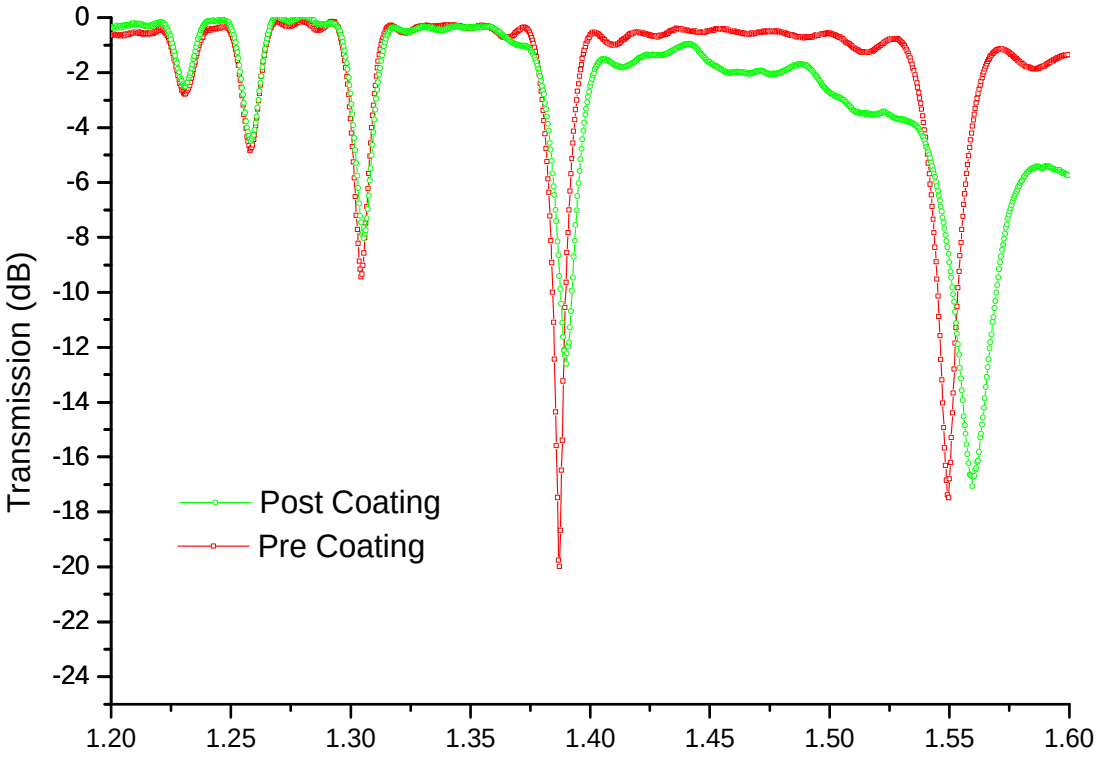

Figure 82: Plots of the transmission spectrum of LPG2 before and after coating. The after coating plot has incorrectly compensated for the tungsten background hence has an error in the transmission increasing with wavelength.

The changes to the amplitude of coupling are harder to analyse. Here there is again a rapid decrease in coupling as the coating process begins with a gradual decrease in coupling over the rest of the coating process. In stark contrast to the wavelength data this gradual decrease in coupling does not return on venting the chamber. It is unlikely to be a purely temperature effect as the fibres have been annealed up to 200°C (although an increase in temperature will have an effect on the coupling). As the fibre is held under strain (and increasing strain due to aluminium expansion) during coating it cannot be a result of bend losses in the LPG region and inspection of the LPG after coating rules out bend losses as a result of the spit movement in the input and output fibre leads.

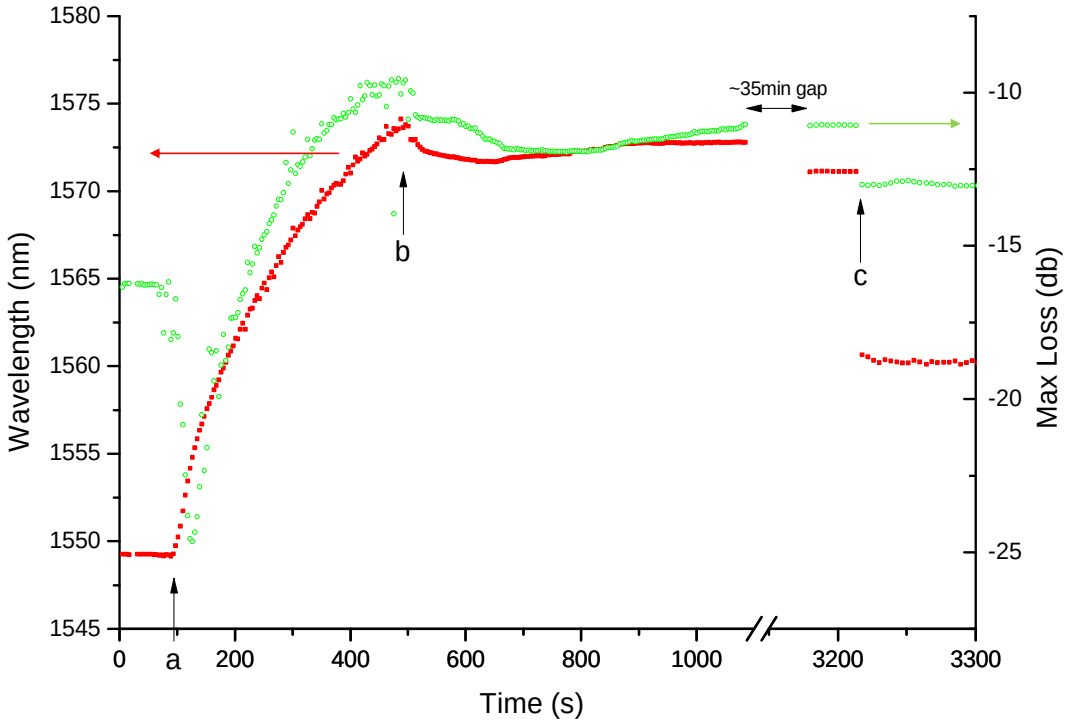

Figure 83: Plot of the amplitude (green) and spectral position (red) of the $LP_{0,9}$ loss band of LPG2 during the application of a 200 nm Pd coating. The temporal position of locations of interest are included: a) Turn on Argon and begin coating b) stop coating c) vent chamber. Note the break in the x axis – the LPG was left to settle for a half hour after coating but before venting. In this case the longer coating time (for 500 s) shows the non-linear increase in temperature more clearly.

Figure 82 & Figure 83 from the second LPG element (LPG2) demonstrate the same features (although in this case there is an issue with background subtraction of the tungsten lamp in the transmission spectrum). The decrease in the coupling efficiency of the LPG can therefore be characterised as a small change due to the change in the optical properties of the fibre (the rapid initial shift) combined with a longer term decrease, the result of an unknown phenomena in the coating process (neither optical, strain, temperature or bending) although it is clearly linked to temperature as evidenced by the similarities in the wavelength and amplitude curves in Figure 83.

6.3.3. Temperature and Concentration Effects on the Response to Hydrogen

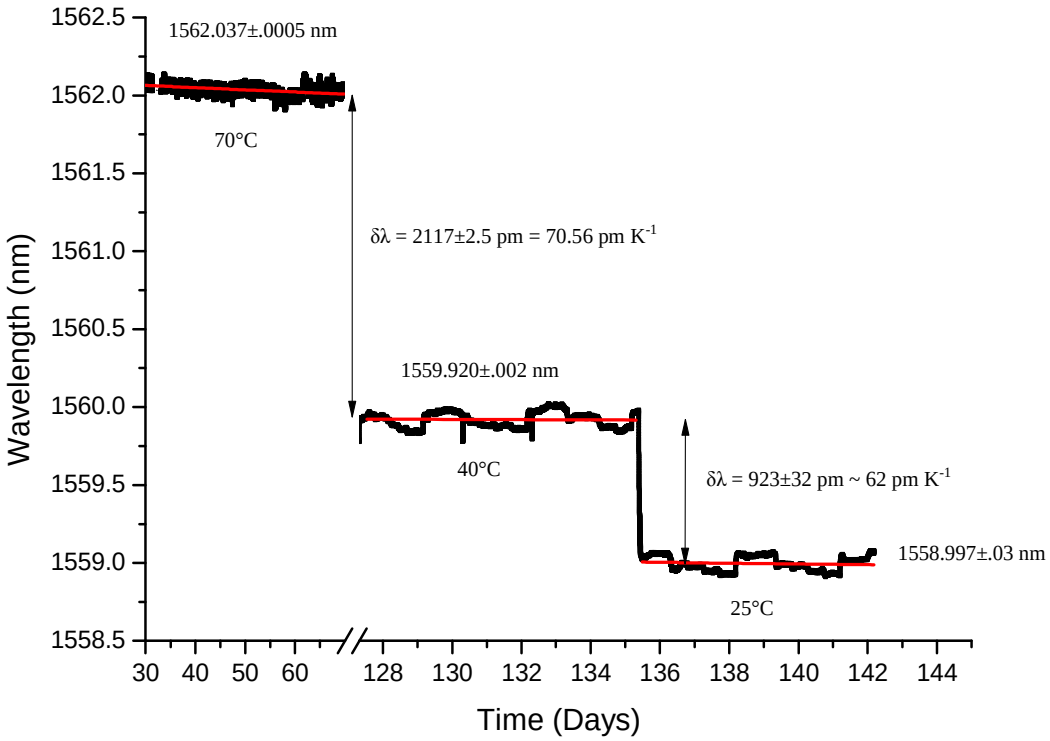

Figure 84: Plot of the response of LPG2 to changes in temperature. Data has been acquired over long term cycling between various levels of hydrogen and nitrogen at three temperatures (cycling is at too high a frequency to be visible on this timescale). A section of data from the centre of the set has been omitted for clarity.

After experiments, reported earlier in section (§6.3.2), a series of data was acquired cycling between 0, 0.25, 0.5, 0.75 and 1% hydrogen in balance nitrogen. At each stage the system was left sufficiently for an equilibrium to be reached before repeating the process. This response was recorded over three different temperatures 70°C, 40°C and 25°C in order to characterise the temperature response of the coated grating.

Figure 84 shows a selection of this data illustrating the LPG wavelength change due to temperature. In this case the mean reading at each of the temperatures has been used to characterise the temperature coefficient. The results here are clouded slightly by a background drift in the response over the time periods indicated. Nevertheless it is possible to extract a figure of 70.6 pm K^{-1} from the shift between 70°C and 40°C. The poor quality of the data at 25°C makes it harder to estimate the shift between 40°C and 25°C but it appears to be substantially lower suggesting the possibility of a non-linear response or an error in temperature measurement.

Additionally it is possible to examine individual cycles at each temperature for the response to hydrogen. The noise in the system is caused by fluctuations in the power of the ASE erbium doped fibre source used to interrogate the LPG, itself caused by temperature fluctuations in the lab. In particular it is possible to make out the ~10min cycle of the lab air-conditioning system in the spectral response – a fluctuation which is markedly lowered at weekends when the lack of foot traffic through the lab reduces the air conditioning workload. Unfortunately changes to the lab air-conditioning system increased this component of the noise in comparison to the earlier proof of principle experiments. Nevertheless it is possible to directly compare the results of a few individual cycles to ascertain the effect of temperature on the LPG-Pd response.

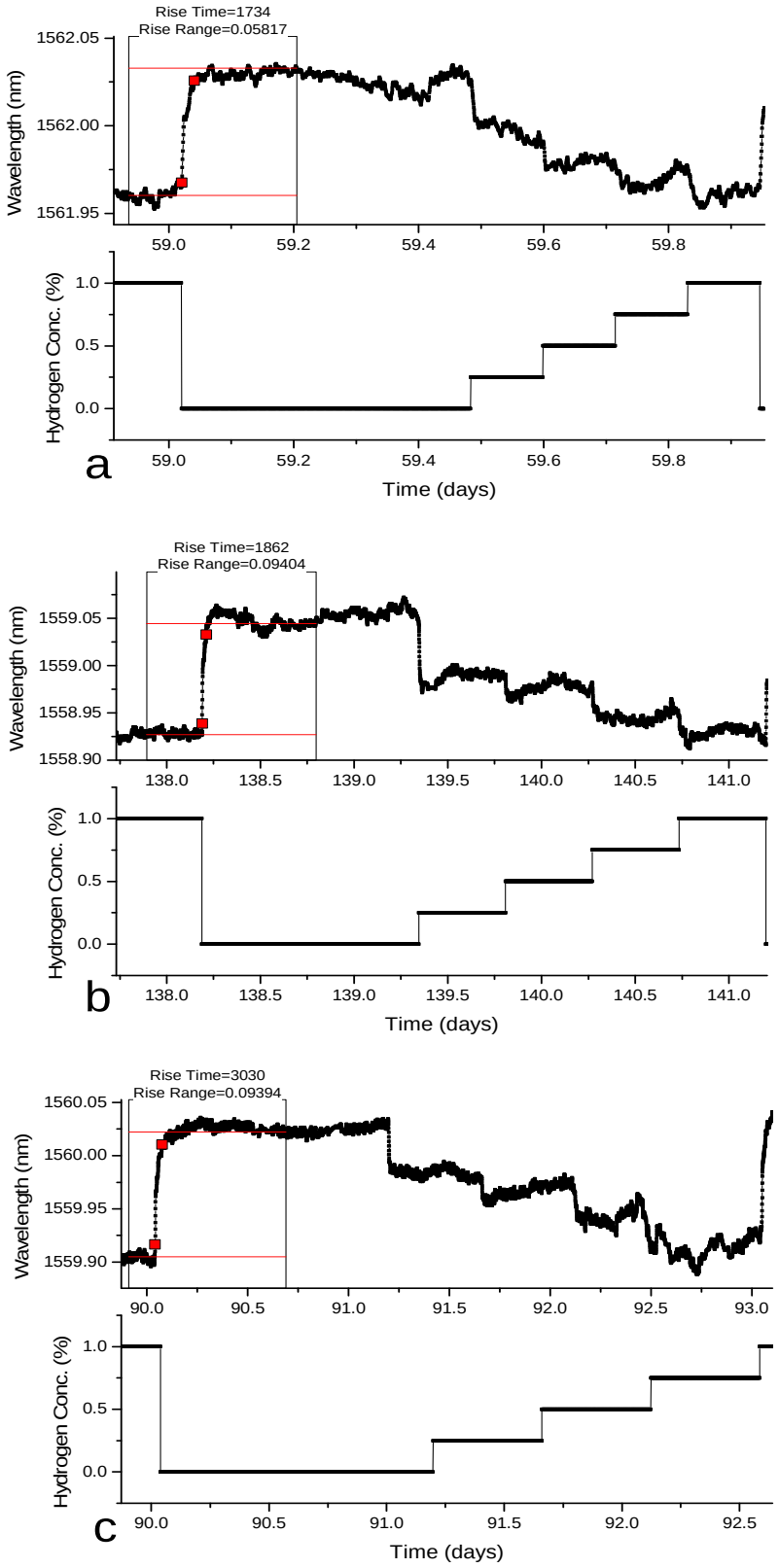

Figure 85: Comparative plot of one complete cycle of hydrogen levels at a) 70°C b) 40°C and c) 25°C. Note that the timescales are different for each example. An approximate rise time and delta (0-90) between 1% H_2 and 0% H_2 has been provided for each.

Figure 85 shows three example plots at 70°C, 40°C and 25°C. While one such dataset does not provide much quantitative data, qualitatively it is possible to see that at 70°C individual steps of 0.25% are close to being lost in the system noise while at 25°C and 40°C they are much clearer, illustrating an increase in response with decreasing temperature. It can also be clearly seen that the rise (or fall) time of each step increases with decreasing temperature.

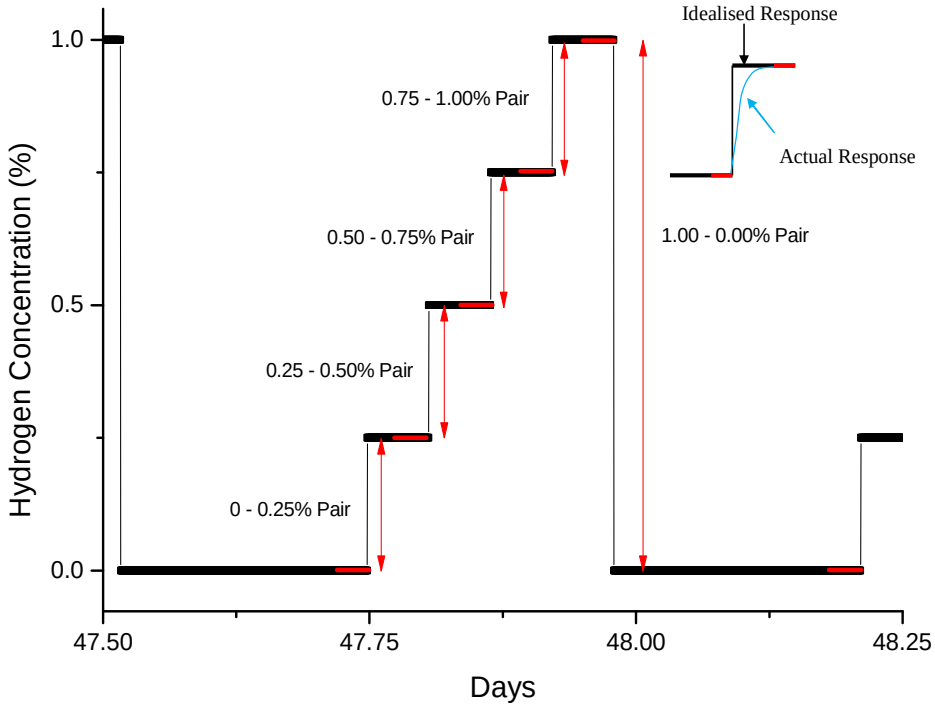

Figure 86: Illustration of the data processing system. A mean of wavelength is taken over the regions highlighted in red, shortly before a shift in concentration. These are then used to calculate the shift in adjacent pairs of concentration.

To gain a more useful quantitative insight it is necessary to statistically analyse the body of the data. This has been done at 70°C and 40°C respectively. The mean wavelength position is taken over 40 points immediately preceding a change to the hydrogen concentration. This ensures, wherever possible, that the system has reached equilibrium before a measurement is taken. Due to the background drift in the peak position it is necessary to calculate the change in the wavelength between adjacent concentration changes (Figure 86) in effect calculating each individual shift between 0%-0.25%,

0.25%-0.5%, 0.5%-0.75%, 0.75%-1% and 1-0% respectively. These data can be used directly or if summed provide a measure of the wavelength shift from 0% for each concentration. Figure 87 shows the derived statistical data illustrating the difference in scale of response for increasing temperature. Interestingly in this case the response appears to be linear over the range 0-1% in balance hydrogen in contrast to the earlier proof of principle experiments, this could be a result of the improved Pd coating techniques depositing a more homogeneous and purer Pd sample or may be indicative of the increase in thermal noise in the system.

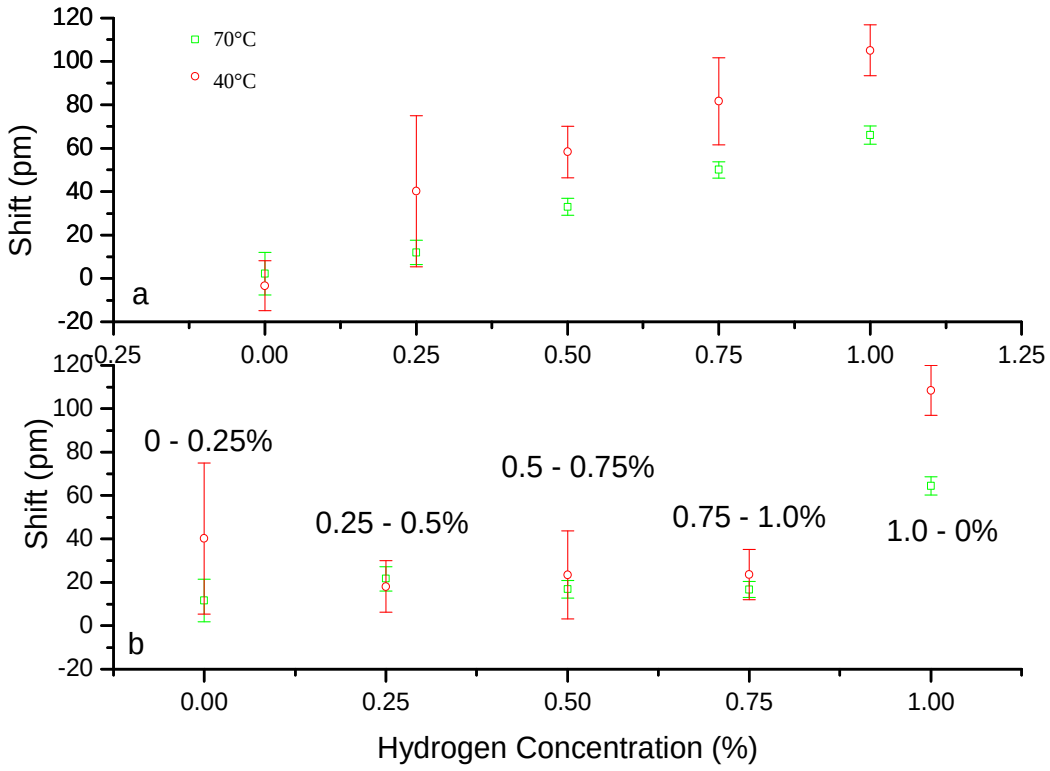

Figure 87: Plots of derived shift in peak position of LPG due to hydrogen. a) summed shifts for each concentration b) individual point pairs.

6.3.4. Long Term Monitoring

It is possible to see from the complete long-term data set (Figure 88) that the drift in the wavelength is reduced by an order of magnitude in comparison to the proof of principle experiments. This is to be expected due to the improvements in the Pd deposition technique underlining the necessity of ensuring a good coating quality for the use of this

form of sensor. While this may form an issue for long term (years) monitoring the relatively predictable nature of this drift should allow for it to be adequately subtracted.

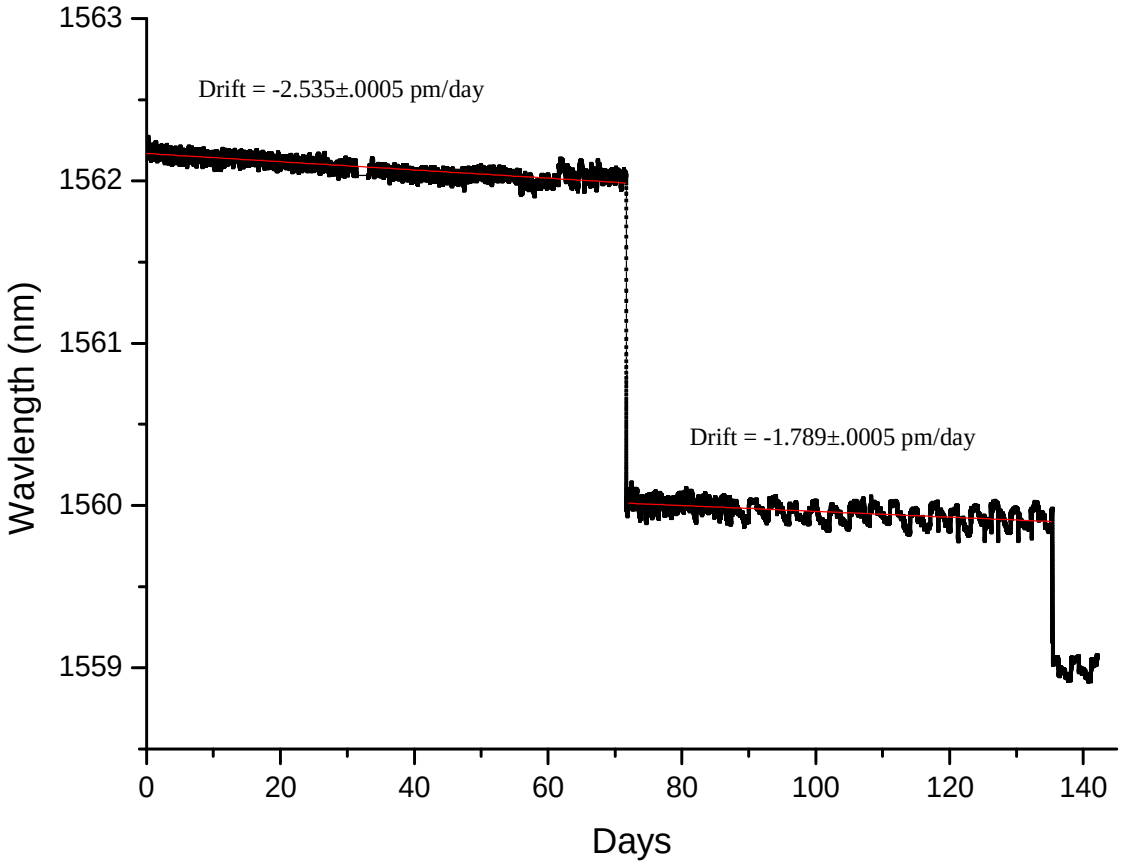

Figure 88: Dataset for LPG2 with linear fit to determine drift at 70°C and at 40°C, there is insufficient data at 25°C to attempt a fit (experiment is still ongoing).

6.4. Modelling of Metal Jacketed LPG

6.4.1. Mode Calculation

The change from total internal reflection to a mode confined through a reflective metal jacket makes it necessary to return to the LPG model to investigate its suitability. The model, from Erdogan [18, 21, 22], described in Chapter 5 is based on the work laid out in Tsao's Optical Waveguide Analysis [66]. It is worth considering each assumption or generalisation in turn in the case of a metal jacketed fibre.

The introduction of a metal layer to the outside of the fibre has no direct impact on the core mode of a standard fibre as even the evanescent field does not penetrate through

the cladding [36, 66]. However, depending on the coating technique and thickness of the coating, it is possible that the introduction of a metal layer may cause stress effects within the cladding. Such stress effects would clearly have a large effect on the cladding modes and with sufficient penetration into the fibre there is the potential for interaction with the core mode and therefore a change to the effective refractive index. In the case of our RF deposited 100nm Pd thin films we do not expect any interaction between the core mode and metal layer. The Pd is simply too thin and deposited too uniformly to introduce any overall or localised effects (cf. Chapter 3).

The cladding modes are, of course, altered as a result of the presence of the metal layer. Change in the external index of refraction will inevitably alter the mode field parameters and the effective refractive index. Not only this, but the mechanism of guiding has also been changed, from total internal reflection to a hollow metal waveguide like structure. The optics of hollow metal waveguides have been well studied in the past [138, 139] and the mathematics required to describe them are well documented. What is striking in this case is that there is such a small shift in the coupling wavelength (and therefore in the cladding mode effective index) as a result of depositing a metal jacket onto the fibre. This suggests that the difference between the metal and non-metal coated fibres is relatively small. This suggests that it may be possible to use Erdogan's formula to describe the modes with relatively minor alterations.

To evaluate this suitability we can return to the more general form of Erdogan's solution presented in Tsao (Chapter 9). Here it is interesting to note that the solution, an implementation of the scalar Debye potentials, is valid for any circularly symmetric three layer structure, including metal layers. As the Pd layer is homogeneous and flat it is reasonable to assume that there is no breaking of the circular symmetry therefore it is only necessary to justify the simplifications and assumptions made by Erdogan when producing his formula to ensure that the validity of a metallic solution has not been lost.

The first of which is in the assumption of the sign of the quantities $u_1{}^2$ and $u_2{}^2$ (Eq. 35 & Eq. 36). In general these could be positive, the assumption used by Erdogan, or negative. Physically a negative sign is caused by the effective refractive index of the cladding being higher than n_1 or n_2 respectively in other words (Eq. 76 & Eq. 77).

$$u_1{}^2 < 0 \; iff \; n_{ecl} > n_1 \qquad \textit{Eq. 76}$$

$$u_2{}^2 < 0 \; iff \; n_{ecl} > n_2 \qquad \textit{Eq. 77}$$

Mathematically this would require the substitution of the modified versions of the Bessel functions (I for J and K for Y respectively), and the inclusion of an additional phase term to cope with the imaginary u_1 and u_2.

It is not entirely possible to rule this out. As part of the mode field extends outside of the cladding into the metal layer it is conceptually possible that the effective index of the mode may increase to the point where it is higher than the cladding ($u_2{}^2 < 0$) or even core ($u_1{}^2 < 0$). Of course in reality what we see is that the effective index of the mode is actually decreasing as a result of the introduction of the metal (this gives a positive λ shift). As such it is impossible for the mode effective indices to become larger than the cladding and the choice of $u_1{}^2, u_2{}^2 > 0$ is still general enough for our system. Note that while the quantity $w_3{}^2$ does become negative this has no consequence to the form of the Bessel functions required for solution and does not raise additional difficulties in the mathematical treatment of the solutions.

Next is the choice of available cladding modes. An LPG will only couple between the core mode and the co-propagating radially symmetric modes ($LP_{0,v}$). A cursory inspection of the mode calculations for a hollow metal waveguide in the visible and near IR region demonstrates that these modes still exist [139]. There is no reason to suppose that the introduction of a metal layer will alter the basic coupling mechanics of the LPG. This is confirmed by the experimental observation that no mode disappears, and no mode is introduced within the 1200-1600 nm region (§6.3.2). It is therefore safe to assume that the $LP_{0,v}$ modes and only the $LP_{0,v}$ modes are required for a complete model, in particular we continue to ignore coupling with the higher azimuthal order $LP_{m,v}$ modes.

The remainder of Erdogan's assumptions are based on the LPG structure. In the case of the metal jacketed fibre it is safe to assume that there is no change to any of the assumptions of the LPG interaction for the same reason there is no change to the core mode; the core (coupling) region is too far removed from the cladding-external interface.

The final assumption is mine, that there is no coupling between the cladding modes. In effect the assumption that each cladding mode may be treated separately with no cladding to cladding coupling (cf. Eq. 74). This assumption is primarily based on the wavelength separation of individual cladding mode resonances. Although there may be some cladding to cladding interactions in the wings of individual resonances the amount of power in these regions is small enough that any inaccuracy introduced will be insignificant. The transmission spectrum after the introduction of the metal layer (Figure 79) demonstrates that this is still the case. In fact, cladding resonance positions are further separated as a result of the introduction of the metal layer.

A final consideration must go to the introduction of a complex index to the external layer. This has the effect of changing real variables to complex variables across the calculation. From a pure mathematical point of view this has little impact on the calculation but in a programming environment care must be taken to ensure that the variables are treated correctly. In particular the dispersion quantities $\xi_0'(\lambda)$ and $\xi_0(\lambda)$ (Eq. 28) will gain non zero real components, however the solution of the dispersion relation is still dependant on the imaginary components becoming equal (the real components will only tend to zero).

6.4.2. Fitting Modelled Transmission Spectra to Experimental Data

As the model outlined in Chapter 5 is applicable for the modelling of a metal jacket, subject to careful handling of complex quantities, it is possible to build the necessary simulation for one of the LPGs provided by the CGCRI, namely LPG1. n_1, n_2, a_1, a_2, and the LPG specifications are assumed to have not altered from the uncoated state while n_3 has altered to a metal layer with refractive index equal to that measured by ellipsometry in §3.6. By assuming that the metal layer is infinitely thick, i.e. above 70nm, then the three layer solution should accurately calculate the available modes and hence the transmission spectrum. Figure 89 shows the theoretical and measured data for LPG1. Of particular note here is that the LPG period has been modelled as slightly lower 398.5μm rather than 400μm in order to provide a more accurate fit. This is necessary because the LPG refractive indices were determined from the assumed period. As there is an error in this period, there is also an error in the derived refractive index of

the core. This becomes more apparent for the Pd coated LPGs as the miscalculation of, in particular, the core mode results in a shift in the LPG coupling position (Eq. 1). To compensate for this shift the modelled period of the fibre can be adjusted slightly. Evidence for a mismatch in the optical constants can also be seen by the incremental mismatch of the resonance position of the lower order modes in the plot.

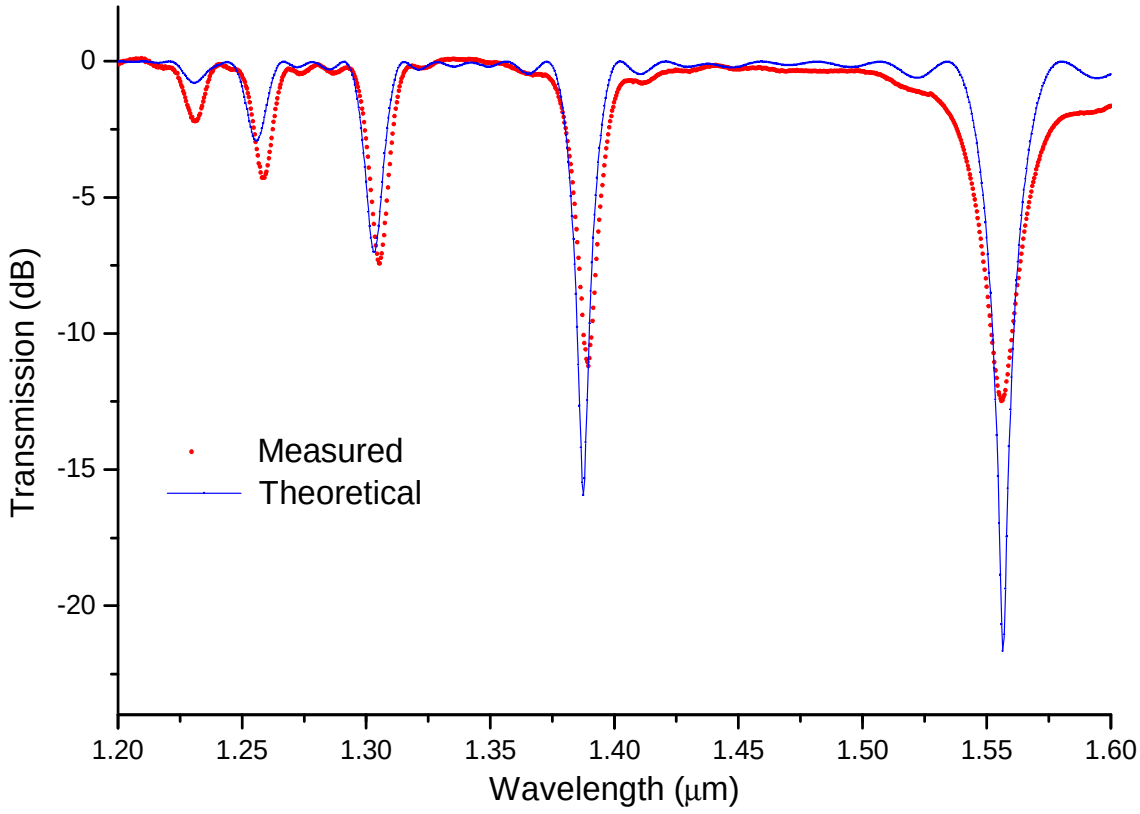

Figure 89: Plot of the modelled, blue line with points, and experimental, red points, transmission spectrum for CGCRI LPG element 2.4. Note that a 0.4 dB loss has been included due to measured connector losses in the measurement system. Fitted values for L and Δn have been derived via correlation analysis while the period, Λ, has been set at 398.5 μm.

Overall, however, the fit between theoretical and experimental data is quite good aside from the expected mismatch in coupling efficiencies. This was recorded in the in situ-measurements (§6.3.2) but does not seem to be caused by the optical presence of the metallic layer and hence would not be included in the model of the LPG.

6.4.3. Sensitivity and Higher Order Modes

The sensitivity of an individual mode to stimuli, particularly to external refractive index, is a difficult calculation. It is possible to derive sensitivity information by calculating the mode phase matching conditions (resonant wavelength) over a range of external indices but this is an extremely long and time consuming calculation. Observation of the mode matching conditions provides much of the required information at a fraction of the processing power and as such is a more convenient means of observing expected mode sensitivity.

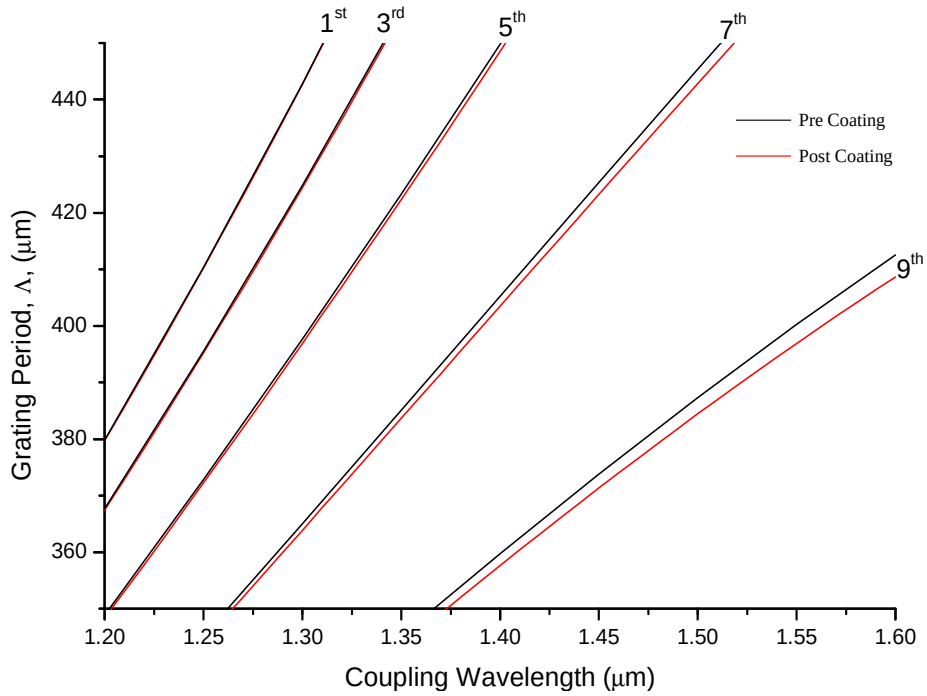

Figure 90: Plot of the phase matching condition for the first 5 odd ordered modes before (black) and after (red) the application of a 100 nm Pd layer.

Figure 90 shows the mode matching conditions for the first five odd ordered cladding modes between 1200 and 1600 nm and over a range of grating periods of interest. Here the gradient of the curve can be seen as analogous to the mode sensitivity – a lower gradient will result in a larger wavelength change with a change in grating period (or any other change to the LPG including external index) and therefore a higher sensitivity. The plot indicates that with increasing mode order there is increasing sensitivity, this

relates directly to the observation that I was unable to measure any change to the $LP_{0,1-0,7}$ modes with hydrogen absorption and only a small change in the $LP_{0,9}$ mode (cf. §6.2.2).

It is also interesting to note that the presence of a metal jacket does not significantly alter the mode matching conditions of these modes – although there is a shift to higher wavelengths and a small increase in sensitivity. As the response of the $LP_{0,9}$ mode to hydrogen is extremely small (~60 pm shift for 1% H_2) it is logical to assume that increasing the mode order further will result in an increased sensitivity. Indeed by increasing the mode order sufficiently it should be possible to access modes exhibiting a mode match turning point – i.e. maximum sensitivity due to the low gradient at a turning point (c.f. §2.1.5) [49].

To access these higher order modes over the same wavelength range it is necessary to decrease the grating period. Figure 91 shows the mode matching conditions, calculated for a Pd jacketed fibre identical to LPG1, for the 10^{th}-21^{st} order modes. These modes have been selected as they exhibit turning points within the 1200-1600 nm region. For completeness the even order modes have also been included since the coupling coefficients are small, but non-zero (cf. Figure 94). Note that the calculation of the even order modes is incomplete in the presence of the Pd layer. These modes have only a very small effect on the dispersion relation (cf. §5.2.3) and as such are much harder to find requiring a much higher resolution simulation than time allowed.

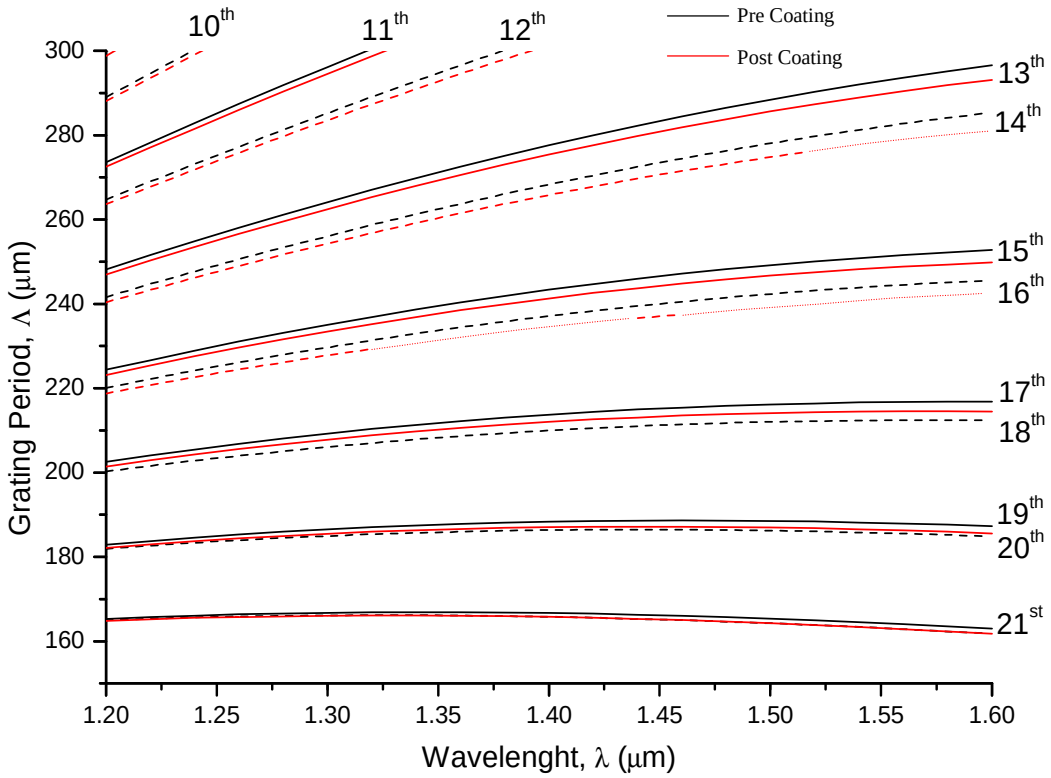

Figure 91: Plot of the calculated coupled mode positions for the 10th-21st order modes at the mode turning point for a bare LPG (black) and for an LPG coated in Pd (red). Even and odd modes are alternated in solid and dashed lines for clarity. The 17th and 18th order modes give a mode turning point at ~ 1550 nm for a period in the region of 215 μm. Note that there are some gaps in the even order lines (filled by dotted red line) caused by too low a resolution in the calculation of the cladding modes.

Due to the shallow gradient of these modes it is reasonable to expect that they should all exhibit sensitivity dramatically larger than the $LP_{0,9}$ mode. As discussed in §2.1.5 the presence of the turning point allows for double coupling, i.e. a single mode can couple to two wavelengths simultaneously. A zoomed in plot of the 17^{th} – 21^{st} odd order modes (Figure 92) shows the mode turning point decreasing in wavelength as the mode order increases (dashed red line Figure 92). This provides the opportunity to perform three forms of sensing. With a period lower than the turning point the mode will couple to two wavelengths simultaneously [140]. Either of these wavelengths could be monitored as a highly sensitive device. Alternatively as the separation of these wavelengths increases with decreasing period it is possible to inscribe a period ~4 μm lower than the mode match position and use the two resonance peaks to double the

sensitivity with a differential measurement [140]; they will move in opposite directions with a change in external index (Figure 92). The third possibility is to inscribe a period just above the mode turning point. Here the resonant wavelength will not change with external index but rather the coupling efficiency will decrease as the mode moves further from the coupling conditions [50]. This provides an intensity based sensor with a single central wavelength of interest.

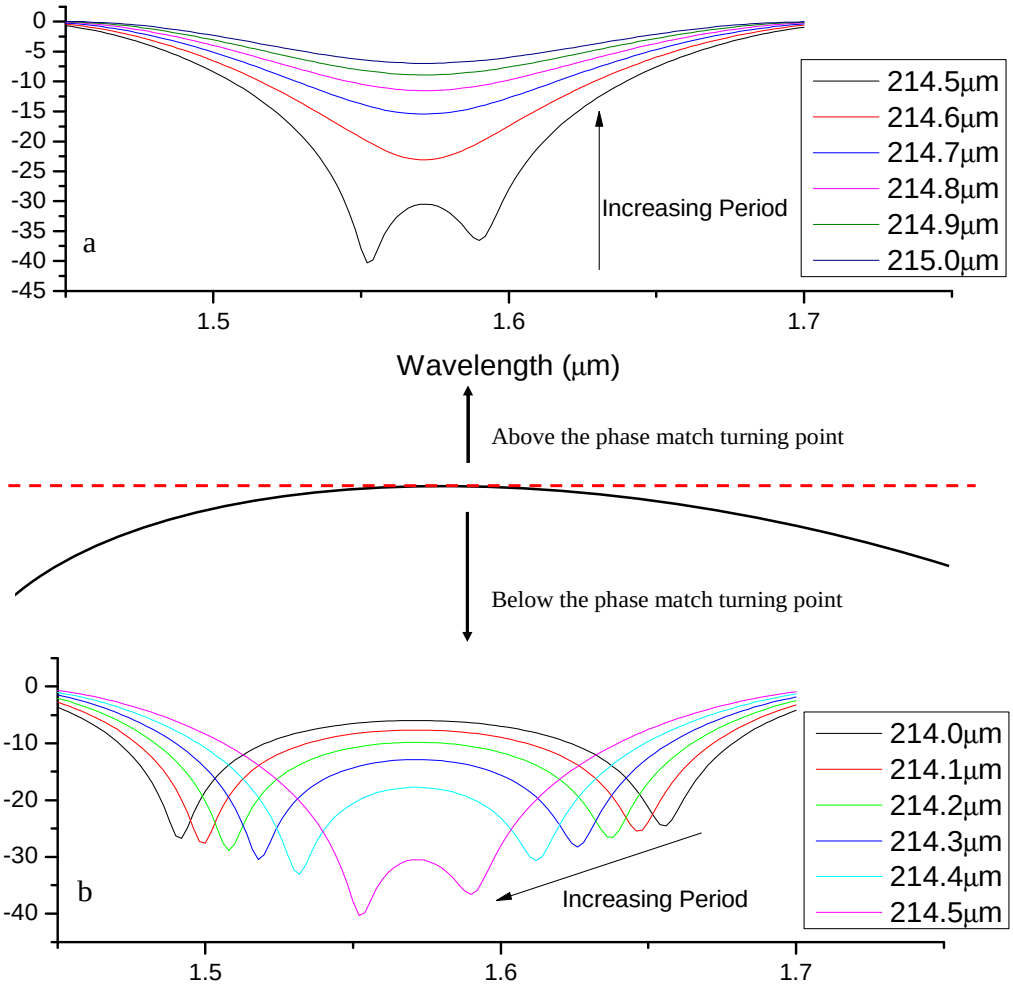

Figure 92: Plots of the transmission spectrum of the 17th order mode with various periods a) above the mode turning point and b) below the mode turning point .

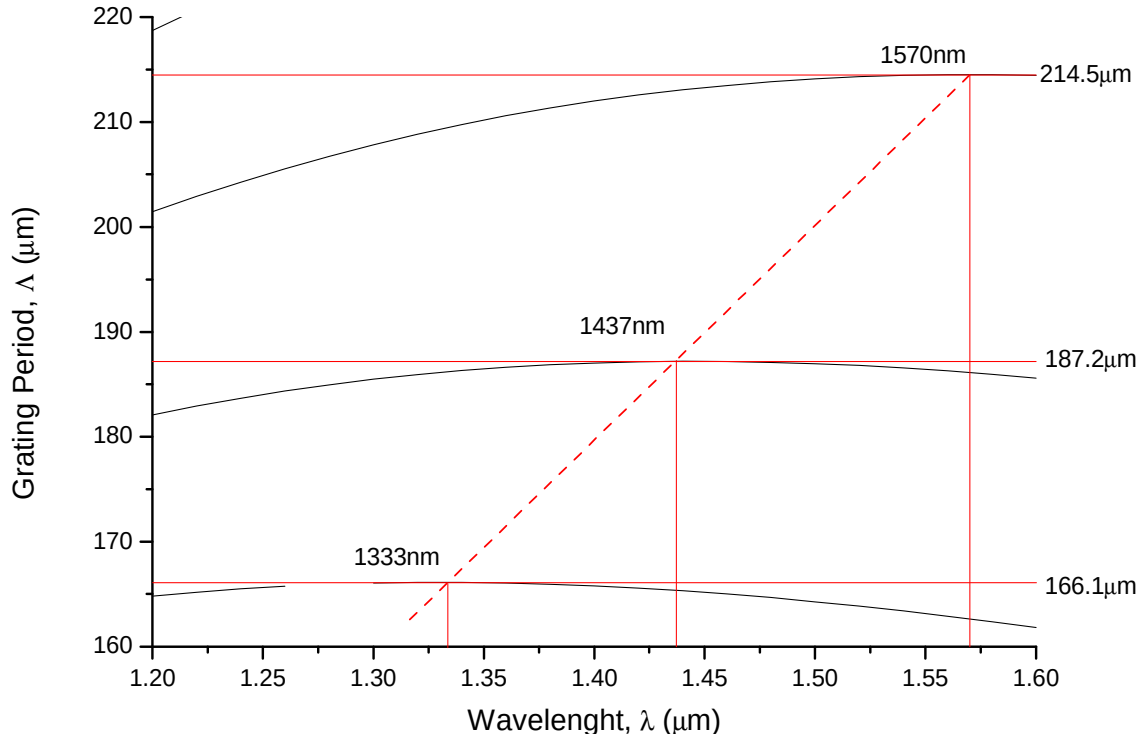

Figure 93: Zoomed in plot of the 17th-21st odd order modes illustrating the decrease in wavelength of the turning point with mode order (red dashed line).

The caveat with using such a system is that the mode matching profiles are extremely flat. There is therefore relatively little margin for error in the period to be inscribed. In addition the phase matching conditions before and after coating are not the same (Figure 91). It is necessary to monitor the LPG transmission spectrum in a different wavelength to the one required after coating in Pd, a problem which is discussed in more detail in the following chapter.

The mode matching profiles, while useful, do not provide the complete picture. These only provide information on the central coupling wavelength there is no information on the strength of the resonance and hence how easy it would be to interrogate a mode. This information is provided by the coupling coefficients. Figure 94 gives a plot of the first 60 modes for a metal jacketed fibre identical to LPG1. The form of this plot is very similar to the non-metal jacketed case (§2.1.5). Here we can see that at low mode orders there is little or no coupling to the even order modes and that the overall shape has a periodic function with a maxima in coupling coefficient between the 7th-19th orders. This suggests that, with the correct choice of grating length, there should be

strong coupling and hence a deep loss band due to these modes. Calculation of the even order modes above order 12 is extremely challenging as the dispersion relation displays little or no modification by these modes (cf. §5.2.3). As a result the even order coupling coefficients have only been displayed up to the 12th order, however we can assume that the higher order modes will display the same general form as the uncoated case (§2.1.5 Figure 11). Within the region of peak coupling the even order cladding modes exhibit significantly lower coupling although this increases with mode order. This combined with the mode wavelength separation (Figure 91) suggests that the < 21st order modes should exhibit low or zero cross talk. At higher orders the wavelength separation decreases and the even order mode coupling coefficient increases suggesting significant cross talk between these modes and making them inadvisable for sensing use. In order to access these higher coupling efficiencies, however, it will be necessary to calculate the transition spectrum more formally and investigate the effect of the length of the LPG.

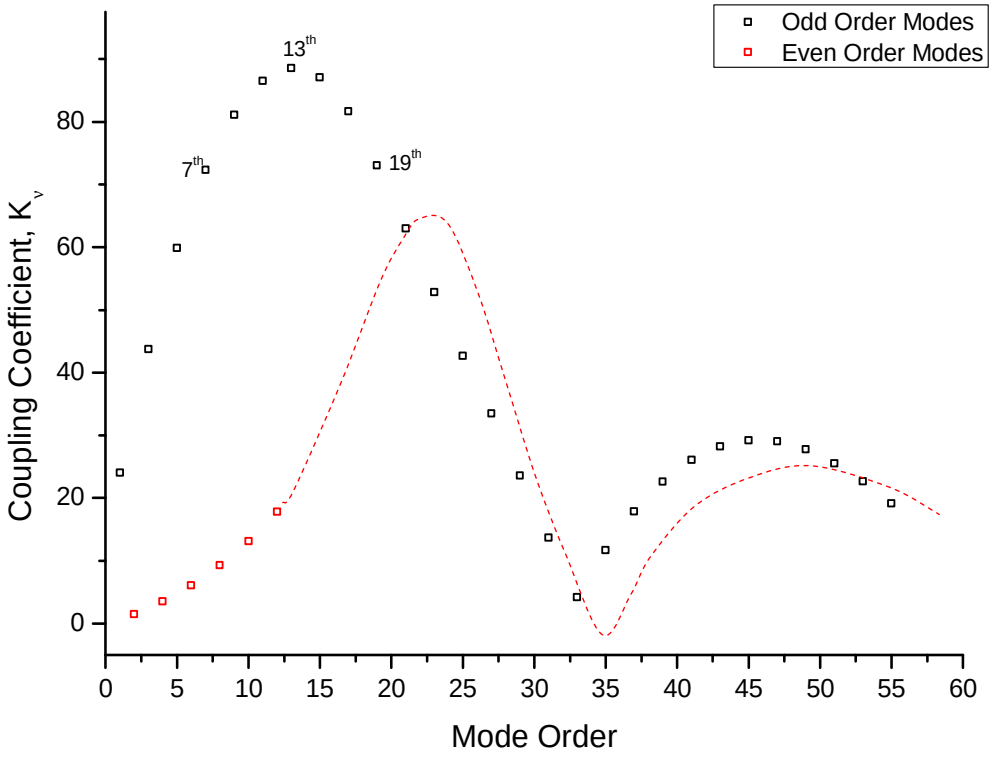

Figure 94: Plot of the coupling coefficients of the first 60 modes for a metal jacketed fibre identical to LPG1. The red dashed line signifies the expected form (based on the uncoated fibre mode coupling) of the missing even order modes above 12th.

Figure 95 shows the transmission spectrum of the 17th order mode with a range of lengths. Here we can see that we can preferentially couple to one or other peak by increasing or decreasing the length of the LPG. In a double coupling arrangement it is preferable to have roughly equal coupling and as such a length of 23.125 mm is optimal. This then provides the last piece of information required to specify an ultra-sensitive LPG-Pd sensor operating around the mode turning point. An LPG with a period (Λ) of 214 μm, a length (L) of 23 mm, a maximum index change (Δn) of 3.2 $x10^{-4}$ RIU and a sinusoidal profile will, theoretically, provide optimal sensitivity in the 1500 nm region.

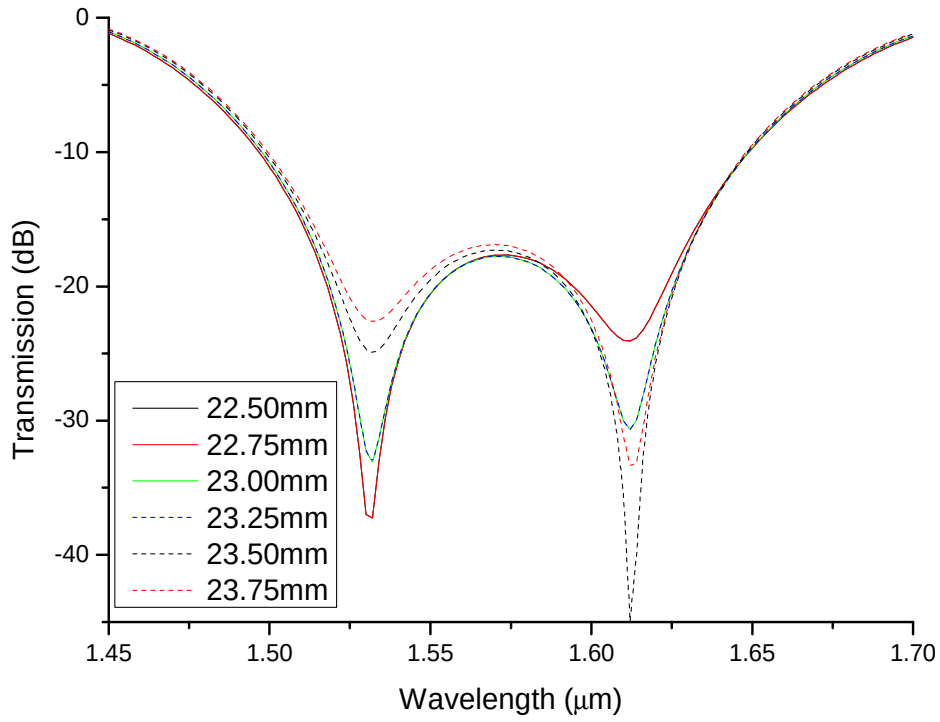

Figure 95: Calculated metal clad transmission spectrum for the double resonance 17th order mode (214 μm period) coupling around 1550 nm over a variety of grating lengths.

6.5. Conclusions

The results of the experiments outlined above demonstrate that it is possible to monitor the absorption of hydrogen into a Pd coating through the change to the resonance position of the cladding modes. The results, particularly the long term drift, highlight the necessity for careful calibration of the coating process to ensure a flat homogeneous

layer. With poor quality coatings problems with surface adhesion have been encountered leading to delamination on timescales of the order of days. With improved lower energy deposition the delamination, while still present, is reduced by an order of magnitude. There is, however, one outstanding issue with the coating process. There is a decrease in the coupling coefficients of the modes during the coating process. Neither the experimental nor the theoretical data supports this as being a consequence of the optical change in the external (n_3) layer nor does it appear to be a function of strain, stress or fibre bending. Most likely this is caused by some form of secondary temperature effect – as the LPGs have been annealed to 200°C it cannot be as a result of the fibre bleaching with increased temperature.

The response as a function of hydrogen deposition requires further investigation. The initial, proof of principle experiments demonstrated a non-linear response in the 0-1% range while the later experiments displayed more of a linear response. This may well be the consequence of the improved coating technique, with the island like structures of the earlier experiments giving a non-linear absorption distribution while the later experiments provide a smooth absorption of hydrogen.

The theoretical model of the LPG system provides a good agreement to the experimental. However there are issues with the optical constants and assumptions regarding the periodicity of the LPGs which give relatively large margins of error for the modelling. This is particularly true for the modelling of the higher order modes, an error of as little as 1 μm in the periodicity results in a change to the resonant position of 70 nm, to say nothing of the error due to the assumptions of the fibre refractive indices. The mode matching conditions for the first ~ 25 modes have been investigated and the sensitivity, within the 1200-1600 nm region has been found to increase with mode order. The 17^{th}-21^{st} order modes exhibit phase matching turning points giving a maximum sensitivity (up to 20 times that of the $LP_{0,9}$ mode). Combined with the plots of coupling coefficient, where the odd order 17^{th}-21^{st} modes are close to maximum and the even order modes are close to zero maxes these modes an attractive possibility for LPG-Pd hydrogen sensing. This must be tempered by the limitations of manufacture and modelling, an issue which will be more thoroughly discussed in the following chapter which pulls together all information in the thesis and discusses the viability of the use of LPGs for hydrogen sensing.

Chapter 7. Conclusions

A palladium coated LPG makes an attractive prospect as a hydrogen sensor.

Many of the difficulties in characterising the complex metal jacketed LPG system have been addressed including:

- Characterisation of our Pd deposition technique (RF sputter coating) has been carried out and significant deviations between the optical properties of our thin films and the (widely varying) literature values have been found
- The effect of absorption of hydrogen on the complex refractive index of Pd have been directly measured for the first time showing discrepancies between these data and published assumptions
- The modelling of metal jacketed LPGs including the development of a full analytical model of an LPG with a metallic overcoat demonstrating higher order cladding modes with a phase match turning point and therefore higher sensitivities to hydrogen
- Studies on the effect of Pd coating quality on long term stability and hydrogen response (drift) have been carried out resulting in an improvement of an order of magnitude
- Direct measurement of LPG refractive index profile along the axis of the fibre has been attempted and the partially successful results indicate that the proposed improved technique should provide the required resolution. This is to be achieved with the continued collaboration between the CGCRI and ourselves turning the QPM proof of principle results presented in this thesis into a useful characterisation tool

There are outstanding issues to address to allow the system to operate to its best potential

- An attempt should be made to couple to the higher order, more sensitive cladding modes. At present the inscription setup at the CGCRI is unable to inscribe short periods of the order of 200 μm, however following a significant redesign this should be possible
- The exact refractive index changes in Pd as a function of hydrogen need to be further investigated either by ellipsometry or with a redesigned SPR system designed to minimise surface contamination of the Pd

LPGs are a complex system responding to stress, strain, temperature, vibration, bending, and external refractive index. Even in an idealised system, isolated from unwanted interference the transmission spectrum of the LPG is difficult to understand as the interaction of multiple resonance conditions which depend on the grating period, the grating length, index contrast between core and cladding, the wavelength, the external index (i.e. the environment) and the grating refractive index perturbation profile all play their parts. With the introduction of a metal layer, like Pd, the already complex LPG system becomes even more difficult to characterise.

The increased understanding of the mechanics of our RF sputter coating technique for the deposition of Pd films has been a major step forward in the characterisation of the Pd-LPG system. The results of the ellipsometry analysis (§3.6) underlines the importance of ensuring that thin films of Pd are well characterised and not to rely solely on published library data. In addition the results presented in (Chapter 6) underline the importance of a well characterised coating technique. Without a flat homogeneous coating many of the assumptions essential for the analysis of the LPG-Pd system are invalid.

The measurements of the optical properties of Pd as a function of hydrogen absorption require some clarification. In particular there is discrepancy between the results in regard to the linearity of the optical change in absorbing 0-1% H_2. Here the proof of principle experiments (§6.2) suggest a non-linear response, although this may be a result of inhomogeneities in the Pd deposition. The results from the surface plasmon resonance (SPR) (§3.7) and characterised gratings (§6.3) suggest more of a linear change within this range although here the quality of data is insufficient to be definitive. The results suggest that the real and imaginary components of the refractive index are both decreased on exposure to hydrogen, as has been assumed in previous publications, but not equally, which was not previously assumed.

The relatively large differences in the measured permittivities of the deposited Pd layers as measured by SPR experiment suggest that the technique is simply too sensitive to surface quality to be of practical use. Should the experiment be reproduced a significant redesign of the apparatus will be necessary. In particular extreme measures must be taken to prevent surface contamination. Plastic tubing should be replaced with metal and a bake-out regime may be required to purge all contaminants from the system prior

to use. The purity of the gases in this case is not thought to be an issue. The angular resolution and accuracy can also be further improved by including a low tolerance (10' at most) gearing system to automatically move the detector at twice the rate of the prism during rotation. This would help considerably in addressing issues in reproducible measurements of the transmitted power as a function of detector angle. A motorised stage for the prism would also be a considerable improvement, decreasing measurement times (and therefore limiting the system noise further) as well as improving accuracy in the angular positioning of the prism. The extremely broad surface plasmon resonance of Pd cannot be helped however and this is liable to be a limiting factor in the accuracy of this measurement technique.

The theoretical model for the calculation of the transmission spectrum of the LPG is a potentially powerful tool. The calculation of the transmission spectrum of a bare uncoated fibre shows good agreement between experimental and theoretical data (§6.4.2), limited only by the accuracy of the optical characterisation of the LPG. Appling the theoretical model in the presence of a Pd layer to design an optimal sensing element should thus be regarded with some caution. The theoretical model outlined in (Chapter 5 & §6.4) should be regarded as a close approximation due to the lack of verifiable measured data concerning the specifications of the LPG.

The spatial dimensions (i.e. radii) of standard telecoms fibres are well documented and can be considered to be accurate enough for modelling as the UV inscription and coating processes will not change these dimensions. The refractive index of the fibre core and cladding are a different matter. The fibre cladding has been assumed to be pure fused silica – which for an SMF-28^{TM} fibre should be an accurate assumption. As there are no Ge-O or Ge-Si sites in the cladding region it will be unaffected by the UV writing process although there is a temporary change to the refractive index due to the hydrogen loading of the fibre. Post inscription annealing should effectively eliminate any residual hydrogen from the cladding (and the core) and it will return to the well characterised refractive index of fused silica.

The core of the fibre is doped with germanium. The exact doping concentration, and - or the resultant refractive index is not provided by the manufacturer. While it would be quite possible to directly measure the optical properties of the core of an SMF-28^{TM} this would not necessarily provide the required information. The LPG UV

writing process can include the introduction of a dc component within the core, on which the actual ac grating resides. Furthermore the annealing process again changes the core refractive index. The measured refractive index of the core of an SMF-28 ^{TM} is therefore not the same as the core of an SMF-28 ^{TM} with an LPG written into it. This makes a considerable difference to the modelling of the effective index of the LPG modes. This primarily affects the core mode as the majority of the power is in this region. But the effect on the cladding modes should not be underestimated. As the coupling occurs as a result of the mode field overlap, which is almost exclusively in the core, accurate determination of the core refractive index is important to calculate the coupling coefficients. Additionally the wavelength of the coupling resonance between modes is dependent on the difference between the core and the cladding effective indices.

In this thesis the optical properties of the LPG have been determined by using this 'difference' relation. In effect the optical properties of the core have been calculated from the period of the LPG. This provides the single largest source of error for the modelling process. There will inevitably be some error in the inscribed period, which will have a knock on error in the core index, the effective indices, the resonant coupling wavelengths and the coupling coefficients. In short every part of the simulation. In the case of the LPGs manufactured by the CGCRI the period error in writing is determined by the size of the slit used for illumination and the accuracy of the positioning system for the slit (it is a multi-pass irradiation system, a misalignment between passes will result in a change in the period). Even assuming that these errors can be minimised there is still some uncertainty in the actual LPG period due to the fibre being held under strain during the wring process. Once released from the writing process the fibre will contract slightly, shortening the period (e.g. 500 με will increase a 400 μm period by 0.1 μm). Measured strain in the fibre during inscription is 606 με and as such a significant shift to the period is not expected although it does add to the uncertainty. In theory this could be managed by carefully measuring the level of strain in the LPG during the writing process, but this would require some significant redesign of the fibre mounts. Finally it is reasonable to assume that the absorption of UV in both the core and cladding regions will increase the temperature of the fibre. The resultant thermal expansion will decrease the strain on the fibre bringing further complication to the written period.

All of which combines to give an LPG inscription process where the period of the fibre is likely to be inscribed with, at best, an accuracy of ±0.1 μm. As this is a multi-pass system there is also the possibility that this error will be between individual periods which will give rise to apodization like effects in the transmission spectrum. The finesse of using a 200 μm slit to inscribe a 400 μm period is also a possible issue. It is simply not possible to inscribe a true sinusoid or square wave with this system. What is worse is that these errors are likely to be non-systematic i.e. that in attempting to inscribe a series of identical fibres the period of each will be different. That being said there is less scope for error in the maximum perturbation within the fibre, the strength of the grating. Provided that the pulse time and power of the UV source is not altered and that each period is made of the same number of passes there is little scope for an error in the total refractive index change.

With the inclusion of the metal layer into the model there is the potential for further error due to the error in the refractive index of the Pd. The lower order odd modes (1-9) demonstrate a reasonable fit between experimental data and theoretical model but there was a significant discrepancy once the Pd layer was included. It was necessary to alter the period of the LPG by 1.5 μm (400 μm to 398.5 μm) to correctly align the position of the $LP_{0,9}$ loss band – a process which suggests that there was an error in the period of the fibre which has been exacerbated by the inclusion of the Pd layer. This is certainly a direct result of assuming, incorrectly, that the quoted period of 400 μm was 100% accurate. As the mode order increases so too does the sensitivity and as a result the impact of any error in the LPG specifications. At higher order modes it is reasonable to expect that there will be a more significant discrepancy between theoretical and experimental data.

The intended use of an LPG, with a metal jacket, also has an impact on the inscription process. At present, the CGCRI fine tune the inscription by attempting to match the spectral transmission to an expected theoretical profile. In the case of a Pd coated LPG the spectral profile during this wring process will not correspond to the final spectral profile after the application of the Pd layer. As the difference between the transmission spectrum before and after coating increases with mode order it is reasonable to assume that this will be exacerbated for the higher, more sensitive modes. This effectively means that it is necessary to calculate two transmission spectra, one for the uncoated LPG and one for the coated LPG. Fortunately the shift in the spectral position is not

significant enough to move the mode outside of the 1200-1600 nm region. It is therefore possible to monitor a mode at a lower wavelength during the coating process with the expectation that it will shift to increased wavelength after Pd deposition (Figure 97).

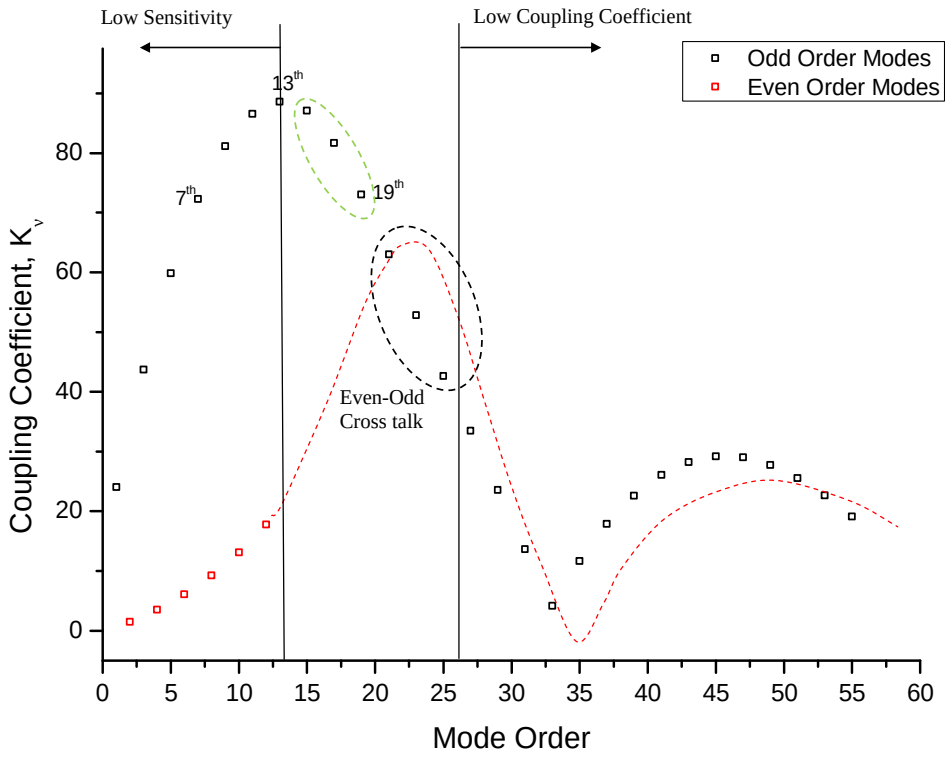

Figure 96: Reproduction of Figure 94. Plot of the coupling coefficients of a Pd coated LPG at 1550 nm similar to LPG1. Only a few even order modes have a high enough coupling coefficient to be of practical use but these will interfere with nearby (in wavelength) odd order modes. Odd modes above 23rd order have low coupling coefficients, modes below 15th order have low sensitivity. The 21st-26th order modes have even-odd order cross talk limiting useful devices to the 15th, 17th and 19th order modes (green ellipse).

The sensitivity of the mode is not the only criteria for selection it is also necessary to consider the effect of the coupling coefficients. Figure 96 reproduces the coupling coefficient data presented in §6.4.3. A highly sensitive mode with a low coupling coefficient can be considered to be useless as it will be too challenging to monitor the peak loss position. We can therefore consider that only the 7th-13th order odd modes are

worth consideration for a sensor based on the maximum in coupling coefficient. Furthermore from the phase matching conditions we can see that the modes below the ~13th order have low sensitivity. Lastly we have noticed that the decreasing wavelength separation between odd and even order modes above the 19th order – and the increasing even order coupling coefficient renders these modes unsuitable due to cross talk. This leaves only the 15th, 17th and 19th order (odd) modes.

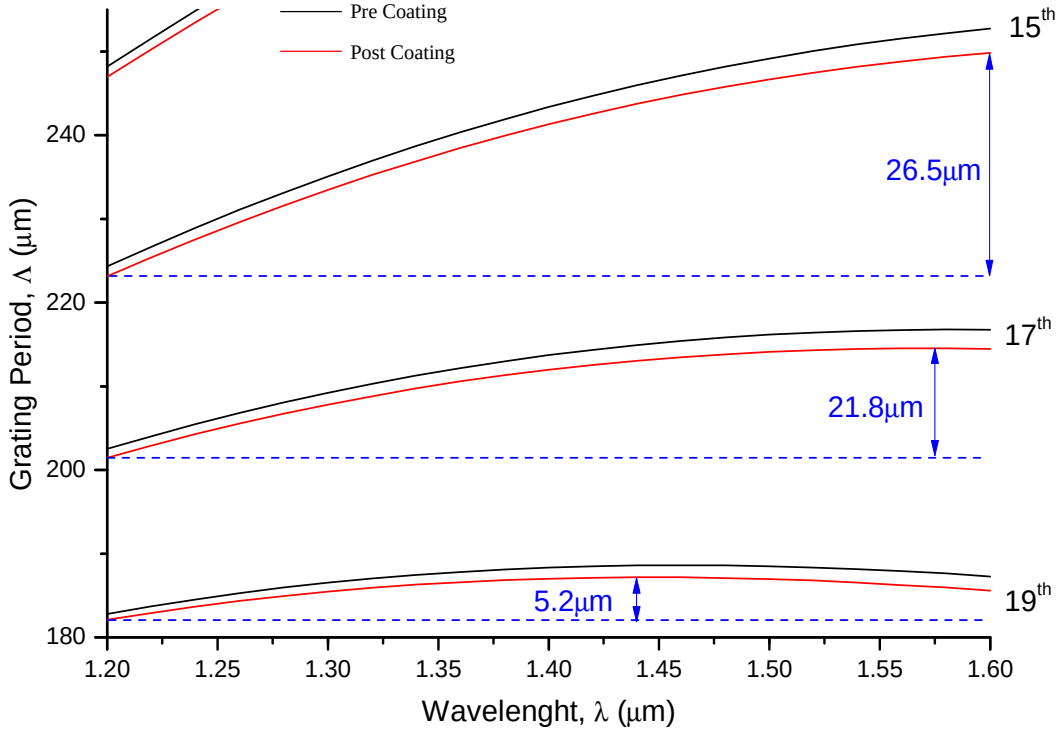

Figure 97: Phase match plot of the 15th-19th Pd coated odd order modes. Illustrating decreasing period window with increasing mode order.

Designing an LPG element to fit to the most useful sensitive modes (15-19th) is likely to be a difficult process. The optimal position for sensitivity is the mode match turning point but the risk of over or under shooting this position is great. If the inscribed period (or modelled period) is too long then the LPG may fail to couple to any modes or to do so only very weakly. Conversely if the period is too short then the desired mode may couple to two wavelengths so widely separated that it is impractical to measure them both simultaneously. The tolerances for the inscription process can be best quantified by considering the range of periods which a particular mode can couple to over the

desired wavelength range. For example the 19th order mode of a Pd coated LPG will provide one or more resonant wavelengths within the 1200-1600 nm region for periods between 182 and 187 μm (a period window of 5.1 μm, Figure 97). This effectively means that if coupling within this region is required the LPG must be inscribed to a period of 184.5 μm with a tolerance of ±2.54 μm – including any error in the theoretical optimal position.

*Table 4: Specification for a single wavelength high sensitivity LPG sensor. * Calculated via the required LPG period and tolerance.*

Parameter	Specification	Tolerance
Fibre Type	SMF-28^{TM}	NA
Period (Λ)	236.5 μm	±10 μm
Length (L)	21.5mm	±0.2mm
Max Index Change (Δn)	3.2x10^{-4} RIU	±0.1x10^{-4} RIU
Coupling λ during inscription*	1316nm	1218-1452nm
Coupling λ after coating*	1335nm	1230-1498nm

The only choice is therefore to concede that there will be some inaccuracy in both the modelled phase matching conditions and in the inscription process and modify the design to anticipate this. This simplest approach here is to abandon the most sensitive modes and couple to a slightly lower mode order. For example the 15th order mode has a period window of 26.5 μm in the 1200-1600 nm region (Figure 97), although the mode match turning point is outside of the monitoring region the mode will still be significantly more sensitive than the 9th order mode. This is an attractive possibility for creating a "fool proof" LPG sensor. During the inscription process the 15th order mode (black line Figure 97) can be monitored and provided that it is observed to be coupling in the 1300-1500 nm region it will be within the 1200-1600 nm regime after coating. This of course requires some flexibility in terms of the central wavelength of the

interrogation system but as only one loss band needs to be monitored this should be quite possible.

This then provides a high tolerance sensitive LPG specification (Table 4), with the accompanying phase match diagram (Figure 98):

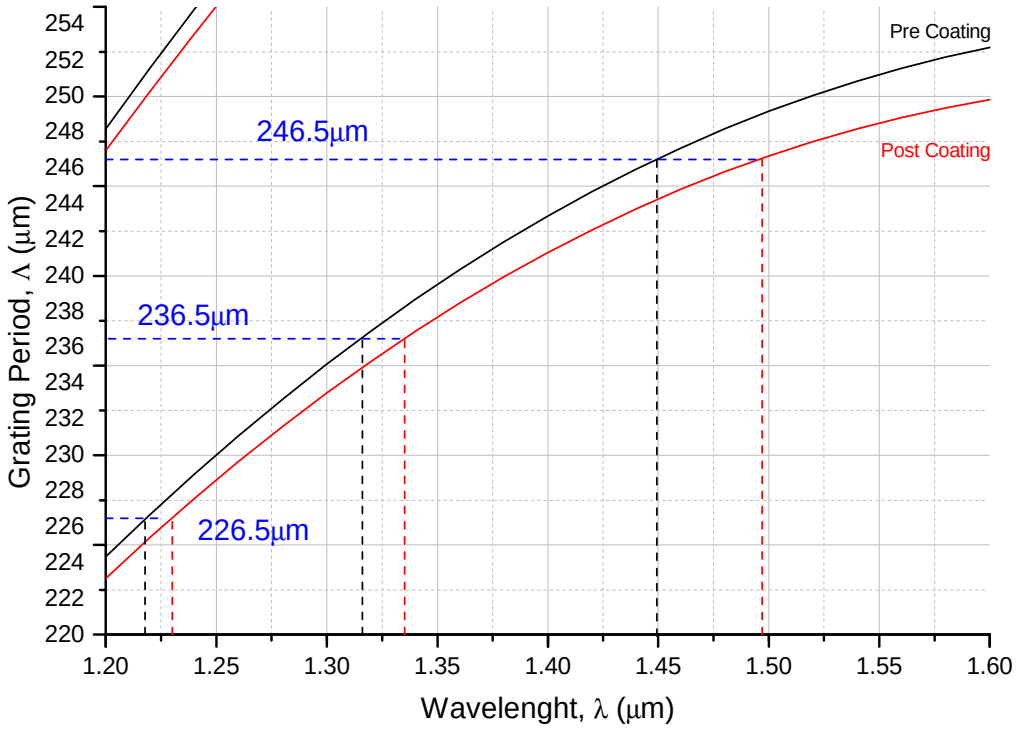

Figure 98: Phase diagram for the inscription of a high tolerance sensitive LPG operating with the 15th order mode. Phase curves before (black) and after (red) Pd coating are included with period and wavelength parameters defined in Table 4.

The second option is to consider the possibility of tuning the LPG period after coating. This can be done by applying strain. This requires less adaptation of the sensing system than may be originally apparent as the LPG requires a small amount of strain to prevent bend losses anyway. There is also no need to exactly measure the amount of strain applied, it is sufficient to simply increase the strain until the desired transmission spectrum is achieved. This process is, of course, mono-directional. It is not practical to apply compression to a fibre. As such it is necessary to deliberately write the LPG with a shorter period than desired.

An estimated 3mε can be applied to the LPG before there is significant alteration of the modes. For a ~200 μm period LPG (17th order with turning point at ~1570 nm) this corresponds to a maximum increase in period of 0.6 μm. By deliberately creating the LPG with a period 0.3 μm less than required the tolerances increase to ±0.3 μm which, although small, are within the capabilities of manufacturing and a test LPG should provide the required information to compensate for the error in the theoretical position.

This provides a specification for a ultra-high sensitivity but lower tolerance LPG as follows (Table 5 & Figure 99):

Table 5: Specification for a double wavelength ultra high sensitivity LPG sensor.

** Calculated via the required LPG period and tolerance.*

Parameter	Specification	Tolerance
Fibre Type	SMF-28^{TM}	NA
Period (Λ)	211.5 μm	±0.3 μm
Length (L)	23.125 mm	±0.125 mm
Max Index Change (Δn)	3.2x10^{-4} RIU	±0.1x10^{-4} RIU
Coupling λ during inscription*	1415 nm	1405-1426 nm
Coupling λ after coating*	1509 nm	1485-1575 nm

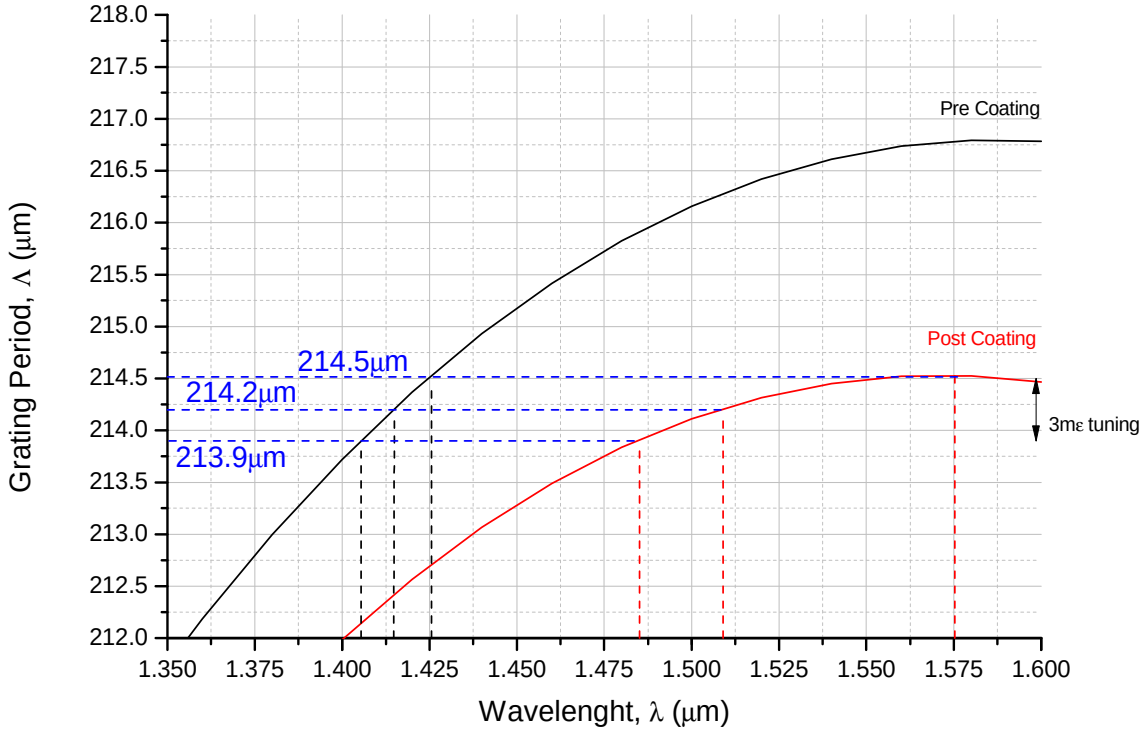

Figure 99: Phase diagram for the inscription of a low tolerance ultra sensitive LPG operating with the 17th order mode. Phase curves before (black) and after (red) Pd coating are included with period and wavelength parameters defined in Table 5.

As an additional benefit the post inscription tuning of an LPG gives the potential for a single LPG to access all three higher mode order sensing regimes. With a period above the phase match turning point the mode will no longer be sensitive in wavelength space, instead a further increase in the period will change only the coupling coefficient (cf. Figure 92). In this manner it becomes an amplitude based sensor which may be desirable for particular applications.

At a period just below the phase matched turning point the mode will simultaneously couple to two, close together periods. As the phase matching conditions of these two resonant positions converge at the phase matching point this gives two losses which move in opposite directions as the result of external stimuli. By taking a differential measurement this potentially gives a doubling in sensitivity. Finally only one of these peaks could be monitored simplifying the interrogation of the sensor, yet would still provide a comparatively sensitive sensor.

For a given application it is therefore necessary to carefully consider the limits of manufacture, the accuracy of the optical constants used for the modelling, the wavelengths to be monitored and the required sensitivity of the sensor. With these parameters in mind it is quite possible to design an optimal LPG specification including built in compensation for expected errors.

These errors in the modelling process can be further reduced by accurately characterising a written LPG element. Provided that there is some expectation of repeatability in the inscription process this should allow for accurate determination of the optical properties of an LPG and further reduce the uncertainties in a design LPG specification. At present there is no means to characterise an LPG profile, by which we mean determine the core refractive index, the profile of the inscribed refractive index change in z, the period, the maximum index change and the ac and dc components of the UV induced change in refractive index. The proof of principle experiment in (§4.3) using quantitative phase microscopy (QPM) provides an attractive possibility.

This technique will ideally give the phase of a single wavelength propagating through the side of the fibre as a function of the cross section. This phase information would allow for direct measurement of the period, the maximum index perturbation and, by comparing the difference between core and cladding, the core refractive index. The prototype schematic in (§4.3), with a specially designed curved grating, should provide this information for a single wavelength, ideally the central wavelength of interest (e.g. 1550 nm). This project is scheduled to continue as a collaboration between the CGCRI and the Applied Optical Physics group here at HWU. The eventual outcome is a robust dedicated system intended to specifically characterise LPGs. Such a device would also prove a powerful, useful tool for the characterisation of the LPG inscription process.

In conclusion the LPG-Pd sensor has potential. If issues in manufacturing and theoretical modelling can be addressed, it is possible to write an LPG sensor with a high sensitivity to the changes in the refractive index of Pd to hydrogen absorption. The temporal response of the Pd (i.e. absorption time) is such that it is unlikely to find use in safety applications where speed of response is critical. This could be addressed by heating the LPG to improve absorption but unless an optical heating arrangement can be implemented this would detract from the advantages of an all optical system. For the application proposed by AWE the monitoring times can be recorded in the order of

weeks and months and as such temporal responses in the order of hours are quite acceptable.

Any bends within the LPG region will quickly shutdown or at least modify coupling between core and cladding modes and therefore alter the characteristics of the sensor. This requires that the mounting of any LPG element include a nominal strain, which will shift the LPG peak position. Care must be taken to ensure that this strain does not change over time but this is primarily a problem in the packaging of the sensor. Correctly implemented this strain can be turned into an advantage, tuning the grating period.

As the thermal coefficient of the LPGs gives a response to 1K of temperature change, on a similar scale as the response to 1% H_2, as shown experimentally in this thesis, temperature compensation would also need to be implemented, even in a closed system like the one required by AWE with low temperature fluctuations. This need is increases when using a double coupling differential measurement with higher order modes implmented. One possibility is to implement a temperature sensor, such as a FBG, either in the same fibre but separated in wavelength, or in a separate fibre. Alternatively a polarisation maintaining fibre with a Pd coating aligned to one optical axis could provide differential temperature compensation however this has not yet been attempted.

Depending on the application care must be taken over the two stage temperature dependence, there is a shift to the LPG position, the scale of response to H_2 and the rate of response to H_2. In slow systems, like the one required by AWE, the LPG and H_2 absorption scale shift could be directly compensated for while the rate of reaction can be ignored.

Long term stability is a potential issue due to delamination of the sensor layer due to weak adhesion, contamination and cyclic straining when exposed to hydrogen. Careful deposition of the Pd coating should provide a sensor with a lifetime in excess of 2 years at room temperature but higher temperatures will accelerate the aging process. The use of a keying layer is unlikely to assist matters as this will interfere with the interaction between the evanescent cladding mode and the Pd layer reducing the sensitivity. An alternative is a capping layer designed to allow hydrogen to permeate through it but to keep the Pd in place. One such possibility is a hydrophobic air gel layer which would

have the added benefit of reducing contamination issues, particularly with humidity which will otherwise kill the sensing.

The key problem in the use of LPGs as sensing elements is the difficulty in reproducible manufacture and in isolating the desired LPG signal from the large number of measurands. Solving these issues is largely an application specific process which is both difficult and time consuming. It is for these reasons that LPG based sensors have not been taken up by industry as rapidly or enthusiastically as FBG based sensors. However, future research and development might change this perception and there are still areas where LPG based sensors have a significant advantage over other sensor concepts and the prime time for LPG based sensor technology might yet come.

Appendix A: Long Period Grating Mathematica Code

Full Solution for Dispersive Media - Air Surround

Sources :
1. Turan Erdogan, "Cladding-mode resonances in short-and long-period fiber grating filters" J. Opt. Soc. Am. A/Vol. 14, No. 8 August 1997 p1760
2. Turan Erdogan, "Errata - Cladding-mode resonances in short-and long-period fiber grating filters" J. Opt. Soc. Am. A 2000 p1760
3. Turan Erdogan, "Fiber Grating Spectra" J.Lightwave Tec. Vol 15 No 8 Aug 1997 1277 - 1294

Sections in Italics are not nessersary for the calculation of the transmission spectrum

1. Preamble: Fibre and LPG definitions

The preamle defines a few usefull constants, sets the current directory and defines both the fibre and the LPG

In[1]:=
```
SetDirectory[
 "H:\\My Documents\\Metal Waveguide models\\Mathematica code\\Eigth
   Generation\\LPG2.4"]

μm = 10^-6;
nm = 10^-9;
mm = 10^-3;
Z0 = Sqrt[4 × 10^-7 π / 8.854 10^12];

(* Fibre Parameters, n1 is core,
n2 cladding and n3 is the external index*)
CoreDiameter = (8.2) μm;
CladdingDiameter = (125) μm;
n3 = 1;
λcentre = 1550 nm;
λrange = Range[1.2, 1.6, .0005] μm;
a1 = (CoreDiameter / 2);
a2 = (CladdingDiameter / 2);

(*LPG parameters, Λ is the period, m is the visability,
n1z is the core index variation, L is the grating
 length σ is the grating envelope (or ac componant)*)
Λ = 400 μm;
Δn = 3.2 × 10^-4;
m = 1;
n1z = (n1) (1 + σ (1 + m Cos[(2 π) / Λ z]));
L = 24.2 × 10^-3;
σ = Δn / (2 n1);
```

Out[1]=
```
H:\My Documents\Metal Waveguide
  models\Mathematica code\Eigth Generation\LPG2.4
```

In[19]:=
```
sela = {0.6961663, 0.4079426, 0.8974794};
selb = {0.0684043, 0.1162414, 9.896161};
n2 = Sqrt[1 + sela[[1]] (λ / μm)^2 / ((λ / μm)^2 - selb[[1]]^2) +
      sela[[2]] (λ / μm)^2 / ((λ / μm)^2 - selb[[2]]^2) + sela[[3]] (λ / μm)^2 / ((λ / μm)^2 - selb[[3]]^2)];
selacore = {0.7040518964521497`, 0.41449879255849215`,
   0.7724974165747513`};
selbcore = {0.07368801242467019`, 0.11548975370833288`,
   9.379570644231709`};
n1 = Sqrt[1 + selacore[[1]] (λ / μm)^2 / ((λ / μm)^2 - selbcore[[1]]^2) +
      selacore[[2]] (λ / μm)^2 / ((λ / μm)^2 - selbcore[[2]]^2) + selacore[[3]] (λ / μm)^2 / ((λ / μm)^2 - selbcore[[3]]^2)];
```

In[25]:=
```
Plot[{n1, n2}, {λ, 1200 nm, 1600 nm}]
```

Out[25]=

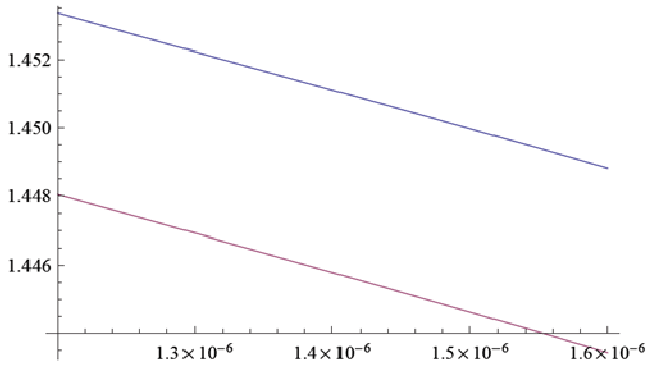

2. Calculate Core Effective Index

Calculating the core effective index is a simple matter of calculating the V number, and solving the dispersion relation for b - the normalised effective index of the fibre.

n.b. Δ is the effective index step .

▪ Equations

In[26]:=
```
Δ = (n1 - n2) / n1;
b = (neco^2 - n2^2) / (n1^2 - n2^2);
V = (2 π) / λ a1 Sqrt[n1^2 - n2^2];
CoreDispLHS = V Sqrt[1 - b] BesselJ[1, V Sqrt[1 - b]] / BesselJ[0, V Sqrt[1 - b]];
CoreDispRHS = V Sqrt[b] BesselK[1, V Sqrt[b]] / BesselK[0, V Sqrt[b]];
```

Calculation

```
In[31]:= CalcNeco =
           Table[
            {λrange[[i]] / μm,
             Re[neco] /. FindRoot[
                (CoreDispLHS /. λ → λrange[[i]]) == (CoreDispRHS /. λ → λrange[[i]]),
                {neco, (n1 /. λ → 1550 nm) - .0001}]
            },
            {i, Length[λrange]}
           ];
```

- **Results**

```
In[32]:= MatrixForm[CalcNeco];

In[33]:= ListPlot[CalcNeco]
```

Out[33]=

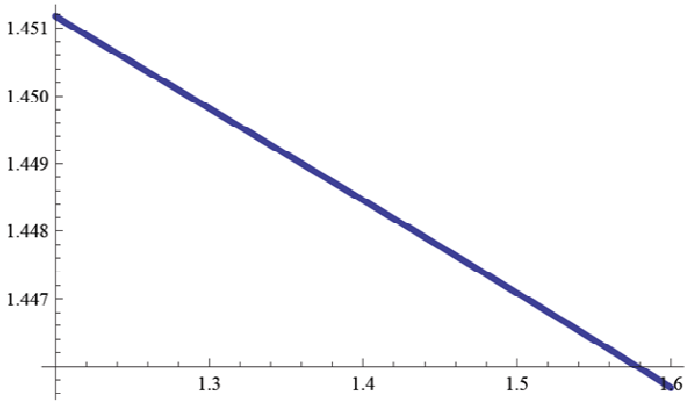


```
In[34]:= Export["CalcNeco.dat", CalcNeco, "Table"]

Out[34]= CalcNeco.dat
```

3. Calculate Cladding Effective Indicies

This step is slightly more complex as we have a three layer model to solve and multiple soultions (each for a seperate mode) all of which needs to be looped over the wavelength range.

- **Equations**

We can start by defining the various parameters nessersary to simplify the dispersion relation
n.b. my notation differs from Erdogan insofar as j and k are lower case rather than upper case and I have explicitly written out the derivatinve of the Bessel Functions as needed.

In[35]:=
$$\sigma 1 = \frac{i\, necl}{Z0};$$

$$\sigma 2 = i\, necl\, Z0;$$

$$u21 = \frac{1}{u2^2} - \frac{1}{u1^2};$$

$$u32 = \frac{1}{w3^2} + \frac{1}{u2^2};$$

$$u1 = \sqrt{\left(\frac{(2\pi)}{\lambda}\right)^2 \left(n1^2 - necl^2\right)};$$

$$u2 = \sqrt{\left(\frac{(2\pi)}{\lambda}\right)^2 \left(n2^2 - necl^2\right)};$$

$$w3 = \sqrt{\left(\frac{(2\pi)}{\lambda}\right)^2 \left(necl^2 - n3^2\right)};$$

$$j = \frac{\frac{1}{2}\left(BesselJ[0, u1\, a1] - BesselJ[2, u1\, a1]\right)}{u1\, BesselJ[1, u1\, a1]};$$

$$k = \frac{\frac{1}{2}\left(-BesselK[0, w3\, a2] - BesselK[2, w3\, a2]\right)}{w3\, BesselK[1, w3\, a2]};$$

$$p1 = BesselJ[1, u2\, r]\, BesselY[1, u2\, a1] - BesselJ[1, u2\, a1]\, BesselY[1, u2\, r];$$

$$q1 = BesselJ[1, u2\, r]\left(\frac{1}{2}\left(BesselY[0, u2\, a1] - BesselY[2, u2\, a1]\right)\right) - \left(\frac{1}{2}\left(BesselJ[0, u2\, a1] - BesselJ[2, u2\, a1]\right)\right) BesselY[1, u2\, r];$$

$$r1 = \left(\frac{1}{2}\left(BesselJ[0, u2\, r] - BesselJ[2, u2\, r]\right)\right) BesselY[1, u2\, a1] - BesselJ[1, u2\, a1]\left(\frac{1}{2}\left(BesselY[0, u2\, r] - BesselY[2, u2\, r]\right)\right);$$

$$s1 = \left(\frac{1}{2}\left(BesselJ[0, u2\, r] - BesselJ[2, u2\, r]\right)\right)\left(\frac{1}{2}\left(BesselY[0, u2\, a1] - BesselY[2, u2\, a1]\right)\right) - \left(\frac{1}{2}\left(BesselJ[0, u2\, a1] - BesselJ[2, u2\, a1]\right)\right)\left(\frac{1}{2}\left(BesselY[0, u2\, r] - BesselY[2, u2\, r]\right)\right);$$

two sides of the disperison relation $\zeta 0$ and $\zeta 0$prime are thus :

In[48]:=
$$\zeta 0 = \frac{1}{\sigma 2}\left(u2\left(j\,k + \frac{(\sigma 1\,\sigma 2\,u21\,u32)}{n2^2\,a1\,a2}\right)(p1 /. r \to a2) - k\,(q1 /. r \to a2) + j\,(r1 /. r \to a2) - \frac{1}{u2}(s1 /. r \to a2)\right) \Big/ \left(-u2\left(\frac{u32}{n2^2\,a2}\,j - \frac{u21}{n1^2\,a1}\,k\right)(p1 /. r \to a2) + \frac{u32}{n1^2\,a2}(q1 /. r \to a2) + \frac{u21}{n1^2\,a1}(r1 /. r \to a2)\right);$$

$$\zeta 0prime = \sigma 1\left(u2\left(\frac{u32}{a2}\,j - \frac{n3^2\,u21}{n2^2\,a1}\,k\right)(p1 /. r \to a2) - \frac{u32}{a2}(q1 /. r \to a2) - \frac{u21}{a1}(r1 /. r \to a2)\right) \Big/ \left(u2\left(\frac{n3^2}{n2^2}\,j\,k + \frac{\sigma 1\,\sigma 2\,u21\,u32}{n1^2\,a1\,a2}\right)(p1 /. r \to a2) - \frac{n3^2}{n1^2}\,k\,(q1 /. r \to a2) + j\,(r1 /. r \to a2) - \frac{n2^2}{n1^2\,u2}(s1 /. r \to a2)\right);$$

- **Plot of Dispersion function**

In[50]:=
```
Plot[Im[(ζ0 - ζ0prime) /. λ → 1550 nm],
 {necl, (n2 /. λ → 1550 nm) - .0026, (n2 /. λ → 1550 nm)}]
```

Out[50]=

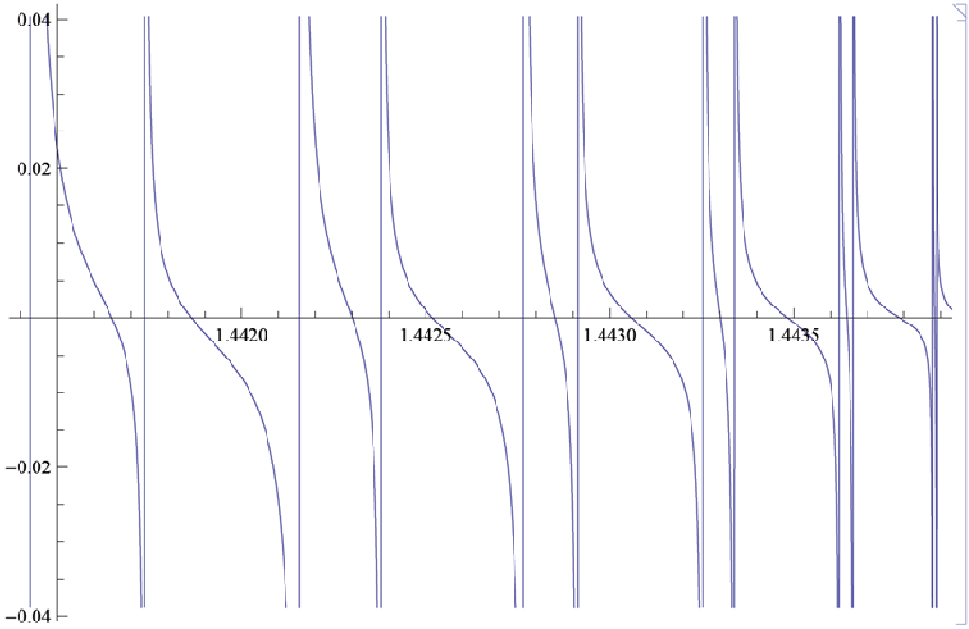

As the disperson is an complex number with Re[ζ0,ζ0prime]= 0 we need only look at the imaginary componants:

Calculation

The Disperson equation for a cladding mode is in general rather complex - (see above). There is no more eligent sloution than a brute force solution to the equation.
This is as follows:
1. Create a range of values for necl between n2 and n2-.0013 say.
2. Calculate the values of $\zeta 0$-$\zeta 0$prime over for these values
3. Find all positions where the sign of $\zeta 0$-$\zeta 0$prime changes between two ajacent test points
4. Use FindRoot at these positions to home in on a solution
5. Remove duplicate solutions and sort in decending order of necl - assending mode order.
6. Loop over all required wavelengths.

This can be rather time consuming but the use of the sign change does significantly speed up the calculation.

In[51]:=
```
eqn = Im[(ζ0 - ζ0prime)];
step = 1 × 10^-6;
Δnmax = .004;
CalcNecl = {};
Print[Length[λrange]];
Do[
 test = Table[{i, eqn /. {λ → λrange[[l]], necl -> i}}, {i,
    (n2 /. λ → λrange[[l]]) - Δnmax, (n2 /. λ → λrange[[l]]) - step, step}];
 test = Thread[{Transpose[test][[1]], Transpose[test][[2]]}];
 testpoints = {};
 Do[If[Sign[test[[i]][[2]]] == Sign[test[[i + 1]][[2]]],
   True, AppendTo[testpoints, test[[i]][[1]]];
   AppendTo[testpoints, test[[i + 1]][[1]]], {i, Length[test] - 1}];
 solns = Reverse[Union[Table[
     Re[Round[necl /. FindRoot[(ζ0 /. λ → λrange[[l]]) ==
           (ζ0prime /. λ → λrange[[l]]), {necl, testpoints[[i]]}],
       .00000001]],
     {i, Length[testpoints]}]]];
 Print[l];
 AppendTo[CalcNecl, solns],
 {l, Length[λrange]}]
```

```
801
```

Results

```
MatrixForm[CalcNecl];
```

In[58]:=
```
ListPlot[CalcNecl]
```

Out[58]=

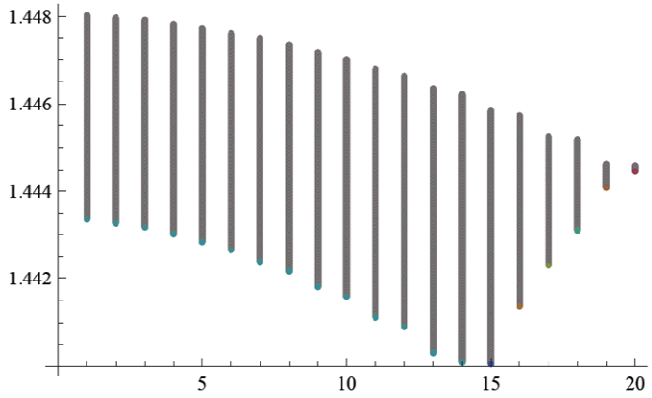

In[59]:=
```
Export["CalcNecl.dat", CalcNecl, "Table"]
```

Out[59]=
```
CalcNecl.dat
```

I am going to define a constant νmax indicating the highest order mode for which we have full information

In[60]:=
```
νmax = Min[Table[Length[CalcNecl[[i]]], {i, Length[CalcNecl]}]]
```

Out[60]=
```
14
```

4. Calculating phase matching position

This step is not strictly speaking nessersary but is of use for seeing the projected peak position of an LPG.

The baskic equation is simple but the data will require a little re - arangement to a useable format

$\Lambda=\lambda/(neco-necl)$

In[61]:=
```
MatchingCondition = Table[
    {CalcNeco[[i]][[1]], CalcNeco[[i]][[1]] / (CalcNeco[[i]][[2]] - CalcNecl[[i]][[1]])},
    {l, νmax}, {i, Length[CalcNeco]}];
```

In[119]:=
```
Manipulate[
 ListLinePlot[MatchingCondition, Frame → True,
  ImageSize → 400, PlotRange → {350, 450},
  FrameLabel → {"λ (μm)", "Grating Period (μm)"},
  AxesOrigin → {1.2, 250}, GridLines → {Range[1.2, 1.6, .01], None},
  GridLinesStyle → Directive[Dashed],
  FrameTicks → {Range[1.2, 1.6, .05], Range[350, 450, 50]},
  LabelStyle → {15, Directive[Bold]}, Epilog → {
    Line[{{1.2, Period}, {1.6, Period}}]}], {Period, 350, 450}]
```

Out[119]=

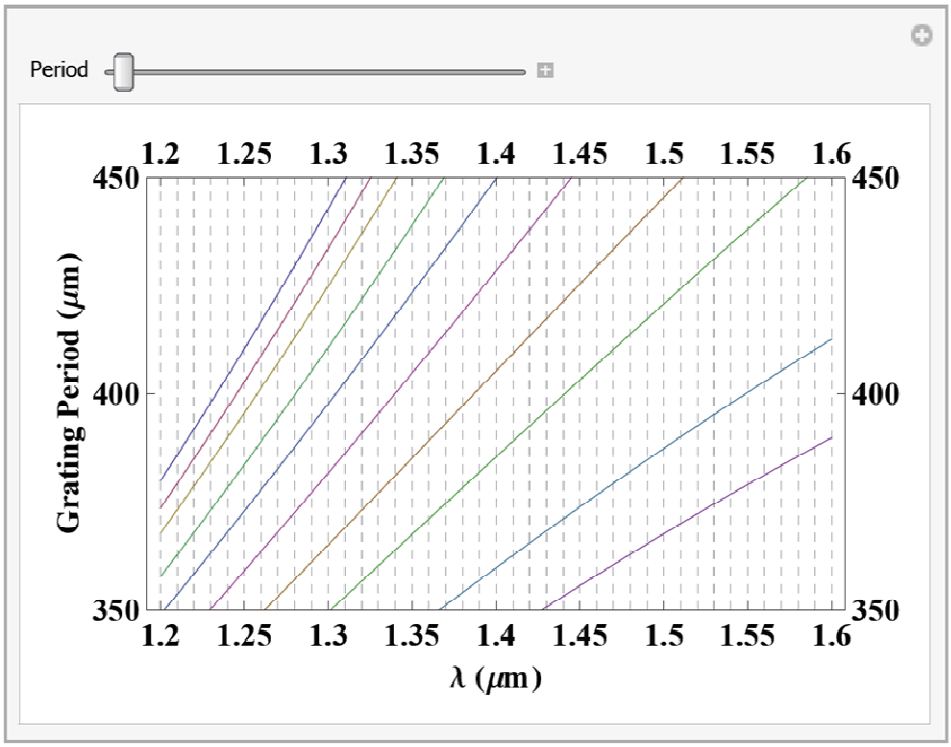

5. Calculate Mode Normalisation Constant

The Mode normalisation constant (Eν) is important for the mode overlap intergrals. In this case we are going to normalise each mode to 1 W. This requires that we define the field coefficents in the core, cladding and surrounding medium for the cladding mode.

■ Equations

Note that I have used a Mod[βz - ωt] in the wave equation elimintates unnessersary factors of 2 π from the wave equation to prevent rounding errors building up in mathematica

The following notation has been used :

Eϕclco

Which in this case shows the ϕ componant of the E field of the cladding mode in the core region

In[63]:=

$$\text{Erclco} = i\,E\nu\,\frac{u1}{2}\left(\text{BesselJ}[2, u1\,r] + \text{BesselJ}[0, u1\,r] - \frac{\sigma 2\,\zeta 0}{n1^2}\,(\text{BesselJ}[2, u1\,r] - \text{BesselJ}[0, u1\,r])\right) e^{i\phi}\, e^{i\,\text{Mod}[\beta\nu\,z-\omega\,t,\,2\pi]};$$

$$\text{E}\phi\text{clco} = E\nu\,\frac{u1}{2}\left(\text{BesselJ}[2, u1\,r] - \text{BesselJ}[0, u1\,r] - \frac{\sigma 2\,\zeta 0}{n1^2}\,(\text{BesselJ}[2, u1\,r] + \text{BesselJ}[0, u1\,r])\right) e^{i\phi}\, e^{i\,\text{Mod}[\beta\nu\,z-\omega\,t,\,2\pi]};$$

$$\text{Ezclco} = E\nu\,\frac{u1^2\,\sigma 2\,\zeta 0}{n1^2\,\beta\nu}\,\text{BesselJ}[1, u1\,r]\, e^{i\phi}\, e^{i\,\text{Mod}[\beta\nu\,z-\omega\,t,\,2\pi]};$$

$$\text{Hrclco} = E\nu\,\frac{u1}{2}\,(i\,\sigma 1\,(\text{BesselJ}[2, u1\,r] - \text{BesselJ}[0, u1\,r]) + i\,\zeta 0\,(\text{BesselJ}[2, u1\,r] + \text{BesselJ}[0, u1\,r]))\, e^{i\phi}\, e^{i\,\text{Mod}[\beta\nu\,z-\omega\,t,\,2\pi]};$$

$$\text{H}\phi\text{clco} = -i\,E\nu\,\frac{u1}{2}\,(i\,\sigma 1\,(\text{BesselJ}[2, u1\,r] + \text{BesselJ}[0, u1\,r]) + i\,\zeta 0\,(\text{BesselJ}[2, u1\,r] - \text{BesselJ}[0, u1\,r]))\, e^{i\phi}\, e^{i\,\text{Mod}[\beta\nu\,z-\omega\,t,\,2\pi]};$$

$$\text{Hzclco} = -i\,E\nu\,\frac{u1^2\,i\,\sigma 1}{\beta\nu}\,\text{BesselJ}[1, u1\,r]\, e^{i\phi}\, e^{i\,\text{Mod}[\beta\nu\,z-\omega\,t,\,2\pi]};$$

$$\text{Erclcl} = i\,E\nu\,\frac{\pi\,a1\,u1^2\,\text{BesselJ}[1, u1\,a1]}{2}\left(-\frac{F2}{r}\,p1 + \frac{1}{u2\,r}\,q1 - \frac{\sigma 2}{n2^2}\left(u2\,G2\,r1 - \frac{n2^2\,\zeta 0}{n1^2}\,s1\right)\right) e^{i\phi}\, e^{i\,\text{Mod}[\beta\nu\,z-\omega\,t,\,2\pi]};$$

$$\text{E}\phi\text{clcl} = E\nu\,\frac{\pi\,a1\,u1^2\,\text{BesselJ}[1, u1\,a1]}{2}\left(\frac{\sigma 2}{n2^2}\left(\frac{G2}{r}\,p1 - \frac{n2^2\,\zeta 0}{n1^2\,u2\,r}\,q1\right) + u2\,F2\,r1 - s1\right) e^{i\phi}\, e^{i\,\text{Mod}[\beta\nu\,z-\omega\,t,\,2\pi]};$$

$$\text{Ezclcl} = -E\nu\,\frac{\pi\,a1\,u1^2\,u2^2\,\sigma 2\,\text{BesselJ}[1, u1\,a1]}{2\,n2^2\,\beta\nu}$$

$$\left(G2\,pl - \frac{n2^2\,\zeta 0}{n1^2\,u2}\,ql\right) e^{i\phi}\, e^{i\,\mathrm{Mod}[\beta\nu\, z-\omega\, t,\,2\pi]};$$

$$Hrclcl = E\nu\,\frac{\pi\, a1\, u1^2\, \mathrm{BesselJ}[1,\,u1\,a1]}{2}$$

$$\left(-i\,\frac{G2}{r}\,pl + i\,\frac{n2^2\,\zeta 0}{n1^2\,u2\,r}\,ql + i\,\sigma 1\,(u2\,F2\,rl - sl)\right) e^{i\phi}\, e^{i\,\mathrm{Mod}[\beta\nu\, z-\omega\, t,\,2\pi]};$$

$$H\phi clcl = i\,E\nu\,\frac{\pi\, a1\, u1^2\, \mathrm{BesselJ}[1,\,u1\,a1]}{2}$$

$$\left(i\,\sigma 1\left(\frac{F2}{r}\,pl - \frac{1}{u2\,r}\,ql\right) - i\,u2\,G2\,rl + i\,\frac{n2^2\,\zeta 0}{n1^2}\,sl\right) e^{i\phi}\, e^{i\,\mathrm{Mod}[\beta\nu\, z-\omega\, t,\,2\pi]};$$

$$Hzclcl = -i\,E\nu\,\frac{\pi\, a1\, u1^2\, u2^2\, i\,\sigma 1\, \mathrm{BesselJ}[1,\,u1\,a1]}{2\,\beta\nu}$$

$$\left(F2\,pl - \frac{1}{u2}\,ql\right) e^{i\phi}\, e^{i\,\mathrm{Mod}[\beta\nu\, z-\omega\, t,\,2\pi]};$$

$$Erclex = i\,E\nu\,\frac{\pi\, a1\, u1^2\, u2^2\, \mathrm{BesselJ}[1,\,u1\,a1]}{4\,w3\,\mathrm{BesselK}[1,\,w3\,a2]}$$

$$\left(-F3\,(\mathrm{BesselK}[2,\,w3\,r] - \mathrm{BesselK}[0,\,w3\,r]) + \frac{\sigma 2\,G3}{n3^2}\,(\mathrm{BesselK}[2,\,w3\,r] + \mathrm{BesselK}[0,\,w3\,r])\right) e^{i\phi}\, e^{i\,\mathrm{Mod}[\beta\nu\, z-\omega\, t,\,2\pi]};$$

$$E\phi clex = E\nu\,\frac{\pi\, a1\, u1^2\, u2^2\, \mathrm{BesselJ}[1,\,u1\,a1]}{4\,w3\,\mathrm{BesselK}[1,\,w3\,a2]}$$

$$\left(-F3\,(\mathrm{BesselK}[2,\,w3\,r] + \mathrm{BesselK}[0,\,w3\,r]) + \frac{\sigma 2\,G3}{n3^2}\,(\mathrm{BesselK}[2,\,w3\,r] - \mathrm{BesselK}[0,\,w3\,r])\right) e^{i\phi}\, e^{i\,\mathrm{Mod}[\beta\nu\, z-\omega\, t,\,2\pi]};$$

$$Ezclex = E\nu\,\frac{\pi\, a1\, u1^2\, u2^2\, \sigma 2\, \mathrm{BesselJ}[1,\,u1\,a1]}{2\,n3^2\,\beta\nu\,\mathrm{BesselK}[1,\,w3\,a2]}$$

$$(G3\,\mathrm{BesselK}[1,\,w3\,r])\, e^{i\phi}\, e^{i\,\mathrm{Mod}[\beta\nu\, z-\omega\, t,\,2\pi]};$$

$$\text{Hrclex} = \text{Ev}\,\frac{\pi\,\text{a1}\,\text{u1}^2\,\text{u2}^2\,\text{BesselJ}[1,\,\text{u1}\,\text{a1}]}{4\,\text{w3}\,\text{BesselK}[1,\,\text{w3}\,\text{a2}]}$$
$$(-\text{i}\,\sigma\text{1}\,\text{F3}\,(\text{BesselK}[2,\,\text{w3}\,\text{r}] + \text{BesselK}[0,\,\text{w3}\,\text{r}]) -$$
$$\text{i}\,\text{G3}\,(\text{BesselK}[2,\,\text{w3}\,\text{r}] - \text{BesselK}[0,\,\text{w3}\,\text{r}]))\,e^{\text{i}\,\phi}\,e^{\text{i}\,\text{Mod}[\beta\text{v}\,\text{z}-\omega\,\text{t},\,2\,\pi]};$$

$$\text{H}\phi\text{clex} = \text{i}\,\text{Ev}\,\frac{\pi\,\text{a1}\,\text{u1}^2\,\text{u2}^2\,\text{BesselJ}[1,\,\text{u1}\,\text{a1}]}{4\,\text{w3}\,\text{BesselK}[1,\,\text{w3}\,\text{a2}]}$$
$$(\text{i}\,\sigma\text{1}\,\text{F3}\,(\text{BesselK}[2,\,\text{w3}\,\text{r}] - \text{BesselK}[0,\,\text{w3}\,\text{r}]) -$$
$$\text{G3}\,(\text{BesselK}[2,\,\text{w3}\,\text{r}] + \text{BesselK}[0,\,\text{w3}\,\text{r}]))\,e^{\text{i}\,\phi}\,e^{\text{i}\,\text{Mod}[\beta\text{v}\,\text{z}-\omega\,\text{t},\,2\,\pi]};$$

$$\text{Hzclex} = \text{i}\,\text{Ev}\,\frac{\pi\,\text{a1}\,\text{u1}^2\,\text{u2}^2\,\text{i}\,\sigma\text{1}\,\text{BesselJ}[1,\,\text{u1}\,\text{a1}]}{2\,\beta\text{v}\,\text{BesselK}[1,\,\text{w3}\,\text{a2}]}$$
$$(\text{F3}\,\text{BesselK}[1,\,\text{w3}\,\text{r}])\,e^{\text{i}\,\phi}\,e^{\text{i}\,\text{Mod}[\beta\text{v}\,\text{z}-\omega\,\text{t},\,2\,\pi]};$$

Where in this case βv is the propergation constant of the vth cladding mode, Ev is the mode normalisation constant of the vth cladding mode, r ϕ and z are the standard cylindical coordinates, F2, F3, G2 and G3 are defined below :

In[81]:=
$$\text{F2} = \text{j} - \frac{\text{u21}\,\sigma\text{2}\,\xi\text{0}}{\text{n1}^2\,\text{a1}};$$

$$\text{F3} = -\text{F2}\,(\text{pl}\,/.\,\text{r}\to\text{a2}) + \frac{1}{\text{u2}}\,(\text{ql}\,/.\,\text{r}\to\text{a2});$$

$$\text{G2} = \xi\text{0}\,\text{j} + \frac{\text{u21}\,\sigma\text{1}}{\text{a1}};$$

$$\text{G3} = -\frac{\text{n3}^2}{\text{n2}^2}\left(\text{G2}\,(\text{pl}\,/.\,\text{r}\to\text{a2}) - \frac{\text{n2}^2\,\xi\text{0}}{\text{n1}^2\,\text{u2}}\,(\text{ql}\,/.\,\text{r}\to\text{a2})\right);$$

$$\omega = \frac{2\,\pi\,(299\,792\,458)}{\lambda};$$

$$\beta\text{v} = \frac{2\,\pi\,\text{necl}}{\lambda};$$

■ Calculation

With these defined we can say that the power in the cladding mode can be calculated as :

$$\text{P} = \frac{1}{2}\text{Re}\left[\int_0^{2\pi} \text{d}\phi \int_0^{\infty} r\,dr\,(E_r^{\text{cl}}\,H_\phi^{\text{cl}^*} - H_r^{\text{cl}^*}\,E_\phi^{\text{cl}}\right]$$

As Ev is a constant multiplicative factor it is outside of these intergrals and as such we can calculate Ev such that P = 1 W as :

n.b. I have used 100μm radius as a stand in for infinity in this case.

```
In[87]:= Cladmodenorm = Table[
           1 / (.5 Re[
                 NIntegrate[
                   (r (Erclco Conjugate[Hϕclco] - Conjugate[Hrclco] Eϕclco)) /.
                    {t → 0, z → 0, necl → CalcNecl[[λi]][[ν]], λ → λrange[[λi]],
                     Eν → 1}, {r, 0, a1}, {ϕ, 0, 2 π}] + NIntegrate[
                   (r (Erclcl Conjugate[Hϕclcl] - Conjugate[Hrclcl] Eϕclcl)) /.
                    {t → 0, z → 0, necl → CalcNecl[[λi]][[ν]], λ → λrange[[λi]],
                     Eν → 1}, {r, a1, a2}, {ϕ, 0, 2 π}] + NIntegrate[
                   (r (Erclex Conjugate[Hϕclex] - Conjugate[Hrclex] Eϕclex)) /.
                    {t → 0, z → 0, necl → CalcNecl[[λi]][[ν]], λ → λrange[[λi]],
                     Eν → 1}, {r, a2, 200 μm}, {ϕ, 0, 2 π}]])^.5,
           {λi, Length[λrange]}, {ν, 1, νmax}];
```

- **Results**

```
In[89]:= MatrixForm[Cladmodenorm];

In[90]:= Export["Cladmodenorm.dat", Cladmodenorm, "Table"];
```

6. Mode Checking

With the mode fields and the mode normalisation constant calculated it is possible to plot the intensity of the modes to check that they look like real solutions to the problem

- **Equations**

```
In[91]:= Ercl = Which[r ≤ a1, Erclco, r ≤ a2, Erclcl, True, Erclex];
         Eϕcl = Which[r ≤ a1, Eϕclco, r ≤ a2, Eϕclcl, True, Eϕclex];
         Ezcl = Which[r ≤ a1, Ezclco, r ≤ a2, Ezclcl, True, Ezclex];
         Hrcl = Which[r ≤ a1, Hrclco, r ≤ a2, Hrclcl, True, Hrclex];
         Hϕcl = Which[r ≤ a1, Hϕclco, r ≤ a2, Hϕclcl, True, Hϕclex];
         Hzcl = Which[r ≤ a1, Hzclco, r ≤ a2, Hzclcl, True, Hzclex];

         Iz = 1 / 2 Re[Ercl Conjugate[Hϕcl] - Conjugate[Hrcl] Eϕcl];
```

■ Plot

In[98]:=
```
νm = 1;
νma = 5;
λplot = Round[Length[λrange] / 2];
ListLinePlot[Table[{i / μm, Iz /. {r → Abs[i]} /.
     {r → Abs[i], λ → λrange[[λplot]], Eν → Cladmodenorm[[λplot]][[ν]],
      ϕ → 0, t → 0, z → 0, necl → CalcNecl[[λplot]][[ν]]}},
  {ν, νm, νma}, {i, 0, 80 μm, a2 / 100}], PlotRange → All,
 Frame → True, FrameLabel → {"Fibre Radius (μm)", "Intensity"},
 InterpolationOrder → 2,
 Epilog → {Directive[Dashed], Line[{{{a1 / μm, 2 × 10^8}, {a1 / μm, 0}},
     {{a2 / μm, 2 × 10^8}, {a2 / μm, 0}}}]}]
```

Out[101]=

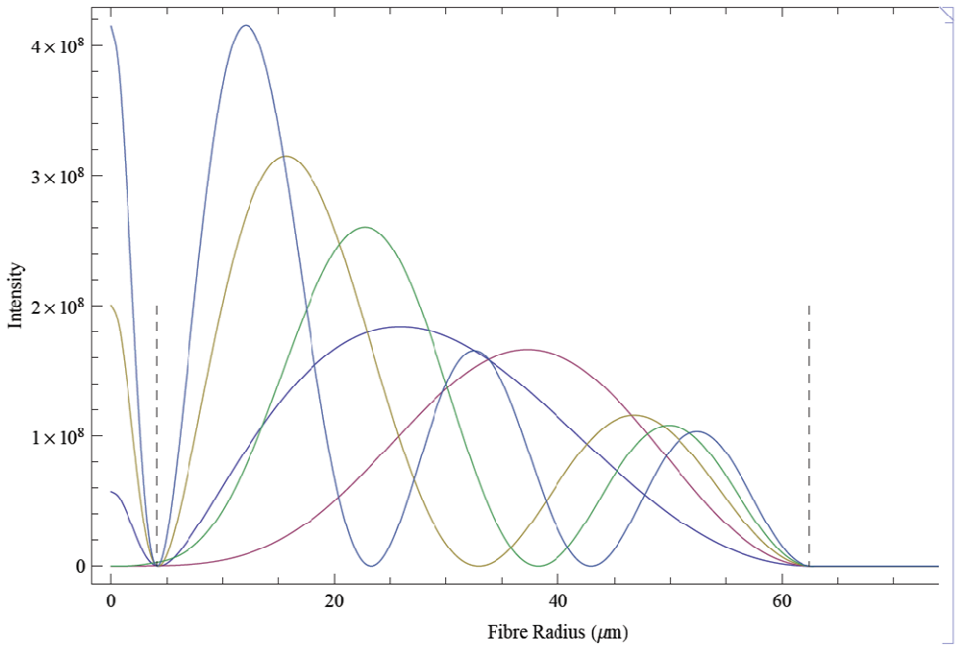

7. Coupling Coefficents

The coupling coefficent can be thus calculated as :
n.b. the grating strength σ is first used here (and for that matter the LPG parameters have not been used up to this point), as such the LPG can be altered, but not the fibre from this point.

■ Equation

In[102]:=
```
Kν = Abs[σ 2 π/λ (π b/(z0 n2 Sqrt[1 + 2 b Δ]))^0.5 n1^2 u1/(u1^2 - ν^2 (1-b)/a1^2)
    (1 + σ2 ζ0/n1^2) Eν (u1 BesselJ[1, u1 a1] BesselJ[0, ν Sqrt[1 - b]]/BesselJ[1, ν Sqrt[1 - b]] -
    ν Sqrt[1 - b]/a1 BesselJ[0, u1 a1])];
```

Calculation

In[103]:=
```
CalcCoupCoeff = Table[Kν /.
      {necl → CalcNecl⟦λi⟧⟦ν⟧,
       λ → λrange⟦λi⟧,
       Eν → Cladmodenorm⟦λi⟧⟦ν⟧,
       neco → CalcNeco⟦λi⟧⟦2⟧},
     {λi, 1, Length[λrange]}, {ν, 1, νmax}];
```

- **Results**

In[104]:=
```
MatrixForm[CalcCoupCoeff];
ListPlot[((CalcCoupCoeff⟦1⟧ / σ) /. λ → 1200 nm) μm, Frame → True,
 FrameLabel → {"Mode Order", "Coupling Coefficient"},
 PlotRange → All]
```

Out[105]=

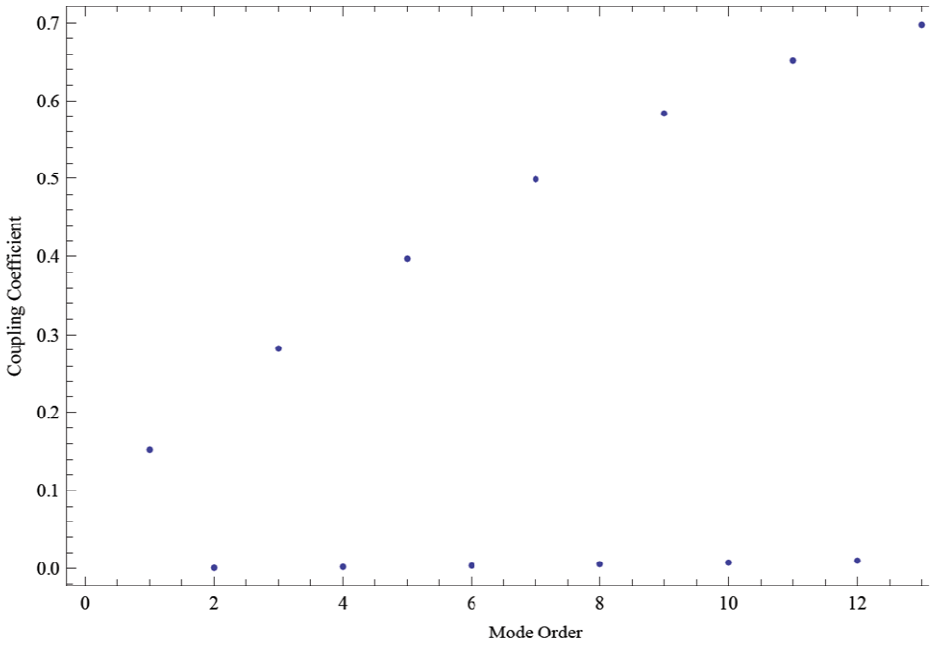

8. Coupled Mode Equations

- **Equations and Calculation**

We can define a small detuning parameter δ and Transmission as follows n.b. the period and the length of the grating appear for the first time here so a change of these variables can be entered at this position in the model

In[108]:=
```
Λ = 400 μm;
Δn = 3.2 × 10^-4;
m = 1;
n1z = (n1) (1 + σ (1 + m Cos[(2 π) / Λ z]));
L = 24.2 × 10^-3;
σ = Δn / (2 n1);
```

```
In[114]:= δ = Table[(π / Λ / λrange[[λi]])
            (((CalcNeco[[λi]][[2]] - CalcNecl[[λi]][[ν]]) Λ) - λrange[[λi]]),
          {λi, 1, Length[λrange]}, {ν, 1, νmax}];
T = Table[(Cos[L √((CalcCoupCoeff[[λi]][[ν]])^2 + (δ[[λi]][[ν]])^2)])^2 +
    1 / (1 + (CalcCoupCoeff[[λi]][[ν]])^2 / (δ[[λi]][[ν]])^2)
     (Sin[L √((CalcCoupCoeff[[λi]][[ν]])^2 + (δ[[λi]][[ν]])^2)])^2,
    {λi, 1, Length[λrange]}, {ν, 1, νmax}];
```

The losses can then be converted into dB combined and the results provided for plot

```
In[116]:= Tdb = -10 Log[10, 1 / T];
          Tran =
            Thread[{λrange / μm, Table[Total[Tdb[[i]]], {i, Length[λrange]}]}];
```

■ Matrix Results

```
MatrixForm[δ];

MatrixForm[T];

MatrixForm[Tran];
```

■ Transmission Plot

```
In[118]:= exampledata = Import["pre.dat", "Table"];
```

In[124]:=
```
title =
  "LPG Transmission: Period: " <> ToString[Λ / μm] <> "μm, Δn: " <>
   ToString[N[Δn]] <> ", Length: " <> ToString[L / mm] <> "mm";
Manipulate[ListLinePlot[Tran, PlotRange →
   {{λrange[[1]] / μm, λrange[[Length[λrange]]] / μm}, {.05, -25}},
  Frame → True, FrameLabel →
   {{"Transmission (dB)", ""}, {"Wavelength (μm)", title}},
  FrameStyle → Directive[FontSize → 10], ImageSize → 400,
  InterpolationOrder → 1, Mesh → Length[Tran], Epilog →
   {Line[{{cursor, 0.05}, {cursor, Min[Transpose[Tran][[2]]] - .05}}],
    Map[Point, exampledata]}],
 {cursor, λrange[[1]] / μm, λrange[[Length[λrange]]] / μm}]
```

Out[125]=

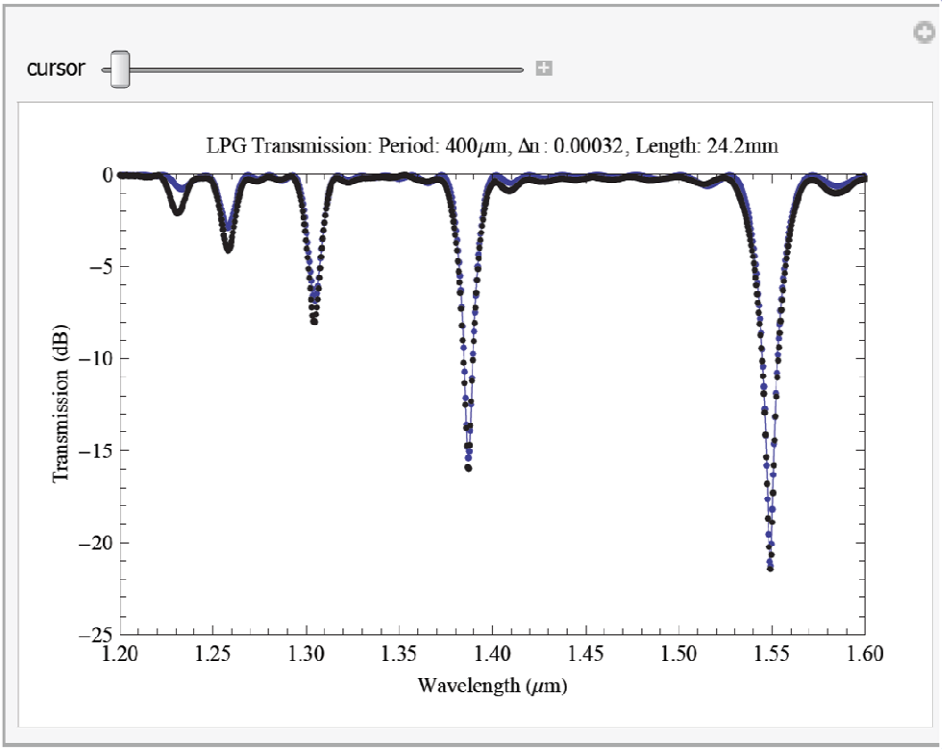

Appendix B: Quantitative Phase Microscopy Model

Quantatative Phase Microscopy

1. Preamble

```
SetDirectory["H:\My Documents\QPM\Grating microscopy"]
μm = 1 × 10^-6;
```

```
H:\My Documents\QPM\Grating microscopy
```

2. Import image files

The images used in this example are not of the best quality, however they should be sufficient for a demonstration.

The image taken by the camera comes as a 5 dot array (c.f. Image in section 4.3), with diagonally opposite images equidistant from focus which is in the centre. This is entirely due to the diffraction grating used. The improved system should provide a different style of image. Provided that they are consistent it should be possible to implement an automated process for extracting the images.

```
im1 = Import["Image3.1.bmp", "GrayLevels"];
im2 = Import["Image3.3.bmp", "GrayLevels"];
im3 = Import["Image3.2.bmp", "GrayLevels"];
```

Note that the import parameter - in this case "GrayLevels" is dependant on the image type - in this case a bitmap.

These images have already been roughly cut out of the main image by a different program, mathematica can replicate this procedure but with the 5 dot image pattern it is non trivial.

im1 = above focus
im2 = below focus
im3 = at focus

```
ArrayPlot[im1]
```

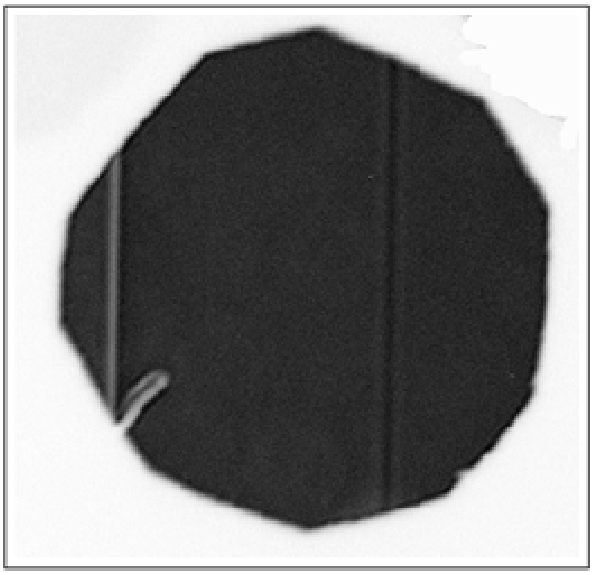

3. Crop and centre images

This is a critical step. As we intend to subtract the out of focus images it is important that we have images of the same size and that the images are correctly centred.

The following uses a centroid algorithm. This simply finds the central position of the "dark" image shape. As the image is pixelated this will have to be rounded to the nearest pixel to give the centre of the aperture area.

```
data = im1;
temp = Flatten[Table[{i, j, data[[i]][[j]]},
    {i, Length[data]}, {j, Length[data[[1]]]}], 1];
(*this flattens the array of data into a more
 useful and workable format*)

centroid = Round[ (Sum_{i=1}^{Length[temp]} temp[[i]][[3]] {temp[[i]][[1]], temp[[i]][[2]]}) / (Sum_{i=1}^{Length[temp]} temp[[i]][[3]]) ]
(*this gives the position of the centroid
 of the image rounded to the nearest pixel*)
{179, 201}
```

Based on this central position it is necessary to crop the image about the centre

```
imagesize = 111;
temp = Delete[data, Partition[
     Join[Range[1, centroid[[1]] - imagesize],
      Range[centroid[[1]] + imagesize, Length[data]]], 1]];
temp2 = Transpose[temp];
cropim1 = Delete[temp2, Partition[
     Join[Range[1, centroid[[2]] - imagesize],
      Range[centroid[[2]] + imagesize, Length[temp2]]], 1]];
ArrayPlot[Transpose[cropim1]]
```

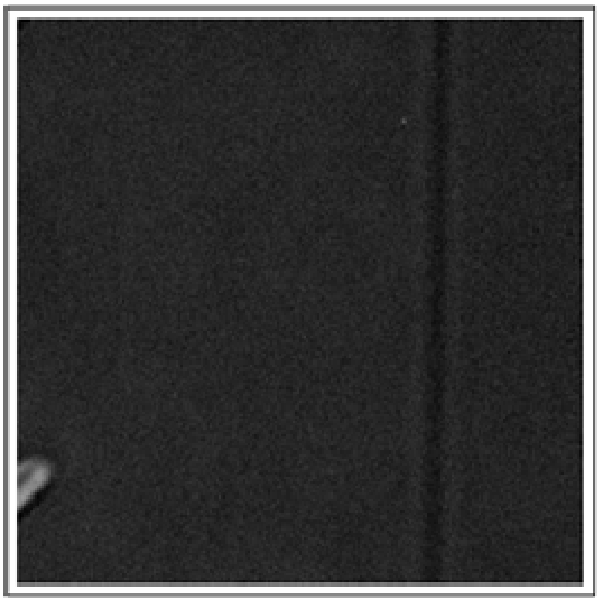

This can then be repeated with the other 2 images

```
data = im2;
temp = Flatten[Table[{i, j, data[[i]][[j]]},
    {i, Length[data]}, {j, Length[data[[1]]]}], 1];
(*this flattens the array of data into a more
 useful and workable format*)
```

$$\text{centroid} = \text{Round}\left[\frac{\sum_{i=1}^{\text{Length}[\text{temp}]} \text{temp}[[i]][[3]]\,(\text{temp}[[i]][[1]],\ \text{temp}[[i]][[2]])}{\sum_{i=1}^{\text{Length}[\text{temp}]} \text{temp}[[i]][[3]]}\right]$$

```
(*this gives the position of the centroid
 of the image rounded to the nearest pixel*)
imagesize = 111;
temp = Delete[data, Partition[Join[Range[1, centroid[[1]] - imagesize],
      Range[centroid[[1]] + imagesize, Length[data]]], 1]];
temp2 = Transpose[temp];
cropim2 =
  Delete[temp2, Partition[Join[Range[1, centroid[[2]] - imagesize],
      Range[centroid[[2]] + imagesize, Length[temp2]]], 1]];
ArrayPlot[Transpose[cropim2]]
```

```
{185, 176}
```

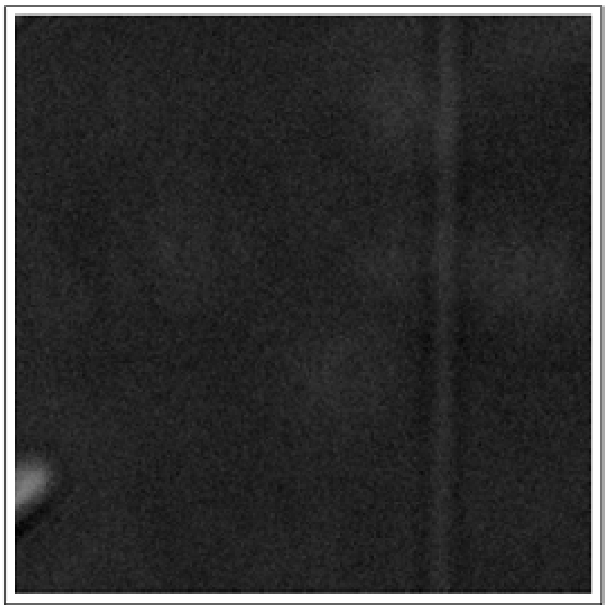

```
data = im3;
temp = Flatten[Table[{i, j, data[[i]][[j]]},
    {i, Length[data]}, {j, Length[data[[1]]]}], 1];
(*this flattens the array of data into a more
 useful and workable format*)

centroid = Round[ (Sum_{i=1}^{Length[temp]} temp[[i]][[3]] {temp[[i]][[1]], temp[[i]][[2]]}) / (Sum_{i=1}^{Length[temp]} temp[[i]][[3]]) ]
(*this gives the position of the centroid
 of the image rounded to the nearest pixel*)
imagesize = 111;
temp = Delete[data, Partition[Join[Range[1, centroid[[1]] - imagesize],
      Range[centroid[[1]] + imagesize, Length[data]]], 1]];
temp2 = Transpose[temp];
cropim3 =
  Delete[temp2, Partition[Join[Range[1, centroid[[2]] - imagesize],
      Range[centroid[[2]] + imagesize, Length[temp2]]], 1]];
ArrayPlot[Transpose[cropim3]]
```

```
{176, 193}
```

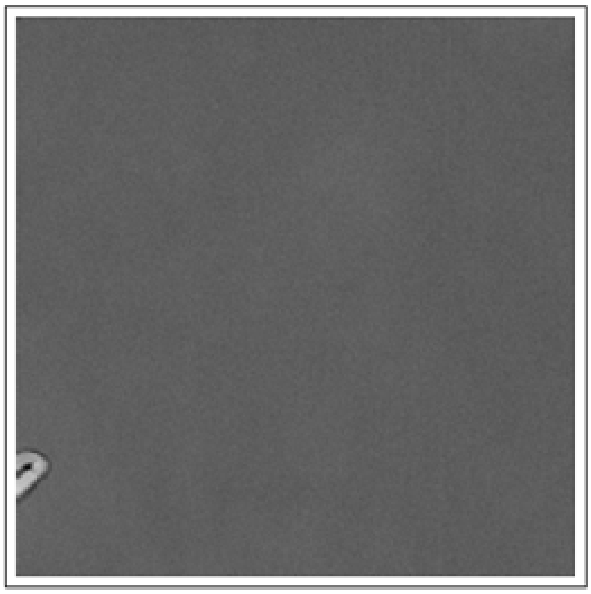

4. Prepare dI for FFT

dI/dz is approximated by the subtraction of the two off focus images. This is then subjected to FFT analysis and as such needs zero padding. This requires the dz (the ± focal position of the two images) and the wavelength used for the image.
n.b. the image has been transposed.

```
di = (cropim1 - cropim2) (2 π / (λ)) / dz;
λ = 6.33 μm;
dz = 4.5 μm;
ArrayPlot[di]
```

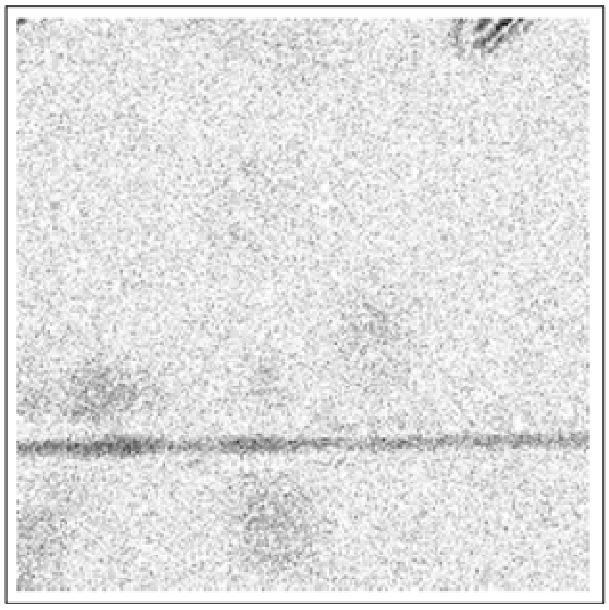

```
padding = 400;
paddat =
  PadRight[PadLeft[di, {Length[di] + padding, Length[di[[1]]] + padding}],
   {Length[di] + 2 padding, Length[di[[1]]] + 2 padding}];
ArrayPlot[paddat]
```

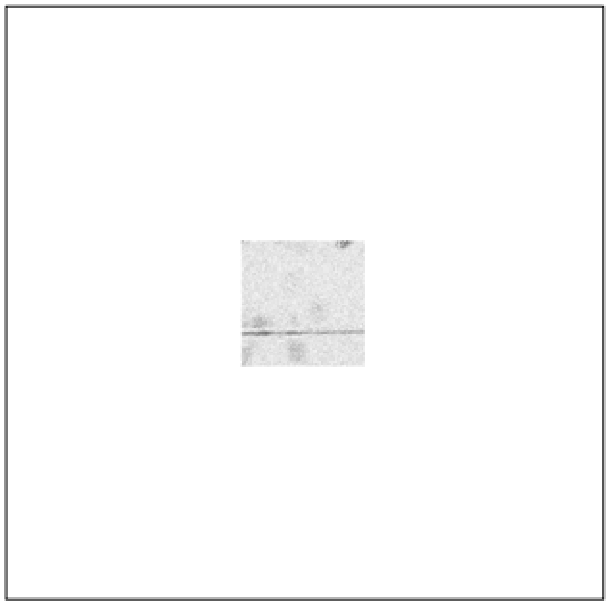

5. Phase algorithm

We first need to define a few constants - dependant on the image size and a *Io* which is the mean image intensity at focus. This is where this example breaks down a bit as the image at focus clearly is at a different image intensity to the others. This will result in scaling problems in the resultant phase profile.

```
fdata = Fourier[paddat];
b = Length[di];
a = Length[di[[1]]];
Io = Mean[Mean[im3]];
```

Next is to create a transform matrix to give the phase transformation

$$T = \text{Table}\left[\frac{(a\,b)^2}{(2\pi)^2\left(m^2 b^2 + n^2 a^2\right) Io},\ \{m, \text{Length}[fdata]\},\ \{n, \text{Length}[fdata[[1]]]\}\right];$$

And a filter for the FFT(F) - this prevents the low frequency components from being blown up to infinity and producing phase aberrations in the phase map.
In this case the example takes the form of a cross filter. The size of the cross has been rather arbitrarily set at >20 (which my previous research suggests is sufficient but this will require testing)

```
f = 25;
F = Table[Which[
     m ≤ f ⋀ n ≤ f, 0,
     m ≥ Length[fdata] - f ⋀ n ≤ f, 0,
     n ≥ Length[fdata[[1]]] - f ⋀ m ≤ f, 0,
     n ≥ Length[fdata[[1]]] - f ⋀ m ≥ Length[fdata] - f, 0,
     True, 1]
    ,
    {m, Length[fdata]}, {n, Length[fdata[[1]]]}];
ArrayPlot[F]
```

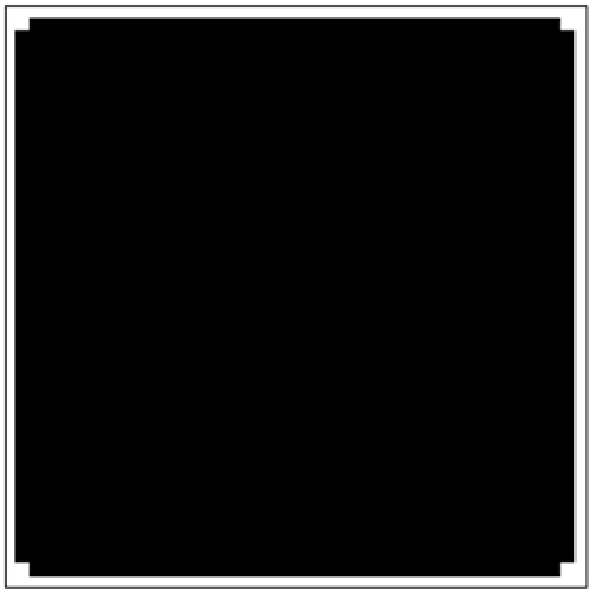

```
transformeddata = fdata FT;
phase = InverseFourier[transformeddata];

crop = Take[phase, {padding, Length[cropim3] + padding},
    {padding, Length[cropim3[[1]] + padding}];
ArrayPlot[
 crop]
```

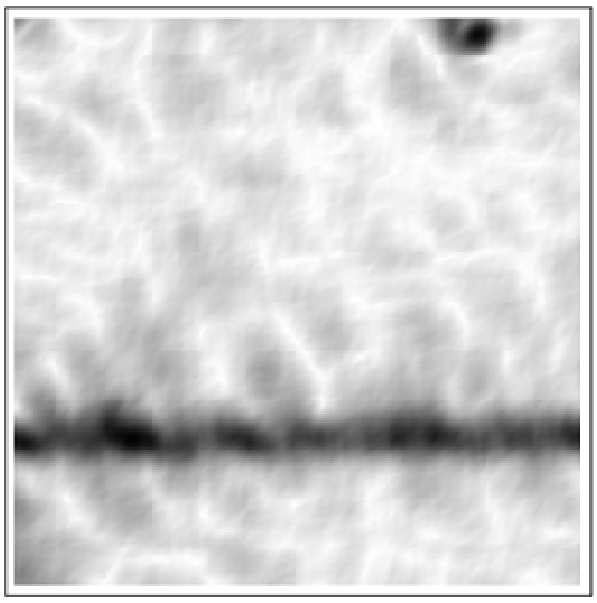

Which in this case is not a terribly convincing phase map but that is due to the original images being pretty poor. Note that the resultant image is incorrectly scaled. This is a combination of the focal image planes not being exactly spaced as assumed and the central focus being of different intensity. The important point is that for a given system it should be possible to create a calibration factor and us this to generate quantitative phase.

```
ListPlot[Re[crop[[50]]]]
ListPlot[Re[Transpose[crop][[50]]]]
```

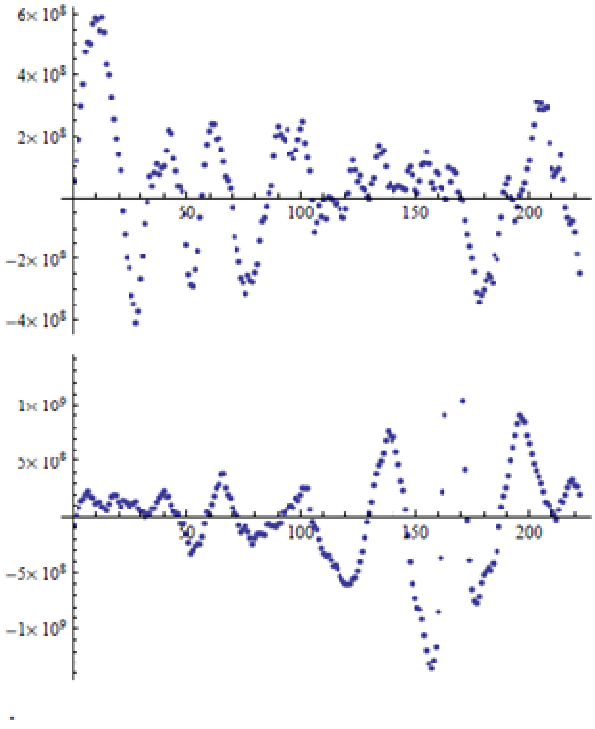

6. Fourier Mask Test

This runs a fairly simple program creating a completely random static image and putting it through the phase unwrap. The resultant phase map should be flat and as such the standard deviation of the image should give some idea of the error due to the low intensity magnification

```
static = Table[Random[], {m, Length[di]}, {n, Length[di]}];
```

```
ArrayPlot[static]
```

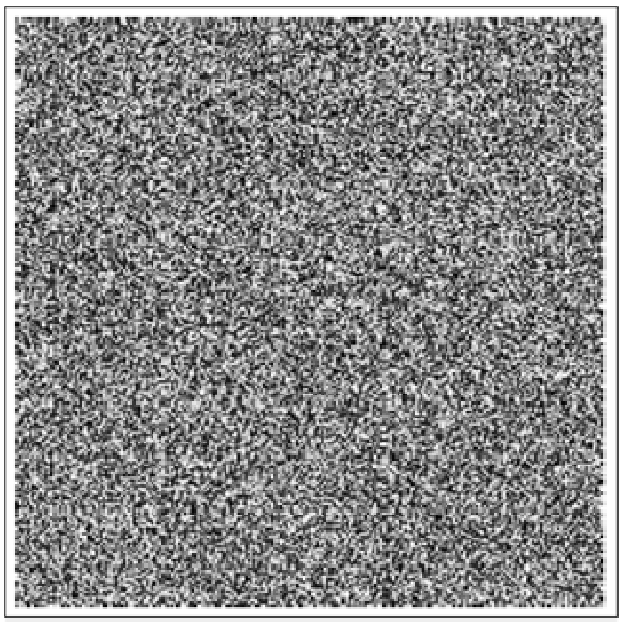

```
padding = 400;
paddat = PadRight[PadLeft[static,
     {Length[static] + padding, Length[static[[1]]] + padding}],
   {Length[static] + 2 padding, Length[static[[1]]] + 2 padding}];
ArrayPlot[paddat]
```

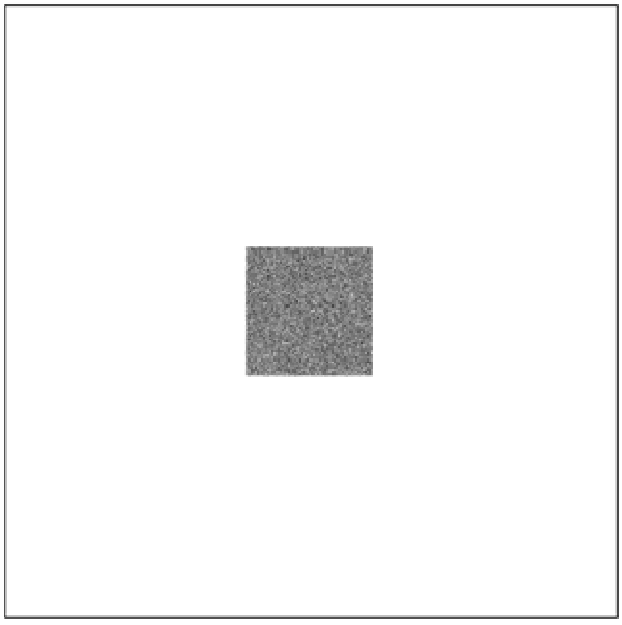

```
fdata = Fourier[paddat];
b = Length[static];
a = Length[static[[1]]];
Iö = 1;
```

```
σ = {};
Do[
 F = Table[Which[
    m ≤ f ∧ n ≤ f, 0,
    m ≥ Length[fdata] - f ∧ n ≤ f, 0,
    n ≥ Length[fdata[[1]]] - f ∧ m ≤ f, 0,
    n ≥ Length[fdata[[1]]] - f ∧ m ≥ Length[fdata] - f, 0,
    True, 1]
   ,
   {m, Length[fdata]}, {n, Length[fdata[[1]]]}];
 transformeddata = fdata F T;
 phase = InverseFourier[transformeddata];
 crop = Take[phase, {padding, Length[static] + padding},
   {padding, Length[static[[1]]] + padding}];
 AppendTo[σ, {f, StandardDeviation[Flatten[crop]]}], {f, 0, 50}]
```

```
Export["data.dat", σ, "Table"]
```

```
data.dat
```

```
ListLinePlot[σ, PlotRange → All, Frame → True, AxesOrigin → {0, 0}]
```

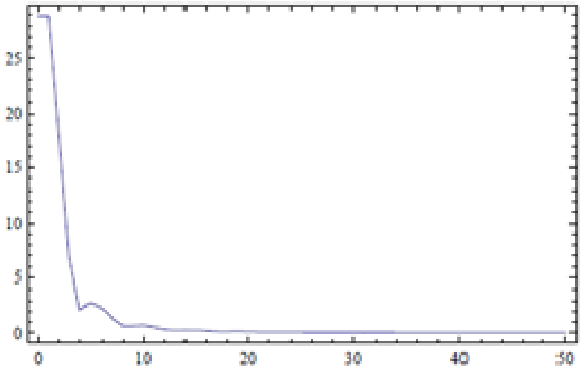

7. 1D approximation

As we are primarily interested in the phase along the length of the fibre (a measure of the grating index variation) it is not necessary to include the full 2 D data. Instead we can collapse the 2 D to 1 D along the axis of the fibre although for the purposes of this demonstration I will collapse it the other way to illustrate the possibility of detecting the fibre phase.

```
ArrayPlot[cropim1]
```

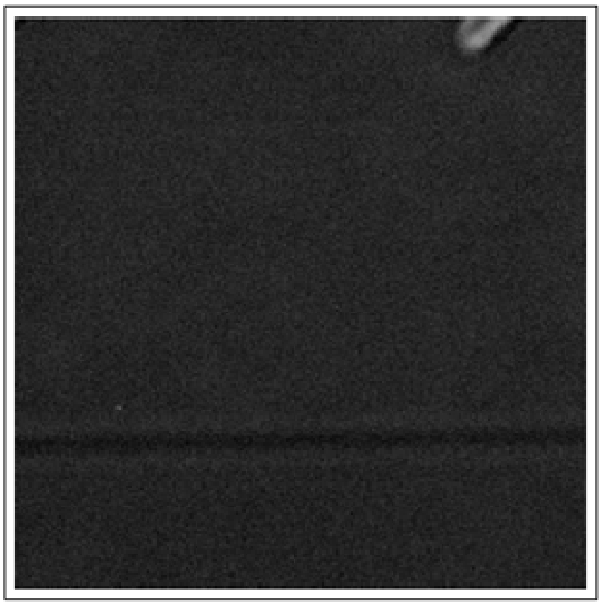

```
ListPlot[Table[Total[cropim1[[i]]], {i, Length[cropim1]}]]
```

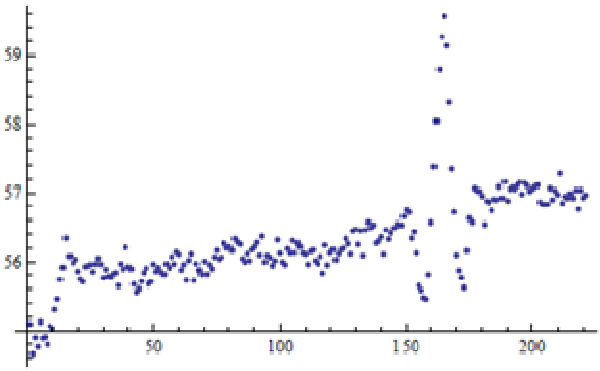

Here we can clearly see that there is a background problem with the image - there is a gradient ... For now we will ignore this.

```
ListPlot[Table[Total[cropim2[[i]]], {i, Length[cropim2]}]]
```

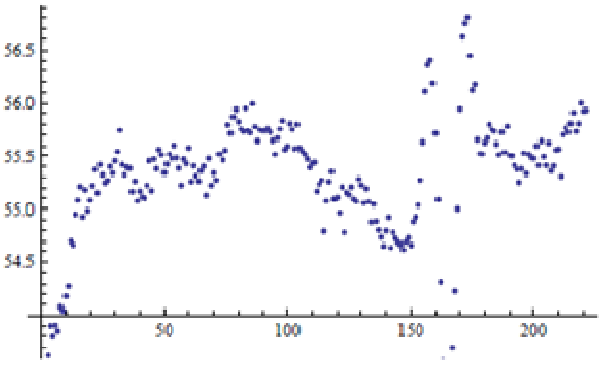

```
di = (Table[Total[cropim1[[i]]], {i, Length[cropim1]}] -
      Table[Total[cropim2[[i]]], {i, Length[cropim2]}]) (2 π / (λ)) / dz;
λ = 6.33 μm;
dz = 4.5 μm;

ListPlot[di, PlotRange → All]
```

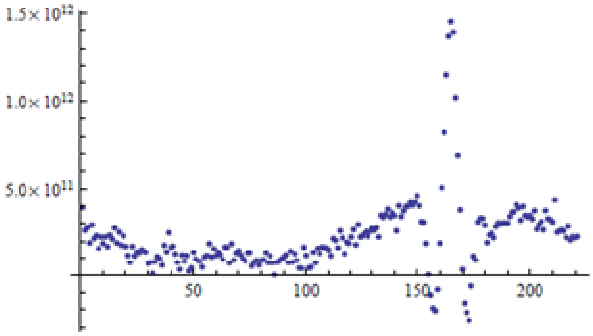

So it seems obvious that the image has not been correctly illuminated as there is a non - flat intensity difference outside the fibre region it is possible to create a background and subtract it but we will persevere as it is - now to pad it.

```
paddat =
  PadRight[PadLeft[di, padding + Length[di]], 2 padding + Length[di]];

ListPlot[paddat, PlotRange → All]
```

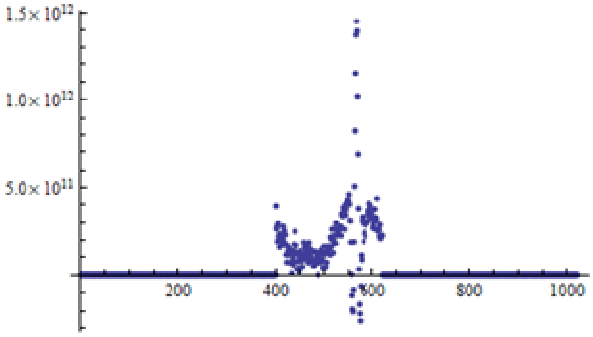


```
fdata = Fourier[paddat];
b = Length[di];
Io = Mean[Mean[im3]];

T = Table[(b)^2 / ((2 π)^2 (m^2 b^2)) Io, {m, Length[fdata]}];

f = 20;
F = PadRight[
    PadLeft[Table[1, {i, Length[T] - 2 f}], Length[T] - f], Length[T]];
```

```
ListPlot[F]
```

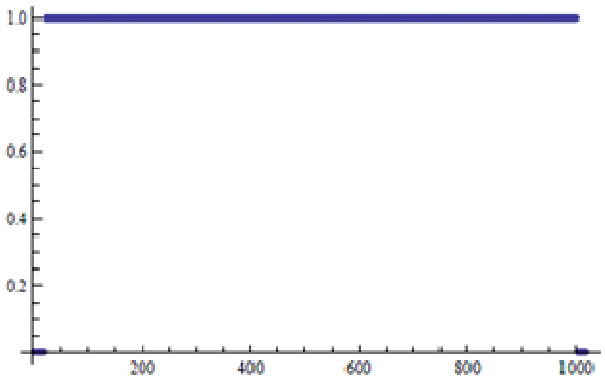


```
transformeddata = fdata F T;
phase = InverseFourier[transformeddata];
ListPlot[Abs[phase], PlotRange → All]
```

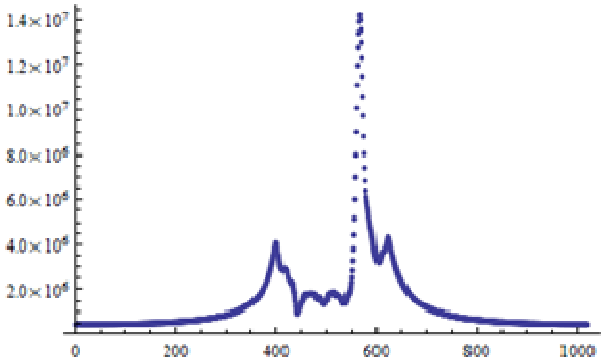

Appendix C: Surface Plasmon Resonance Model

Surface Plasmon Modeling 30.03.11

```
In[1]:= SetDirectory["H:\\My Documents\\SPR\\BK-7\\30.3.11"]
Out[1]= H:\My Documents\SPR\BK-7\30.3.11
```

Equations

First to define the various angles within the prism in terms of the measured refractive index θm

```
In[2]:= θ1 = π / 4 - θm;
        θ2 = ArcSin[Sin[θ1] / np];
        θa = π / 4 - θ2;
        θ3 = π / 4 - θa;
        θ4 = ArcSin[Sin[θ3] np];
```

With these angles defined it is possible to calculate the Fresnel Reflections at the air - glass and glass - air interface

```
In[7]:= R1 = ((Cos[θ2] - np Cos[θ1]) / (Cos[θ2] + np Cos[θ1]))^2;
        R2 = ((np Cos[θ2] - Cos[θ1]) / (np Cos[θ2] + Cos[θ1]))^2;
```

Define optical constats and seperate the comples permittivity of the metal into a real and imaginary component

```
In[9]:= εp = np^2;
        θm = θr + θ0;
        εm = εmr + I εmi;
        ω = (2 π c) / λ;
        c = 299 792 458;
```

Calculate the reflected power (R) from the glass - metal interface based on Chen

```
In[14]:= γ31 = (εp Kz1 - εm Kz3) / (εp Kz1 + εm Kz3);
         γ12 = (εm Kz2 - Kz1) / (εm Kz2 + Kz1);

         Kz1 = Sqrt[(εm ω^2) / c^2 - Kx^2];
         Kz2 = Sqrt[(ω^2) / c^2 - Kx^2];
         Kz3 = Sqrt[(εp ω^2) / c^2 - Kx^2];
         Kx = (Sqrt[εp] ω) / c Sin[θa];
         R = Abs[(γ31 + γ12 Exp[I 2 Kz1 d]) / (1 + γ31 γ12 Exp[I 2 Kz1 d])]^2;
```

Converting all three reflection losses to dB

```
In[21]:= R1dB = 10 Log[10, (1 - R1) / 1];
         R2dB = 10 Log[10, (1 - R2) / 1];
         RdB = 10 Log[10, R / 1];
```

It is also possible to include the absorption losses of the glass (which are negligable)

```
In[24]:= H1 = 25 / Sqrt[2] / Sin[π / 2 - θa];
         B = H1 Sin[θa];
         Ee = (25 / Sqrt[2] + B) Sin[π / 4];
         H2 = Ee / Sin[π / 4 + θa];
         Dtravel = H1 + H2;
         Tloss = Tl Dtravel;
```

The combined losses can be added (in dB)

```
ReflecteddB = R1dB + R2dB + RdB + Tloss;
ReflectedP = A 10^(ReflecteddB / 10);
```

The measured Pd values may be use as starting values for the fit

```
In[43]:= erpd = -57.52047660480001`
         eipd = +59.6633990936`
Out[43]= -57.5205
Out[44]= 59.6634
```

Experimental Fits :

Import the data sets for nitrogen (file 1 and file 2 combined) and re-format them into a mathematica friendly format

```
In[32]:= file1 = Import["run1.dat", "Table"];
         file2 = Import["run2.dat", "Table"];
         data1 = Thread[
            {Transpose[file1][[1]] Degree, Transpose[file1][[2]] / Transpose[file1][[3]]}];
         data2 = Thread[{Transpose[file2][[1]] Degree,
             Transpose[file2][[2]] / Transpose[file2][[3]]}];
         ndata = Delete[Join[data1, data2], 37];

In[37]:= ListPlot[ndata]
```

Out[37]=

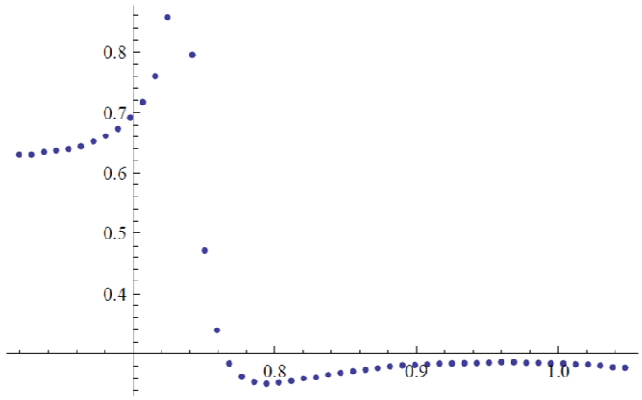

Find a fit between the model based on known values (fixed) and estimated values (guess)

In[45]:=
```
fixed = {λ → 1523.5 × 10^-9, np → 1.501, Tl → 10 Log[10, 0.98] / 25};
variable =
  {{A, 1.35}, {θ0, -0.037}, {d, 2.4 × 10^-8}, {ϵmi, ϵipd}, {ϵmr, ϵrpd}};
nfit = NonlinearModelFit[ndata, ReflectedP /. fixed, variable, θr];
nfit[{"BestFitParameters", "ParameterTable"}]
Plot[(ReflectedP) /. Join[fixed, nfit["BestFitParameters"]],
 {θr, 0.5, 1.1}, PlotRange → All, Epilog → Map[Point, ndata]]
```

Out[48]=

$$\{\{A \to 1.50928,\ \theta 0 \to -0.029325,\ d \to 2.20643 \times 10^{-8},\ \epsilon mi \to 51.3963,\ \epsilon mr \to -43.8615\}\},$$

	Estimate	Standard Error	t Statistic	P-Value
A	1.50928	0.000902707	1671.95	2.58066×10^{-107}
θ0	−0.029325	0.0000439477	−667.269	9.19474×10^{-90}
d	2.20643×10^{-8}	1.21165×10^{-10}	182.101	5.8556×10^{-65}
ϵmi	51.3963	0.30279	169.742	1.28428×10^{-63}
ϵmr	−43.8615	0.137972	−317.902	1.34511×10^{-75}

Out[49]=

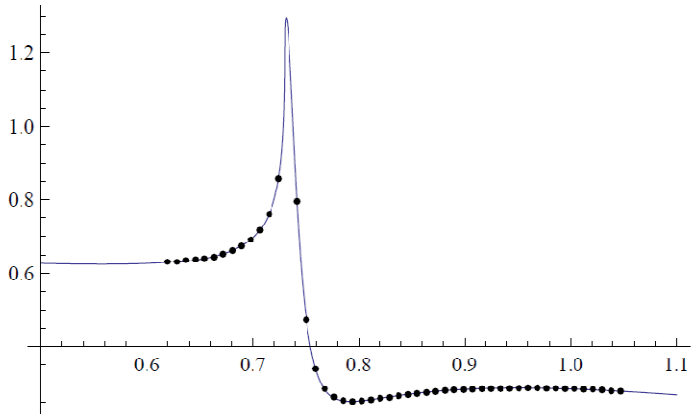

References

[1] I.B.O.W.M., and B. N. Taylor, [The international system of units (SI)] US Dept. of Commerce, Technology Administration, National Institute of Standards and Technology, (2001).

[2] D. Colladon, “Sur les réflections d'un rayon de lumiére à l'intérieur d'une veine liquid parabolique,” Comptes Rendus, 15, 800-802 (1842).

[3] G. P. Agrawal, [Fiber-optic communication systems] Wiley New York, (1997).

[4] B. Dussardier, and W. Blanc, "Novel Dopants for Silica-Based Fiber Amplifiers," National Fiber Optic Engineers Conference, 1-3 (2007).

[5] J. Wilson, and J. Hawkes, [Optoelectronics an Introduction] Prentice Hall, (1998).

[6] T. Huebert, L. Boon-Brett, G. Black *et al.*, “Hydrogen sensors - A review,” Sensors and Actuators B-Chemical, 157(2), 329-352 (2011).

[7] S. F. Silva, L. Coelho, O. Frazao *et al.*, “A Review of Palladium-Based Fiber-Optic Sensors for Molecular Hydrogen Detection,” IEEE Sensors Journal, 12(1), 93-102 (2012).

[8] K. C. Lin, C. J. Lin, and W. Y. Lee, "Effects of gamma radiation on optical fibre sensors," IEEE Optoelectronics, 151, 12-15 (2004).

[9] E. V. Anoikin, A. N. Guryanov, D. D. Gusovsky *et al.*, “UV and gamma-radiation damage in silica glass and fibres doped with germanium and cerium,” Nuclear Instruments & Methods in Physics Research Section B-Beam Interactions with Materials and Atoms, 65(1-4), 392-396 (1992).

[10] E. M. Dianov, I. A. Bufetov, A. A. Frolov *et al.*, “Catastrophic destruction of optical fibres of various composition caused by laser radiation,” Quantum Electronics, 32(6), 476-478 (2002).

[11] E. M. Dianov, L. S. Kornienko, E. P. Nikitin *et al.*, “Radiation-optical properties of silica-glass fiber-optic waveguides,” Kvantovaya Elektronika, 10(3), 473-496 (1983).

[12] M. N. Ott, "Radiation effects data on commercially available optical fiber: database summary," IEEE Radiation Effects Data Workshop, 24-31 (2002).

[13] E. M. Dianov, K. M. Golant, R. R. Khrapko *et al.*, [Radiation resistance of optical fibres with fluorine-doped silica cladding], (1994).

[14] E. Dianov, K. Golant, R. Khrapko *et al.*, “Nitrogen doped silica core fibres: a new type of radiation-resistant fibre,” Electronics Letters, 31(17), 1490-1491 (1995).

[15] N. Nikitenkova, A. Hashhashb, T. Sigfussonc *et al.*, "Study of the Hydrogen–Metal Systems," International Congress on Advances in Applied Physics and Materials Science, (2012).

[16] A. Othonos, K. Kalli, D. Pureur *et al.*, “Fibre Bragg gratings,” Wavelength Filters in Fibre Optics, 189-269 (2006).

[17] R. Kashyap, [Fiber bragg gratings] Academic Press, (1999).

[18] T. Erdogan, “Cladding-mode resonances in short- and long-period fiber grating filters,” Journal of the Optical Society of America A, 14(8), 1760-1773 (1997).

[19] E. Anemogiannis, E. N. Glytsis, and T. K. Gaylord, “Transmission characteristics of long-period fiber gratings having arbitrary azimuthal/radial refractive index variations,” Journal of Lightwave Technology, 21(1), 218-227 (2003).

[20] A. Cusano, A. Iadicicco, P. Pilla *et al.*, “Mode transition in high refractive index coated long period gratings,” Optics Express, 14(1), 19-34 (2006).

[21] T. Erdogan, “Cladding mode resonances in short- and long-period fibre grating filters: errata,” Journal of the Optical Society of America A, 17(11), 2113 (2000).

[22] T. Erdogan, “Fiber grating spectra,” Journal of Lightwave Technology, 15(8), 1277-1294 (1997).

[23] R. Hou, Z. Ghassemlooy, A. Hassan *et al.*, "Modeling of long-period fibre grating response to refractive index higher than that of cladding," Measurement Science and Technology, 12, 1709-1713 (2001).

[24] H. J. Patrick, A. D. Kersey, and F. Bucholtz, "Analysis of the response of long period fiber gratings to external index of refraction," Journal of Lightwave Technology, 16(9), 1606-1612 (1998).

[25] D. B. Stegall, and T. Erdogan, "Leaky cladding mode propagation in long-perod fiber grating devices," IEEE Photonics Technology Letters, 11(3), 343-345 (1999).

[26] K. O. Hill, Y. Fujii, D. C. Johnson *et al.*, "Photosensitivity in optical fiber waveguides: Application to reflection filter fabrication," Applied Physics Letters, 32(10), 647-649 (1978).

[27] D. P. Hand, and P. S. J. Russell, "Photoinduced refractive-index changes in germanosilicate fibers," Optics Letters, 15(2), 102-104 (1990).

[28] D. K. W. Lam, and B. K. Garside, "Characterization of single-mode optical fiber filters," Applied Optics, 20(3), 440-445 (1981).

[29] B. A. Childers, M. E. Froggatt, S. G. Allisonb *et al.*, "Use of 3000 Bragg grating strain sensors distributed on four eight-meter optical fibers during static load tests of a composite structure," Laser, 2(C1), C2 (2001).

[30] G. D. Lloyd, L. A. Everall, K. Sugden *et al.*, "Resonant cavity based fibre Bragg grating sensor interrogation using ratiometric detection," Optical Communications, 244(193-197), (2005).

[31] M. Majumder, T. K. Gangopadhyay, A. K. Chakraborty *et al.*, "Fibre Bragg gratings in structural health monitoring - present status and applications," Sensors and Actuators A: Physical, 147(1), 150-164 (2008).

[32] Y. J. Rao, "In-fibre Bragg grating sensors," Measurement Science and Technology, 8, 355-375 (1997).

[33] A. Trouillet, E. Marin, and C. Veillas, "Fibre gratings for hydrogen sensing," Measurement Science and Technology, 17, 1124-1128 (2006).

[34] R. R. J. Maier, B. J. S. Jones, J. S. Barton *et al.*, "Fibre optics in palladium-based hydrogen sensing," Journal of Optics A: Pure and Applied Optics, 9(6), S45-S59 (2007).

[35] V. Bhatia, "Applications of long-period gratings to single and multi-parameter sensing," Optics Express, 4(11), 457-466 (1999).

[36] K. Gao, J. X. Geng, A. B. Yu *et al.*, "Characteristics of metal-coated long-period fiber gratings," Optical Fiber and Planar Waveguide Technology II (Proceedings of SPIE), 4904, 166-170 (2002).

[37] S. W. James, and R. P. Tatam, "Optical fibre long-period grating sensors: Characteristics and applications," Measurement Science and Technology, 14, R49-R61 (2003).

[38] V. Bhatia, D. K. Campbell, D. Sherr *et al.*, "Temperature-insensitive and strain-insensitive long-period grating sensors for smart structures," Optical Engineering, 36(7), 1872-1876 (1997).

[39] L. Zhang, Y. Liu, L. Everall *et al.*, "Design and realization of long-period grating devices in conventional and high birefringence fibers and their novel applications as fiber-optic load sensors," IEEE Journal of Selected Topics in Quantum Electronics, 5(5), 1373-1378 (1999).

[40] B. Lee, and J. Nishii, "Cladding-surrounding interface insensitive long-period grating," Electronics Letters, 34(11), 1129-1130 (1998).

[41] B. H. Lee, Y. Liu, S. B. Lee *et al.*, "Displacements of the resonant peaks of a long-period fiber grating induced by a change of ambient refractive index," Optics Letters, 22(23), 1769-1771 (1997).

[42] D. M. Costantini, C. A. P. Muller, S. A. Vasiliev *et al.*, "Tunable loss filter based on metal-coated long-period fiber grating," IEEE Photonics Technology Letters, 11(11), 1458-1460 (1999).

[43] O. Duhem, A. DaCosta, J. F. Henninot *et al.*, "Long period copper-coated grating as an electrically tunable wavelength-selective filter," Electronics Letters, 35(12), 1014-1016 (1999).

[44] Y.-J. He, Y.-L. Lo, and J.-F. Huang, "Optical-fiber surface-plasmon-resonance sensor employing long-period fiber gratings in multiplexing," Journal of the Optical Society of America B, 23(5), 801-811 (2006).

[45] A. K. Sharma, R. Jha, and B. D. Gupta, "Fiber-optic sensors based on surface plasmon resonance: A comprehensive review," IEEE Sensors Journal, 7(8), 1118-1129 (2007).

[46] T. P. Leervad Pedersen, C. Liesch, C. Salinga *et al.*, "Hydrogen-induced changes of mechanical stress and optical transmission in thin Pd films," Thin Solid Films, 458(1-2), 299-303 (2004).

[47] O. Heavens, "Optical properties of thin films," Reports on Progress in Physics, 23, 1 (1960).

[48] X. Shu, X. Zhu, Q. Wang *et al.*, "Dual resonant peaks of LP_{015} cladding mode in long-period gratings," Electronics Letters, 35(8), 649-651 (1999).

[49] C. S. Cheung, S. M. Topliss, S. W. James *et al.*, "Response of fiber-optic long-period gratings operating near the phase-matching turning point to the deposition of nanostructured coatings," Journal of the Optical Society of America B, 25(6), 897-902 (2008).

[50] V. Grubsky, and J. Feinberg, "Long-period fiber gratings with variable coupling for real-time sensing applications," Optics Letters, 25(4), 203-205 (2000).

[51] R. M. Atkins, P. J. Lemaire, T. Erdogan *et al.*, "Mechanisms of enhanced UV photosensitivity via hydrogen loading in germanosilicate glasses," Electronics Letters, 29(14), 1234-1235 (1993).

[52] S. A. Slattery, and D. N. Nikogosyan, "Long-period fiber grating inscription under high-intensity 352 nm femtosecond irradiation: Three-photon absorption and energy deposition in cladding," Optics Communications, 255(1-3), 81-90 (2005).

[53] G. Meltz, W. W. Morey, and W. H. Glenn, "Formation of Bragg gratings in optical fibers by a transverse holographic method," Optics Letters, 14(15), 823-825 (1989).

[54] A. Martinez, I. Y. Khrushchev, and I. Bennion, "Thermal properties of fibre Bragg gratings inscribed point-by-point by infrared femtosecond laser," Electronics Letters, 41(4), 176-178 (2005).

[55] M. Fujimaki, Y. Ohki, J. L. Brebner *et al.*, "Fabrication of long-period optical fiber gratings by use of ion implantation," Optics Letters, 25(2), 88-89 (2000).

[56] E. M. Dianov, V. I. Karpov, M. V. Grekov *et al.*, "Thermo-induced long-period fibre gratings." 2, 53-56 vol. 2.

[57] C. S. Kim, Y. Han, B. H. Lee *et al.*, "Induction of the refractive index change in B-doped optical fibers through relaxation of the mechanical stress," Optics Communications, 185, 337-342 (2000).

[58] P. Palai, M. N. Satyanarayan, M. Das *et al.*, "Characterization and simulation of long period gratings fabricated using electric discharge," Optics Communications, 193, 181-185 (2001).

[59] D. D. Davis, T. K. Gaylord, E. N. Glytsis *et al.*, "Long-period fibre grating fabrication with focused CO_2 laser pulses," Electronics Letters, 34(3), 302-303 (1998).

[60] Y. Kondo, K. Nouchi, T. Mitsuyu *et al.*, "Fabrication of long-period fiber gratings by focused irradiation of infrared femtosecond laser pulses," Optics Letters, 24(10), 646-648 (1999).

[61] V. Bhatia, and A. M. Vengsarkar, “Optical fiber long-period grating sensors,” Optics Letters, 21(9), 692-694 (1996).
[62] Coherent Inc., 2007, "BraggStar S-Industrial Series," [Datasheet]: http://www.coherent.com/downloads/BraggStar_S-Industrial_DS_04-07.pdf, [12/3/12]
[63] E. Hecht, [Optics,] IE, Addison-Wesley Publishing Company, (1998).
[64] E. Lindner, C. Chojetzki, S. Brückner *et al.*, “Thermal regeneration of fiber Bragg gratings in photosensitive fibers,” Optics Express, 17(15), 12523-12531 (2009).
[65] A. M. Vengsarkar, P. J. Lemaire, J. B. Judkins *et al.*, “Long-period fiber gratings as band-rejection filters,” Journal of Lightwave Technology, 14(1), 58-65 (1996).
[66] C. Tsao, [Optical fibre waveguide analysis] Oxford University Press, (1992).
[67] K. Morishita, “Numerical analysis of pulse broadening in grated index optical fibers,” IEEE Transations on Microwave Theory and Techniques, MTT-29(4), 348-352 (1981).
[68] D. K. Benson, C. E. Tracy, G. Hishmeh *et al.*, "Low-cost fiber optic chemochromic hydrogen detector." NREL/CP-570-25315.
[69] J. N. Huiberts, R. Griessen, J. H. Rector *et al.*, “Yttrium and lanthanum hydride films with switchable optical properties,” Nature, 380(6571), 231-234 (1996).
[70] Y. Imai, Y. Okuhara, Y. Noguchi *et al.*, “Optically readable hydrogen sensor using Pd/Y double-layered thin films,” AZojomo (ISSN 1833-122X), 2, (2006).
[71] G. K. Mor, L. K. Malhotra, and D. Bhattacharyya, “Effect of palladium cap layer thickness on desorption of hydrogen from PrH_x films: A spectroscopic ellipsometry study,” Journal of Applied Physics, 90(4), 1795-1800 (2001).
[72] K. V. Rottkay, M. Rubin, F. Michalak *et al.*, “Effect of hydrogen insertion on the optical properties of Pd-coated magnesium lanthanides,” Electrochimica Acta, 44(18), 3093-3100 (1999).
[73] M. Ando, “Recent advances in optochemical sensors for the detection of H_2, O_2, O_3, CO, CO_2, and H_2O in air,” Trends in Analytical Chemistary, 25(10), 937-948 (2006).
[74] J. Isidorsson, I. Giebels, H. Arwin *et al.*, “Optical properties of MgH_2 measured in situ by ellipsometry and spectrophotometry,” Physical Review B, 68(11), 115112 (2003).
[75] K. Ito, and T. Ohgami, “Hydrogen detection based on coloration of anodic tungsten oxide film,” Applied Physics Letters, 60(8), 938-940 (1992).
[76] S. Moehlecke, C. F. Majkrzak, and M. Strongin, “Enhanced hydrogen solubility in niobium films,” Physical Review B, 31(10), 6804-6806 (1985).
[77] M. Pasturel, M. Slaman, H. Schreuders *et al.*, “Hydrogen absorption kinetics and optical properties of Pd-doped Mg thin films,” Journal of Applied Physics, 100, 023515 (2006).
[78] M. Pasturel, R. J. Wijngaarden, W. Lohstroh *et al.*, “Influence of the chemical potential on the hydrogen sorption kinetics of Mg2Ni/TM/Pd (TM = transition metal) trylayers,” Chemical Materials, 19, 624-633 (2007).
[79] F. A. Lewis, “Solubility of hydrogen in metals,” Pure and Applied Chemistry, 62(11), 2091 (1990).
[80] F. A. Lewis, “The palladium hydrogen system,” Academic Press Inc. New york, (1967).
[81] M. Wang, and Y. Feng, “Palladium–silver thin film for hydrogen sensing,” Sensors and Actuators B: Chemical, 123(1), 101-106 (2006).
[82] Z. Zhao, Y. Sevryugina, M. A. Carpenter *et al.*, “All-optical hydrogen-sensing materials based on tailored palladium alloy thin films,” Analytical Chemistry, 76(21), 6321-6326 (2004).
[83] P. Zoltowski, and E. Makowska, “Diffusion coefficient of hydrogen in-phase palladium and palladium–platinum alloy,” Physical Chemistry Chemical Physics, 3, 2935-2942 (2001).

[84] F. A. Lewis, “The palladium-hydrogen system: a survey of hydride formation and the effects of hydrogen contained within the metal lattices,” Platinum Metals Review, 26(1), 20-27 (1982).

[85] F. A. Lewis, “The palladium-hydrogen system: part II of a survey of features ” Platinum Metals Review, 26(2), 70-78 (1982).

[86] F. A. Lewis, “The palladium-hydrogen system: part III: alloy systems and hydrogen permeation,” Platinum Metals Review, 26(3), 121-128 (1982).

[87] L. W. McKeehan, “The crystal structures of the system palladium-hydrogen,” Physical Review, 21(3), 334-342 (1923).

[88] A. C. Bailey, N. Waterhouse, and B. Yates, “The thermal expansion of palladium-silver alloys at low temperatures,” Journal of Physics C: Solid State Physics, 2(5), 769-776 (1969).

[89] R. Caputo, and A. Alavi, “Where do the H atoms reside in PdH_x systems?,” Molecular Physics, 101(11), 1781-1787 (2003).

[90] A. Fabre, E. Finot, J. Demoment *et al.*, “In situ measurements of elastic properties of PdH_x, PdD_x and PdT_x,” Journal of Alloys and Compounds, 356-357, 372-376 (2003).

[91] S. Krüger, S. Vent, F. Nörtemann *et al.*, “The average bond length in Pd clusters Pd_n, n = 4–309: A density-functional case study on the scaling of cluster properties,” Journal of Chemical Physics, 115(5), (2001).

[92] T. Mitsui, M. K. Rose, E. Fomin *et al.*, “Dissociative hydrogen adsorption on palladium requires aggregates of three or more vacancies,” Nature, 422(6933), 705-707 (2003).

[93] D. Tománek, Z. Sun, and S. G. Louie, “Ab initio calculation of chemisorption systems: H on Pd (001) and Pd (110),” Physical Review B, 43(6), 4699-4713 (1991).

[94] C. Christofides, and A. Mandelis, “Solid-state sensors for trace hydrogen gas detection,” Journal of Applied Physics, 68(6), R1-R30 (1990).

[95] F. DiMeo, I. S. Chen, P. Chen *et al.*, “MEMS-based hydrogen gas sensors,” Sensors and Actuators B, 117(1), 10-16 (2006).

[96] Y. Cao, H. L. Li, J. A. Szpunar *et al.*, “Modeling of hydrogen trapping in the deformed Pd and $Pd_{77}Ag_{23}$ alloy,” Materials Science and Engineering A, 379(1-2), 173-180 (2004).

[97] T. E. Felter, E. C. Sowa, and M. A. Van Hove, “Location of hydrogen adsorbed on palladium (111) studied by low-energy electron diffraction,” Physical Review B: Condensed Matter, 40(2), 891-899 (1989).

[98] K. M. Ho, C. Elsasser, C. T. Chan *et al.*, “First-principles pseudopotential calculations for hydrogen in 4d transition metals: I. Mixed-basis method for total energies and forces,” Journal of Physics: Condensed Matter, 4(22), 5189-5206 (1992).

[99] F. A. Lewis, “Hydrogen in palladium and palladium alloys,” International Journal of Hydrogen Energy, 21(6), 461-464 (1996).

[100] X. W. Wang, S. G. Louie, and M. L. Cohen, “Hydrogen interactions in PdH_n ($1 \le n \le 4$),” Physical Review B, 40(8), 5822-5825 (1989).

[101] I. Wei, and J. Brewer, “Desorption of Hydrogen from Palladium Plating,” AMP Journal of Technology, 5, 49-53 (1996).

[102] F. A. Lewis, “The palladium-hydrogen system: structures near phase transition and critical points,” International Journal of Hydrogen Energy, 20(7), 587-592 (1995).

[103] Y. Okuhara, Y. Imai, Y. Noguchi *et al.*, “Influence of phase transformation in Pd hydride on the recovery characteristics of optical hydrogen sensors,” Bullitin of Materials Science, 22(6), 999–1001 (1999).

[104] J. B. Hunter, “A new hydrogen purification process: commercial development of palladium alloy diffusion cells,” Platinum Metals Review, 4(4), 130-131 (1960).

[105] A. Magnouche, and R. Fromageau, “Hydrogen dissolution in palladium: A resistometric study under pressure,” Journal of Applied Physics, 56, 1617 (1984).

[106] P. Wright, “The effect of occluded hydrogen on the electrical resistance of palladium,” Proceedings of the Physical Society A, 63(7), 727-739 (1950).
[107] D. P. Arndt, R. M. A. Azzam, J. M. Bennett *et al.*, “Multiple determination of the optical constants of thin-film coating materials,” Applied Optics, 23(20), 3571-3596 (1984).
[108] J. P. Ferraton, G. Leveque, and S. Robin-Kandare, “Optical properties of silver-palladium alloys,” Journal of Physics F: Metal Physics, 5(7), 1433-1438 (1975).
[109] M. A. Ordal, L. L. Long, R. J. Bell *et al.*, “Optical properties of the metals Al, Co, Cu, Au, Fe, Pb, Ni, Pd, Pt, Ag, Ti, and W in the infrared and far infrared,” Applied Optics, 22(7), 1099-1120 (1983).
[110] B. T. Sullivan, “Optical properties of palladium in the visible and near UV spectral regions,” Applied Optics, 29(13), 1964-1970 (1990).
[111] P. B. Johnson, and R. W. Christy, “Optical constants of transition metals: Ti, V, Cr, Mn, Fe, Co, Ni, Pd,” Physics Review B: Solid state, 9(12), 5056-5070 (1974).
[112] B. T. Sullivan, and R. R. Parsons, “A spectroellipsometric investigation of the effect of argon partial pressure on sputtered palladium films,” Journal of Vacuum Science and Technology A: Vacuum, Surfaces, and Films, 5(6), 3399-3407 (1987).
[113] X. Bévenot, A. Trouillet, C. Veillas *et al.*, “Surface plasmon resonance hydrogen sensor using an optical fibre,” Measurement Science and Technology, 13, 118-124 (2002).
[114] K. Kalli, A. Othonos, C. Christofides *et al.*, “Temperature-induced reflectivity changes and activation of hydrogen sensitive optically thin palladium films on silicon oxide,” Review of Scientific Instruments, 69(9), 3331-3338 (1998).
[115] R. Musket, “Effects of contamination on the interaction of hydrogen gas with palladium: a review,” Journal of the Less Common Metals, 45(2), 173-183 (1976).
[116] P. Albers, J. Pietsch, and S. F. Parker, “Poisoning and deactivation of palladium catalysts,” Journal of Molecular Catalysis A: Chemical, 173(1-2), 275-286 (2001).
[117] A. B. Antoniazzi, A. A. Haasz, and P. C. Stangeby, “The effect of adsorbed carbon and sulphur on hydrogen permeation through palladium,” Journal of Nuclear Materials, 162-164, 1065-1070 (1989).
[118] F. J. Castro, G. Meyer, and G. Zampieri, “Effects of sulfur poisoning on hydrogen desorption from palladium,” Journal of Alloys and Compounds, 330-332, 612-616 (2002).
[119] P. O. Nilsson, and M. S. Shivaraman, “Optical properties of PdO in the range of 0.5-5.4 eV,” Journal of Physics C: Solid State Physics, 12, 1423-1427 (1979).
[120] E. H. Voogt, A. J. M. Mens, O. L. J. Gijzeman *et al.*, “Adsorption of oxygen and surface oxide formation on Pd (111) and Pd foil studied with ellipsometry, LEED, AES and XPS,” Surface Science, 373(2-3), 210-220 (1997).
[121] K. J. Stout, and L. Blunt, [Three-dimensional surface topography] Butterworth-Heinemann, (2000).
[122] C. Wagner, “Handbook of X-ray photoelectron spectroscopy,” Surface And Interface Analysis, 3(4), (1981).
[123] S. A. Maier, [Plasmonics: fundamentals and applications] Springer Verlag, (2007).
[124] J. N. Hilfiker, N. Singh, T. Tiwald *et al.*, “Survey of methods to characterize thin absorbing films with spectroscopic ellipsometry,” Thin Solid Films, 516, 7979-7989 (2008).
[125] D. A. Usanov, A. V. Skripal, A. V. Skripal *et al.*, “Measurement of the parameters of nanometer films by optical and microwave methods,” Semiconductors, 45(13), 1694-1698 (2011).
[126] E. Kretschmann, “Die bestimmung optischer konstanten von metallen durch anregung von oberflächenplasmaschwingungen,” Zeitschrift fur Physik A, 241, 313-324 (1971).

[127] W. P. Chen, and J. M. Chen, "Use of surface plasmon waves for determination of the thickness and optical constants of thin metallic films," Journal of the Optical Society of America, 71(2), 189-191 (1981).
[128] Z. D. Genchev, N. M. Nedelchev, E. Mateev *et al.*, "Analytical approach to the prism coupling problem in the kretschmann configuration," Plasmonics, 3, 21-26 (2008).
[129] H. J. Simon, D. E. Mitchell, and J. G. Watson, "Surface plasmons in silver films—a novel undergraduate experiment," American Journal of Physics, 43, 630 (1975).
[130] D. A. Flavin, R. McBride, and J. D. C. Jones, "Interferometric fiber-optic sensing based on the modulation of group delay and first order dispersion: application to strain-temperature measurand," Journal of Lightwave Technology, 13(7), 1314-1323 (1995).
[131] D. A. Flavin, R. McBride, J. D. C. Jones *et al.*, "Combined temperature and strain measurement with a dispersive optical fiber Fourier-transform spectrometer," Optics Letters, 19(24), 2167-2169 (1994).
[132] P. Harrison, [Fibre optic interferometry for long-term configuration monitoring in complex and harsh engineering enviroments] Heriot-Watt, Edinburgh(2006).
[133] A. Barty, K. A. Nugent, D. Paganin *et al.*, "Quantitative optical phase microscopy," Optics Letters, 23(11), 817-819 (1998).
[134] E. D. Barone Nugent, A. Barty, and K. A. Nugent, "Quantitative phase amplitude microscopy I: Optical microscopy," Journal of Microscopy, 206(3), 194-203 (2002).
[135] K. A. Nugent, T. E. Gureyev, D. F. Cookson *et al.*, "Quantitative phase imaging using hard x rays," Physical Review Letters, 77(14), 2961-2964 (1996).
[136] A. Greenaway, "Seeing more clearly," Physics World, 23(8), 33-36 (2010).
[137] I. H. Malitson, "Interspecimen comparison of the refractive index of fused silica," Journal of the Optical Society of America, 55(10), 1205-1209 (1965).
[138] L. Rayleigh, "On the passage of electric waves through tubes, or the vibrations of dielectric cylinders," Philosophical Magazine, 43(261), 125-132 (1897).
[139] E. A. J. Marcatili, and R. A. Schmeltzer, "Hollow metallic and dielectric wave-guides for long distance optical transmission and lasers," The Bell System Technical Journal, 43, 1783-1809 (1964).
[140] Y. G. Han, B. H. Lee, W. T. Han *et al.*, "Resonance peak shift and dual peak separation of long-period fiber gratings for sensing applications," Photonics Technology Letters, IEEE, 13(7), 699-701 (2001).